Parity violating asymmetries in the G^0 experiment: Pion photoproduction on the Δ resonance

---

by

Alexandre F. C. Coppens

A thesis submitted to the Faculty of Graduate Studies of
The University of Manitoba
in partial fulfilment of the requirements for the degree of

DOCTOR OF PHILOSOPHY

Department of Physics and Astronomy
University of Manitoba
Winnipeg

ABSTRACT

Symmetry tests and more precisely parity violation experiments using the properties of the weak interaction give us unique insight into the internal hadronic structure of matter. The G^0 experiment at Jefferson Laboratory used parity violating electron scattering to probe the strange quark contribution to the electromagnetic nucleon form factors, G_M^s and G_E^s as well as the axial contribution, G_A^e. The data taken during the experiment provide further information on the axial transition form factor of the N - Δ transition, $G_{N\Delta}^A$, as well as the scale of the low energy constant d_Δ characterizing the parity violating $\gamma N\Delta$ coupling. The analysis of backward angle G^0 data taken with a liquid deuterium target to deduce the parity violating asymmetry for pion photoproduction on the Δ resonance, and the first experimental constraint on the value of d_Δ, are reported in this thesis. The results showed that $d_\Delta = (8.3 \pm 25.3)g_\pi$ where the uncertainty is dominated by statistics, and that 75 % of the theory range would be excluded by this measurement at 1 σ.

Acknowledgments

A person can consider themselves lucky to have one great advisor, I had the chance to have two of them; I want to thank my primary advisor, Dr. Shelley Page, first of all for allowing me to come to Canada to work on my PhD, but also for her precious help and support. Despite being a very busy person, she always had the time to help me when I needed the most, I learnt a lot from her and owe her a lot. I am also indebted to Dr. Jeff Martin who accepted to be my co-advisor when my thesis topic changed about a year from when I started. I want to thank him for his help, especially for sharing his expertise on the physics problems related to this work.

I would like to thank the committee members, Dr. Jim Birchall, Dr. Georg Schreckenbach and Dr. Gerald Gwinner for their advice and guidance. I would also like to thank the external examiner, Dr. David Hornidge.

I would certainly not be able to complete this work without the help of the G^0 collaboration. The first person that comes to my mind is the spokesperson, Dr. Doug Beck; I would like to thank him for allowing me to participate in this experiment. I wish to especially acknowledge Dr. Betsy Beise, Dr. Greg Smith, Dr. Dave Gaskell, Dr. Jean-Sebastien Real, Dr. Christophe Furget, Dr. Paul King, Dr. Damon Spayde, Dr. Brian Quinn, Dr. Peter Bosted, Dr. Herbert Breuer, Dr. Steve Wells, Dr. Larry Lee, Dr. Michael Gericke, Dr. Philippe Pillot and Dr. Dave Armstrong for their precious

help and advice. I would also like to thank the Analysis Coordinator, Dr. Fatiha Benmokhtar. I would like also to acknowledge the staff who worked on the accelerator side of the experiment, they did a great job.

I would like to thank all the fellow graduate students that worked with me on this experiment, Carissa Capuano 😁, Dr. Mat Muether 😉, Juliette Mammei 🙂, Dr. Maud Versteegen 🎧, Colleen Ellis 😛, John Schaub 😐 and Dr. Stephanie Bailey 😮.

I would like to thank Professor Willem T. H. Van Oers, leader of the Canadian G^0 collaboration, for his wise advice and his financial support. Many thanks also to Juris Svenne for reading carefully Chapter 1 of my thesis and Peter Blunden for his help on theoretical aspects for the simulation part of my analysis. I would like to acknowledge the secretary, Susan Beshta, who was very helpful when I struggled with administrative tasks. I also wish to acknowledge Peiqing Wang, who helped me finding my way around Winnipeg when I first arrived in Canada.

I wish to thank my friends (online and offline) for their support, Jon M., Jon T., Jon. Z, Tim, Larissa, Khatima, Yacine, Zakaria, Stasi, Adam, Chelsea, Marie Helene, Niel, Jonas... to name a few. To my brothers and sister, Jerome, Guillaume and Flavie, thank for supporting me. To my parents, I would not be where I am now without you.

The G^0 collaboration:[1] D. Androić, D. S. Armstrong, J. Arvieux[2], S. L. Bailey, D. H. Beck, E. J. Beise, J. Benesch, F. Benmokhtar, L. Bimbot, J. Birchall, P. Bosted, H. Breuer, C. L. Capuano, Y.-C. Chao, A. Coppens, C. A. Davis, C. Ellis, G. Flores, G. Franklin, C. Furget, D. Gaskell, M. T. W. Gericke, J. Grames, G. Guillard, J. Hansknecht, T. Horn, M. Jones, P. M. King, W. Korsch, S. Kox, L. Lee, J. Liu, A. Lung, J. Mammei, J. W. Martin, R. D. McKeown, M. Mihovilovic, A. Micherdzinska, H. Mkrtchyan, M. Muether, S. A. Page, V. Papavassiliou, S. F. Pate, S. K. Phillips, P. Pillot, M. L. Pitt, M. Poelker, B. Quinn, W. D. Ramsay, J.-S. Real, J. Roche, P. Roos, J. Schaub, T. Seva, N. Simicevic G. R. Smith, D. T. Spayde, M. Stutzman, R. Suleiman, V. Tadevosyan, W. T. H. van Oers, M. Versteegen, E. Voutier, W. Vulcan, S. P. Wells, S. E. Williamson, S. A. Wood.

---

[1] For G^0 in backward angle mode.

[2] Deceased.

Contents

List of Tables

List of Figures

List of Abbreviations

AA	Axial-Axial
ADC	Analog to Digital Converter
ARS	Analog Ring Sampler
AV	Axial-Vector
BPO	Beam Pick-Off
BCM	Beam Current Monitor
BCS	Beam Current Scan
BPM	Beam Position Monitor
CC	Charged Current
CEBAF	Continuous Electron Beam Accelerator Facility
CED	Cryostat Exit Detector
CFD	Constant Fraction Discriminator
CKM	Cabibbo Kobayashi Maskawa
CM	Center of Mass
CVC	Conserved Vector Current
DAQ	Data Acquisition
DC	Direct Current
DT	DeadTime
E1	Electric Dipole
EM	ElectroMagnetic
e-N	electron-nucleon
e-p	electron-proton
ET	Event Transfer
FPD	Focal Plane Detector
FPGA	Field Programmable Gate Array
FSI	Final State Interaction
GaAsP	Gallium-Arsenide-Phosphide
HC	Helicity Correlated
HPC	Helicity Pockels Cell
HWP	Half-Wave Plate
IARSSUM	Integrated ARS pulses summed over Cerenkov PMTs
IHWP	Insertable HWP
LD_2	Liquid Deuterium
LEC	Low Energy Constant
LH_2	Liquid Hydrogen
LPH	Low Power Heater
LUMI	Lumonisity Monitor
M1	Magnetic Dipole
MAID	Mainz unitary isobar model
MC	Monte Carlo
MPS	MacroPulse
MH	MultiHit
MT	Mean-Timer
NC	Neutral Current
NBM	Natural Beam Motion
NR	Non-Resonant

PC	Parity Conserving
PE	PhotoElectron
PID	Proportional Integral Differential
PMT	PhotoMultiplier Tube
PRL	Physical Review Letter
PV	Parity Violating
QED	Quantum Electro-Dynamics
QCD	Quantum Chromo-Dynamics
QRT	Quartet
RCS	Ratio of Counting to Statistics
RF	Radio Frequency
RHWP	Rotating HWP
RMS	Root Mean Square
ROC	Readout Controller
RSM	Resonance Saturation Model
SOS	Short Orbit Spectrometer
SMS	Superconducting Magnet System
SM	Standard Model
TDC	Time to Digital Converter
ToF	Time of Flight
TS	Trigger Supervisor
VA	Vector-Axial
VMD	Vector Meson Dominance
VV	Vector-Vector
χPT	Chiral Perturbation Theory

Chapter 1

Introduction

1.1 Theoretical background

The discovery that the weak interaction violates parity in 1956 contributed to the development of the Standard Model (SM) of the electroweak interaction of Weinberg, Salam and Glashow. In the 1980's, several experiments were proposed to use parity violation as a tool to probe the nucleon structure. This effort started with the SAMPLE experiment at the MIT-Bates laboratory, and was followed by HAPPEx and G^0 at Jefferson laboratory, and PVA4 at Mainz. The G^0 experiment done at Jefferson laboratory used parity violating (PV) asymmetries in elastic electron nucleon (e-N) scattering as a tool to measure the strange-quark contribution to the electromagnetic form factors and the weak axial form factor over a broad range of four-momentum transfer.

The G^0 apparatus in backward angle mode also made possible measurements of axial $N-\Delta$ transition form factors via PV asymmetries in inelastic e-N scattering, and also a measurement of the low energy constant (LEC) parameter d_Δ characterizing the weak $\gamma N\Delta$ coupling that enters in the radiative corrections required for the extraction of the axial $N-\Delta$ transition form factors. Parity violating asymmetry measurements of pion production on the $\Delta(1232)$ resonance in the photoproduction limit enabled the extraction of d_Δ. While its natural scale ($\sim 10^{-8}$) is almost 2 orders of magnitude below the sensitivity of the G^0 experiment, the resonance saturation model predicts potential enhancements of a factor 100, making a measurement of d_Δ possible in this context.

The topic of this thesis is the analysis of the G^0 data related to the pion asymmetry measurements and a preliminary extraction of the low energy constant d_Δ. An overview of the theory related to the form factors and also to the low energy constant d_Δ is given in this chapter. In particular, the resonance saturation model predicting a reasonable range of values for d_Δ will be discussed. At the end of this chapter, a review of previous experiments aiming at the extraction of the strange-quark contributions to the form factors $G_E^s(Q^2)$ and $G_M^s(Q^2)$ and a summary of available data on the axial $N-\Delta$ transition form factors are given. The second chapter focuses on details of the G^0 experiment in backward angle mode that collected data between August 2006 and March 2007 for the Q^2 values of 0.22 (GeV/c)^2 and 0.63 (GeV/c)^2, corresponding to electron beam energies of 362 and 687 MeV respectively. The main focus is on the lower energy data as the relevant pion asymmetry measurement was made possible at these kinematics. The analysis of the pion asymmetry data is discussed in Chapter 3 and an extraction of the LEC parameter d_Δ is described in Chapter 4.

1.1.1 e-N elastic scattering kinematics

To leading order in Quantum Electro-Dynamics (QED), the electron-Nucleon (e-N) elastic scattering process is described by the Feynman diagram in Figure 1.1. The notations used for a four-momentum k in this writing is $k : (\epsilon, \vec{k})$ where ϵ is an energy and $\vec{k}$ is a three-momentum. The four-momentum components are noted k^μ ($k^0 \equiv \epsilon$ and $(k^1, k^2, k^3) \equiv \vec{k}$). The expression for the four-momentum transfer squared carried by the virtual photon, $Q^2 = -q^2 > 0$, is obtained from conservation of four-momentum between the initial and final states of the scattered particles. It is written as:

$$\begin{aligned} Q^2 &= -q^2 = -(k_i - k_f)^2 \\ &= -2m_e^2 + 2(\epsilon_i \epsilon_f - \sqrt{\epsilon_i^2 - m_e^2}\sqrt{\epsilon_f^2 - m_e^2}\cos\theta_f) \quad (1.1) \\ Q^2 &= 4\epsilon_i \epsilon_f \sin^2\frac{\theta_f}{2} \quad (1.2) \end{aligned}$$

where $\epsilon_{i,f}$ and $\vec{k}_{i,f}$ are the energies and 3-momenta of the incoming and scattered electrons, m_e is the electron mass and θ_f is the electron scattering angle with respect to the incident electron direction. Equation (1.2) is the standard expression for Q^2 in high energy scattering when the electron mass can be neglected.

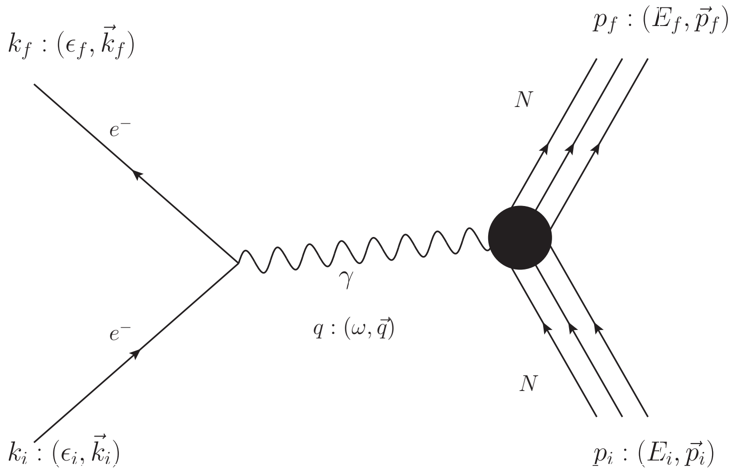

Figure 1.1: Feynman diagram of elastic electron proton scattering via γ boson exchange. The 3 lines on the right represent the 3 valence quarks of the nucleon. The four-momenta k , p and q correspond to the electron, nucleon and virtual photon respectively with an energy ϵ, E and ω. The three-momenta have the same notation as the four-momenta with the addition of an arrow at the top. The indices “i” and “f” correspond to the initial and final states.

1.1.2 Cross section and form factors

The elastic e-N scattering cross section can be derived from the interaction amplitude containing electromagnetic and neutral (weak) current contributions. Its differential form is written as [1]:

$$d\sigma = \frac{\overline{|\mathcal{M}|^2}}{4[(k_i \cdot p_i)^2 - m_e^2 M_N^2]} (2\pi)^4 \delta^{(4)}(k_f + p_f - k_i - p_i) \frac{d^3 k_f}{(2\pi)^2 2\epsilon_f} \frac{d^3 p_f}{(2\pi)^2 2E_f} \tag{1.3}$$

in which $k_{i,f}$ and $E_{i,f}$ are defined in Section 1.1.1, M_N is the mass of the nucleon and $\delta^{(4)}$ is the Dirac delta function. In Equation (1.3), $\overline{|\mathcal{M}|^2}$ is the spin average of the interaction amplitudes squared with:

$$\mathcal{M} = \mathcal{M}_\gamma + \mathcal{M}_Z \approx \mathcal{M}_\gamma \,. \tag{1.4}$$

The electromagnetic (EM) interaction amplitude ($\mathcal{M}_\gamma$) dominates, as its strength is 4 orders of magnitude larger than for the weak interaction ($\mathcal{M}_Z$), so the latter is neglected for unpolarized e-N scattering. The electromagnetic amplitude consists of the product between the electroweak currents of the electron and nucleons with a γ boson propagator in between [1] [2]:

$$\mathcal{M}_\gamma \quad = \quad 4\pi\alpha \mathcal{J}^{e,\mu}_{EM} \frac{g_{\mu\nu}}{Q^2} \mathcal{J}^{N,\nu}_{EM} \tag{1.5}$$

where $g_{\mu\nu}$ are the elements of the Minkowski tensor and $\alpha = e^2/(4\pi\varepsilon_0\hbar c)$ is the fine structure constant. $\mathcal{J}^{e,\mu}_{EM}$ and $\mathcal{J}^{N,\mu}_{EM}$ are the electromagnetic currents of the electron and nucleon respectively.

Assuming that the electrons are elementary spin 1/2 point-like particles, and denoting the initial and final states of said fermions $|k_i, s_i\rangle$ and $|k_f, s_f\rangle$ respectively, one can write the matrix elements of the electromagnetic current of the electron [1] [2]:

$$\mathcal{J}^{e,\mu}_{EM} \quad = \quad \langle k_f, s_f| \, \hat{\mathcal{J}}^{e,\mu}_{EM} \, |k_i, s_i\rangle = Q\bar{\mathcal{U}}(k_f, s_f)\gamma^\mu \mathcal{U}(k_i, s_i) \tag{1.6}$$

in which Q is the electric charge (in units of the electron charge: e) and γ^μ are the Dirac matrices [1] and $\bar{\mathcal{U}}(k,s)$ and $\mathcal{U}(k,s)$ are the Dirac spinors defined in the Dirac-Pauli representation as [1]:

$$\mathcal{U}(k,s) = \sqrt{E+m} \begin{pmatrix} \chi^{(s)} \\ \dfrac{\vec{\sigma}\cdot\vec{k}}{E+m}\chi^{(s)} \end{pmatrix} \tag{1.7}$$

with:

$$\chi^{(1)} = \begin{pmatrix} 1 \\ 0 \end{pmatrix}, \quad \chi^{(2)} = \begin{pmatrix} 0 \\ 1 \end{pmatrix} . \tag{1.8}$$

In Equation (1.7), $s = 1, 2$ is the index of the spin state of the particle, $\vec{\sigma}$ are the Pauli spin matrices and the product $\vec{\sigma}\cdot\hat{k}$ (where $\hat{k} = \vec{k}/k$) is the helicity operator [1] $\hat{h}$, with possible eigenvalues +1 or -1 (assuming $\vec{k}$ along the z axis) corresponding to $s = 1$ and 2 respectively.

Due to their extended structure, the nuclear electromagnetic currents are functions of the electric and magnetic form factors also known as the Sachs form factors [1], $G_E^{\gamma,N}$ and $G_M^{\gamma,N}$:

$$\mathcal{J}_{EM}^{\mu,N} \;=\; \bar{\mathcal{U}}(p_f,s_f)\left[G_M^{\gamma,N}\gamma^\mu - (p_f^\mu + p_i^\mu)\frac{1}{2M_N}\frac{G_M^{\gamma,N} - G_E^{\gamma,N}}{1+\tau}\right]\mathcal{U}(p_i,s_i) \tag{1.9}$$

where $\tau = Q^2/(2M_N^2)$ is a kinematic factor, p_f^μ and p_i^μ are the four-vector components of the initial and final nucleon momentum respectively, and the superscript N can refer to either a proton (p) or neutron (n). At $Q^2 = 0$, the electromagnetic form factors are normalized to the values of the nucleon electric charge and magnetic moments (in units of the nuclear magneton $\mu_N = e\hbar/(2m_p)$):

$$
\begin{aligned}
G_E^{p,\gamma}(0) &= 1, \; G_M^{p,\gamma}(0) = 2.793 && (1.10)\\
G_E^{n,\gamma}(0) &= 0, \; G_M^{n,\gamma}(0) = -1.931 \, . && (1.11)
\end{aligned}
$$

Replacing the electroweak currents in Equation (1.5) by their respective expressions (Equations (1.6) and (1.9)), the differential elastic cross section in the laboratory frame can be calculated from Equation (1.3) [1] and written as a product of the Mott cross section corresponding to point-like nucleons and a structure function containing the EM form factors of the nucleons:

$$
\begin{aligned}
\left.\frac{d\sigma}{d\Omega_f}\right|_{el} &\equiv \left(\frac{d\sigma}{d\Omega}\right)_{Mott} |F(Q^2)|^2 && (1.12)\\
&= \left(\frac{\alpha^2}{4\epsilon_i^2 \sin^4\frac{\theta}{2}}\right)\frac{\epsilon_f}{\epsilon_i}\left(\frac{(G_E^{N,\gamma})^2+(G_M^{N,\gamma})^2}{1+\tau}\cos^2\frac{\theta}{2}+2\tau(G_M^{N,\gamma})^2\sin^2\frac{\theta}{2}\right)
\end{aligned}
$$

where $d\Omega_f = d\phi_f d\cos\theta_f$ is the differential solid angle of the outgoing electron with respect to its incidental direction, $(d\sigma/d\Omega)_{Mott}$ is the Mott cross section for point-like particles and $F(Q^2)$ is the structure function containing the form factors. Equation (1.12) is known as the Rosenbluth formula [1] [3]. A set of measurements of the elastic cross section at different momentum transfers and scattering angles can be performed to extract the electromagnetic form factors, $G_M^{N,\gamma}(Q^2)$ and $G_E^{N,\gamma}(Q^2)$.

1.1.3 Parity violating e-N elastic asymmetries

In 1989, McKeown and Beck [4][5] proposed parity violating (PV) e-N elastic scattering as an experimental probe to measure the weak form factors of the proton, $G^{Z,p}_{E,M}$. The strategy is to use the parity violating nature of the weak interaction to enhance the sensitivity to $\mathcal{M}_Z$ neglected earlier and dependent on the weak nucleon form factors analogous to the EM form factors of Equation (1.9).

The Z^0 boson exchange contribution to the weak interaction amplitude corresponding to the Feynman diagram of Figure 1.2 is written as:

$$\mathcal{M}_Z = -\frac{G_F g_{\mu\nu}}{2\sqrt{2}} \mathcal{J}^{e,\mu}_{NC} \mathcal{J}^{N,\nu}_{NC} \tag{1.13}$$

where $G_F = 1.16637 \times 10^{-5}$ GeV^{-2} is the Fermi constant which governs the scale of the weak interaction. This expression is approximate for $Q^2 << M_Z^2$ where M_Z is the invariant mass of the Z^0 boson[1]. $\mathcal{J}^{e,\mu}_{NC}$ and $\mathcal{J}^{N,\mu}_{NC}$ are the electron and nucleon neutral currents (NC) respectively, they are defined as [1] [2]:

$$\begin{aligned} \mathcal{J}^{e,\mu}_{NC} &= \bar{\mathcal{U}}(k_f, s_f)\gamma^\mu (c_V + c_A \gamma^5)\mathcal{U}(k_i, s_i) \\ &\equiv \mathcal{J}^{e,\mu}_{NC,V} + \mathcal{J}^{e,\mu}_{NC,A} \end{aligned} \tag{1.14}$$

---

[1] This regime is appropriate for the present discussion, and hence the Z^0 boson propagator $1/(Q^2 - M_Z^2)$ has been intentionally omitted from Equation (1.13).

$$\begin{aligned}\mathcal{J}^{N,\mu}_{NC} &= \bar{\mathcal{U}}(p_f,s_f)\left[G_M^{Z,N}\gamma^\mu - (p_f^\mu+p_i^\mu)\frac{1}{2M_N}\frac{G_M^{Z,N}-G_E^{Z,N}}{1+\tau}+\gamma^\mu\gamma_5 G_A^{Z,N}\right]\mathcal{U}(p_i,s_i)\\ &\equiv \mathcal{J}^{N,\mu}_{NC,V}+\mathcal{J}^{N,\mu}_{NC,A} \qquad (1.15)\end{aligned}$$

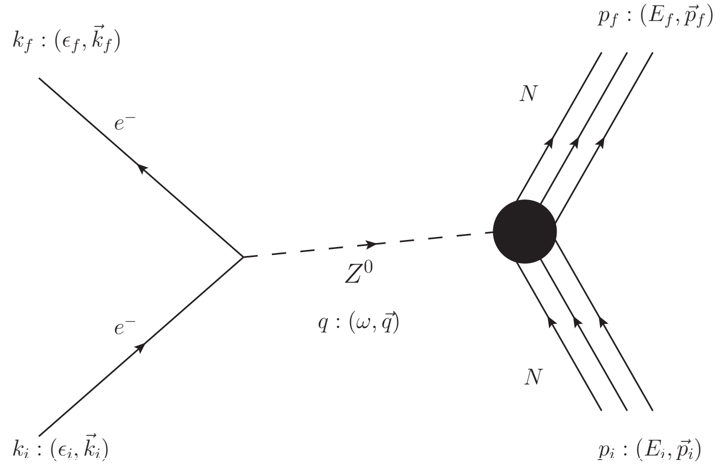

Figure 1.2: Feynman diagram of elastic electron proton scattering via Z^0 boson exchange. The 3 lines on the right represent the 3 valence quarks of the nucleon.

where c_V and c_A are the weak vector and axial charges of the electron respectively, γ^μ are the Dirac matrices and $\gamma^5 = i\gamma^0\gamma^1\gamma^2\gamma^3$. Note that the EM current operators defined in the previous section are pure Lorentz vectors whereas the neutral currents display both vector and axial contributions. Indeed, the neutral current of the nucleon not only contains the weak form factors, $G_E^{Z,N}$ and $G_M^{Z,N}$, but also axial form factors, $G_A^{Z,N}$.

For the electron weak current, c_V and c_A are given by [6]:

$$
\begin{aligned}
c_V &= 2T_3^f - 4\sin^2\theta_W Q && (1.16)\\
c_A &= -2T_3^f && (1.17)
\end{aligned}
$$

where T_3^f is the third isospin component of the fermion in the SU(2) weak isospin space and $\sin^2\theta_W = 0.2397 \pm 0.0013$ [7] displays the Weinberg angle, θ_W, also known as the weak mixing angle between U(1) and SU(2) [1]. Q is the electric charge in units of e in this context. A summary of the electric and weak vector/axial charges for the different elementary fermions is given in Table 1.1.

Fermion		Q	T_3^f	c_V	c_A
leptons	ν_e,ν_μ,ν_τ	0	$\frac{1}{2}$	1	-1
	e,μ,τ	-1	-$\frac{1}{2}$	$-1+4\sin^2\theta_W$	1
quarks	u,c,t	$\frac{2}{3}$	$\frac{1}{2}$	$1-\frac{8}{3}\sin^2\theta_W$	-1
	d,s,b	-$\frac{1}{3}$	- $\frac{1}{2}$	$-1+\frac{4}{3}\sin^2\theta_W$	1

Table 1.1: Electric (Q) and weak charges (c_V and c_A) of elementary fermions in the Standard Model.

According to Equations (1.13)-(1.15), the interaction amplitude contains axial-axial (AA), axial-vector (AV), vector-axial (VA) and vector-vector (VV) contributions. The axial part violates parity maximally while the vector part conserves parity. For a longitudinally polarized electron with helicity states $h = +1$ (right-handed: R) or -1 (left-handed: L), the following relations can be written:

$$\mathcal{M}^{PV}_{Z,R} = \mathcal{M}^{VA}_{Z,R} + \mathcal{M}^{AV}_{Z,R} = -\mathcal{M}^{PV}_{Z,L} \tag{1.18}$$

$$\mathcal{M}^{PC}_{Z,R} = \mathcal{M}^{VV}_{Z,R} + \mathcal{M}^{AA}_{Z,R} = \mathcal{M}^{PC}_{Z,L} \tag{1.19}$$

in which the superscripts PV and PC stand for parity violating and parity conserving respectively. An observable referred to as the parity-violating (PV) asymmetry can then be defined [8]:

$$A^{el}_{PV} = \frac{d\sigma_R - d\sigma_L}{d\sigma_R + d\sigma_L} = \frac{|\mathcal{M}^R|^2 - |\mathcal{M}^L|^2}{|\mathcal{M}^R|^2 + |\mathcal{M}^L|^2} = \frac{2\Re(\mathcal{M}^*_\gamma \mathcal{M}^{PV}_Z)}{|\mathcal{M}_\gamma|^2} \tag{1.20}$$

where $d\sigma_R(d\sigma_L)$ is the differential cross section for a right-handed(left-handed) electron scattering from an unpolarized target. The only term left in the numerator is the interference term between the EM and the parity violating part of the weak amplitude as all the other terms cancel since they do not depend on helicity. Only the dominant term $|\mathcal{M}_\gamma|^2$ was taken into account in the denominator of Equation (1.20). The scale of the PV asymmetry is 10^{-5} to 10^{-6}, which is given by relative size of the EM and weak couplings.

The parity violating asymmetry is a function of the electromagnetic and weak form factors, since the interaction amplitudes $\mathcal{M}_\gamma$ and $\mathcal{M}_Z$ contain the electroweak currents of the nucleons defined in Equations (1.9) and (1.15). After a standard calculation [9],

A_{PV}^{el} can be written as a function of the various form factors:

$$A_{PV}^{el} = -\frac{G_F Q^2}{2\sqrt{2}\pi\alpha}\left[\frac{\varepsilon G_E^\gamma G_E^Z + \tau G_M^\gamma G_M^Z - (1-4\sin^2\theta_W)\varepsilon' G_M^\gamma G_A^e}{\varepsilon (G_E^\gamma)^2 + \tau (G_M^\gamma)^2}\right] \tag{1.21}$$

where

$$\tau = \frac{Q^2}{2M_N^2}, \quad \varepsilon = \left[1 + 2(1+\tau)\tan^2\frac{\theta_f}{2}\right]^{-1}, \quad \varepsilon' = \sqrt{\tau(1+\tau)(1-\varepsilon^2)} \tag{1.22}$$

in which the electron mass is neglected ($Q^2 >> m_e^2$) in the expression for the transverse polarization (ε) of the virtual photon exchanged. Note that the asymmetry vanishes at zero four-momentum transfer; also, G_A^e appears instead of the previously defined G_A^Z as in Equation (1.15). In fact G_A^e is a notation for the effective weak axial form factor including significant radiative corrections ($\sim$ 30 %) [10] as opposed to G_E^Z and G_M^Z displaying minor radiative corrections. It should also be noted that the term $\varepsilon G_E^\gamma G_E^Z + \tau G_M^\gamma G_M^Z$ arises from $\mathcal{M}_Z^{VA}$ and the term $-(1-4\sin^2\theta_W)G_A^e$ from $\mathcal{M}_Z^{AV}$.

The nucleons are not elementary particles; they are comprised of quarks and gluons. The naive picture of the nucleon in the context of the Standard Model consists of 3 valence quarks. In a more accurate picture, massless gluons interact with each other to create virtual quark-antiquark pairs within the nucleon itself. Therefore, instead of the proton and neutron comprised of (uud) and (udd) exclusively, there is a small fraction of $u\bar{u}$, $d\bar{d}$ and $s\bar{s}$ configurations where u, d and s are the up, down and strange quarks.

Heavier quark contributions are highly suppressed [11] as the energy scale of Quantum Chromodynamics (QCD), Λ_{QCD} is 200 MeV, and the next lightest quark after s (with a mass of 95 MeV/c^2) on the mass scale is the charm with a mass of 1.25 GeV/c^2.

The electromagnetic and weak form factors contain contributions from the various quark flavours in the nucleon weighted by their EM and weak charges respectively as indicated in Table 1.1 [11] [2]:

$$G^{\gamma,N}_{E,M} = \frac{2}{3}G^{u}_{E,M} - \frac{1}{3}(G^{d}_{E,M} + G^{s}_{E,M}) \tag{1.23}$$

$$G^{Z,N}_{E,M} = \left[1 - \frac{8}{3}\sin^2\theta_W\right] G^{u}_{E,M} - \left[1 - \frac{4}{3}\sin^2\theta_W\right] (G^{d}_{E,M} + G^{s}_{E,M}) \tag{1.24}$$

where $G^{u}_{E,M}$, $G^{d}_{E,M}$ and $G^{s}_{E,M}$ are the electromagnetic form factors corresponding to the u, d and s quarks in the nucleon. Charge symmetry of the strong interaction implies that:

$$G^{u,p}_{E,M} = G^{d,n}_{E,M}, \quad G^{d,p}_{E,M} = G^{u,n}_{E,M}, \quad G^{s,p}_{E,M} = G^{s,n}_{E,M} \tag{1.25}$$

where the s flavour form factor is the same for both neutron and proton. The breaking of this symmetry is generally at the level of 1 % or less [12]. Given the current experimental level of precision for nucleon form factors, charge symmetry breaking can be neglected. Equations (1.23) and (1.24) will then become:

$$\begin{aligned}
G_{E,M}^{\gamma,p} &= \frac{2}{3}G_{E,M}^{u} - \frac{1}{3}(G_{E,M}^{d} + G_{E,M}^{s}) && (1.26)\\
G_{E,M}^{\gamma,n} &= \frac{2}{3}G_{E,M}^{d} - \frac{1}{3}(G_{E,M}^{u} + G_{E,M}^{s}) && (1.27)\\
G_{E,M}^{Z,p} &= \left[1 - \frac{8}{3}\sin^2\theta_W\right] G_{E,M}^{u} - \left[1 - \frac{4}{3}\sin^2\theta_W\right] (G_{E,M}^{d} + G_{E,M}^{s}) && (1.28)\\
G_{E,M}^{Z,n} &= \left[1 - \frac{8}{3}\sin^2\theta_W\right] G_{E,M}^{d} - \left[1 - \frac{4}{3}\sin^2\theta_W\right] (G_{E,M}^{u} + G_{E,M}^{s})\,. && (1.29)
\end{aligned}$$

The electromagnetic form factors of the nucleons, $G_{E,M}^{\gamma,p}$ and $G_{E,M}^{\gamma,n}$, have been extensively measured over the past 60 years; they are treated here as known quantities [13]. An experimental determination of $G_{E,M}^{Z,p}$ would then reduce Equations (1.26), (1.27) and (1.28) to 3 equations with 3 unknowns ($G_{E,M}^{u}$, $G_{E,M}^{d}$, $G_{E,M}^{s}$) which can be trivially solved. In that case, Equation (1.29) will also be fully determined.

Equation (1.21) is generic for both nucleons. Using $G_{E,M}^{Z,p}$ as described by Equation (1.28), Equation (1.21) can be rewritten as:

$$\begin{aligned}
A_{PV}^{el} &= -\frac{G_F Q^2}{4\sqrt{2}\pi\alpha}\frac{1}{\varepsilon(G_E^{\gamma,p})^2 + \tau(G_M^{\gamma,p})^2} && (1.30)\\
&\times \Big[(\varepsilon(G_E^{\gamma,p})^2 + \tau(G_M^{\gamma,p})^2)Q_W^p + (\varepsilon G_E^{\gamma,p}G_E^{\gamma,n} + \tau G_M^{\gamma,p})G_M^{\gamma,n})Q_W^n\\
&+ \varepsilon G_E^{\gamma,p}(G_E^s + \eta G_M^s)Q_W^{(0)} - \varepsilon'(1 - 4\sin^2\theta_W)G_M^{\gamma,p}G_A^e\Big]
\end{aligned}$$

where $\eta = \tau G_M^{\gamma,p}/(\epsilon G_E^{\gamma,p})$ and Q_W^p, Q_W^n, $Q_W^{(0)}$ are the weak charges of the proton and neutron and the singlet weak charge respectively. These are calculated from the elementary charges listed in Table 1.1:

$$Q_W^p = 2c_V^u + c_V^d = 1 - 4\sin^2\theta_W \tag{1.31}$$

$$Q_W^n = c_V^u + 2c_V^d = -1 \tag{1.32}$$

$$Q_W^{(0)} = c_V^u + c_V^d + c_V^s = -1\ . \tag{1.33}$$

Equation (1.30) shows that a measurement of A_{PV}^{el}, together with knowledge of $G_{E,M}^{\gamma,n}$ from previous experiments, and knowledge of G_A^e determines a linear combination of G_E^s and G_M^s. Therefore, as in the case of the Rosenbluth formula discussed previously, a set of measurements of this asymmetry for different kinematics (that is different values of η, ε and ε'), will allow to extract the strange flavour electromagnetic form factors, G_E^s and G_M^s.

Figure 1.3 illustrates the angular dependence of the kinematic factors η, ε and ε'. For small scattering angles, asymmetry measurements would be more sensitive to G_E^s, as ε is relatively larger than ε' and η, as shown in the figure. For larger scattering angles, which is the case for the G^0 experiment in backward angle mode, the kinematic parameter η increases as a function of Q^2 (as it is proportional to τ), providing an enhanced sensitivity to G_M^s. On the other hand, the sensitivity to G_A^e is increased since the value of ε is lower relatively to ε' as seen in Figure 1.3. This can lead to enhanced uncertainties in the extraction of G_E^s and G_M^s.

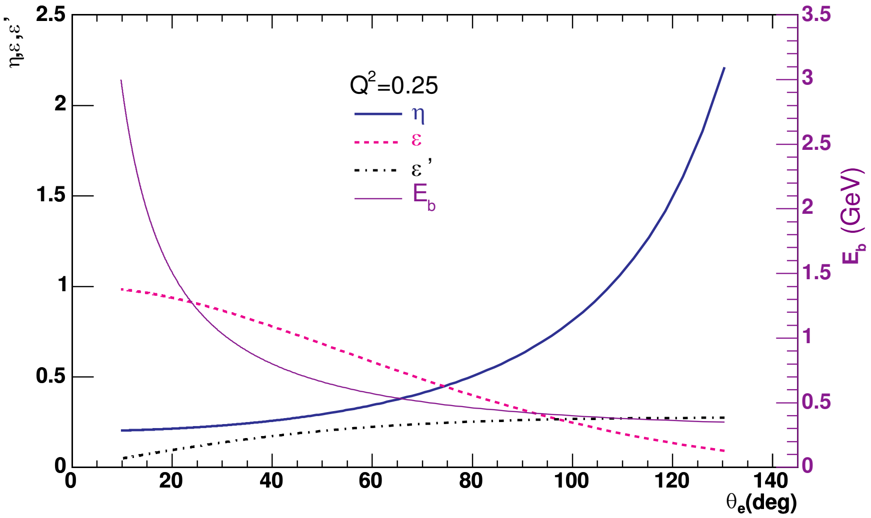

Figure 1.3: The dependence of η (blue solid), ε (pink dashed) and ε' (black dot-dashed) on the electron scattering angle for $Q^2 = 0.25$ (GeV/c)^2. The required beam energy (solid purple) at different angle is also overlaid. Figure taken from Ref. [2].

The uncertainty resulting from G_A^e can be resolved with the help of additional asymmetry measurements of quasielastic electron scattering with a deuterium target. Indeed, under the static approximation, the quasielastic asymmetry for scattering of electrons from deuterium is given by:

$$A_d = \frac{A_p \sigma_p + A_n \sigma_n}{\sigma_p + \sigma_n} \tag{1.34}$$

in which A_p (A_n) and σ_p (σ_n) are the asymmetries and cross sections for elastic scattering from the proton (neutron) respectively. It can be shown that the sensitivity of A_d to G_A^e is greater than for a proton measurement at backward angles [6]. The G^0 experiment includes measurements of parity violating asymmetries of electron-proton scattering at forward angles and electron-proton (and deuteron) scattering at backward angles to extract G_E^s, G_M^s and G_A^e. Both forward and backward angle measurements have already successfully been carried out and published [14] [15], and a summary of the results will be discussed in a later section.

1.1.4 Inelastic scattering asymmetry on the Δ resonance

The electron scattering process is said to be inelastic when the energy transfer ω is sufficient to make changes in the structure of the target nucleon. The Delta resonance, also referred to as $\Delta(1232)$, is the first excited state of the nucleon [7] with a mass and width of 1232 $(\mathrm{MeV/c})^2$ and 115 $(\mathrm{MeV/c})^2$, respectively. In the simple quark model, this resonance corresponds to a magnetic dipole excitation (M1) [16] leading to the spin-flip of one quark. The quantum numbers of the resonance corresponding to the total spin (J) and intrinsic parity (P) are $J^P = 3/2^+$. The $N - \Delta$ transition can occur through inelastic electron nucleon scattering if the energy transferred to the nucleon is at or near the resonance, ($\omega \approx 310$ MeV). Figure 1.4 shows a general Feynman diagram of this transition via inelastic e-N scattering.

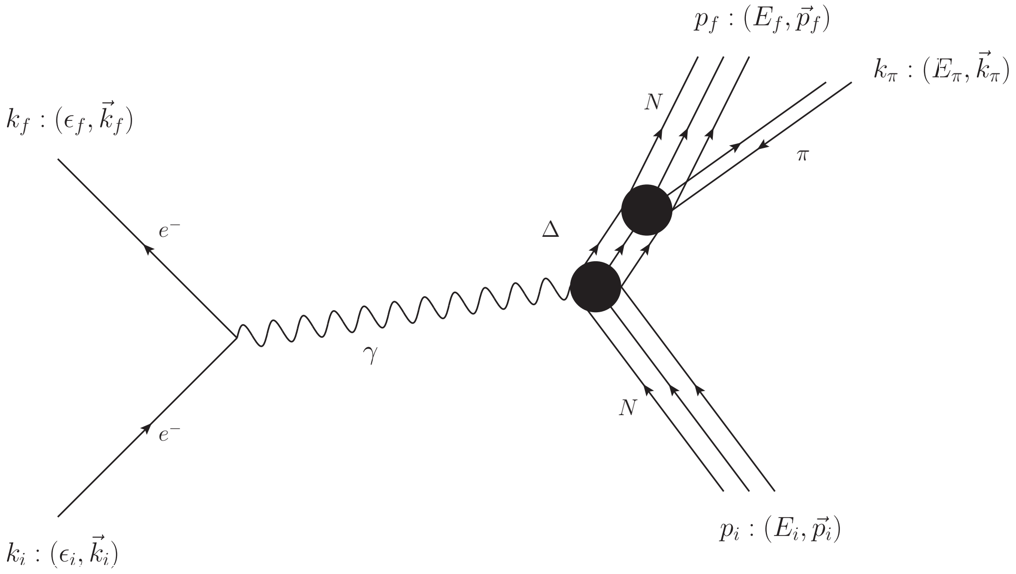

Figure 1.4: Feynman diagram of the $N - \Delta$ transition through virtual photon exchange from electron inelastic scattering. The dominant decay channel for the Δ is also represented, where a meson π is produced with four-momentum k_π, energy E_π and three-momentum $\vec{k}_\pi$.

Similarly to the elastic electron-nucleon scattering scenario described earlier, the PV inelastic asymmetry for the $N - \Delta$ transition can be calculated. The relevant processes are:

$$e + N \rightarrow e + \Delta \rightarrow e + N + \pi \qquad \text{Resonant} \qquad (1.35)$$

$$e + N \rightarrow e + N + \pi \qquad \text{Non-Resonant} \qquad (1.36)$$

where N is a nucleon, π is a pion and Δ is the resonance. Using the notation of Ref. [17], the inelastic asymmetry is written as:

$$A_{PV}^{inel} = \frac{d\sigma_R - d\sigma_L}{d\sigma_R + d\sigma_L} = -\frac{G_F}{\sqrt{2}}\frac{Q^2}{4\pi\alpha}[\Delta^\pi_{(1)} + \Delta^\pi_{(2)} + \Delta^\pi_{(3)}] \ . \qquad (1.37)$$

Each term of Equation (1.37) arises as an interference between PC amplitudes (as in Figure 1.4) and PV amplitudes (e.g. Figures 1.6 and 1.7) for Δ excitation. It will be seen later that only $\Delta^{\pi}_{(3)}$ can lead to a non-vanishing asymmetry at $Q^2 = 0$, due to its divergent $1/Q^2$ behaviour. $\Delta^{\pi}_{(1)}$ is an essentially structure independent resonant contribution arising from a vector coupling of the Z^0 to the hadronic current. $\Delta^{\pi}_{(2)}$ arises similarly to $\Delta^{\pi}_{(1)}$ but contains non-resonant background contributions. $\Delta^{\pi}_{(3)}$ is a PV transition form factor accounting for the axial vector response of the hadronic current; it contains the weak vector and axial transition form factors C_i^V and C_i^A ($i = 3..5$) respectively [17].

The three contributions to A_{PV}^{inel} described above are plotted in Figure 1.5 as functions of $|q^2| = -Q^2$, taken from Ref. [18]. The $\Delta^{\pi}_{(1)}$ and $\Delta^{\pi}_{(2)}$ contributions result in asymmetries that are approximately linear in Q^2 and vanish at $Q^2 = 0$. For $Q^2 \geq 0.05$ (GeV/c)^2, $\Delta^{\pi}_{(1)}$ gives the dominant contribution, and since it is essentially structure independent, this term is in fact the most reliably known; according to Ref. [18], $\Delta^{\pi}_{(1)} = 2(1 - 2\sin^2\theta_W) \approx 1.041$. The non-resonant nature of $\Delta^{\pi}_{(2)}$ means that it is intrinsically smaller than $\Delta^{\pi}_{(1)}$ and much more complicated to express [6].

As discussed in Ref. [18], the axial form factor contribution $\Delta^{\pi}_{(3)}$ is given by:

$$\Delta^{\pi}_{(3)} \approx 2(1 - 4\sin^2\theta_W)F(Q^2, s) \equiv \Delta^{\pi}_{(3)}(NC) \qquad (1.38)$$

where:

$$F(Q^2,s) = \frac{C_5^A}{C_3^V}\left[1 + \left(\frac{M_\Delta^2 - Q^2 - M_p^2}{2M_p}\right)\frac{C_4^A}{C_5^A} + \left(\frac{q_0 + W - M_p}{2M_p}\right)\frac{C_3^A}{C_5^A}\right]\mathcal{P}(Q^2,s) \tag{1.39}$$

where $P(Q^2, s)$ is a function of the kinematics and masses only and has a non-vanishing finite value at $Q^2 = 0$. Figure 1.5 illustrates the expected Q^2 dependence of $\Delta^\pi_{(3)}$, which incorporates a larger uncertainty due to radiative corrections especially at low Q^2. Note the high degree of cancellation in the scale factor $(1 - 4\sin^2\theta_W) \approx 0.04$ of Equation (1.38), which suppresses the overall scale of $\Delta^\pi_{(3)}$.

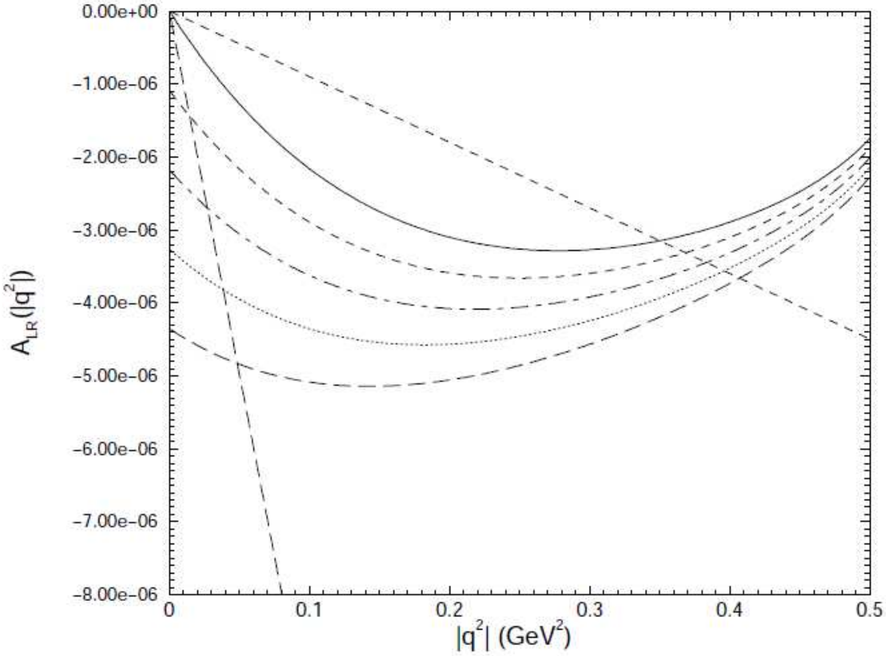

Figure 1.5: Different contributions to the inelastic asymmetries as a function of $|q^2|$. Vertical scale: $A_{LR}(|q^2|) \equiv A^{inel}_{PV}(Q^2)$. Horizontal scale: $|q^2| = Q^2$. The long-dashed/dashed straight line corresponds to $A^{inel}_{PV}(\Delta_{(1)})$ / $A^{inel}_{PV}(\Delta_{(2)})$ respectively. The curves represents different possibilities for $A^{inel}_{PV}(\Delta_{(3)})$ depending on the predicted size of the radiative corrections. This Figure, taken from Ref. [18], was produced for a beam energy of 424 MeV.

The function $F(Q^2, s)$ in Equation (1.38) contains the $N - \Delta$ transition form factors. Notably, the $N - \Delta$ transition is purely isovector, implying a change in spin $\Delta S = 1$. The consequence is that the asymmetry is not sensitive to the $\bar{s}s$ contributions to the form factors, which are isoscalar, in contrast to the elastic case.

The form factors $C_i^{V,A}$ are defined in the neutral current channel of Δ production. Making standard assumptions, they can be related to the electroproduction and weak charged current production of the Δ by performing a rotation in isospin space and exploiting the conserved vector current (CVC) hypothesis [19]. Measurements of the $N-\Delta$ transition axial form factors were performed in the weak charged current channel through neutrino excitation [20], and have considerably larger uncertainties than for the vector current channel. A measurement of the inelastic electron asymmetry on the $p - \Delta^+$ transition resonance could yield a significantly improved measure of the axial response of the nucleon in the neutral current channel which is a secondary goal of the G^0 experiment proposed in Ref. [21].

1.1.5 Radiative corrections to $\Delta_{(3)}^{\pi}$ and A_{PV}^{inel} at low Q^2

The goal of this thesis is a measurement of A_{PV}^{inel} at low Q^2. It was seen in Section 1.1.4 that this asymmetry is dominated by the $\Delta_{(3)}^{\pi}$ term in this regime. Radiative corrections can be potentially large at low Q^2 for the $\Delta_{(3)}^{\pi}$ term of the inelastic asymmetry, A_{PV}^{inel} [18]. There are two classes of contributions; the first involves "one quark" corrections that are calculable in the Standard Model. The second class of corrections, involves weak interactions between quarks in the hadron. From the work of S-L Zhu et al [22] [23] [10] [18], this type of correction was shown to generate considerable theoretical uncertainty in the PV, axial vector e-p amplitudes at low Q^2. The $\Delta^{\pi}_{(3)}$ term of the inelastic asymmetry can be expressed as a sum of the following contributions:

$$\Delta^{\pi}_{(3)}(TOT) = \Delta^{\pi}_{(3)}(NC) + \Delta^{\pi}_{(3)}(Siegert) + \Delta^{\pi}_{(3)}(anapole) + \Delta^{\pi}_{(3)}(d - wave) \quad (1.40)$$

where the first term corresponds to the neutral current contribution without the radiative corrections (see Equation (1.38)), the Siegert and anapole terms arise from the interference between PC M1 transition amplitude and the PV E1 amplitude described by the Feynman diagram in Figure 1.6. The PV $N\Delta\pi$ d-wave contribution arising from the diagram in Figure 1.7 was included in Figure 1.5 but can be neglected as its value is at least 1 order of magnitude lower for $0 < Q^2 < 1$ (GeV/c)^2 [18].

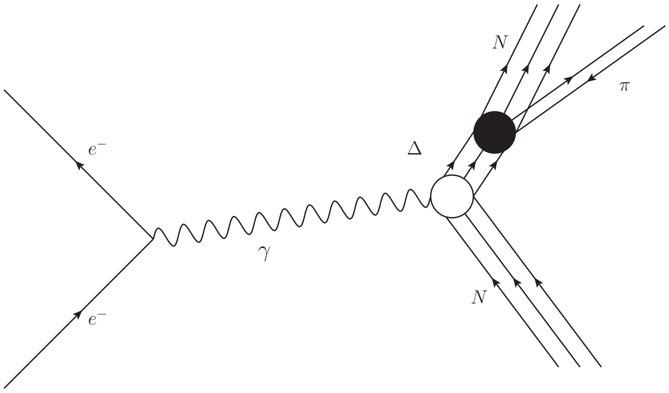

Figure 1.6: Feynman diagrams describing the Siegert and anapole contributions to resonant pion electroproduction. The empty circle located at the $\gamma N\Delta$ "vertex" indicates a parity violating coupling.

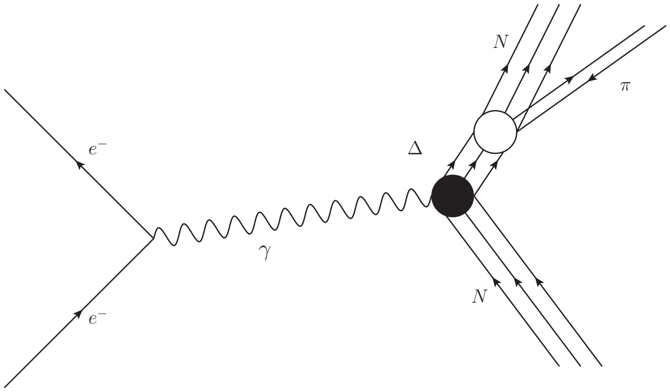

Figure 1.7: Feynman diagrams describing the d-wave contribution to resonant pion electroproduction. The empty circle located at the $N\Delta\pi$ "vertex" indicates a parity violating coupling.

The Siegert and anapole terms arise from the extended Siegert theorem [24] [25], giving a calculation framework for electric multipole transitions and thus making photonuclear experiments interpretable theoretically. The leading PV γ-nucleon coupling shown in Figure 1.6 corresponds to matrix elements of the parity-odd transverse electric dipole (E1) operator $\hat{T}^{E}_{J=1\lambda}$ ($\lambda = \pm 1$) which contains a Q^2 independent contribution and a term linear in Q^2. The corresponding asymmetry is an interference between a PC M1 transition amplitude and the PV E1 amplitude described above:

$$A^{T(E1)}_{LR} = \frac{2\Re(\mathcal{M}^{*}_{M1}\mathcal{M}_{E1})}{|\mathcal{M}_{M1}|^2} \tag{1.41}$$

where $\mathcal{M}_{M1}$ and $\mathcal{M}_{E1}$ are the corresponding matrix elements. Taking into account the $1/Q^2$ photon propagator in both amplitudes leads to a Q^2-independent contribution to the asymmetry (Siegert) and a term linear in Q^2 (anapole). According to the authors of Ref. [18], in the context of Heavy Baryon Chiral Perturbation Theory (HBχPT), these contributions to $\Delta^{\pi}_{(3)}$ can be written explicitly as:

$$\Delta^{\pi}_{(3)}(Siegert) = \frac{8\sqrt{2}\pi\alpha}{G_F Q^2}\frac{d_\Delta}{C_3^V}\frac{(\omega + W - M_N)}{2\Lambda_\chi}\mathcal{P}(Q^2, s) \quad (1.42)$$

$$\Delta^{\pi}_{(3)}(anapole) = \frac{8\sqrt{2}\pi\alpha}{G_F \Lambda_\chi^2}\frac{a_\Delta}{C_3^V}\mathcal{P}(Q^2, s) \quad (1.43)$$

where a_Δ, d_Δ are low energy constants (LECs) whose scale is set by hadronic weak interactions, W is the total energy in the virtual photon-nucleon center of mass and $\Lambda_\chi = 1.16$ GeV is the scale of chiral symmetry breaking [26]. The presence of the $1/Q^2$ factor in the Siegert term, as opposed to the other terms, leads to cancellation of the Q^2 dependence of the corresponding PV asymmetry defined in Equation (1.37). The low energy constants a_Δ and d_Δ have very large theoretical uncertainties and have never been measured experimentally. A comparison of the respective size of Equation (1.42) and (1.43) can be made assuming that $(\omega + W - M_N)/(2\Lambda_\chi) \approx 0.3$ near the resonance peak. If $a_\Delta \sim d_\Delta$, then the ratio of the two radiative corrections is written as:

$$\frac{\Delta^{\pi}_{(3)}(Siegert)}{\Delta^{\pi}_{(3)}(anapole)} \approx \frac{0.3\Lambda_\chi^2}{Q^2}\ . \quad (1.44)$$

In Equation (1.44), the Siegert term is the only non-vanishing contribution to the inelastic asymmetry in the photoproduction limit ($Q^2 = 0$). Therefore we can rewrite

Equation (1.37) as:

$$A_{PV}^{inel}(Q^2 \to 0) = -\frac{G_F Q^2}{\sqrt{2}4\pi\alpha}\Delta_{(3)}^{\pi} = C' d_\Delta \tag{1.45}$$

where the proportionality constant C' can be evaluated from Equation (1.42); in practise, the predictions of Figure 1.5 will be used to extract d_Δ from the asymmetry measurements as discussed in Chapter 4.

1.1.6 Predictions of d_Δ

The natural scale of d_Δ is set by the scale for charged current hadronic PV effects:

$$d_\Delta = g_\pi \approx \frac{G_F F_\pi^2}{2\sqrt{2}} = 3.8 \cdot 10^{-8} \tag{1.46}$$

in which $F_\pi \approx 94$ MeV is the pion decay constant as defined in Ref. [27] and g_π is the scale of weak charged current hadronic PV effects [28]. Possible enhancements from this natural scale arise in the context of the resonance saturation model (RSM) [29] [30] [31], which successfully predicts the measured ($\Delta S = 1$) amplitudes of hyperon[2] weak decays [32] [33]. The RSM is also the only model explaining the large parity violating asymmetries seen in their radiative decays. Indeed, the restrictions posed by Hara's theorem requires the vanishing[3] of the E1 term in the expressions for the hyperon radiative decay amplitudes in the SU(3) limit [34]. This also requires the vanishing of

---

[2] A hyperon is a baryon containing at least one strange quark.

[3] The E1 term would contain the tensor matrix element $\sigma_{\mu\nu}\gamma_5 F^{\mu\nu}$ (where $F^{\mu\nu}$ is the EM tensor), which is traceless.

the PV asymmetry of the decays. In the real world, SU(3) breaking considerations could lead to non-zero asymmetries [35] [36] [37] on the order of 0.1, but those effects are not sufficient to explain the very large asymmetries (~ 1) seen in decays such as $\Sigma^+ \to p + \gamma$ [7].

The Resonance Saturation Model features the inclusion of negative parity resonance intermediate states in the hyperon decay amplitudes. In practice, negative parity spin-1/2 octet baryons are coupled to their positive parity counterparts in the Lagrangian of the decay process. The same method can also be used to make predictions in the $\Delta S = 0$ channel[4] including $\gamma + n \to \Delta$ as studied in this thesis. This provides a reasonable range of possible values for the low energy constant d_Δ. The dominant part of d_Δ corresponds to the "counterterms" where the actual mixing with negative parity states occur. Because they are governed in part by the short-distance ($r < 1/\Lambda_\chi$) strong interaction, such terms are difficult to compute from first principles in QCD [18]. In order to estimate d_Δ^{CT}, contributions from $J^\pi = \frac{1}{2}^-$ and $\frac{3}{2}^-$ baryon resonances are considered, as shown in Figure 1.8. In that case, a pseudoscalar nonleptonic weak interaction mixes states of the same spin and opposite parity in the initial and final baryon states. The γ vertex is what generates the $\Delta J = 1$ transition. This mechanism is very similar to the one used to describe the hyperon decays.

---

[4] Meaning no change in the strangeness quantum number.

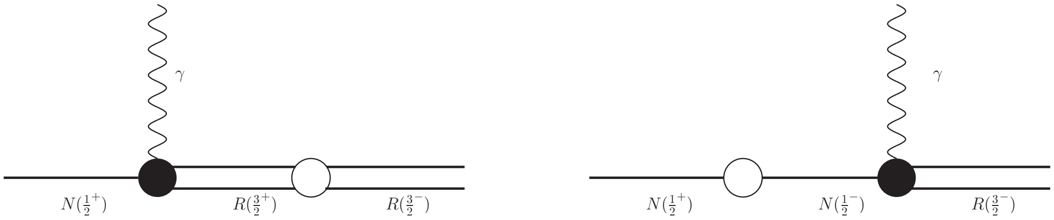

Figure 1.8: Feynman diagrams describing the resonance saturation contributions to d_Δ^{CT}. The empty circle represents a PV hadronic coupling. The labels R and N denote baryon resonance and nucleon respectively.

The estimation of d_Δ requires a number of considerations [18]:

- In contrast to the purely charged current (CC) $\Delta S = 1$ nonleptonic weak interaction, the Hamiltonian $\mathcal{H}_W^{PV}(\Delta S = 0)$ contains contributions from both charged and neutral currents. In addition, possible enhancements of the CC components of $\mathcal{H}_W^{PV}(\Delta S = 0)$ relative to $\mathcal{H}_W^{PV}(\Delta S = 1)$ might occur due to the ratio of the Cabibbo-Kobayashi-Maskawa (CKM) matrix elements [7], $V_{ud}/V_{us} \approx 4.5$. This can be understood naively from the fact that the $N - \Delta$ transition is not sensitive to the $\bar{s}s$ components of the "quark sea" as previously mentioned, in contrast to hyperon decays where the change in strangeness quantum number, $\Delta S = 1$.

- There is already a great deal of information available on the $\Delta S = 1$ hadronic weak interaction from hyperon decay data. This is not the case for $\Delta S = 0$. Therefore, the results from Ref. [29] are used for guidance to set the scale of the $\Delta S = 0$ amplitudes.

- The lowest lying well-established resonances which may contribute to the amplitudes of Figure 1.8 are $N(1520)$ with $I(J^\pi) = \frac{1}{2}(\frac{3}{2}^-)$ and $\Delta(1700)$ with $I(J^\pi) = \frac{3}{2}(\frac{3}{2}^-)$ [7]. The $J^\pi = \frac{1}{2}^-$ resonances are not included, as their transitions to the $\Delta(1232)$ have not been observed experimentally. Therefore, only contributions from the Feynman diagram on the left of Figure 1.8 are considered.

From the lowest EM and Weak Lagrangian contributions to Figure 1.8, the counterterm of d_Δ is expressed as [18]:

$$d_\Delta^{CT}(RES) = \frac{C_R W_R}{M_R - M_\Delta} \tag{1.47}$$

in which M_R is the mass of the intermediate negative parity resonance considered, C_R and W_R are constants for a given resonance R characterizing the electromagnetic and weak amplitudes respectively. From $N(1520)$ and $\Delta(1700)$ experimental decay widths, $|C_{1520}|$ and $|C_{1700}|$ are estimated to be 0.98 ± 0.05 and 0.70 ± 0.13 respectively. As for W_R, only its value in the $\Delta S = 1$ case is known from Ref. [29], which is $|W_R(\Delta S = 1)| \approx 2 \times 10^{-7}$ GeV. Hence the estimate for d_Δ is scaled by this quantity, giving [18]:

$$d_\Delta^{CT} \approx g_\pi \left[17 \frac{W_{1520}}{W_R(\Delta S = 1)} + 8 \frac{W_{1700}}{W_R(\Delta S = 1)} \right] \tag{1.48}$$

where there is an uncertainty due to the fact that only the absolute values of W_R and C_R are known. Hence, assuming $|W_R(\Delta S = 1)| = |W_R(\Delta S = 0)|$, the predicted range for the absolute value of d_Δ is $(9 \rightarrow 25)\ g_\pi$. As discussed above, possible enhancements could arise from V_{ud}/V_{us}, leading to a full range of $|d_\Delta| = (0 \rightarrow 100)\ g_\pi$. Table 1.2 summarizes the range of predictions [18] for the LECs d_Δ and a_Δ contributing to the radiative corrections of the inelastic asymmetries at low Q^2.

LEC	Best value	Reasonable range
$\vert d_\Delta(RES)\vert$	25 g_π	$(0 \to 100)$ g_π
$a_\Delta(VMD)$	15 g_π	$(-15 \to 70)$ g_π

Table 1.2: Best values and predicted ranges for the low energy constants that contribute to the radiative corrections of the inelastic asymmetry. The predicted range of values for a_Δ was calculated using Vector Meson Dominance [38] [18].

To first order, d_Δ is potentially the only contribution to the parity-violating asymmetry when $Q^2 = 0$. A non-vanishing a_Δ would give the asymmetry slope for $Q^2 \neq 0$ as seen from Equation (1.42) and (1.43). Theoretical uncertainties in the value of d_Δ can potentially have a great impact on the extraction of the axial $N - \Delta$ transition form factors. The impact of the measurement of d_Δ is discussed in Chapter 4.

1.1.7 Pion photoproduction on the Δ resonance

The value of d_Δ can be accessed experimentally through a measurement of pion production asymmetries on the Δ resonance in the photoproduction limit, that is, when the propagator of the electromagnetic interaction, γ, becomes a real photon. The process of interest pictured by the Feynman diagram of Figure 1.9 is:

$$\vec{\gamma} + n \to \Delta^0(1232) \to p + \pi^- \qquad (1.49)$$

where the arrow above γ emphasizes the polarization dependence of the process. Experimentally, the polarized photon beam is created via Bremsstrahlung radiation within the target arising from the high electron beam energy (362 MeV) in the G^0 experiment.

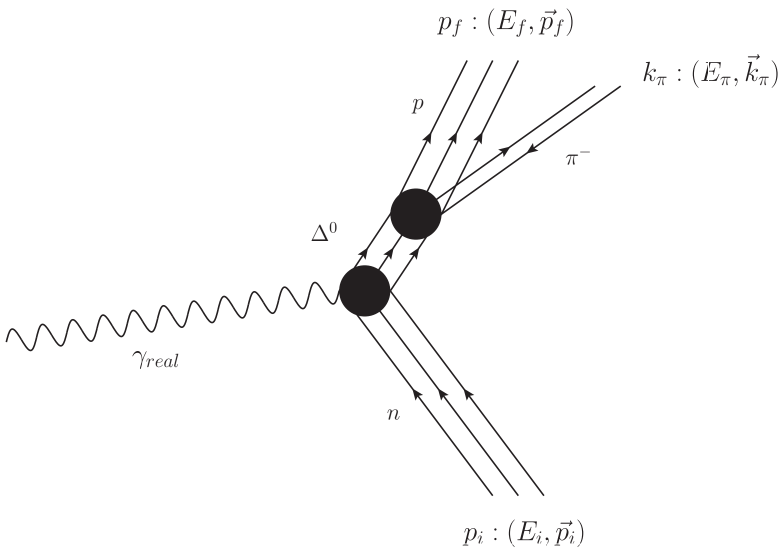

Figure 1.9: Feynman diagram describing resonant pion photoproduction.

In χPT, the parity violating asymmetry for pion photoproduction on the Δ^0 resonance, Equation (1.49), can be written to lowest order as [39]:

$$A^{\gamma}_{\pi^-} = -\frac{2d_\Delta^-}{C_3^V}\frac{M_N}{\Lambda_\chi} + ... \tag{1.50}$$

where C_3^V is the dominant $N - \Delta$ vector transition form factor and d_Δ^- is the LEC characterizing the weak $\gamma N \Delta$ coupling. The "..." in Equation (1.50) represents higher order contributions from non-resonant backgrounds. A few remarks have to be made regarding this equation. First, the photoproduction asymmetry corresponds to the $Q^2 = 0$ limit of A_{PV}^{inel} discussed in Section 1.1.4 (see Equation (1.45)). Secondly, an additional contribution to π^- production on the Δ^0 resonance of equivalent magnitude at very low four-momentum transfer ($Q^2 < 0.01$ (GeV/c)^2) has to be considered in the G^0 experiment:

$$e + n \rightarrow \Delta^0(1232) \rightarrow e + p + \pi^- \ . \tag{1.51}$$

Since the electro-/photo-production contributions cannot be separated experimentally, one has to estimate the respective size of the two contributions and perform an extrapolation to $Q^2 = 0$ of the virtual photon prediction using Figure 1.5. As mentioned earlier, the natural scale for d_Δ^- (where the "-" superscript means that the LEC is measured for π^- production) is 10^{-8}. However, as shown in Section 1.1.6, the magnitude of observed $\Delta S = 1$ PV asymmetries suggests enhancements of d_Δ^- up to the 10^{-6} scale.

1.1.8 Experimental observables and goals of the G^0 experiment

The experimental observables in the G^0 experiment are asymmetries between the scattering rates on a proton or deuteron target with an incident electron (or photon) polarized with helicity $h = +1$ (right-handed: R) and -1 (left-handed: L) respectively.

The G^0 experiment is sensitive to the following:

- A_{el}^{LR}: the elastic electron asymmetries (Equation (1.30)), which enable the extraction of the strange quark contribution to the form factors $G_E^s(Q^2)$, $G_M^s(Q^2)$ and the axial form factor G_A^e.
- A_{inel}^{LR}: the inelastic electron asymmetry (Equation (1.37)) containing the $N - \Delta$ transition axial form factors $C_i^A(Q^2)$.
- A_{π}^{LR}: the pion asymmetry, enabling a measurement of the low energy constant d_{Δ}.

The pion asymmetry A_{π}^{LR} is closely related to Equation (1.50). The focus of this thesis is on A_{π}^{LR} and the extraction of the low energy constant d_{Δ}^{-}. However an overview of the previous experiments on G_E^s, G_M^s and G_A^e will be discussed first, as this sets the context motivating the G^0 experiment, and of the pion asymmetry analysis.

1.2 Review of experimental data

In this section, a brief review of the past and present experiments on PV e-N scattering and a summary of the implications for G_E^s, G_M^s and G_A^e are provided. A discussion of the current data on the $N - \Delta$ transition form factors is also given.

1.2.1 Previous PV elastic e-N scattering experiments

Table 1.3 shows a summary of the recent measurements of G_E^s, G_M^s and G_A^e. Following the pioneering Prescott experiments which were pivotal in establishing the Weinberg-Salam electro-weak part of the Standard Model [40][41], SAMPLE [42][43][44] at MIT Bates was the first PV elastic e-N scattering experiment at low momentum transfer aimed at extracting these form factors; this was followed by PVA4 [45][46] at Mainz (Germany) and G^0 [47] in forward angle mode at Jefferson laboratory (in Hall C), then HAPPEx I and II [48][49][50][51] in Hall A of the same laboratory. The most recent experiments are the new HAPPEx measurement at $Q^2 = 0.1$ (GeV/c)^2 [51] and now G^0 in backward angle mode at $Q^2 = 0.22$ and 0.63 (GeV/c)^2 [15]. The kinematics leading to the sensitivity of forward and backward angle measurements to the various form factors are understood from the previous discussion at the end of Section 1.1.3 (see Figure 1.3).

Experiment	HAPPEx	SAMPLE	PVA4	G^0 Forward	G^0 Backward
Facility	J. Lab	MIT Bates	Mainz	J. lab	J. lab
Target	H, ^{4}He	H, D	H	H	H, D
Sensitivity	G_E^s, G_M^s	G_M^s, G_A^e	G_E^s, G_M^s	$G_E^s + \eta G_M^s$	$G_E^s + \eta G_M^s$, G_A^e
Q^2 (GeV/c)^2	0.1, 0.48	0.04, 0.1	0.1, 0.23	0.12 - 1.0	0.22 , 0.62
θ_f	Forward	Backward	F / B	Forward	Backward

Table 1.3: Summary of previous PV e-N scattering experiments with their respective main kinematic settings and sensitivity to the form factors. The G^0 backward kinematics are also shown.

1.2.2 The G^0 Experiment

The G^0 experiment [52] aimed at measuring accurately over a broad range of Q^2 the strange quark contributions to the elastic nucleon form factors. The main feature that differentiates the G^0 experiment in forward angle [53] [47] mode from previous experiments is the broad range of Q^2 it covered. Combined with the backward angle mode, G^0 is also the most complete measurement, as it is sensitive to all 3 contributions G_E^s, G_M^s and G_A^e. For this purpose, the G^0 experiment makes use of the electron beam accelerator located at the Jefferson laboratory, Newport News, VA. The latter can accelerate electrons up to 6 GeV, with a polarization of more than 80 % and with helicity correlated beam properties small enough to achieve PV scattering asymmetry measurements at the part per million (ppm) level.

A key feature of the G^0 experiment is that the same basic equipment can be used to perform both forward and backward angle measurements. Kinematic considerations and the design of the detection apparatus lead to dramatically different Q^2 acceptances for the G^0 experiment in forward and backward angle mode. In forward angle configuration, G^0 measured A_{PV}^{el} for a wide range of Q^2 simultaneously (see Figure 1.10). In contrast, the backward angle measurements were done at two averaged values of Q^2, specifically 0.22 and 0.62 $(\mathrm{GeV/c})^2$, set by two different beam energies, 687 and 362 MeV respectively. Details of the G^0 apparatus and experimental conditions are discussed in Chapter 2.

1.2.3 Global data on G_E^s, G_M^s and G_A^e

The results from the forward angle measurements [47] of G^0 are shown in Figure 1.10. The inner error bars are purely statistical and the outer error bars are the total point to point experimental errors. The grey bar at the bottom of Figure 1.10 corresponds to model dependent errors and the bar at the top of the figure represents global systematic errors. The results from the G^0 experiment at forward angle and HAPPEx show a small systematic positive trend for $G_E^s + \eta G_M^s$ suggesting that either G_E^s or G_M^s differ from 0 at some values of Q^2. The HAPPEx measurements, shown as diamonds, are consistent with zero.

Extracted values of G_E^s, G_M^s and G_A^e from the G^0 experiment in backward angle mode combined with the forward angle measurements are summarized in Figure 1.11 [15]. The square data points correspond to the results from the G^0 experiment in backward angle mode combined with the forward angle results at similar Q^2 values. For G_E^s and G_M^s, the round data points correspond to the PVA4 measurement at $Q^2 = 0.22$

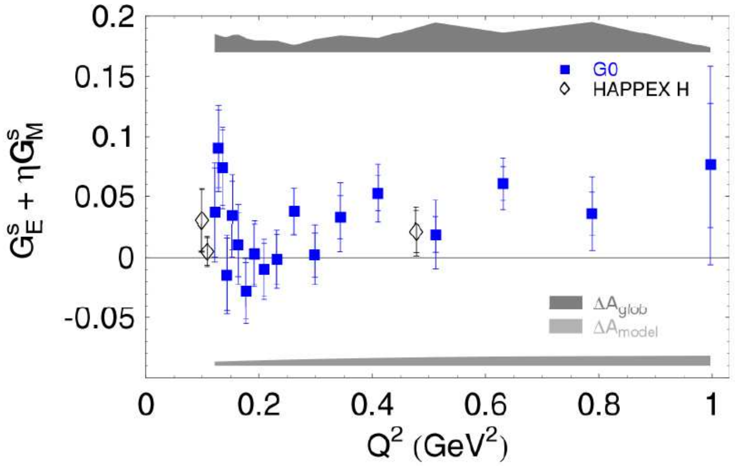

Figure 1.10: G^0 forward angle result: $G_E^s + \eta G_M^s$ as a function of Q^2. Description of the Figure (taken from Ref. [54]) is in the text.

(GeV/c)^2 [45]. The triangles represent a global fit of the available data on G_E^s and G_M^s near $Q^2 = 0.1$ (GeV/c)^2 performed by the authors of Ref. [55]. The results indicate that the strange quark contribution to the elastic charge and magnetic form factors of the nucleons is less than 10 %. The non-zero value of G_E^s at $Q^2 = 0.63$ (GeV/c)^2 arises from the results of G^0 measurements in forward angle mode (see Figure 1.10). Future forward angle experiments at $Q^2 = 0.63$ (GeV/c)^2 at Jefferson Lab and Mainz will further improve the accuracy of the precision of these determinations. Recent calculations from Adelaide [56] [57] [58] (brown bars) and Kentucky [59] (empty triangles) groups are also shown.

The results of the G^0 experiment for G_A^e are shown in the bottom graph of Figure 1.11. The diamond-shaped data point at low Q^2 is a calculation from the authors of Ref. [10] and the triangles are from the SAMPLE measurements [44]. A parametrization of

$G^e_{A,cc}$ measured through charged current neutrino scattering and corresponding to G^e_A to lowest order is also drawn in Figure 1.11 [60].

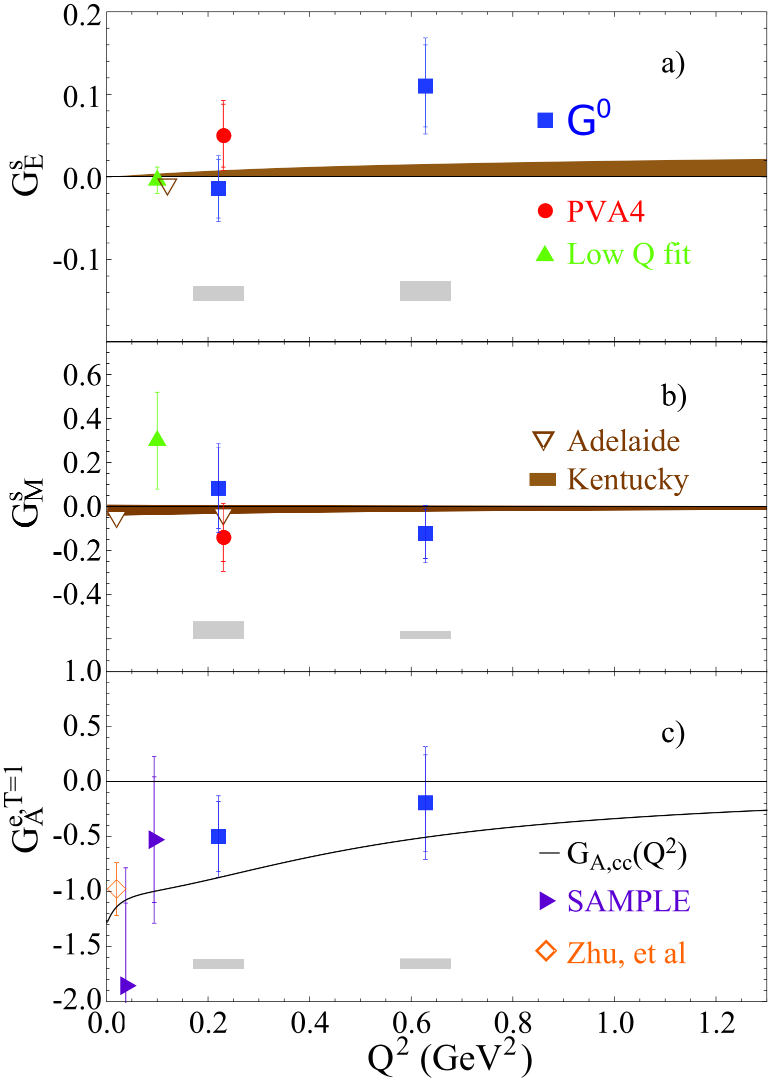

Figure 1.11: The form factors G^s_E (a), G^s_M (b) and G^e_A (c) determined by the forward and backward angle modes of the G^0 experiment. Error bars show statistical and statistical plus point-to-point systematic uncertainties (added in quadrature). Shaded bars below the corresponding points show global systematic uncertainties (for G^0). A description of the various data points is in the text. Figure taken from Ref. [15].

1.2.4 N-Δ transition form factors

Presently, there exist considerable data on the vector current transition form factors C_i^V which have been obtained with electromagnetic probes. A comparison of these experimentally determined quantities to theoretical predictions points to significant disagreement [17]. Both lattice QCD calculations [61] and spin-flavour SU(6) based constituent quark models [62], for example, underpredict the data by $\sim 30\%$. In contrast, only a limited amount of data exist for the axial transition form factors C_i^A [20], obtained from charged current experiments, and these data have considerably larger uncertainties than the vector current form factors.

The form of the $C_i^{V,A}$ that best fit the data so far is given by the Adler parametrization [63]:

$$C_i^A(Q^2) = C_i^A(0)\left(1+\frac{a_iQ^2}{b_i+Q^2}\right)\left(1+\frac{Q^2}{M_A^2}\right)^{-1} \tag{1.52}$$

$$C_i^V(Q^2) = C_i^V(0)\left(1+\frac{Q^2}{M_V^2}\right)^{-1} \tag{1.53}$$

where $C_i^{A,V}(0)$, a_i and b_i are the model-dependent axial-vector form-factor parameters determined for the Adler model [17]. In Equation (1.52) and (1.53), the Q^2 dependence is mainly a function of the vector and axial masses, $M_V \approx 0.85$ GeV/c^2 and $M_A \approx 1$ GeV/c^2 which are determined experimentally [20]. The current values of C_i^A are incorporated in the prediction of A_{PV}^{inel} of Figure 1.5 that will be used to extract d_Δ from the G^0 experimental data.

There are currently no experimental data on the axial N-Δ transition form factors in the neutral current channel, which the G^0 experiment aimed to address. Given the large theoretical uncertainties from radiative corrections described earlier, a measurement of the low energy constant d_Δ is important for the extraction of the C_i^A's in the neutral current sector. This measurement is the main topic of this thesis.

Chapter 2

The G^0 experiment

The G^0 apparatus was designed to have a large acceptance for e-p scattering in forward and backward angle mode to measure PV asymmetries for a wide range of Q^2. The scattered recoil proton (forward) or electron (backward) momenta were analyzed in a large superconducting toroid spectrometer and detected in arrays of scintillation counters. The detector/magnet configuration was physically reversed in the experimental hall to go from forward to backward angle mode, and additional instrumentation was added for particle identification in backward angle mode. The original proposal [52] of the G^0 experiment was first approved in 1993. Since then, the forward angle measurements were performed, and the results were published [47] in 2005. For the backward angle measurements, data were collected in 2006-2007, and results for the main data were published [15]. Table 2.1 gives the main milestones related to the G^0 experiment.

Year	Event
1993	First Proposal
2003	Installation
2004	Forward angle data taking
2005	Publication of forward angle results
2006/2007	Backward angle data taking
2009	Backward angle results (PRL)

Table 2.1: Main milestones related of G^0 experiment.

The details of the G^0 backward angle apparatus will be discussed in this chapter, but a brief comparison with the forward mode is needed, to understand its current design.

2.1 The G^0 experiment at forward angle

Figure 2.1 summarizes the design of the G^0 apparatus in forward angle mode. Polarized electrons accelerated to 3.03 GeV were scattered from a 20 cm liquid hydrogen target. The recoil protons were deflected by the Superconducting Magnet System (SMS) onto 8 azimuthally arranged sets (octants) of 16 scintillator bars, also referred to as Focal Plane Detectors (FPDs). Essentially, each scintillator defines a separate Q^2 bin for the scattered electrons. The large range of Q^2, from 0.1 to 1 $(\mathrm{GeV/c})^2$, results from the large acceptance created by the combination of the SMS and the FPDs. The G^0 experiment at forward angle was a "counting" mode experiment, in which the time of flight (ToF) of the particles between the target and the FPDs was used to identify and count the recoil protons corresponding to e-p elastic scattering. Given the geometry and kinematics, this ToF separation of the scattered particles could be achieved only if the electron beam was pulsed at a relatively low frequency (31 MHz) compared to the accelerator RF.

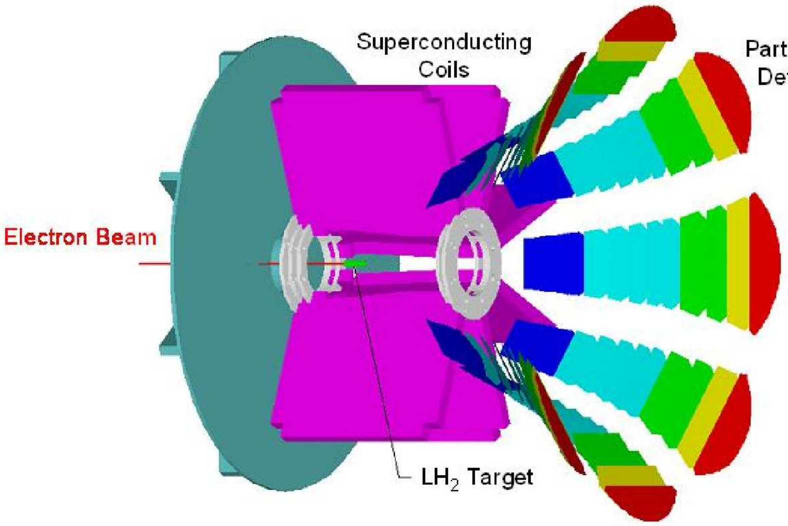

Figure 2.1: An overview of the G^0 forward angle setup. The superconducting magnet coils are shown in purple. The colored bars on the right are the FPDs. One octant was removed from the picture for clarity. Figure taken from [2].

Figure 2.2 shows an example of a ToF spectrum for FPD 8, where we see a clear elastic peak corresponding to the recoil protons and a secondary peak coming from π^+. There is also a broader inelastic spectrum underneath the main peaks. Details on data analysis related to the forward angle measurement are found in [2].

2.2 Comparison with backward angle measurements

A schematic of the G^0 apparatus in forward and backward angle modes is given in Figure 2.3. The target is located at the center of the magnet system. This allows the magnet to deflect the final state particles one way or another simply by reversing the polarity of the power supply. At forward angles, since the outgoing electrons are very

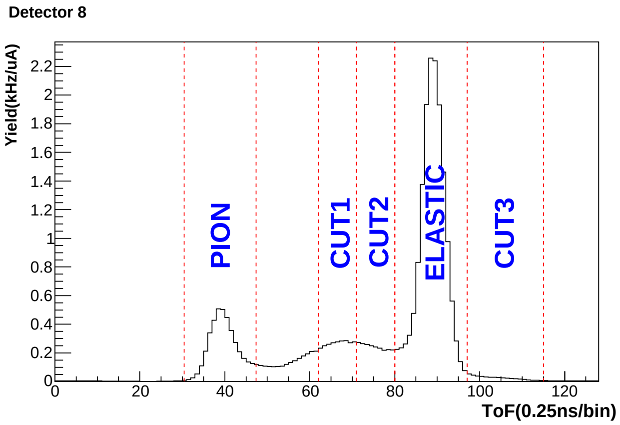

Figure 2.2: ToF spectrum for FPD 8 in the G^0 experiment at forward angle. Figure taken from [2].

close to the beam line, the recoil protons were detected instead.

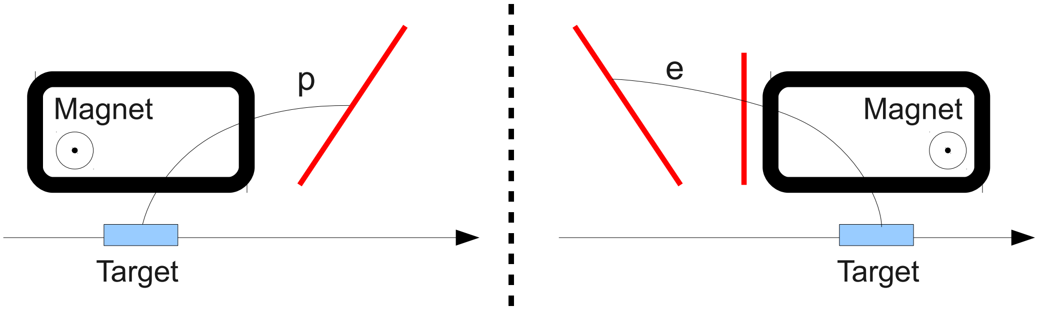

Figure 2.3: Schematic of the G^0 apparatus in forward and backward angle modes. The red bars represent arrays of detectors, and the arrows represent the direction of the electron beam.

The reaction kinematics have implications for the method used to track particles at forward and backward angles. At forward angles, the time needed by a proton to reach the detectors starting from the target is relatively large (22 ns) due to its mass. This makes a time of flight method appropriate to track and count recoil protons as shown previously in Figure 2.2. This can be done if the beam is pulsed at a frequency of

$1/(22 \times 10^{-9}) \approx 45$ MHz or lower. At backward angles, the scattered electrons are relatively faster, but also the scattering cross section is smaller. To achieve a comparable statistical accuracy, the beam current has to be higher, and a time of flight method cannot be used for particle identification. Therefore, additional detectors were added for particle identification to use the G^0 apparatus in coincidence mode at backward angles.

There are differences in the covered kinematic ranges for elastic scattering between the forward angle and backward angle modes of the experiment. At backward angle, the outgoing electrons are highly relativistic due to their light mass; therefore, the magnetic field only selects a narrow range of angles. At forward angle, the recoil protons have a much broader range of velocities, leading to an increased acceptance with respect to the spectrometer. Given the higher beam energy at forward angle, this translates into a wider range of Q^2 acceptance, as shown in Figure 2.4.

At backward angle, the detectors cover a narrow range of angles (0.07 rad). Therefore the backward angle measurements are done at two averaged values of Q^2, specifically 0.22 and 0.62 $(\mathrm{GeV/c})^2$, set by two different beam energies, 362 and 687 MeV respectively. The description of the G^0 apparatus in the next sections is focused on the 362 MeV data set with the LD_2 target, as the measurement of pion photoproduction asymmetries on the Δ resonance was possible at this particular energy/target setting. While a few references to the 687 MeV data set are given in this writing, a full discussion of the G^0 apparatus for all data sets is given in Ref. [8].

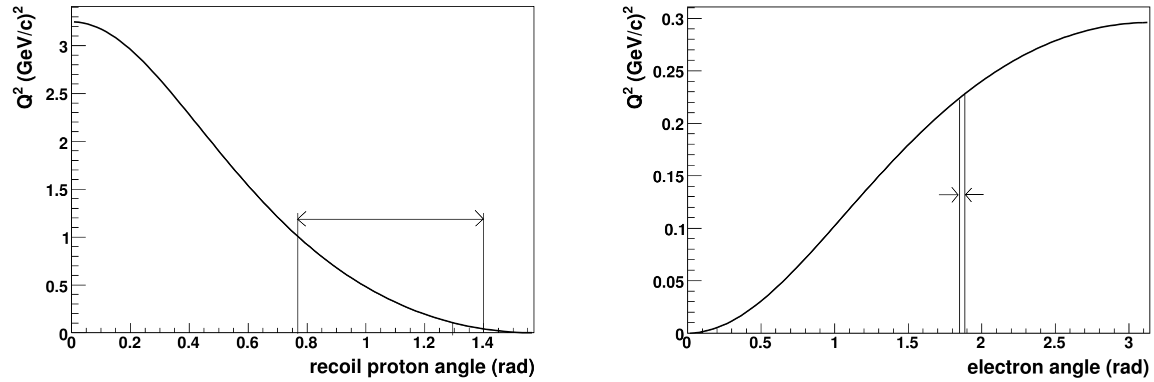

Figure 2.4: Four-momentum transfer versus scattering angle for recoil protons at forward angle on the left (beam energy is 3 GeV) and for scattered electrons at backward angle on the right (beam energy is 362 MeV) on the right. The angular acceptance of the apparatus is indicated by the vertical bands shown on the graphs.

2.3 G^0 apparatus in backward angle configuration

The G^0 backward angle measurements were made with liquid hydrogen and deuterium targets. For the LH_2 target cell, the G^0 apparatus in backward angle configuration is sensitive to the following processes:

$$\text{elastic:} \qquad e + p \to \underline{e} + p \tag{2.1}$$

$$\text{inelastic:} \qquad \begin{cases} e + p \to e + \Delta^+ \to e + p + \underline{\pi}^0 \\ \gamma + p \to \Delta^+ \to p + \underline{\pi}^0 \end{cases} \tag{2.2}$$

where the particles detected by the apparatus are underlined.

The neutron target is indirectly provided by liquid deuterium (LD_2). In that case, the apparatus is sensitive to additional processes:

$$\text{quasi-elastic:} \qquad e + n \rightarrow \underline{e} + n \tag{2.3}$$

$$\text{inelastic } (\pi^0)\text{:} \qquad \begin{cases} e + n \rightarrow e + \Delta^0 \rightarrow e + n + \underline{\pi}^0 \\ \gamma + n \rightarrow \Delta^0(1232) \rightarrow \gamma + n + \underline{\pi}^0 \end{cases} \tag{2.4}$$

$$\text{inelastic } (\pi^-)\text{:} \qquad \begin{cases} e + n \rightarrow e + \Delta^0(1232) \rightarrow e + p + \underline{\pi}^- \\ \gamma + n \rightarrow \Delta^0(1232) \rightarrow \gamma + p + \underline{\pi}^- \end{cases} \tag{2.5}$$

The neutral pions are detected indirectly through their decays:

$$\pi^0 \rightarrow \gamma + \gamma \rightarrow 2\underline{e}^+ + 2\underline{e}^- \tag{2.6}$$

Elastic scattering (2.1) with a proton target, and quasielastic scattering (2.3) from a neutron target are the processes of interest for the primary goal for the G^0 experiment. The two inelastic processes (2.5) are the ones of interest for the measurements of π^- asymmetries in the photoproduction limit and thus for the extraction of d_Δ. Section 3.9 of Chapter 3 will provide a detailed simulation of π^- production for the G^0 experiment at backward angle with a beam energy of 362 MeV and a LD_2 target and will demonstrate that $\langle Q^2 \rangle < 0.01$ $(\text{GeV/c})^2$ in that configuration.

The contributions to the expected rates in the G^0 apparatus with an LD_2 target at a beam energy of 362 MeV are listed in Table 2.2. This shows that negatively charged pions are the most significant source of background for the quasi-elastic electron data. This demonstrates the need for an additional particle identification system with a high efficiency for detection of electrons and a π^- rejection factor of 1/100 or better in order to measure quasi-elastic electron asymmetries. The absence of inelastic electron rates for a beam energy of 362 MeV is due to the low energy and the spectrometer acceptance.

Particle	Reaction number	Expected Rates ($kHz/\mu A$)
Quasi-elastic e^-	(2.1),(2.3)	100
π^-	(2.5)	160 (320)
Inelastic e^-	$e + N \rightarrow \Delta \rightarrow \underline{e} + N' + \pi$	0
π^0	(2.2),(2.4),(2.6)	7

Table 2.2: Total expected rates in the G^0 apparatus for the backward angle measurement with a beam energy of 362 MeV and a LD_2 target. The rates are normalized to the beam current given in μA. The number in parentheses for the expected π^- rates comes from the early simulations performed before the running of the G^0 experiment at backward angle. No inelastic electrons are expected to be detected at 362 MeV as they lose too much energy during the inelastic scattering process. Inelastic electrons are detected at the higher beam energy, 687 MeV.

The main requirements that guided the design of the apparatus were as follows:

- Detect outgoing electrons for elastic and inelastic asymmetries: The separation between elastic and inelastic events was achieved through the use of a toroidal superconducting magnet spectrometer and coincidences between scintillation detectors (CED-FPD).

- Identify particles, mainly to suppress π^- background: The identification was done through a third coincidence with a Cerenkov detector. The pion events were also recorded for the measurement of d_Δ, as discussed above.
- Count raw detector rates of a few MHz and correlate them with the beam structure: A custom data acquisition system combined with fast electronics was used to resolve all the coincidences and also to collect data from ancillary measurements.

The high π^- rates, and the requirements for an additional particle identification system, also enabled a measurement of pion asymmetries to be made concurrently with the quasi-elastic electron asymmetries using the same apparatus and electron beam.

An overview of the G^0 apparatus in backward angle mode is pictured in Figure 2.5. The detector package consists of 8 sectors also referred to as octants, arranged symmetrically around the beam line. One octant contains two arrays of scintillator bars; the Cryostat Exit Detectors (CED) and the FPDs. There is also a Cerenkov detector located at the exit of the CEDs with respect to the outgoing particles from the target to perform the identification between pion and electron tracks.

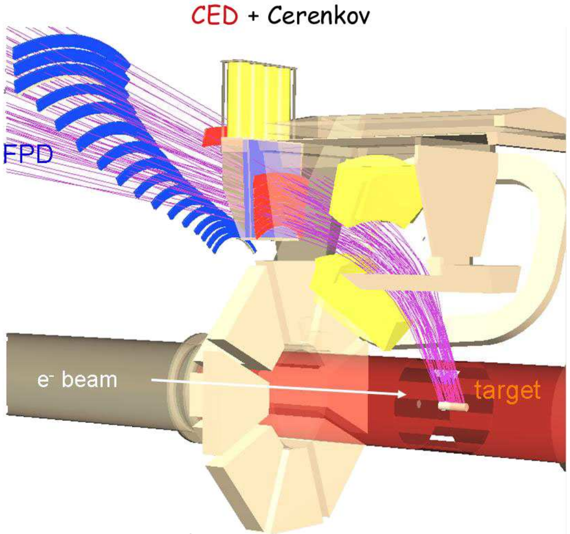

Figure 2.5: Simplified view of the G^0 apparatus for one octant. The blue (FPD) and red (CED) bars represent the arrays of scintillators. The yellow blocks on the right represent the collimator system.

2.3.1 Beam requirements

To achieve the statistical and systematic accuracy required to measure parity violating asymmetries in e-p and e-n scattering at the part per million level, a polarized electron beam, with helicity correlated parameters small enough to not generate any significant false asymmetries is required. Appropriate values for those beam parameters were defined in Ref. [64] and are listed in Table 2.3.

In the next sections, a description of the polarized electron beam and its transport to the apparatus will be provided. This will be followed by an overview of the different components of the G^0 apparatus with an emphasis on the particle identification system, and a brief description of the DAQ system. Then a summary of the data collected for the dataset corresponding to the LD_2 target and the electron beam energy of 362 MeV will be presented.

Beam Parameter	nominal DC value	maximum helicity correlations
Energy	360 MeV	0.0005 keV
Average Current	80 μA	2 ppm
Position at target	"0"	40 nm
Angle at target	"0"	4 nr
RMS width at target	200 μm	4 μm
Polarization	70 %	(N/A)

Table 2.3: Required nominal beam parameters and allowed limits on their helicity correlated variations. The latter correspond to average values over the running of the experiment.

2.4 Polarized electron beam

The Jefferson Laboratory features a Continuous Electron Beam Accelerator Facility (CEBAF) that can provide beams of highly polarized electrons up to 6 GeV. CEBAF consists of an injector, two linear accelerators connected to recirculation arcs and an extractor, also referred to as the beam switchyard, as seen in Figure 2.6. The electron beam, which is essentially DC, can be delivered to 3 experimental halls simultaneously at 499 MHz each, to meet the demands of the experimental program. The G^0 apparatus was located in Hall C.

The injector contains a 100 kV GaAsP photoemission electron gun to generate a polarized e^- beam, as seen in Figure 2.7. There are three independent fiber-based laser systems [65] ideally providing independent polarized beams to each experimental hall. The laser light is circularly polarized through a Helicity Pockels Cell (HPC), as required to produce spin polarized electrons. The high voltage applied to the HPC is reversed

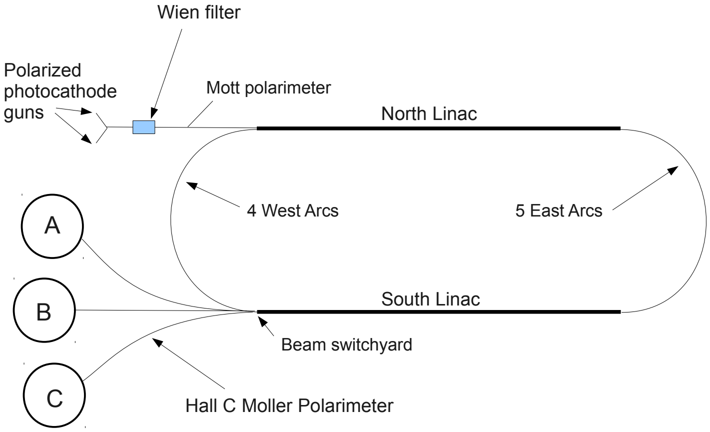

Figure 2.6: Schematic view of the CEBAF accelerator and experimental halls.

periodically, which in turn reverses the polarization of the electron beam. This creates an 85 % polarized electron beam pulsed at 499 MHz that can reach DC currents of up to 200 μA. The electron gun is stabilized through feedback loops to the rotating half wave plate RHWP and piezoelectric mirrors (PZT) to minimize helicity correlated changes in beam parameters. The beam intensity is adjusted with the Intensity Attenuator (IA).

The spin reversal frequency at CEBAF is 30 Hz, in order to cancel 60 Hz noise due to the cycle of the power line. Each 1/30 s will be referred as a macro-pulse (MPS) representing about 15×10^6 RF pulses with the same helicity state. The electron helicity of a given MPS is defined by the polarity of the electric field in the Helicity Pockels Cell. In between MPSs, there was a $\sim$500 μs period, during which the data taking was inhibited, to allow the high voltage on the HPC to settle. The helicity flip sequence

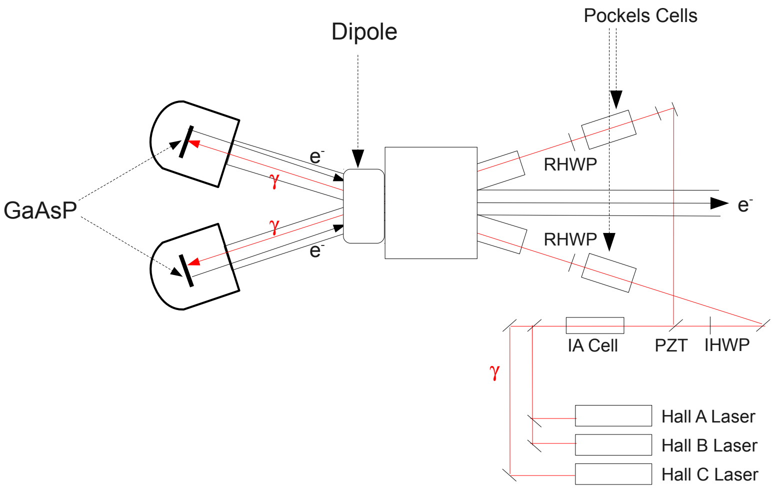

Figure 2.7: Schematic of the electron gun. A description of the different components is given in the text.

was generated in a quartet pattern, such as $+--+$ or $-++-$, in order to minimize the effect of long term drifts.

To avoid bias in the data sequence, the helicity bit of the first MPS within a quartet was set by a software pseudo-random bit generator [66]. To further eliminate potential cross-talk of the helicity bit with the detector electronics, the actual helicity state that was reported to the experimental data acquisition was delayed by 8 MPSs, to be reconstructed later in software. In addition to the 30 Hz spin reversal, an insertable half wave plate (IHWP), seen in Figure 2.7, can be placed in front of the laser every few days to reverse the overall helicity of the electron beam.

Ideally, the electron beam polarization is fully longitudinal at the G^0 target; in reality this may not be exactly the case. Spin precession along the trajectory of the electron beam arises due to interations with the magnetic field used steer it through the injector and recirculating arcs. Electron spin misalignments were partially corrected through the use of a Wien filter [67] at the injector, but small residual transverse polarization components were found in the data, as discussed in Section 3.8.2 of Chapter 3.

2.5 Polarimetry

The electron beam polarization, P_b, is approximately 85 % at CEBAF. It is important to measure the beam polarization, as the measured PV asymmetries are proportional to its value. The polarization of the G^0 beam was measured periodically with the standard Hall C Møller polarimeter [68] [69] but also with a Mott polarimeter [70] for the low energy setting of G^0.

2.5.1 Møller polarimeter

The Møller polarimeter is based on the well known spin dependence of electron-electron scattering. If both the incident beam and the target atomic electrons are polarized longitudinally with polarizations P_b and P_t respectively, then the asymmetry of the scattering cross section between the beam-target spin parallel and anti-parallel configurations is given by [68]:

$$A_{mol} = \frac{\frac{d\sigma^{\uparrow\uparrow}}{d\Omega} - \frac{d\sigma^{\uparrow\downarrow}}{d\Omega}}{\frac{d\sigma^{\uparrow\uparrow}}{d\Omega} + \frac{d\sigma^{\uparrow\downarrow}}{d\Omega}} = P_b P_t A_{zz}\,, \quad A_{zz}(\theta_{CM}) = -\frac{\sin^2\theta_{CM}(8-\sin^2\theta_{CM})}{(4-\sin^2\theta_{CM})^2}\,, \tag{2.7}$$

where $d\sigma/d\Omega$ is the differential cross section for electron-electron scattering, $A_{zz}(\theta_{CM})$ is the analyzing power of the Møller scattering, and θ_{CM} is the center-of-mass scattering angle. The first superscript in $d\sigma/d\Omega$ indicates the target spin while the second superscript indicates the electron beam spin. The expression for $A_{zz}(\theta_{CM})$ is a very good approximation for high energy electrons ($\gamma \gg 1$). With a known target polarization P_t, a measurement of the scattering asymmetry, A_{mol}, allows the beam polarization to be deduced. The analyzing power A_{zz} peaks at $\theta_{CM} = 90°$, giving $A_{zz} = -7/9$. Background due to Mott scattered electrons (described in the next section) is reduced by detection of the 2 Møller scattered electrons in coincidence.

The Hall C Møller polarimeter is located 40 m upstream of the Hall C target; there is no further polarization change due to beam transport before the electron beam reaches the G^0 target. The layout of the polarimeter is shown in Figure 2.8. The Møller target is made from a 4 μm thick Fe foil oriented perpendicular to the incoming beam direction. The target is polarized to saturation with an out-of-plane 4 T magnetic field provided by a pair of superconducting Helmholtz coils. For pure iron, the polarization under this circumstance is very well known: $P_t = 8.00 \pm 0.02\%$ [68].

The electron spectrometers are made up of two quadrupole magnets, Q_1 and Q_2, separated by 3.2 m, with a collimator in between to exclude small angle and high energy scattered electrons from elastic electron-nucleus scattering, and focus only the Møller electrons with 90° center-of-mass scattering angles onto the detectors. Located 7.85 m

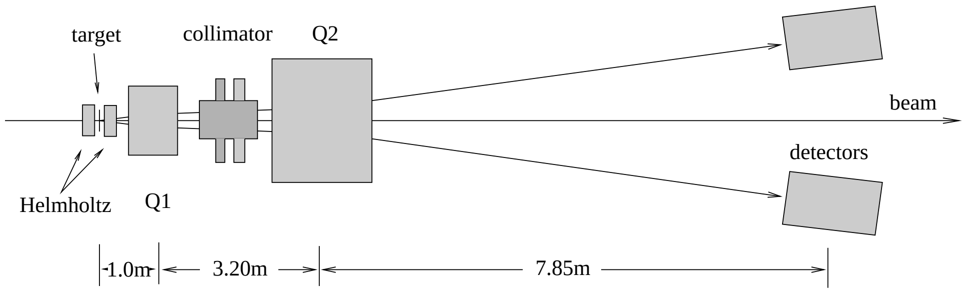

Figure 2.8: The layout of the Hall C Møller polarimeter. Figure taken from [67].

downstream of Q_2, two left - right symmetric detectors are positioned with lead slits in front of both of them, to further define the angular acceptance. In front of the main detectors, there are two hodoscopes, each made up of 14 vertical scintillator bars, which provide information on the scattering angle. A left/right detector coincidence is required such that the Møller scatter/recoil pairs are detected with essentially no background. The asymmetry between the two beam helicity states is measured, which leads to a determination of the beam polarization using Equation 2.7.

The system of a movable collimator and the pair of quadrupole magnets allows the Møller polarimeter to be tuned for a beam energy range of 0.8 to 6 GeV, determined by the angular acceptance of the detectors. Below 800 MeV, the laboratory angle for Møller scattering at 90° center-of-mass angle increases rapidly, as shown in Figure 2.9. By shifting the first quadrupole about 21 cm closer to the superconducting solenoid, a measurement of the polarization at 687 MeV beam energy was made possible. Unfortunately, attempts at 362 MeV were largely unsuccessful at providing an accurate measurement of the beam polarization [71].

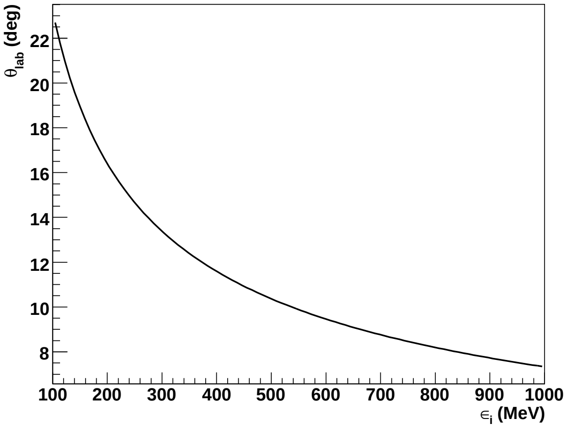

Figure 2.9: Møller scattering angle in the laboratory frame as a function of beam energy when the center of mass angle is 90°.

As the Møller measurement process is invasive requiring a separate beam tune and insertion of a polarized target foil into the beam, the beam polarization measurements could not be performed simultaneously during the G^0 PV asymmetry measurements. Instead, several measurements of the beam polarization were made at regular intervals during the G^0 backward angle experiment. The graphs in Figure 2.10 show all the measurements performed during the 687 MeV data runs for G^0.

These measurements are consistent with a constant average value of [71]:

$$P_b(687) = 85.78 \pm 0.07_{stat} \pm 1.38_{sys} \ \% \tag{2.8}$$

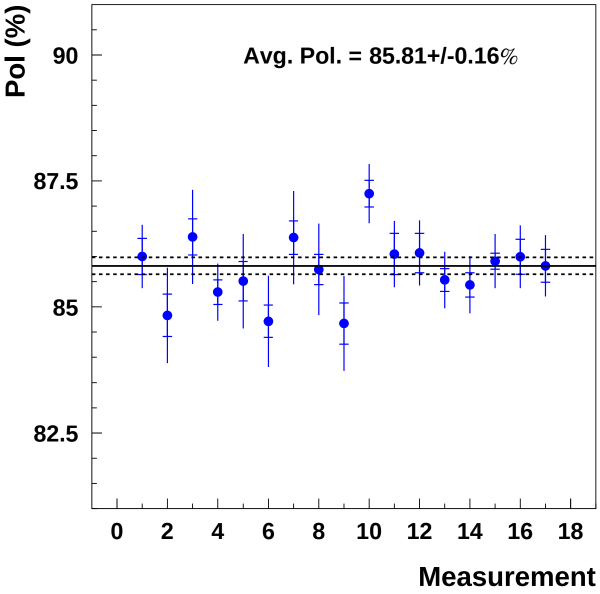

Figure 2.10: Møller polarization measurements taken during 687 MeV running for G^0. Inner error bars denote statistical errors only, while the outer error bars denote the statistical and point to point errors added in quadrature. The solid line is a constant fit to the data (reduced χ^2 is 0.80). Figure taken from [71].

For 362 MeV, the Møller polarization measurements yielded an average result of:

$$P_b(362) = 89.22 \pm 3.24_{stat} \pm 4.61_{sys}\ \% \tag{2.9}$$

Unfortunately, the accuracy of the Møller polarization measurement at 362 MeV was not satisfactory to meet the precision required for G^0. The problem is that only one measurement at 362 MeV was partially successful with an unusual Møller optics tune and a maximum solenoid field of 1 Tesla [71]. This issue was addressed by additional polarization measurements using the Mott polarimeter at the polarized injector, as described in the next section.

2.5.2 Mott Polarimetry

The Mott polarimeter [70][67] allows a measurement of the beam polarization within the injector, where the beam energy is 5 MeV. The Mott polarization measurement is based on transversely polarized electron-electron scattering from a high Z target. The interaction of the orbital angular momentum (magnetic field) with the magnetic moment of the scattered electron (spin) leads to a spin-orbit coupling term in the scattering potential. Referring to Figure 2.11, the differential cross section as function of the scattering angles (θ, ϕ) is given by [67]:

$$\frac{d\sigma(\theta,\phi)}{d\Omega} = \frac{d\sigma_0(\theta)}{d\Omega}(1 + S(\theta)\vec{P}\cdot\hat{n}) \tag{2.10}$$

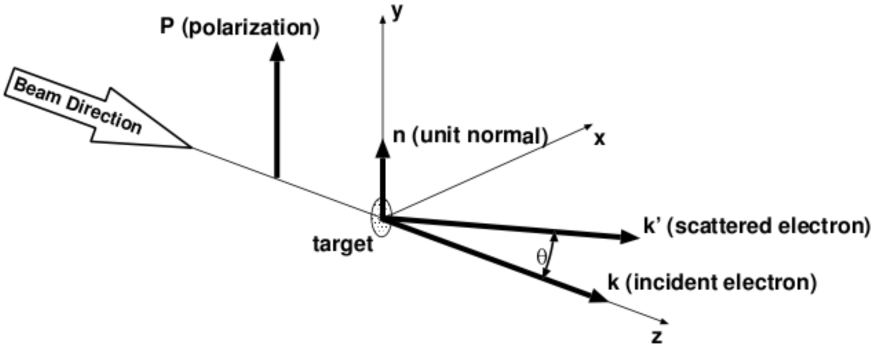

Figure 2.11: Diagram of Mott scattering from a target. In this diagram, the scattering angle is in the plane formed by $\hat{x} - \hat{z}$. The azimuthal angle (ϕ) is zero in this case, as $\hat{n} = \hat{k} \times \hat{k}'$ is aligned with $\vec{P}$. Figure taken from [67].

where $\sigma_0(\theta)$ is the unpolarized cross section, $\hat{n}$ is the unit vector normal to the scattering plane and $\vec{P}_b$ is the incident electron polarization. $S(\theta)$ is known as the Sherman function [72]. From Equation (2.10), a scattering asymmetry is defined as:

$$A = \frac{d\sigma_R - d\sigma_L}{d\sigma_R + d\sigma_L} = PS_{eff}(\theta) \tag{2.11}$$

where the labels “R” and “L” refer to a scattered electron on the right or left side of the beam line (looking downstream) respectively. $S_{eff}(\theta)$ is the effective Sherman function which takes the target thickness into account [67] [70] and is maximized at large angle ($S(172.6°) \approx -0.5$). Therefore, an asymmetry measurement of Mott scattering at large angle permits the beam polarization to be deduced.

The setup of the Mott polarimeter is shown in Figure 2.12. The target consists of a 5 μm gold foil. A set of collimators defines a scattering angle of 172.6° and a solid angle of 0.18 msr. Two sets of detectors, each containing a pair of scintillators attached to photomultiplier tubes, are located on each side of the beam line. The asymmetry in detected elastic events between them enables a measurement of the beam polarization using Equation 2.11.

Mott measurements were performed during both the 687 and 362 MeV running periods. Figure 2.13 shows a clear consistency between the 2 sets of measurements indicating that the average polarization did not change between the two running periods; however, the measurements are much noisier, and the reduced χ^2 is significantly larger than unity for both sets of data as compared to the Møller measurements at the higher

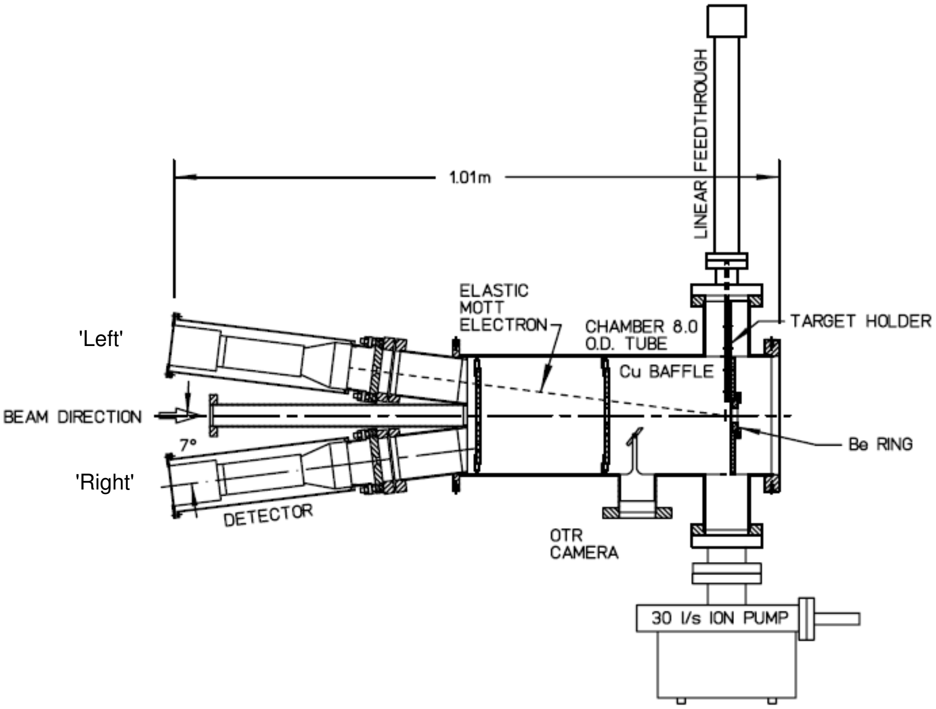

Figure 2.12: Main view of the Mott polarimeter apparatus; the electron beam comes from the left and hits the gold foil on the target ladder. The scattered particles at large angle go through thin aluminium windows to reach the scintillation detectors. Figure taken from Ref. [67].

beam energy. The electron beam polarizations as measured by the Mott polarimeter are systematically lower than for the Møller measurements which were discussed in the previous section. Given that the Møller polarimeter is intrinsically a much more accurate device, Møller polarization measurements were used to calibrate the Mott polarimeter asymmetries resulting in a renormalization factor of: 85.8/82.86. The systematic error was increased due to fluctuations of the Mott results [71] during the 362 MeV running period, and the final beam polarization that was deduced for the 362 MeV pion data is:

$$P_b(362) = 85.78 \pm 0.07_{stat} \pm 1.95_{sys}\ \% \tag{2.12}$$

This polarization value corresponds to the value of the Møller measurement at 687 MeV with an increased error. The systematically lower value for the Mott measurements with respect to those from the Møller was attributed to an increased sensitivity to and insufficient handling of potential background contributions in the Mott data analysis [71].

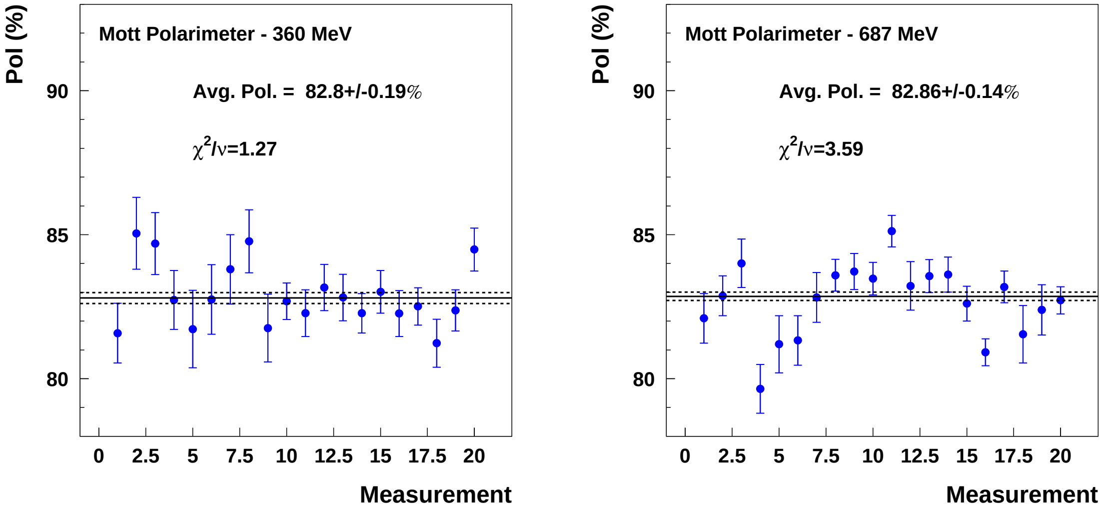

Figure 2.13: Comparison of the Mott beam polarization results for 362 and 687 MeV run periods. Figure taken from Ref. [71].

2.6 Beam monitoring and helicity correlated effects

Ideally, when the spin of the electron is flipped, only the longitudinal beam polarization should reverse. However, other important beam parameters have potentially small correlations with the electron helicity, and could hence create false asymmetries in the G^0 experiment. To quantify the helicity correlated (HC) changes in beam parameters, the beam current as well as its position and incident angles were measured using beam current/position monitors (BCM/BPM) as described in this section. The beam energy was monitored with the use of a BPM at the end of the arc section. The halo, which corresponds to a cloud of unfocused electrons around the beam line, was monitored using scintillation detectors. All the parameters that were monitored were associated with the helicity state of the electron beam.

The HC difference for beam parameter i is defined as:

$$\Delta P_i = P_i^+ - P_i^- \tag{2.13}$$

where $P_i^{+,-}$ represents the value for the beam parameter i for + and - helicity states. The helicity correlated changes in beam current are defined in a slightly different way. In that case we refer to a charge asymmetry that is given by:

$$A_Q = \frac{I_b^+ - I_b^-}{I_b^+ + I_b^-} \tag{2.14}$$

where I_b is the beam current. The HC beam parameter differences contribute to a false asymmetry defined as:

$$A_{false} = \sum_{i=1}^{n} \frac{\partial A}{\partial P_i} \Delta P_i \tag{2.15}$$

where n is the number of beam parameters considered, $\partial A/\partial P_i$ is the sensitivity of the measurements to the ith hc beam parameter variation, and ΔP_i is defined above. Simulations of apparatus yield estimates for $\partial A/\partial P_i$ were used to set the acceptable limits on ΔP_i (see Table 2.3). Induced modulations during data taking enabled actual $\partial A/\partial P_i$ to be measured. The devices used to monitor the beam parameters were located just upstream of the G^0 target as seen in Figure 2.14.

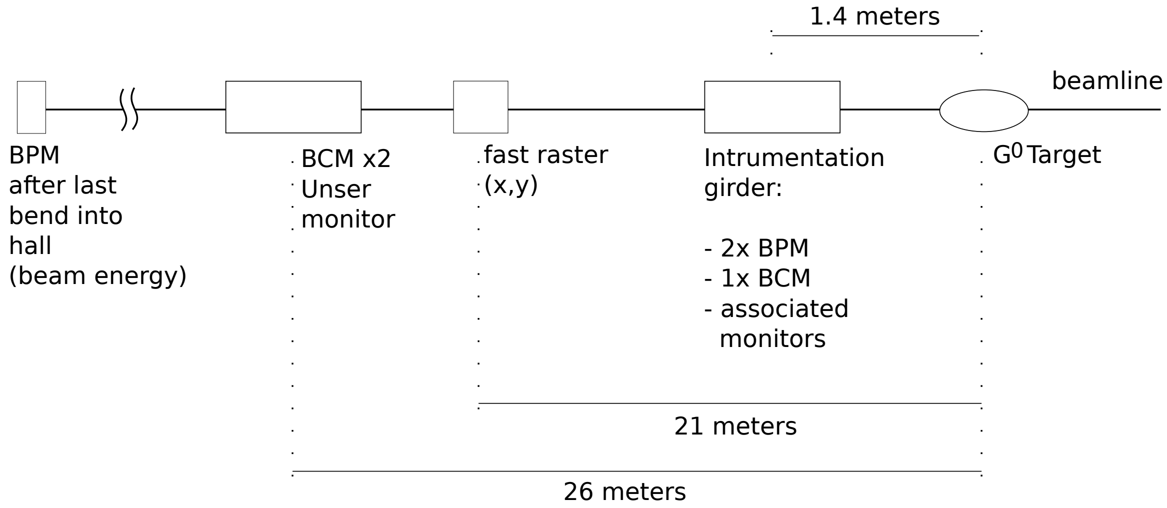

Figure 2.14: Schematic of the beamline from the Hall C extractor to the target. The fast raster system in the figure was used to increase the width of the beam profile to minimize boiling the target. Figure based on Ref. [8].

The charge asymmetry A_Q needed to be measured with an accuracy better than 2 ppm. For that purpose, two types of monitor allowed measurements of the current of the electron beam. The first type is the Unser monitor, based on the principle of a DC current transformer [73]. The Unser, consisting of 2 magnetic toroids around the beam line, enabled non invasive beam current measurements. While the gain of the Unser monitor is well known, the device is sensitive to ambient temperature variations and magnetic fields, creating DC offset fluctuations and drifts of the current signal. Therefore, the Unser monitor could not be used for accurate beam current measurements.

Instead, two resonant cavities also referred to as beam current monitors (BCMs) displaying the required stability (see Table 2.3) were used for G^0. Consisting of a 15.2 cm long metal cylinder with a diameter of 15.5 cm, the BCM is a waveguide designed to be sensitive to the RF frequency of the beam (499 MHz). While traversing through the cavity, the beam excites its transverse mode TM010 [74] and produces an electromagnetic field. The induced current collected by an antenna, consisting of a wire loop around the beam line, is proportional to the beam current. The BCMs are calibrated with respect to averaged Unser measurements at selected values of beam current. The BCMs cover a range of current from 0.5 to 200 μA. Figure 2.15 shows the BCM charge asymmetry data accumulated during the pion asymmetry measurement at 362 MeV. The high χ^2 of the Gaussian fit is due to the use of a slow active feedback loop to reduce the average charge asymmetry. The average value is consistent with zero, thus indicating that the systematic correction for this effect should be negligibly small.

The beam position monitors (BPM) are devices designed to measure vertical and horizontal positions of the beam. Each BPM consists of a 4-wire antenna array of open-ended wire striplines tuned to 499 MHz. The 4 strip lines run along a cylinder and the layout of the antennae is shown in Figure 2.16.

As the beam passes through the cylinder, it generates a current in each of the strips as described for the BCMs. The beam position relative to the center of the BCM is then determined by the relative intensity between two opposite lines. A larger beam current will generate more current in the lines; this effect enables the BPM devices to also be

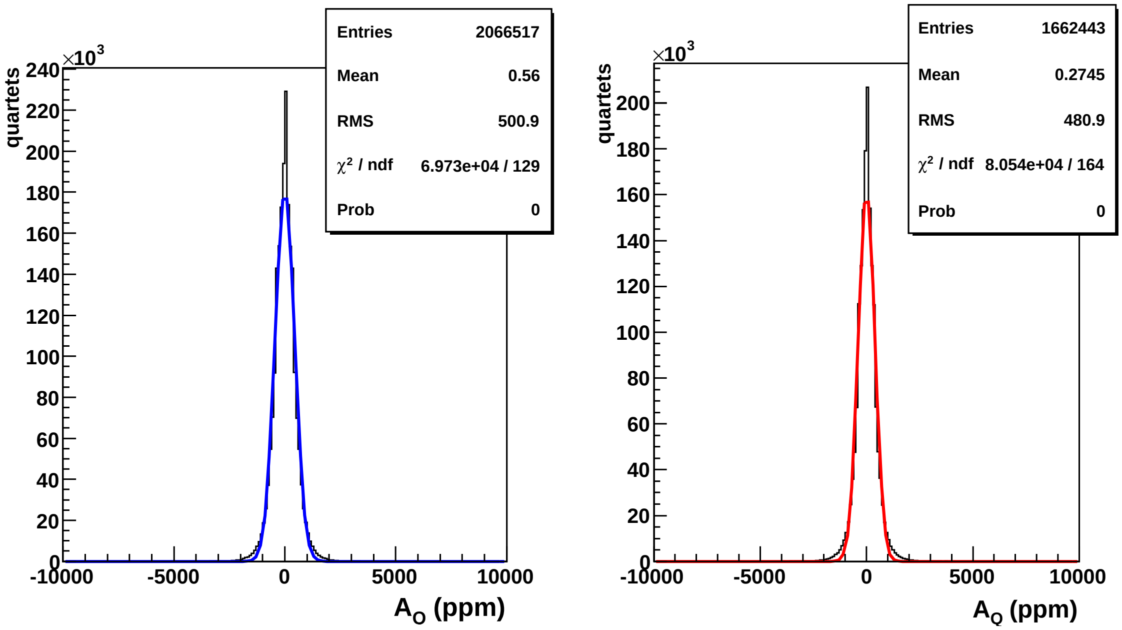

Figure 2.15: Charge asymmetry histogram for the pion measurement at 362 MeV with the LD_2 target. The graph on the left corresponds to the Insertable Half Wave Plate (IHWP) “in” and the graph on the right corresponds to the Insertable Half Wave Plate “out”. Both average values are consistent with zero, indicating a negligible charge asymmetry.

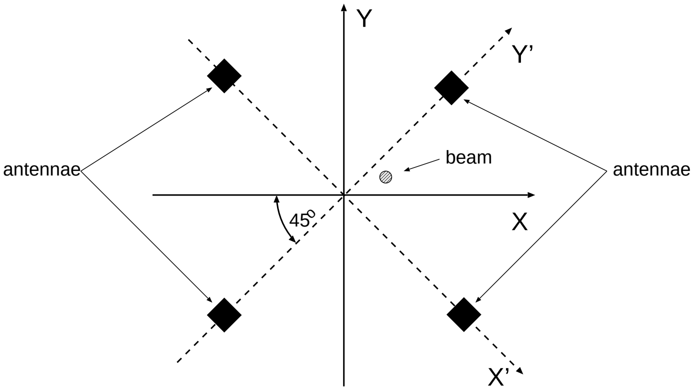

Figure 2.16: Diagram of the orientation of the BPM antennae. The cylindrical housing is not shown. The beam travels out of the page and is slightly off center, leading to a position dependent signal. Figure taken from Ref. [75].

used as beam current monitors. Assuming that the monitor is perfectly parallel to the beamline and a linear dependence between the beam current and the total currents in the wires, we can write:

$$x \propto \frac{I^R_{wire} - I^L_{wire}}{I^R_{wire} + I^L_{wire}}, \quad y \propto \frac{I^T_{wire} - I^B_{wire}}{I^T_{wire} + I^B_{wire}} \tag{2.16}$$

where x and y are the the beam positions on their respective axis and $I^{R,L,T,B}_{wire}$ are the current intensities in the Right/Left/Top/Bottom wires respectively. BPMs with acceptable linearities were calibrated according to the Unser monitor and used for beam position measurements. The beam position monitors have a typical resolution of a few μm for the absolute position and can measure helicity correlated position differences down to the nanometer scale.

The beam energy measurement was performed indirectly in the arc section of the accelerator (see Figure 2.6). In that region, the electrons experience a perpendicular magnetic field to guide them through the beam line [8]. By tuning the magnetic field to the appropriate value and measuring the position at the end of the arc section with a BPM, the beam energy can be deduced. The halo around the electron beam was monitored with the help of scintillator detectors near the beam line.

Two different methods can be used to estimate the sensitivities $\partial A/\partial P_i$ discussed earlier in this section. The first method is to impose controlled modulations of the beam parameters P_i to measure the effect on the asymmetry measurements [76]. The second method is to perform a correlation analysis of main asymmetry data using natural beam motion. This second method was found to be most reliable and was used for evaluating $\partial A/\partial P_i$ for data analysis as discussed in Chapter 3.

Table 2.4 shows key beam properties, their natural range of random fluctuations (RMS) and the run-averaged hc values over the course of the experiment. Associated corrections to the PV asymmetry data are discussed in Chapter 3.

Parameter	DC	NBM (RMS)	HC
x (mm)	"0"	0.02 mm	82.5 ± 4.2 nm
y (mm)	"0"	0.01 mm	-36.2 ± 5.6 nm
θ_x	"0"	0.001 mrad	5.4 ± 0.3 nrad
θ_y	"0"	0.01 mrad	-1.5 ± 0.5 nrad
Current	35 μA	0.3 μA	-0.17 ± 0.22 ppm
Energy	362 MeV	0.003 MeV	0.008 ± 0.0007 keV

Table 2.4: Range of beam beam parameter variations for natural beam motion (NBM) and size of the corresponding HC effects. Note the change in scale for the HC properties. The values for NBM were taken for one production run (∼1 hour) of the pion data.

2.7 Liquid deuterium target system

The main component of the target consisted of a 20 cm long aluminium cell containing liquid deuterium (or hydrogen) maintained at a constant temperature of 22±0.01 K by a Proportional-Integral-Differential (PID) feedback system which used the measured beam current to regulate the power output of a low power heater (LPH) placed upstream of the heat exchanger. Beam current heating under normal running conditions was 450 Watts [77]. Target temperature stability and uniformity as well as high fluid flow to minimize boiling were very important considerations for the G^0 target. The length of the target associated with a beam current of 35 μA provides a luminosity of:

$$\mathcal{L} = \mathcal{N}_a \frac{t}{m_{mol}} \frac{I_b}{e} = 2.22 \times 10^{38}\ \mathrm{cm}^{-2}\ \mathrm{s}^{-1} \tag{2.17}$$

where $\mathcal{N}_a$ is the Avogadro number, t is the target thickness in g/cm^2, m_{mol} is the molecular mass of the deuterium, I_b is the beam intensity, and e is the charge of the electron. The target was positioned horizontally near the center of the magnet system, which will be described in Section 2.8.

The target manifold consists of 2 cylindrical cells entirely made of aluminium (Al-6061 T6). The outer shell is 0.0174 cm thick all around, except on the exit window where it is only 0.0076 cm thick. The manifold is seen in Figure 2.17 where the 22 K liquid deuterium enters from the flange at the bottom, then goes through the middle of the cell where the interaction region is and escapes from the flange on the other side of the manifold. The liquid is guided toward the end of the cell by a conical tube (light blue in Figure 2.17) that has some holes in its wall to help remove heated liquid from the interaction region.

The electron beam enters from the right in Figure 2.17. A helium gas-filled cell was placed upstream to preserve the azimuthal symmetry of the manifold. It was also designed with the same curvature as the deuterium cell (the left side of the helium cell

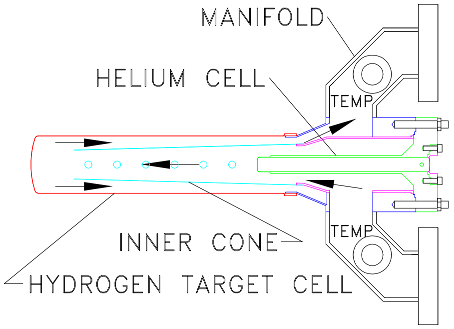

Figure 2.17: Schematic view of the target manifold. The target cell is represented in red and can handle either liquid hydrogen or deuterium. The helium cell appears in green. The hydrogen/deuterium flow is indicated by solid arrow. Figure taken from Ref. [78].

in the figure) to minimize the change in target length for variations in beam position. The intrinsic width of the beam profile (200 μm) was increased by a fast raster system upstream of the target (2x2 mm^2) to minimize local heating.

Bremsstrahlung is electromagnetic radiation produced by the acceleration of a charged particle, such as an electron, when deflected by another charged particle, such as an atomic nucleus. This process is what dominates the energy loss of the electrons within the target. A secondary photon beam is thus created at very forward angle in the liquid deuterium. The mean distance, also referred to as radiation length, over which a high-energy electron loses all but $1/e$ (e = 2.71..) of its energy by bremsstrahlung is given by the expression [7]:

$$X_0(\text{cm}) = \frac{716.4A}{\rho Z(Z+1)\ln\dfrac{287}{\sqrt{Z}}} \tag{2.18}$$

where A is the atomic number within the material considered, Z is the nuclear charge and ρ (g/cm^3) is the density of the material. The radiation lengths of the various materials in the target cell are listed in Table 2.5.

Target	L(cm)	t(g/cm^2)	$t(X_0)$(%)	ρ(g/cm^3)	X_0(cm)
LD$_2$	20	3.350	2.66	0.1674	752.9
Vacuum Window	0.0174	0.047	0.1956	2.699	8.896
Entrance Window	0.0229	0.062	0.2570	2.699	8.896
Exit Window	0.0076	0.021	0.0857	2.699	8.896
He Cell(gas)	16	0.066	0.0026	0.0041	21925

Table 2.5: Thicknesses, densities, and radiation lengths of the materials. The vacuum window is the upstream window of the Helium cell, the entrance and exit windows are the Aluminium walls that the beam is going through before and after interacting with LD$_2$ respectively. $L(t)$, ρ and X_0 correspond to the thickness, density and radiation length respectively.

The target walls and the helium cell are a source of background events in the G^0 apparatus. Their respective thicknesses, densities and radiation lengths are summarized in Table 2.5. The thickness referred to as L in the table is defined along the central axis of the target, and t is defined as $L \times \rho$, which represents of the amount of material the electron beam is interacting with. Backgrounds originating from the target cell were estimated by replacing the liquid deuterium by gaseous deuterium for a beam energy of 687 MeV; unfortunately, those measurements were not repeated at 362 MeV. However, backgrounds from the target walls at 362 MeV were estimated to be roughly ~ 2 %. The background asymmetry contribution is discussed in Chapter 3. This estimate was performed by measuring the counting rates from thin (0.3 and 0.08 cm) Al frames that were substituted for the main target.

2.7.1 Luminosity Monitors

Given that the beam intensity has to be as high as possible to achieve the small required statistical errors for G^0, there is a potential risk that the cryogenic target will boil. Boiling would generate additional random fluctuations in the detector rates and thereby increase the statistical error in the measured asymmetries. Therefore, a special set of target luminosity monitors (LUMI) was constructed for G^0 [79], whose main purpose was to provide an independent check on the target stability, as described below.

The LUMIs consist of a set of 8 quartz Cerenkov detectors, as shown in Figure 2.18, which were placed ∼3.5 meters downstream of the target to intercept electrons at very small scattering angle. Under these conditions, the scattered electron rate was much larger than for the main detectors (arising from the $1/Q^4$ dependence of the cross section), and the PV longitudinal asymmetry was much smaller (since it scales as Q^2, which increases with scattering angle). Thus LUMIs with much higher statistical precision were able to detect any increase in noise due to target boiling. The relative increase of the LUMI asymmetry width at nominal beam current with respect to low beam current ($\sim 5\ \mu$A) measurements was more than 50 times smaller than the asymmetry width of the main detectors, hence the boiling effect was found to be negligible [79].

Since they are 8-fold symmetric around the beam line, the luminosity monitors also

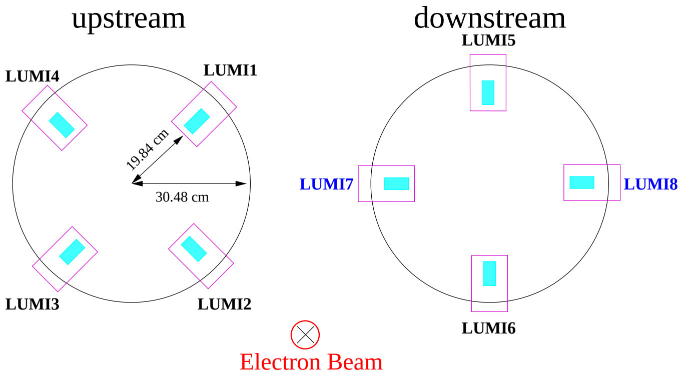

Figure 2.18: Cross section view of the G^0 luminosity monitors. Figure taken from Ref. [2].

detected the characteristic azimuthal dependence of the scattered electron asymmetries due to unwanted transverse polarization components in the beam. This effect is discussed further in Chapter 3.

2.8 Superconducting Magnet System (SMS)

The superconducting magnet system [80] was designed to separate and focus the elastic and inelastic electron trajectories onto the G^0 main detectors. As seen in Figure 2.19, the SMS consists of a toroidal apparatus made up of eight superconducting coils enclosed in a single cryostat. The toroid magnetic field configuration has the advantage of providing a large acceptance arising from a relatively unobstructed geometry, and an intrinsic axial symmetry. Each coil, made up of 144 turns of integrated superconductors, is contained in an aluminium case; the system is cooled to 4 K by liquid helium. In order to provide line-of-sight shielding of the detectors from neutral particles (π^0,γ) originating at the target, collimator modules consisting mainly of lead blocks (yellow boxes in Figure 2.19) were hung from the straight sections of the octagonal rings between each pair of adjacent coils.

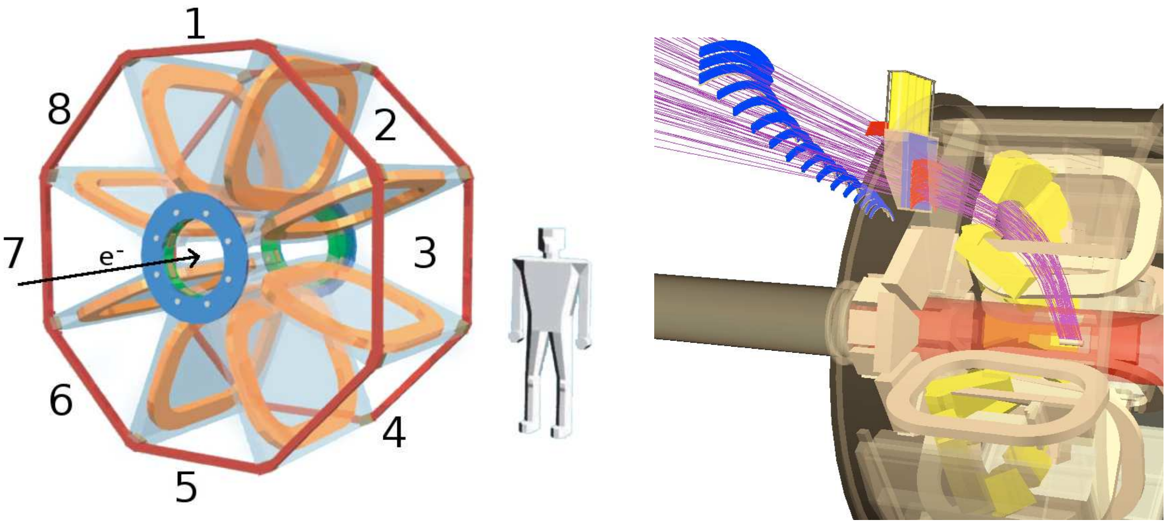

Figure 2.19: Schematic of the G^0 spectrometer on the left with the labels corresponding to the octant numbers and the beam direction given for the backward angle mode. The iron-man shows the scale of the apparatus. On the right, the same G^0 spectrometer is seen in a cutaway view with the collimator shown in yellow and the detector package located at the exit of the SMS for one octant.

The nominal current in each coil is 2650 A for the 362 MeV data set, leading to a field integral of 0.85 $T \cdot m$. The combination of the collimator system and magnetic field leads to an angular acceptance of $108 \pm 2°$ for elastic events and $98 \pm 5°$ for pions. The azimuthal acceptance of the apparatus is 160°. The current in the coils can be adjusted, and the polarity of the power supply can be inverted for background studies [81].

2.9 Detector Package

The detector package for each octant consists of two arrays of scintillators with a Cerenkov detector in between, as seen in Figure 2.20. The detectors corresponding to octants 1, 3, 5 and 7 were built in France, while octants 2, 4, 6 and 8 were built in North America; however, differences in design were minor. The octant numbering starts from 1 at the top of the apparatus and increases clockwise looking downstream with respect to the beam, as shown in Figure 2.19. The first array of scintillators after the exit of the SMS is referred to as the Cryostat Exit Detector array (red bars in Figure 2.20). The second array of scintillators, also called Focal Plane Detectors, is located downstream of the rest of the apparatus with respect to the direction of scattered particles, as seen in blue in Figure 2.20. The Cerenkov detector (grey in Figure 2.20) is located directly in front of the CEDs. The combination of segmented CED/FPDs permits particle tracking at low resolution, sufficient to separate elastic (green tracks in Figure 2.20) and inelastic (red tracks in Figure 2.20) events. The Cerenkov detector was designed to provide improved separation between pions and electrons.

2.9.1 Cryostat Exit/Focal Plane Detectors (CED/FPD)

As mentioned in Section 2.1, the FPDs were used in the forward angle [2] measurements of the G^0 experiment. In backward angle mode, only FPD numbers 3 to 16 were inside the kinematic acceptance (there were 16 FPDs in total for the forward angle measurements). Each FPD has 2 separate layers of scintillator. The material used in the CED and FPD scintillators was plastic (Bicron BC-408), well suited for fast detection of charged particles, as the response time is less than a nanosecond. The scintillation light from the passage of charged particles is guided through light-guides

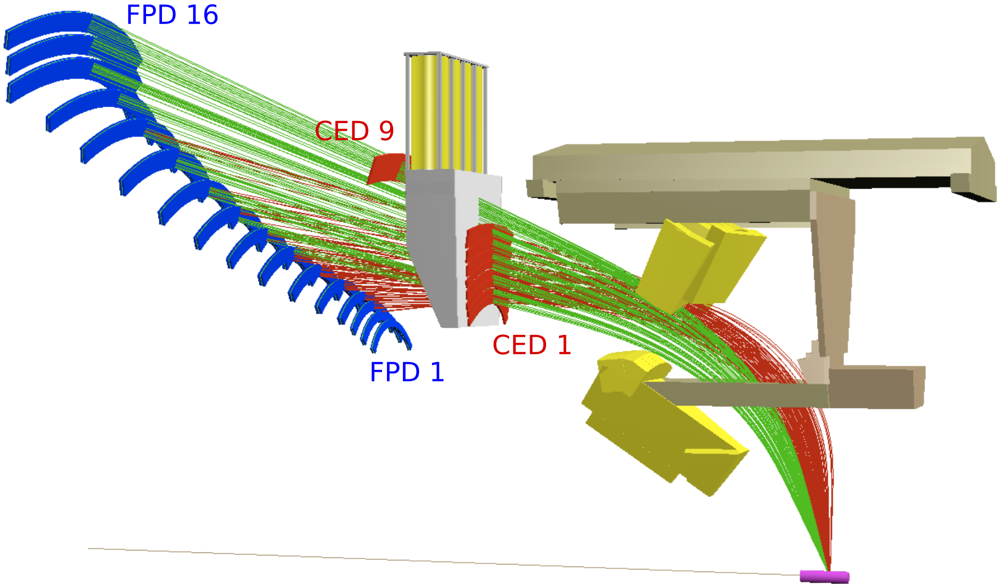

Figure 2.20: Schematic of the detector package for one octet. A detailed description is in the text. Figure taken from Ref. [82].

(as seen in Figure 2.21) to photomultiplier tubes (PMT) which are attached on one end of each of the two FPD layers (one left and one right). Typical signal output for an electron passing through a scintillation layer is about 70 photoelectrons. While the pions do not deposit as much energy as the electrons in the scintillators, their detection efficiency is nevertheless nearly 100 % in all cases.

The CEDs were designed specifically for the backward angle mode, permitting (CED-FPD) coincidences to identify the particles. The CED array consists of 9, 0.5 to 1 cm thick mono-layer scintillator bars with PMTs attached to each end, as seen in Figure 2.22. The intrinsic detection efficiency of the CEDs and FPDs is nearly 100%. The azimuthal acceptance covered by the CED/FPD combination is about 20 degrees per octant, which leads to a total of 160 degrees of angular acceptance for all 8 octants.

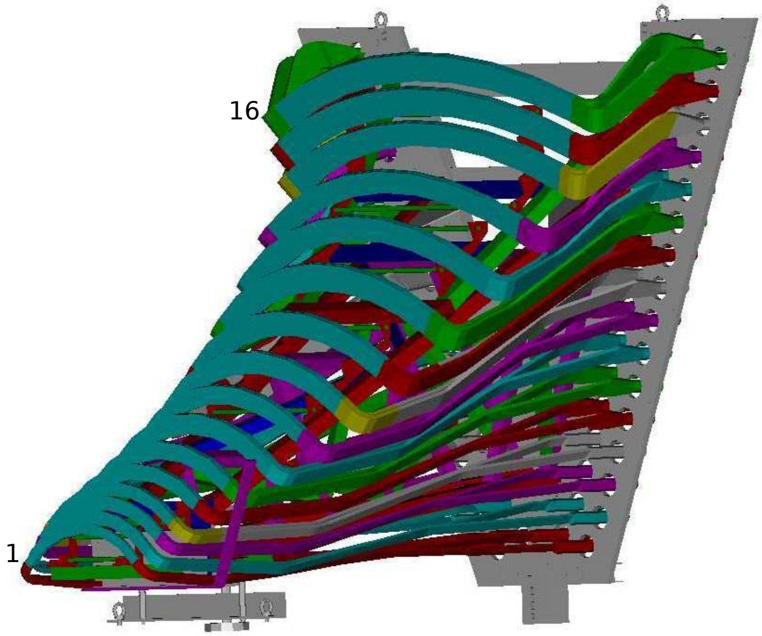

Figure 2.21: Schematic view of the FPD package for one octant as it was used in forward angle mode. The light-guides appear on each side of the scintillator bars. The FPDs are numbered from 1 to 16 from the bottom to the top.

Figure 2.22: Picture of the CED detector packages before mounting them on the apparatus. The CEDs are numbered from 1 to 9 from the bottom to the top of the picture. The black Cerenkov detector box is also seen in the middle of the picture.

2.9.2 Cerenkov Detectors

Given a medium of index of refraction n, when a charged particle moves at a speed greater than the speed of light in that medium, it emits a cone of Cerenkov light along its path, as illustrated by Figure 2.23. The condition for emitting Cerenkov light is $v > c/n$ where v is the speed of the particle and c is the speed of light in vacuum. The Cerenkov angle is given by $\cos\theta_C = 1/(\beta n)$ where $\beta = v/c$. Because of their difference in mass, pions and electrons have different momentum thresholds for producing Cerenkov light in a given medium. If n is 1.03, the threshold momenta for producing Cerenkov light are:

$$\text{electron:} \qquad p_e = \frac{m_e}{\sqrt{n^2-1}} = 2.07 \text{ MeV/c} \tag{2.19}$$

$$\text{pion:} \qquad k_\pi = \frac{m_\pi}{\sqrt{n^2-1}} = 567 \text{ MeV/c} \tag{2.20}$$

Given the fact that electron and pion momenta are both in the 200 MeV range for the G^0 backward angle experiment at 362 MeV, electrons would produce Cerenkov light in such a medium but pions would not, leading to a clear distinction between particles.

The Cerenkov detector material for G^0 consists of 5 layers of 1 cm thick aerogel with index of refraction 1.03. The Cerenkov detector for each octant is contained in a light tight diffusion box which is 46 cm wide near the beamline and 60 cm wide on the opposite side; it is 70 cm long along the radial axis of the G^0 apparatus and 20 cm deep [83], as seen in Figure 2.24. The front wall of the box consists of a 0.8 mm thick aluminium plate, as thin as practically possible in order to minimize the production of secondary background particles traversing the detector.

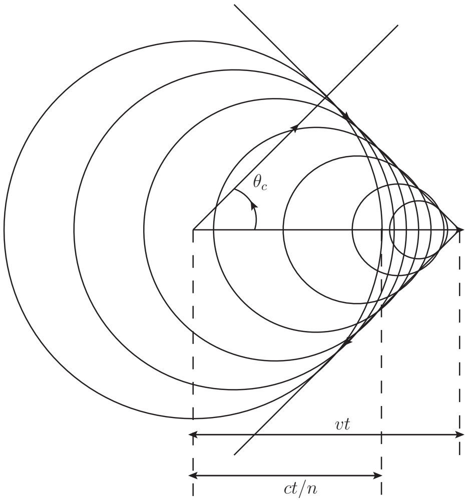

Figure 2.23: Cerenkov radiation. Spherical wavelets of EM radiation field of a particle traveling at velocity greater than the velocity of light in the medium. Figure inspired from Ref. [74].

The inner walls of the detector box are lined with white millipore paper to enable homogeneous diffusion of the Cerenkov light within the box. The light bounces several times on the walls before either being absorbed or impinging on one of the 4, 5" phototubes. For this reason, the time response of the Cerenkov detector is slow compared to that of the CED and FPD scintillators. Its signal is therefore used for a scaler veto but not as a fast trigger for the experiment. Each of the PMTs is housed inside a 1.4" thick low carbon 1024 steel cylinder to shield against the residual magnetic field ($\sim$ 40 Gauss) of the SMS [83] [84]. The Cerenkov detector trigger is set in a coincidence mode between the 4 phototubes; if two out of the four tubes detects a single photoelectron

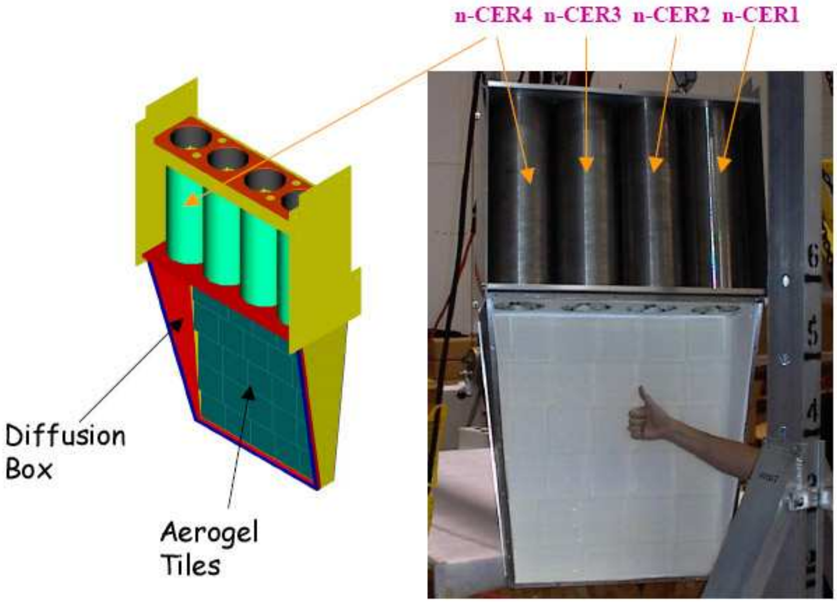

Figure 2.24: Schematic view of a Cerenkov detector on the left. The corresponding photograph can be seen on the right. The Cerenkov detector is shown with the cover removed in this case.

signal within 20 ns, then the event is recorded as an electron, if not then it is recorded as a pion. A more detailed discussion of the Cerenkov detector performance for pion detection will be given in Chapter 3 as well as a more general discussion in Appendix B.

Ideally, the Cerenkov detectors would only be sensitive to electrons scattered from the G^0 target. However, inelastic electron scattering from the liquid deuterium target is a source of neutrons which later thermalize in the experimental hall. Initially, the Cerenkov PMTs (XP4572B [85]) contained borosilicate in the glass part (window, sides) of the tube. Hence neutrons could end up being absorbed in the PMTs [86]. The cross section for thermal neutron absorption in boron (^{10}B) is very high, via the following process:

$$^{10}\mathrm{B} + n \rightarrow {}^{7}\mathrm{Li} + \alpha + T[2.31\ \mathrm{MeV}] + \gamma[0.48\ \mathrm{MeV}] \tag{2.21}$$

where α is a ^{4}He nucleus and T is the kinetic energy in the final state. The process has a branching ratio of 94 %[1] [87]. The resulting γ rays can interact with the photocathodes of the PMTs releasing electrons, and hence generating random background noise. At significant rate, this process can not only damage the tubes but also artificially increase the rates recorded from the Cerenkov detector.

In an attempt to reduce the neutron background, extra shielding was initially placed on the SMS exit windows and around the Cerenkov PMTs, but no significant improvements were noticed [86]. The borosilicate photomultiplier tubes were eventually replaced by quartz tubes (custom made from Photonis [85]), which decreased the singles rates in each PMT from typically 200 to 80 kHz/μA. The new quartz tubes were already installed at the time of the measurements with the LD$_2$ target at 362 MeV, but not for the liquid hydrogen target at both beam energies, and they were only partially implemented for the high energy deuterium measurements. As a result, careful attention had to be paid to the individual Cerenkov detector analysis for those data. Corrections for random noise in the PMTs are part of the analysis described in Chapter 3, Section 3.5.

---

[1] The remaining 6 % directly goes to the ground state of ^{7}Li, hence not producing any γ radiation.

2.10 Electronics and DAQ System

The electronics for the G^0 backward angle measurement were designed to generate coincidence signals between CED and FPD detectors and use the Cerenkov detector outputs to distinguish between electrons and pions. The time separation between electron beam micro-pulses is 2 ns, but given the expected coincidence rates (see Table 2.2), a coincidence between any CED and FPD is produced every 100 ns on average. This allows the definition of coincidences within a few nanosecond time window. Two sets of electronic logic systems were used in the experiment, one being North American (NA) and the other French (Fr). As those 2 logic systems were very similar, they can be described generally by the logic diagram in Figure 2.25.

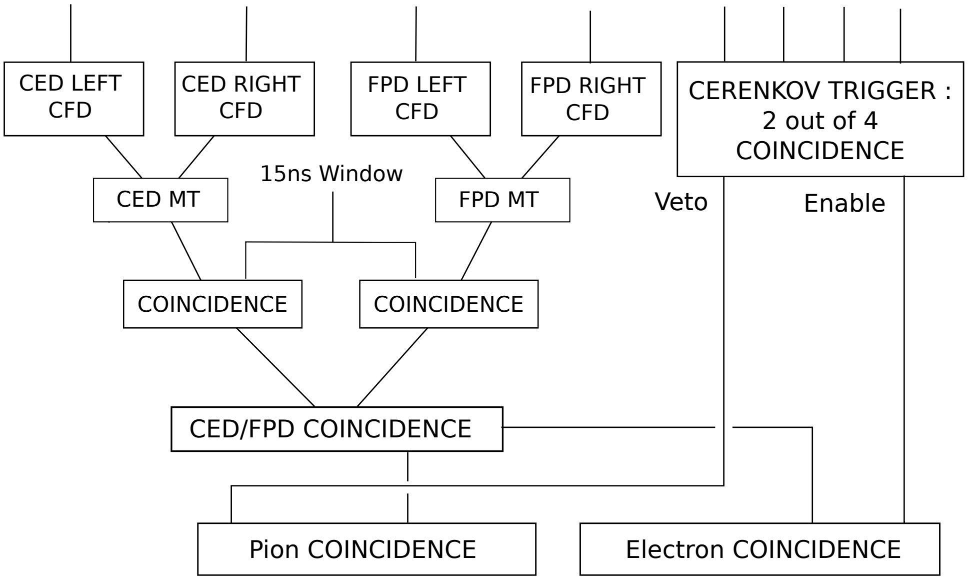

Figure 2.25: Logic diagram of the NA electronics.

As shown in the figure, the detector pulses coming from the left and right PMT of each scintillator bar are fed to Constant Fraction Discriminators (CFD) to generate logic signals, and their timing is averaged to create a meantimer (MT) signal with a 20 ns pulse width. If any CED MT and FPD MT within an octant record a logic signal, a 15 ns trigger window is created[2]. Then for each CED/FPD combination, the meantimers are placed in coincidence with the 15 ns trigger, and a 10 ns overlap between the 2 meantimers and the trigger timing gates is required. If for one CED, multiple FPDs are hit (and likewise for one FPD and multiple CEDs), the event is referred to as a multihit (MH). All the different types of coincidences are then counted incrementally by custom scaler modules and read out at a frequency of 30 Hz, synchronized with the helicity reversal of the beam pulses.

At the scaler inputs, the CED/FPD coincidences are labeled by the Cerenkov trigger generated according to Figure 2.26. The analog signals from the Cerenkov PMTs are fed through CFDs, and the width of the output logic signal is adjusted to 20 ns. If any 2 of the 4 Cerenkov PMT signals are detected within their timing gate of 20 ns with an overlap of at least 2 ns, then a Cerenkov trigger is created with a width of 32 ns. Its start is synchronized with the arrival time of the first signal coming from any PMT of the Cerenkov detector. More details on the Cerenkov trigger are given in Section B.2 of Appendix B.

---

[2] 12 ns for the French electronics.

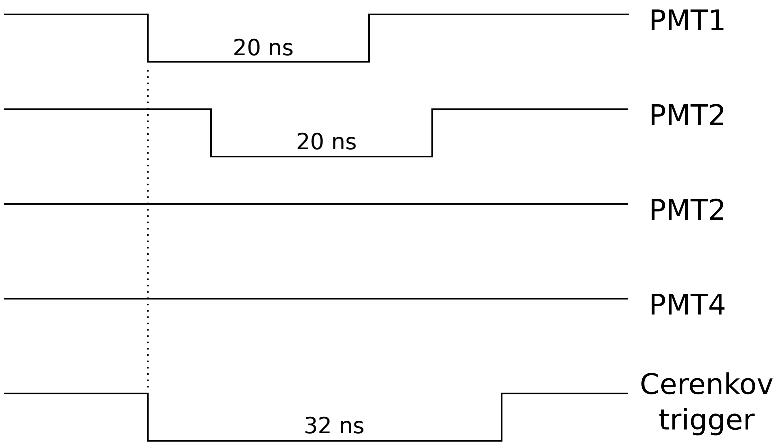

Figure 2.26: Schematic of the Cerenkov Trigger logic. At least 2 PMTs must fire to generate a trigger.

2.10.1 Monitoring electronics

As described above, custom electronics were required to accumulate data at the very high rates needed to give sufficient statistics to measure PV asymmetries at the ppm level. The system developed for G^0 was able to accumulate high statistical accuracy with a custom system designed to be read out only at the relatively low spin reversal rate of 30 Hz. A necessary compromise of this technique was that event-by-event recording was not possible.

In order to study the performance of the Cerenkov detectors in detail and also to study the electronic deadtime and random event rates, a special beam structure at 31 MHz, also used in the G^0 forward angle measurement, was implemented to increase the time separation between beam pulses to 32 ns. Only a very small fraction of the data were taken in this special mode. The specific 31 MHz beam structure was used in combination with a separate set of conventional Fastbus ADCs (Analog to Digital Converters) and TDCs (Time to Digital Converters), to record more detailed information on an event by event basis for a small fraction of the beam pulses. In particular, the ADCs recorded the integral of the analog signals coming from all the PMTs. In addition, a custom module called an Analog Ring Sampler (ARS) was used to separately record signals from the Cerenkov PMTs. The ARS module could sample pulse heights at a frequency of 1 GHz over a range of 128 ns each time a Fastbus event was recorded.

2.10.2 Data acquisition

The G^0 data acquisition (DAQ) was based on the CODA system [88] developed at Jefferson Laboratory, and ran on a Linux computer in the Hall C counting house. The DAQ computer sent the trigger command to a "command module", called the trigger supervisor (TS), which then passed appropriate signals to the readout controllers (ROC) of each G^0 electronics crate. The data from the ROCs were transfered to the DAQ computer through Ethernet.

The data were stored in the standard CODA format onto a disk in a "bank" structure: the data from a given ROC were written into a bank, with the ROC number and the length of the data encoded in the bank header. Data were collected in typically one hour runs, after which each run was analyzed by a replay routine running on an dedicated analysis computer. The run-average data were then written into a dedicated

MySql database, and a data file containing all MPS events for each run was automatically generated.

Real time monitoring was done through a shared memory buffer, also called an event-transfer (ET) buffer. A custom program running on the same analysis machine read the data from the ET buffer in real time and produced diagnostic plots that were monitored during data taking, including detector rates, beam parameters, etc.

2.11 Raw data summary for LD_2 at 362 MeV

A summary of the G^0 data collected for the LD_2 target with a beam energy of 362 MeV is given in Table 2.6. These data were analyzed to extract the PV pion asymmetry as described in Chapter 1. Details of the analysis are presented in Chapter 3.

dataset	N_{runs}	Charge (C)	I (μA)	A_{meas} (ppm)
electron	649	70	35	-14.05 ± 0.81
pion	154	17	35	- 0.17 ± 0.75

Table 2.6: Summary of the LD_2 data at 362 MeV. N_{runs} represents the number of runs (∼1 hour long) collected; the integrated beam charge is given in the third column. I represents the average beam current and A_{meas} is the total measured asymmetry before corrections.

Unfortunately, pion data were recorded only for a subset of the 362 MeV runs. While the main goal of the G^0 backward angle measurements was to acquire precise electron asymmetry measurements, it was possible in principle to acquire pion data simultaneously. However, the problem encountered with neutron background in the Cerenkov detectors described in Section 2.9.2 led to the use of the pion related electronics for random neutron background measurements for a significant fraction of the time. The loss of statistical error on the pion measurement was mitigated, however, by the relatively higher pion rates and near 100 % pion detection efficiency of the Cerenkov detector (in veto mode).

2.11.1 Coincidence rates

To identify tracks of scattered particles through the G^0 apparatus, two coincidence matrices were defined for each octant: one for the signals tagged as electrons, and one for the pions. Each matrix contains 126 cells (9 CEDs × 14 FPDs). Coincidence counting rates are normalized to the primary beam current. The electron matrix containing the normalized scattering rates shown in Figure 2.27 is more easily understood by looking back at Figure 2.20; elastic electron events are less deflected by the magnet, so they occur in the upper right corner of the coincidence matrix. Inelastic events on the other hand are located in the lower CED/FPD corner of the matrix. The bottom right corner of the matrix is not populated, as no particle tracks coming from the target are allowed by the geometry (see, e.g. at CED 1 and FPD 16 in Figure 2.20). As mentioned at the beginning of this chapter, there are no expected inelastic rates in the detectors at 362 MeV because the beam energy is too low. Indeed the rates seen in the lower left corner of Figure 2.27 originate from the radiative tail [89] of the elastic scattering process. The rates in the upper left corner, while relatively low, consist mainly of electrons coming from $\pi^0 \to \gamma\gamma \to 2e^+ + 2e^-$ decay.

The regions in the coincidence matrices corresponding to elastic/inelastic electron and pion events are referred to as the corresponding loci. The locus definition of the electron matrix was found by using the results from the field scan analysis [81]. This method consisted of varying the SMS field to change the deflection and focusing of the particles on the CEDs and FPDs, and measuring corresponding variations of the rates for each cell of the coincidence matrix to quantify the respective contributions of elastic and inelastic events. The inelastic locus definition for the electron matrix is more relevant at 687 MeV, as significant inelastic rates were detected by the G^0 apparatus at that energy [8].

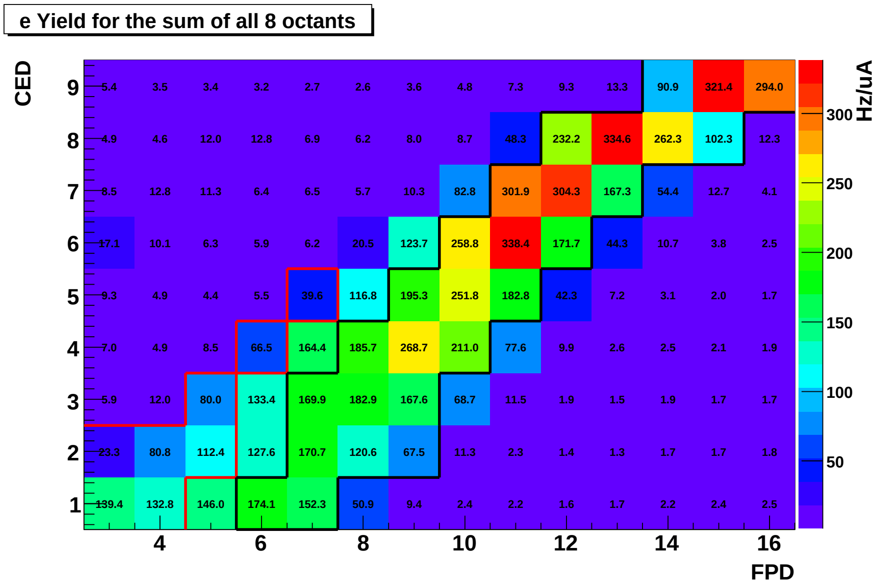

Figure 2.27: Electron coincidence matrix for LD_2 at 362 MeV. The rates are averaged over the 8 octants. The rates are given in Hz per μA of beam current. The elastic/inelastic loci are defined by the black/red lines respectively.

Figure 2.28 shows the raw coincidence rates for pion events defined when a CED/FPD coincidence occurs but the Cerenkovs do not trigger. Most of the pion events are located in the bottom left corner of the matrix, which is where inelastic events are expected. The pion locus shown in Figure 2.28 was defined based on the rates and on the purity with respect to the electron contamination, as described in Section 3.8.1 of Chapter 3.

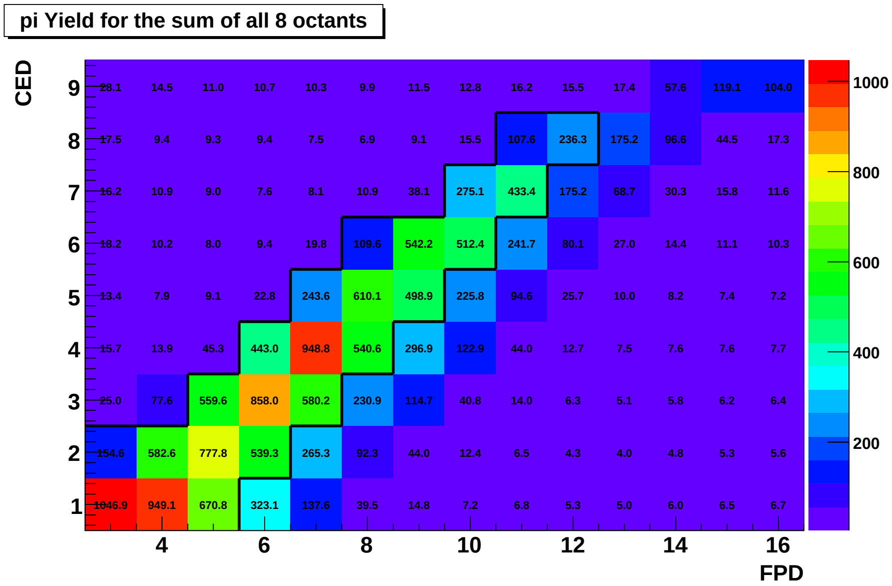

9	28.1	14.5	11.0	10.7	10.3	9.9	11.5	12.8	16.2	15.5	17.4	57.6	119.1	104.0
8	17.5	9.4	9.3	9.4	7.5	6.9	9.1	15.5	107.6	236.3	175.2	96.6	44.5	17.3
7	16.2	10.9	9.0	7.6	8.1	10.9	38.1	275.1	433.4	175.2	68.7	30.3	15.8	11.6
6	18.2	10.2	8.0	9.4	19.8	109.6	542.2	512.4	241.7	80.1	27.0	14.4	11.1	10.3
5	13.4	7.9	9.1	22.8	243.6	610.1	498.9	225.8	94.6	25.7	10.0	8.2	7.4	7.2
4	15.7	13.9	45.3	443.0	948.8	540.6	296.9	122.9	44.0	12.7	7.5	7.6	7.6	7.7
3	25.0	77.6	559.6	858.0	580.2	230.9	114.7	40.8	14.0	6.3	5.1	5.8	6.2	6.4
2	154.6	582.6	777.8	539.3	265.3	92.3	44.0	12.4	6.5	4.3	4.0	4.8	5.3	5.6
1	1046.9	949.1	670.8	323.1	137.6	39.5	14.8	7.2	6.8	5.3	5.0	6.0	6.5	6.7

Figure 2.28: Pion coincidence matrix for LD_2 at 362 MeV. The rates are averaged over the 8 octants. The pion locus definition is defined by the black line around the cells.

Chapter 3

Data Analysis

3.1 Note on contributions discussed in this thesis.

As noted in the Acknowledgements Section, the G^0 experiment was carried out over many years by a large collaboration. The backward angle data which are the focus of this work were jointly analyzed by a team of Ph.D. students from Canada, the USA and France. As one of the Ph.D. students working on the backward angle mode of the G^0 experiment, I helped with the testing of the CEDs before their installation and joined the backward angle measurement effort during data taking. I spent one year at Jefferson Laboratory to take shifts. Common analysis tasks were shared amongst this group, led by an Analysis Coordinator. Each student also focused on a unique physics topic for his/her Ph.D.

My broader contributions to the experiment included:

- Contributions to the main analysis passes.
- Cerenkov performance studies: Those studies were especially important for the 687 MeV LD_2 elastic data, for which a determination of the pion contamination in the elastic sample was an essential part of the analysis. A full discussion of the Cerenkov detector analysis is provided in Appendix B.

My unique contributions, as described in this thesis were:

- Analysis tasks specific to the pion data. Those are discussed in Section 3.8 of this chapter.
- Pion simulations discussed in Section 3.9 of this chapter.
- Determination of the LEC d_Δ which is found in Chapter 4.

These topics are discussed in more detail in the remainder of this thesis.

3.2 From raw to physics asymmetries

The focus of this chapter is the analysis of the pion data for the LD_2 target and 362 MeV beam energy setting, which leads to the measurement of the low energy constant d_Δ discussed in Chapter 1. However, the elastic and “inelastic” electron data may also be discussed for the same data set when required and a few comments about the other energy/target settings are given for clarity as needed.

The analysis strategy leading from the raw asymmetry to the final physics asymmetry and extraction of physics quantities is summarized by the flow chart given in Figure 3.1. Starting from the raw pion asymmetry at the top of the figure, the experimental corrections (passes) were applied at the macropulse level (MPS) on the coincidence yields before calculating the asymmetries, or by quartet. The analysis passes were:

- Pass 1: Data quality cuts and calibrations. This is also referred to as the "raw pass".
- Pass 2: Cuts on the coincidence rates to eliminate faulty scaler data.
- Pass 3: Rate corrections arising from deadtime and random coincidences.
- Pass 4: Removal of helicity-correlated systematic effects though linear regression.

Once averaged over the entire data set, the asymmetries from pass 4 were corrected for physics backgrounds, for residual transverse spin asymmetries and for beam polarization to obtain the final physics asymmetry.

Monte Carlo (MC) simulations were performed to confirm the measured pion rates and to extract other physical quantities associated with the pion physics asymmetry. Those quantities are the average four-momentum transfer squared $\langle Q^2 \rangle$ and the average real photon depolarization, $\langle D(y) \rangle$ for the process: $\gamma n \to p + \pi^-$. This chapter will cover the steps described above in detail.

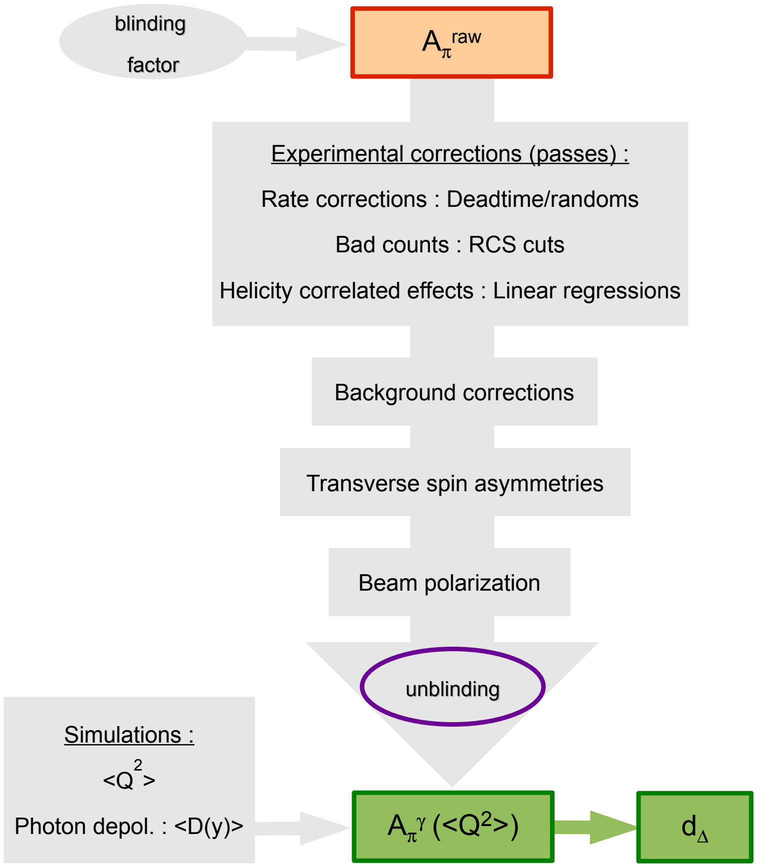

Figure 3.1: Flow chart of the data analysis strategy. The various steps are discussed in the text. An encrypted blinding factor of order unity was applied to the data before the analysis and removed at the end, to prevent unintentional bias in applying the various data corrections.

3.3 Pass 1: Calculation of the raw asymmetries

The asymmetries were calculated for each helicity quartet from the normalized detector coincidence yields by the analyzer. Before calculating the asymmetries, cuts were imposed MPS by MPS[1] to ensure the data quality. The main cut concerns the beam

---

[1] Recall that each helicity state (30 Hz) is referred to as a macropulse MPS; a set of 4 helicity states +−+ or -++- is a quartet, as defined in Chapter 2.

current. If the beam current was lower than its nominal value by a significant amount (chosen arbitrarily depending on the run period) then the corresponding MPS was excluded, as well as the 3 other MPSs of the quartet. The beam current was typically kept within 10 % of its nominal value. Furthermore, the first 500 MPSs after a beam trip recovery were removed, in order to allow time for the target to stabilize thermally. In addition, there were other cuts associated with scaler overflows or any anomalous behaviour of the readout electronics.

For the events passing the data quality cuts, a helicity asymmetry can be defined. This asymmetry can be calculated before and after rate corrections or any correction being made on a MPS basis. Those corrections will be described in the next sections. The normalized detector yield is defined as:

$$Y_i = \frac{R_i}{I_{b,i}} \tag{3.1}$$

where R_i is the detector rate for the MPS i in the quartet and $I_{b,i}$ is the measured beam current (in μA) for the corresponding MPS. The helicity asymmetry for a quartet is then given by:

$$A = \mathcal{H}\frac{Y_1 + Y_4 - (Y_2 + Y_3)}{Y_1 + Y_4 + Y_2 + Y_3} \tag{3.2}$$

where $Y_{1,2,3,4}$ correspond to the normalized yields for the quartet pattern (+ - - +) or (- + + -) for $\mathcal{H}$ being equal to +1 or -1 respectively. $\mathcal{H}$ is representing the helicity pattern. Equation (3.2) is general for all the measured yields in the G^0 experiment. The charge asymmetry is computed in a similar fashion from the BCM data as described in Chapter 2. In order to store and analyze the data more efficiently, the computed asymmetries and their errors as well as all the other measurements are averaged over each run and stored in a database with a label corresponding to the run number. The statistical width of the measured asymmetries over a run is given by:

$$\sigma_A = \sqrt{\frac{\langle A^2 \rangle - \langle A \rangle^2}{N_{QRT}}} \tag{3.3}$$

where N_{QRT} is the number of good quartets during the run. It is assumed here that each quartet during the run has comparable statistical weight. This is justified by the stability of the beam current imposed by the cut described above. Asymmetries can be computed cell by cell in the coincidence matrix, but for the first passes of the analysis, they were computed only for each locus. A comparison of the average asymmetry from the two methods showed an agreement better than 0.1 ppm, which is much smaller than the statistical error (~ 1 ppm).

The weighted average of the locus asymmetries over all runs can be compared for each of the detector octants. Figure 3.2 shows the locus weighted average of the elastic electron asymmetries over all the runs for the LD_2 data at 362 MeV as a function of octant number. The data are divided into two groups, one for each half wave plate state which controls the overall beam helicity (described in Section 2.4). As seen in

Figure 3.2, the elastic electron asymmetries are at the 10^{-5} level, with statistical errors below 1 ppm; they change sign with respect to the half wave plate state. There is no noticeable azimuthal dependence of the asymmetry for the elastic electron data.

Figure 3.3 shows the raw asymmetries versus detector octant number for the "inelastic" electron locus[2]. The statistical error is relatively larger and the average asymmetry is smaller. The sign of the asymmetry also changes consistently with respect to the half wave plate state. The reduced χ^2 is also fairly close to 1 which is consistent with the constant fit.

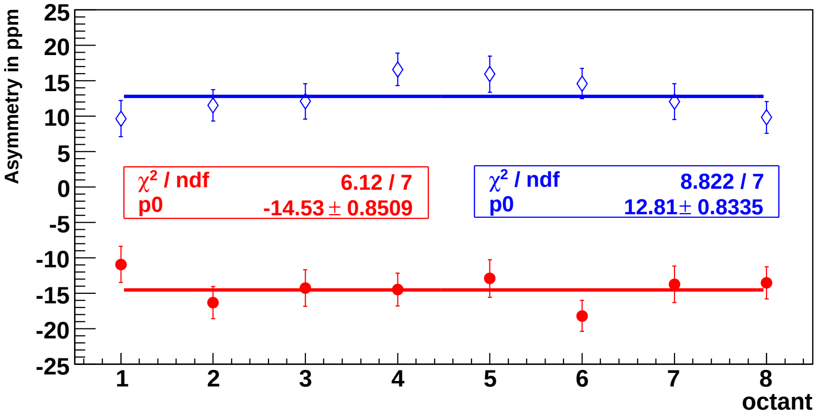

Figure 3.2: Raw elastic asymmetries vs octant number for LD_2 at 362 MeV. The filled circles correspond to the HWP "out". The diamonds correspond to the HWP "in". Note that the standard definition of the asymmetry given in Chapter 1 corresponds to the HWP "out" state.

The raw pion asymmetries as shown in Figure 3.4 are qualitatively different to the electron asymmetries. Values are close to zero, with relatively large variations from octant to octant. Note the non reversal of the average value with respect to the half

---

[2] For 362 MeV beam energy, the inelastic locus contains events arising primarily from the radiative tail of the elastic process as mentioned in Chapter 2.

wave plate state. Moreover, the larger reduced χ^2 indicates a non-statistical spread in the data and possibly an azimuthal dependence of the asymmetry. The overall statistical error is larger than in the elastic electron case despite higher pion rates in the corresponding locus (comparing Figure 2.27 and 2.28). The reason is that pion coincidence data were only acquired for a fraction of the running time for this beam energy setting, as explained in Section 2.9.2.

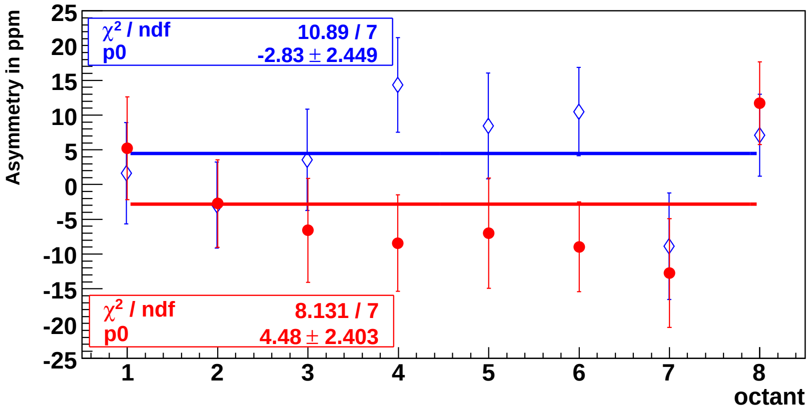

Figure 3.3: Raw "inelastic" electron asymmetries vs octant number for LD_2 at 362 MeV. The filled circles correspond to the HWP "out". The diamonds correspond to the HWP "in".

The average pion asymmetry for the first analysis pass is:

$$A_{\pi}^{p1} = -0.17 \pm 0.76_{stat} \text{ ppm} . \tag{3.4}$$

Note that the value of A_{π}^{p1} is consistent with zero, and the statistical error is ~0.8 ppm. Corrections to the asymmetry, and their systematic uncertainty as discussed in subsequent sections, should be viewed in this context.

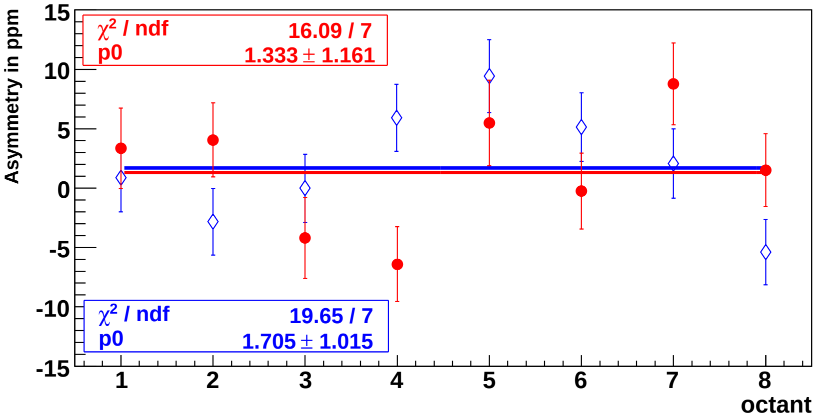

Figure 3.4: Raw pion asymmetries vs octant numbered for LD_2 at 362 MeV. The filled circles correspond to the HWP "out". The diamonds correspond to the HWP "in".

3.4 Pass 2: Exclusion of faulty scaler data

The ratio of the asymmetry error to that expected from counting statistics (Ratio of Counting to Statistics: RCS) is defined as:

$$RCS = \frac{\sigma_A}{\sigma_{stat}} \tag{3.5}$$

where σ_A is the error on the measured asymmetry and σ_{stat} is the expected error from counting statistics. The RCS value should be ideally unity if the distribution of the measured asymmetries is consistent with counting statistics. For certain data-taking modes, it was found to be as large as $RCS = 1.5$. This was eventually determined to arise from a combination of effects which were reduced via improvements to the electronics during the course of the experiment. Data quality cuts were placed on MPS yields at the 4 σ level to reduce the fraction of bad counts. Figure 3.5 shows that the cuts reduce the RCS values from 1.4 to about 1.06 for the data affected by the faulty scaler problem.

Eventually, the counting problem was addressed by reprogramming the coincidence boards to output logic signals with a fixed 10 ns width. Dramatic improvements are seen in Figure 3.6, comparing electron asymmetry data for the same CED/FPD coincidence in two different run periods. Those improvements are also seen in Figure 3.5.

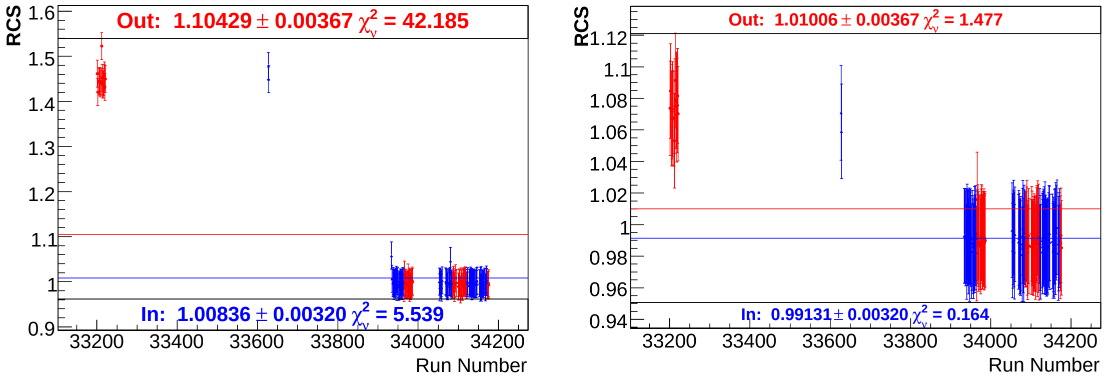

Figure 3.5: RCS values for the pion locus (LD_2, 362 MeV) as function of run number. The graph on the left shows pass 1, and the graph on the right shows pass 2, where additional data quality cuts were applied on the normalized yields. Note that the faulty scaler problem was fixed, as described in the text below, for more than half of the pion data set. For pass 1, the average pion asymmetry was $A_\pi^{p1} = -0.17 \pm 0.76$ ppm and for pass 2, A_π^{p2} was -0.17 ± 0.75 ppm.

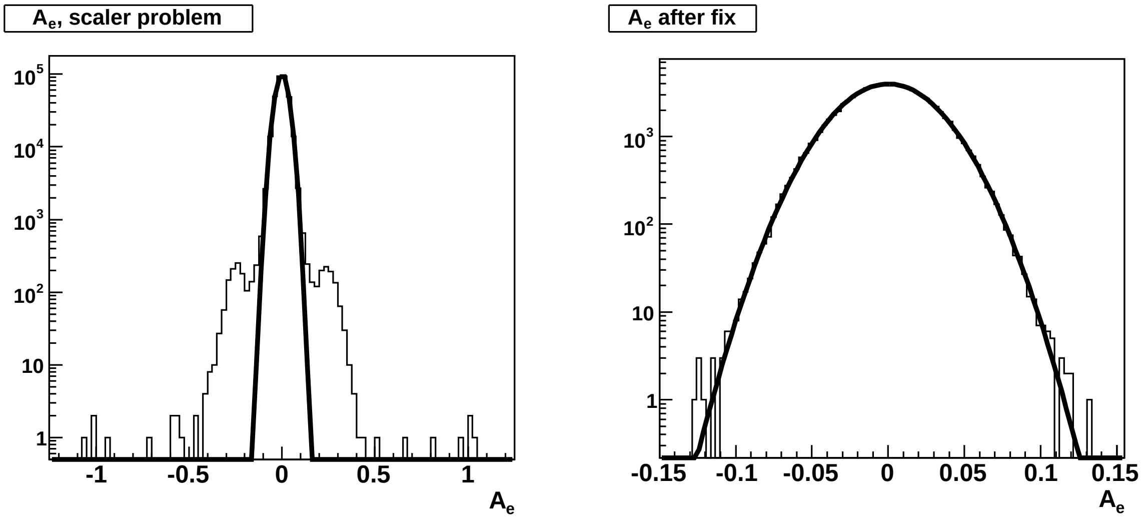

Figure 3.6: Example of electron asymmetry spectra before (on the left) and after (on the right) reprogramming the coincidence modules. Note the change in horizontal scale.

The FPGA reprogramming is independent of another problem: random bit flip errors in the scalers. Simulations were performed to understand better the mis-behaviour of the scaler modules [90] [91], and confirm the appropriateness of the RCS cuts procedure.

The residual false asymmetry after data quality cuts was found to be directly proportional to the physics asymmetry[3] [92] [8]:

$$A_{false} = -\frac{\alpha n}{2}\sigma_{qrt}A_{phys} \tag{3.6}$$

where n represents the shift of the quartet asymmetries between the corrupted events and the mean of the asymmetry distribution normalized to the distribution width, α

---

[3] For all data sets.

is the fraction of events that were not rejected by the cuts on the yields, and σ_{qrt} is the width of the quartet asymmetry distribution for a given run (typically 45000 ppm). α was found to be less than 1 % from simulations [90] [91], leading to a false asymmetry of less than 10^{-3} ppm. Moreover, for these data, the cuts on the yield account for only a 0.27 % reduction in number of good quartets, hence not significantly reducing the data set. The systematic error related to this scaler problem was therefore concluded to be negligible.

The data quality cuts performed on the normalized MPS yields did not change the average pion asymmetry from pass 1, and the statistical error was reduced to 0.75 ppm from 0.76 ppm. Hence, the average pion asymmetry after pass 2 corrections is:

$$A_{\pi}^{p2} = -0.17 \pm 0.75_{stat} \text{ ppm} . \tag{3.7}$$

3.5 Pass 3: Rate corrections to the coincidence yields

The rate corrections based on the work of Ref. [93] and [8] were applied to all the datasets of the G^0 experiment. The basic principles of rate corrections will be discussed first in this section. The results obtained for the electron elastic data in Ref. [8] will then be used to estimate the systematic errors associated with the correction for the 362 MeV pion data.

3.5.1 Principle and application to pion data

Deadtime is the time after each event during which the data acquisition system is busy and therefore not available to record another event. Given a system with an intrinsic time response τ and a rate of incoming events R, the average probability that the system is busy and therefore fails to record valid incoming data is:

$$f_{dead} = 1 - e^{-R\tau} \approx R\tau \tag{3.8}$$

which is also referred to as the fractional deadtime of the system. The G^0 electronics system is comprised of many elements, so this simple formula does not apply; however, the overall deadtime of the system under typical operating conditions, which will be discussed later in this section, was about 20 %. The last step in Equation (3.8) assumes $R\tau << 1$. The measured rate, r is then expressed as:

$$r^{\pm} = (1 - f^{\pm}_{dead})R^{\pm}\,, \quad f^{\pm}_{dead} \simeq R^{\pm}\tau\,, \tag{3.9}$$

in which the labelling ± corresponds to the helicity state. This implies that the deadtime can generate false asymmetries, since $R^+ \neq R^-$ and that if a correction is made, it would need to be applied at the MPS level[4]. In terms of normalized coincidence

---

[4] To extract the true pion asymmetry, we need to apply the definition of Equation (3.2) to the corrected normalized detector yields $Y^{\pm}_{real}$; thus far we have been using the measured yields $Y^{\pm}_{meas}$ in pass 1 and 2.

yield, Equation (3.9) becomes:

$$Y^{\pm}_{meas} = (1 - f^{\pm}_{dead})Y^{\pm}_{real} = (1 - I^{\pm}_{b}\tau Y^{\pm}_{real})Y^{\pm}_{real} \tag{3.10}$$

in which $R^{\pm} = Y^{\pm}_{real} I^{\pm}_{b}$ where $I^{\pm}_{b}$ is the beam current (and the beam current monitor does not require any deadtime correction). Therefore, there is a linear dependence between the measured normalized yield and the beam current. The measured normalized apparent yield decreases as the beam current increases.

A random count occurs when two uncorrelated events are recorded in two different detector channels in time to register a coincidence. Random counts artificially increase the measured coincidence rate. The measured rates are then written as:

$$r^{\pm} = r^{\pm}_{real} + r^{\pm}_{rand} \tag{3.11}$$

where $r^{\pm}_{rand}$ corresponds to a false coincidence rate produced by random events. For a coincidence between two detectors i and j, $r^{\pm}_{rand}$ is proportional to the product of the rate $r^{\pm}_{i}$, in detector i with the rate $r^{\pm}_{j}$, in detector j, with neither of them corresponding to a real coincidence. The beam current dependence of the measured rates then is given by:

$$r^{\pm} = r^{\pm}_{real} + r^{\pm}_{i} r^{\pm}_{j} \tau_r = Y^{\pm}_{real} I^{\pm}_{b} + Y^{\pm}_{i} I^{\pm}_{b} Y^{\pm}_{j} I^{\pm}_{b} \tau_r \tag{3.12}$$

where τ_r is the trigger gate width of the coincidence electronics. The normalized yields, $Y^{\pm}_{real}$, $Y^{\pm}_{i}$ and $Y^{\pm}_{j}$ correspond to the absolute rates $r^{\pm}_{real}$, $r^{\pm}_{i}$ and $r^{\pm}_{j}$ respectively. A quadratic term in beam current ($I^{\pm}_{b}$) is seen in this expression, which leads to only a linear relation for the normalized yield as in the deadtime case.

In order to make a proper rate correction, specific data were taken while the beam intensity was varied during the run from about 10 μA to the nominal current of 35 μA. This procedure was referred to as a beam current scan (BCS). Assuming the detector rates vary linearly with respect to the beam current as shown above, these data allow for an extrapolation to $I_b = 0$, allowing the true normalized rates to be determined. The rate correction needs to be done MPS by MPS because of the non-trivial rate dependence of the overall fraction of deadtime and random events which can carry an asymmetry. For that purpose, an accurate calculation [93] [8] of the expected deadtime and random contributions to the rate was performed using the logic diagram of the electronics (see Figure 2.25 in Section 2.10) and the various widths of the logic signals. Those calculations were compared with the results of the BCS for each cell in each coincidence matrix to estimate the efficiency of the correction and the residual deadtime and random effects. The formula deduced for the CED/FPD deadtime for total coincidence rates (sum of electron and pion rates) in the G^0 apparatus is [93]:

$$Y_{ij}^{DTcorr} = \frac{Y_{ij}^{meas} - Y_{ij}^{rand}\overline{f_{ij}^{MH12}}(1 - f_{Trig} - f_{ij}^{MH22})}{\overline{f_{ij}^{MH12}}(1 - f_{Trig} - f_{ij}^{MH22})(1 - f_{i}^{CFD} - f_{i}^{MT})(1 - f_{j}^{CFD} - f_{j}^{MT})} \qquad (3.13)$$

in which Y_{ij}^{DTcorr} and Y_{ij}^{meas} are the corrected and measured total (e+π) normalized coincidence yields respectively, for a given CED i and a given FPD j. The Y_{ij}^{rand} correspond to the random coincidence yields in the relevant cell. The fractional deadtimes are denoted f_i^{CFD}, f_i^{MT} and f_{Trig} for the constant fraction discriminators (CFDs), the meantimer (MT) and the coincidence trigger (Trig) respectively. The fractional deadtimes for multihit events are denoted f_{ij}^{MH22} (2 CEDs and 2 FPDs are hit) and f_{ij}^{MH12} (one hit in one array of scintillators and 2 hits in the other array)[5]. Given that the contribution from Y_{ij}^{rand} is small compared to Y_{ij}^{meas}, Equation (3.13) can be written in a simplified form:

$$Y_{DTcorr} \approx \frac{Y_{meas}}{(1 - f_{DT})} \tag{3.14}$$

where $f_{DT} \approx 11\%$ is an effective fraction of CED/FPD deadtime accounting for both deadtime and random coincidence effects.

Additional corrections to Equation (3.13) due to Cerenkov randoms and deadtime were made using the following equations [93]:

$$Y_{e,ij}^{true} = \frac{Y_{e,ij}^{DTcorr} - f_{Rdm}^{c}(Y_{\pi,ij}^{DTcorr} + Y_{e,ij}^{DTcorr})}{1 - f_{DT}^{c} - f_{Rdm}^{c}} \tag{3.15}$$

$$Y_{\pi,ij}^{true} = \frac{Y_{\pi,ij}^{DTcorr} - f_{DT}^{c}(Y_{\pi,ij}^{DTcorr} + Y_{e,ij}^{DTcorr})}{1 - f_{Rdm}^{c} - f_{DT}^{c}} \equiv \frac{Y_{\pi,ij}^{DTcorr}}{1 - f_{Cer}^{\pi}} \tag{3.16}$$

---

[5] This symbol is not directly present in Equation (3.13); instead we make use of $\overline{f_{ij}^{MH12}} = 1 - f_{ij}^{MH12}$, in which f_{ij}^{MH12} is the corresponding fractional deadtime.

where f^{c}_{DT} is the fractional Cerenkov deadtime and f^{c}_{Rdm} is the fraction of Cerenkov randoms contributing to the rates. The latter was found to be relatively large in some cases due to neutron backgrounds described in Chapter 2. In the last step of Equation (3.16), the effective fraction of Cerenkov randoms and deadtime f^{π}_{Cer} is defined. Note that the fraction of Cerenkov randoms f^{c}_{Rdm} has the same effect as a deadtime in the pion case, while its main contribution appears in the numerator of Equation (3.15) for the electron case. The contribution from f^{c}_{DT} in the numerator of Equation (3.16) is negligible, as $f^{c}_{DT} \approx 1\%$ [8] and the measured electron rate is 10 times lower than the pion rate in the pion locus.

A typical example of the resulting deadtime/random corrections in the case of the pion matrix for the LD$_2$ target at 362 MeV is shown in Figure 3.7. Both the measured and corrected rates are consistent with the same value at $I_b = 0$. At the nominal beam current of 35 μA, the total deadtime is about 20 %. In subsequent analysis, the residual rate dependence will be treated as a source of systematic error.

At the nominal beam current setting $I_b = 35$ μA, the total fraction of deadtime f^{tot}_{ij} for each cell is defined as:

$$f^{tot}_{ij} = \frac{Y^{meas}_{ij}(0) - Y^{meas}_{ij}(35)}{Y^{meas}_{ij}(0)} = f^{corr}_{ij} + f^{resid}_{ij} \qquad (3.17)$$

where $Y^{meas}_{ij}(0)$ corresponds to the true pion coincidence yield determined by linear

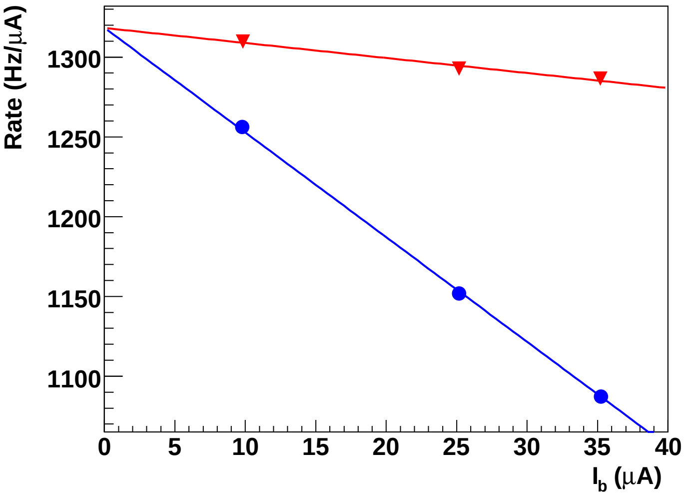

Figure 3.7: Normalized pion yield versus beam current for octant 4. The coincidence cell shown is CED1/FPD3. The filled circles represent the uncorrected data. The triangular markers represent rates corrected using equations (3.16) and (3.13). Statistical errors are smaller than the size of the markers.

extrapolation of the beam current dependence of the yield to its value at 0 μA, and $Y_{ij}^{meas}(35)$ is the measured pion coincidence yield at 35 μA. The rate correction f_{corr} is the sum of three contributions; the fraction of CED/FPD deadtime f_{ij}^{DT}, the fraction of CED/FPD randoms $f_{ij,rand}^{\pi}$, and the fraction of Cerenkov randoms and deadtime f_{Cer}^{π}. The deadtime and random corrections averaged over the coincidence cells (weighted by the yield in each cell) and octants are summarized in Table 3.1.

f_{tot}	f_{corr}	f_{DT}	f_{Cer}^{π}	f_{rand}^{π}	f_{resid}
19.6	16.7	11.1	6.7	1.0	2.9

Table 3.1: Average fraction of deadtime and randoms (in percent). A description of each entry is given in the text. Values are taken from [94] and [95].

The CED/FPD deadtime (f_{DT}) accounts for more than 60 % of the correction. The Cerenkov randoms contribute about 30 % of the correction, and the CED/FPD randoms account for the rest. The residual fraction of deadtime not eliminated by the application of corrections (3.13) and (3.16) is $f_{resid} = 2.9\ \%$. This will be accounted for as a systematic uncertainty in A_π as described in the next section. The pion asymmetry after deadtime and random corrections is:

$$A_\pi^{p3} = -0.54 \pm 0.78 \text{ ppm} . \tag{3.18}$$

3.5.2 Estimate of systematic asymmetry due to rate dependent effects

In the previous section, a systematic rate correction applied to the normalized detector yields at the MPS level was developed and applied to the data; the corrected yields then produced a corrected pion asymmetry (Equation (3.18)). Now we wish to make an independent assessment of these corrections by examining data from auxiliary scalers which recorded rates of singles, multihits, randoms and Cerenkov signals during the run, corresponding to the various quantities in equations (3.15), (3.16) and (3.13). It has been shown in Ref. [8] that the asymmetries from the auxiliary scalers sum to account for the total rate dependent systematic asymmetry as:

$$\begin{aligned} A_{sys} &= A_{meas} - A_{true} \\ &= A_{single} + A_{Trig} + A_{MH12} + A_{Cer} \end{aligned} \tag{3.19}$$

where:

- A_{single} corresponds to effects related to the CFD and MT, affecting the singles events, as well as random CED/FPD coincidences Y_{rand}.
- A_{Trig} contains the DT contribution and multihit (MH22) contributions.
- A_{MH12} is the multihit contribution MH12.
- A_{Cer} is associated with the contamination due to the Cerenkov electronics; this contribution will be different for pions and electrons as described below.

The asymmetries A_{single}, A_{Trig} and A_{MH12} affect both electron and pion data equally, since both e^- and π^- contribute to these overall rates. The asymmetries listed above can be calculated from the rate/asymmetry measurements at each stage of the coincidence logic, which were also stored in the database, as mentioned in Chapter 2. A formal expression for A_{single}, A_{Trig} and A_{MH12} can be found in Ref. [8], and a description of A_{Cer} is given later in this section. A summary of the contributions to the systematic asymmetry in the elastic electron case for the LD_2 target at 362 MeV is given in Table 3.2 [8]. Good agreement between the expected size of systematic asymmetry and the asymmetry change resulting from the rate correction is shown. Moreover, the level of agreement between A_{sys} and the size of the correction is about 25 % of the asymmetry change between pass 2 and 3 for all datasets [8]. This value was assigned as the systematic error due to the rate corrections for the elastic electron data [15].

	in	out
A_{single}	-0.014	0.009
A_{Trig}	-0.258	0.250
A_{MH12}	-0.148	0.137
A^e_{Cer}	-0.359 ± 0.198	0.396 ± 0.214
A^e_{sys}	-0.762 ± 0.198	0.784 ± 0.215
pass2 -pass3	-0.92	0.78

Table 3.2: Systematic asymmetry (ppm) contributions to the rate corrections for the elastic electron sample (LD_2, 362 MeV). The labels “in” and “out” refer to the two HWP states. Values taken from Ref. [8].

For the pion data, a similar level of agreement between the rate corrections to yields at the MPS level and the overall rate asymmetries described above is expected. The size of the correction in this case is 0.37 ppm (pass3-pass2) so it is reasonable to assign 0.1 ppm systematic error to this correction. Note that this uncertainty is small compared to the statistical error of ∼0.8 ppm.

A similar dedicated, scaler based assessment of the rate-dependent asymmetry correction (A^{π}_{Cer}) was not implemented for the 362 MeV pion data. However, a qualitative comparison of the terms shown in Equation (3.19) with the elastic electron case can be made. The Cerenkov deadtime and random contribution to the systematic asymmetry for elastic electrons is calculated from Equation (3.15) [8]:

$$\begin{aligned} A^e_{Cer} &= A^e_{DTcorr} - A^e_{true} \\ &= f_\pi (A^\pi_{true} - A^e_{true}) - (1 - f_\pi)\frac{f^c_{DT}}{1 - f^c_{DT}} A(f^c_{DT}) + f_\pi A(f^c_{Rdm}) \end{aligned} \tag{3.20}$$

where $f^c_{DT} \approx 1$ % is the fractional Cerenkov deadtime and $f^c_{Rdm} \approx 7$ % is the fraction of Cerenkov randoms contributing to the rates [96]. The fraction of pions in the electron coincidence matrix due to Cerenkov randoms, f_π, is defined as:

$$f_\pi = \frac{Y^\pi_{true} f^c_{Rdm}}{Y^e_{DTcorr}} \tag{3.21}$$

The main contribution arising from A^e_{Cer} is the first term $f_\pi(A^\pi_{true} - A^e_{true})$ given that f^c_{DT}, $A(f^c_{DT})$ and $A(f^c_{Rdm})$ are relatively small [8].

The Cerenkov deadtime and random contribution to the systematic asymmetry for the pion sample may be derived from Equation (3.16):

$$\begin{aligned} A^\pi_{Cer} &= A^\pi_{DTcorr} - A^\pi_{true} \qquad (3.22) \\ &= f_e(A^e_{true} - A^\pi_{true}) - (1 - f_e)\frac{f^c_{Rdm}}{1 - f^c_{Rdm}} A(f^c_{Rdm}) + f_e A(f^c_{DT}) \end{aligned}$$

where the fraction of electrons in the pion matrix due to Cerenkov deadtime, f_e, is defined as:

$$f_e = \frac{Y^{true}_e f^c_{DT}}{Y^\pi_{DTcorr}} \tag{3.23}$$

which is known to be about 1 % or less. The dominant contributions in Equation (3.22) are the first two terms, given that the fraction of Cerenkov randoms, f^c_{Rdm} is still approximately 7 % according to the scale of f^π_{Cer} given in Table 3.1. The systematic asymmetry contribution from Cerenkov deadtime and randoms, A^π_{Cer}, is expected to be a small fraction of a ppm in magnitude with an uncertainty of about 0.1 ppm [97]. The other contributions to A^{π}_{sys} are assumed to not be significantly different from the elastic electron case [97]. Therefore, the uncertainty on A^{π}_{Cer} remains the dominant systematic error on the rate correction.

After rate corrections, errors associated with the residual beam current dependence of the rates have to be taken into account as mentioned in Section 3.5.1. The rate corrections described above do not fully correct two effects; the first residual contribution corresponds to CFD deadtime; the associated asymmetry, A^{DT}_{resid} is 0.04 ppm [8]. The other residual effect is attributed to the fraction of CED/FPD randoms (f_{rand}) in the analyzer that is not corrected for in the electron sample but is fully assigned to the pion sample, leading to an over-correction. The expected size of the corresponding residual asymmetry due to CED/FPD randoms should about 0.05 ppm. Since both effects are not corrected for in the analyzer, a systematic error of 0.1 ppm is assigned [97].

An estimate of the overall systematic error due to the rate corrections of the pion data is given by adding in quadrature the expected uncertainty on A^{π}_{sys} (0.1 ppm) and the systematic error due to residuals. The final systematic error was increased to a more conservative 0.2 ppm. The average pion asymmetry after rate corrections is:

$$A^{p3}_{\pi} = -0.54 \pm 0.78_{stat} \pm 0.20_{p3} \text{ ppm} \tag{3.24}$$

3.6 Pass 4: Helicity correlated effects

3.6.1 Formalism

As mentioned in Chapter 2, false asymmetries occur when fluctuations of the beam parameters at the target are correlated with the electron beam helicity. For instance, if the beam position at the target varied by δx, the measured yield Y in the G^0 apparatus would change by δY_x. Given small variations of the measured yields, the relation between the change in yield corresponding to the variations of the beam parameters is assumed to be linear:

$$\delta Y = \sum_{i=1}^{n} \mathcal{C}_i \delta P_i \tag{3.25}$$

where δY and δP_i represent variations of the normalized yields and the beam parameter i respectively, with respect to their average values. The coefficients $\mathcal{C}_i = \partial Y / \partial P_i$ are the sensitivities, also referred to as slopes. If each parameter is a function of the beam helicity, the measured asymmetry can be written as:

$$\begin{aligned} A_{meas} &= \frac{Y^+_{meas} - Y^-_{meas}}{Y^+_{meas} + Y^-_{meas}} = \frac{Y^+_{PV} - Y^-_{PV} + \displaystyle\sum_{i=1}^{n} \mathcal{C}_i (\delta P_i^+ - \delta P_i^-)}{Y^+_{PV} + Y^-_{PV} + \displaystyle\sum_{i=1}^{n} \mathcal{C}_i (\delta P_i^+ + \delta P_i^-)} \\ &= A_{PV} + \sum_{i=1}^{n} \mathcal{C}_i \frac{\Delta P_i}{2\langle Y \rangle} = A_{PV} + A_f \end{aligned} \tag{3.26}$$

where A_{PV} is the parity violating asymmetry, $Y^{\pm}_{meas}$ are the measured yields and $\langle Y \rangle \approx Y^+_{PV} + Y^-_{PV}$ assuming that $\mathcal{C}_i(\delta P_i^+ + \delta P_i^-)$ are relatively small. The helicity correlated beam parameter differences can be any of the following:

$$\text{Current:} \qquad A_Q = \frac{I_b^+ - I_b^-}{I_b^+ + I_b^-} \tag{3.27}$$

$$\text{Energy:} \qquad \Delta E_b = E_b^+ - E_b^- \tag{3.28}$$

$$\text{Position:} \qquad \Delta x = x^+ - x^-, \quad \Delta y = y^+ - y^- \tag{3.29}$$

$$\text{Angle:} \qquad \Delta\theta_x = \theta_x^+ - \theta_x^-, \quad \Delta\theta_y = \theta_y^+ - \theta_y^- \tag{3.30}$$

where A_Q is the charge asymmetry, ΔE_b is the difference of beam energies and $\Delta x(y)$ and $\Delta\theta_x(\theta_y)$ are the beam position and incident angle differences in $x(y)$ respectively. It can be shown [98] [2] that one can extract the correlation slopes by a linear regression method, giving:

$$\langle \delta P_j \delta Y \rangle = \sum_i \mathcal{C}_i \langle \delta P_j \delta P_i \rangle \tag{3.31}$$

in which δY is the net change of yield with respect to its average value for a variation of the beam parameters δP_i, and P_j is one of the parameters considered[6]. The variations of beam parameter δP_i arise from natural beam motion, as discussed in Chapter 2. In Equation (3.31), the brackets $\langle\rangle$ represent an average over N measurements (at the quartet level). This expression can be rewritten in a matrix representation:

$$\vec{\zeta} = \mathcal{P}\vec{\mathcal{C}} \tag{3.32}$$

where $\vec{\mathcal{C}}$ is a vector containing the sensitivities, $\vec{\zeta}$ is the vector covariance between

---

[6] The index i may be equal to j in the summation.

the yield and the beam parameters and $\mathcal{P}$ is the covariance matrix between the beam parameters, which can be written explicitly as:

$$\begin{aligned}\mathcal{P}_{j,i} &\equiv \langle \delta P_j \delta P_i \rangle = \langle (P_i - \langle P_i \rangle)(P_j - \langle P_j \rangle) \rangle \\ &= \langle P_i P_j - P_i \langle P_j \rangle - \langle P_i \rangle P_j + \langle P_i \rangle \langle P_j \rangle \rangle = \langle P_i P_j \rangle - \langle P_i \rangle \langle P_j \rangle \qquad (3.33)\end{aligned}$$

where the matrix elements of the covariance matrix represent the correlations between the parameters. Equation (3.32) is in fact a system of n linear equations with n unknowns $\mathcal{C}_i$ that can be solved by inverting the matrix $\mathcal{P}$; the results for the sensitivities are given by:

$$\vec{\mathcal{C}} = \mathcal{P}^{-1}\vec{\zeta} \qquad (3.34)$$

3.6.2 Size of the corrections and stability for the pion data

The extracted values of the normalized correlation slopes $\mathcal{C}_i/(2\langle Y \rangle)$ are listed in Table 3.3 for the pion data together with the values of the helicity correlated (HC) ΔP_i averaged over the running period. The product of the two is also given to show the order of magnitude of the false asymmetries A_f arising from HC effects. Note that all of these effects are smaller than the statistical error in A_π (0.8 ppm). The yields were corrected MPS by MPS using the slopes $\mathcal{C}_i$ extracted from the linear regression. The difference between the final pion asymmetry before and after slope corrections was found to be only 0.02 ppm, which is an order of magnitude smaller than the estimated false asymmetries given in Table 3.3.

Beam Parameter	Value	Slope	A_f (ppm)
A_Q (ppm)	-0.17 ± 0.22	0.00103 ± 10^{-5} %/nC	0.00 ± 0.00
Δx (nm)	82.5 ± 4.2	-0.0653 ± 0.003 %/mm	-0.06 ± 0.004
Δy (nm)	-36.2 ± 5.6	0.183 ± 0.004 %/mm	-0.06 ± 0.01
$\Delta\theta_x$ (nrad)	5.4 ± 0.3	-2.80 ± 0.08 %/mrad	-0.15 ± 0.01
$\Delta\theta_y$ (nrad)	-1.5 ± 0.5	-2.29 ± 0.07 %/mrad	0.03 ± 0.01
ΔE_b (keV)	0.008 ± 0.0007	-0.711 ± 0.017 %/MeV	-0.06 ± 0.005

Table 3.3: Average of helicity correlated beam parameter differences and asymmetry for the pion data with their respective normalized correlation slopes $\mathcal{C}_i/(2\langle Y\rangle)$.

Relatively large slope fluctuations are seen on a run by run basis, as illustrated by Figure 3.8 for octant 1. Similar effects are found to occur for the electron data as well, for the same running period. These slope fluctuations could be partially explained by correlations with other corrections performed by the analyzer [99].

Simulations were performed to estimate the size of the normalized slopes $\mathcal{C}_i/(2\langle Y\rangle)$, and these indicated that the expected size of the effects is smaller than what is shown in Table 3.3 by at least an order of magnitude [100]. Moreover, the impact of the slope corrections on the asymmetries for the elastic electron dataset is 5 times smaller than for the forward angle measurement, as expected [8] [2]. However, given the range of measured slopes, a conservative error of 0.16 ppm, corresponding to the largest estimate of false asymmetry A_f in Table 3.3, was assigned to the correction. This error is 8 times larger than the size of the net correction on an MPS by MPS basis.

When plotted on a run-by-run basis, relatively large fluctuations of $\mathcal{C}_i/(2\langle Y\rangle)$ can be seen. An example of $(dY/d\theta_x)/Y$ for octant 1 for the relevant runs is shown[7] in Figure 3.8. This is not unique to the pion locus, and similar fluctuations are seen in the electron case. Therefore, the same strategy to the electron case was followed, and an error of 0.16 ppm was assigned. Averaging over the full data set, there is an exceedingly small correction with no impact on statistics and in agreement with simulation.

The average pion asymmetry after pass 4 is:

$$A_\pi^{p4} = -0.52 \pm 0.78_{stat} \pm 0.16_{p4} \text{ ppm} \tag{3.35}$$

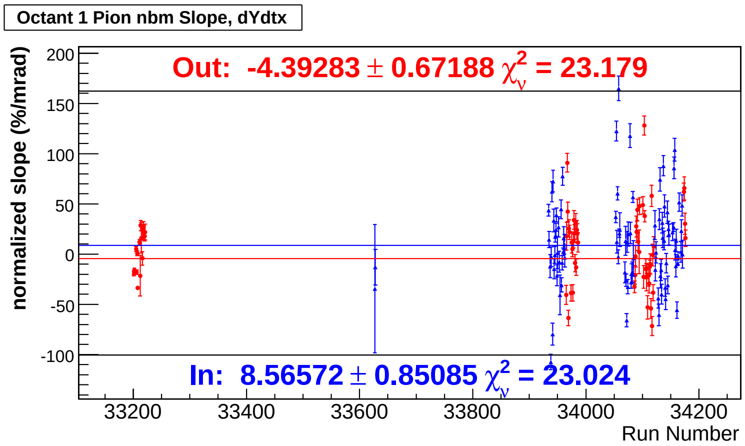

Figure 3.8: Normalized slope $\mathcal{C}_{\theta_x}/\langle Y\rangle$ versus run number for octant 1. The run period corresponds to the pion dataset (LD_2 at 362 MeV). Note the high χ^2 values from the linear fits indicating relatively large variations of the slope with time.

---

[7] The slope numbers in Table 3.3 would be 1/2 of what is shown in Figure 3.8.

3.7 Slow helicity reversal

As described in Section 2.4, a half-wave plate (HWP) was periodically inserted and removed from the laser beam in the injector to reverse the definition of + and - helicities seen by the experiment. Figure 3.9 shows the average octant asymmetries for the 362 MeV pion data after the pass 4 correction. The data are grouped by HWP state "in" and "out".

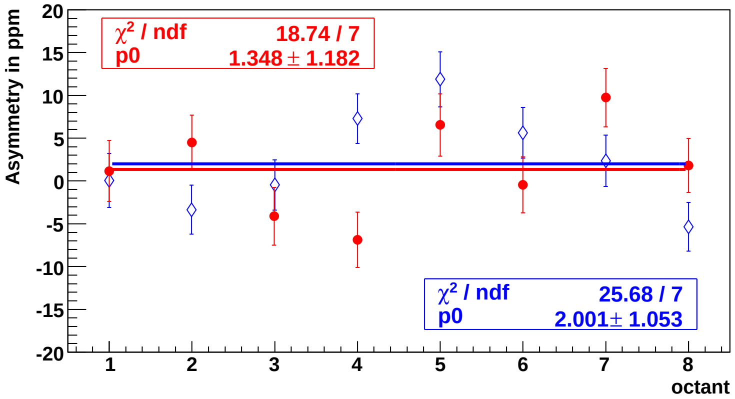

Figure 3.9: Half wave plate "in" (diamond) and "out" (filled cirle) asymmetry values as a function of octant number after pass 4. The parameter p0 (2.19 for "in" and 1.48 for "out") is the resulting average asymmetry value.

The average indicates both measurements agree with zero within errors. However, there is some evidence of a lack of sign reversal with HWP state.

Figure 3.10 shows the sum ("in" + "out") of the pion asymmetries seen in Figure 3.9, which should be ideally zero if the asymmetries reverse sign by changing the half-wave plate state. The reduced χ^2 for a constant fit to the sum ("in" + "out") of asymmetry data is about 2.9, indicating a very poor quality of fit (probability of 0.55 %). This indicates a poor consistency of sign reversal upon HWP state change octant by octant. The consistency is worst for octant 5, where a 3 σ discrepancy is seen. Despite hints that octant 5 might have experienced a problem due to noisy Cerenkov PMTs (see Section B.2 of Appendix B), there was no clear evidence of correlation between the asymmetries and the PMT noise found in that octant. The constant resulting from the fit is in agreement with zero to within 2.2 σ, which is just within error. Therefore, no additional systematic uncertainty due to lack of sign reversal is assigned.

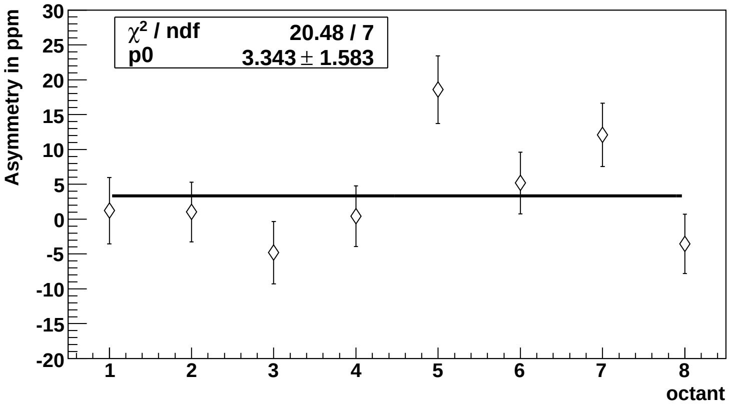

Figure 3.10: “in+out” asymmetry values as a function of octant number after pass 4.

The average of the pion asymmetries taking the half wave plate state into account is shown in Figure 3.11. The reduced χ^2 of the constant fit is again not satisfactory. This is a hint for possible transverse spin asymmetry contaminations that will be discussed in Section 3.8.2 of this chapter.

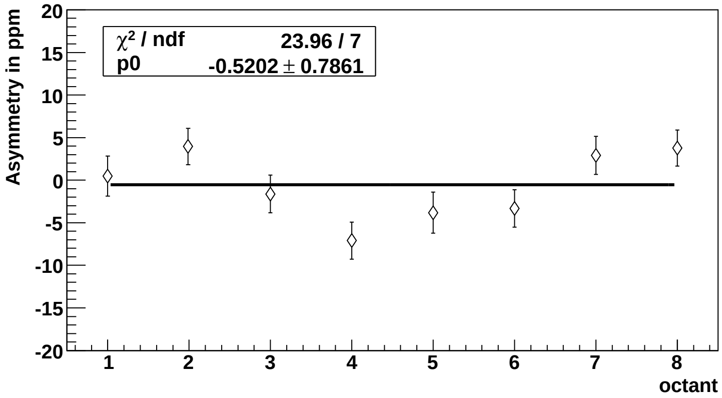

Figure 3.11: Average (over “in” and “out” HWP states) pion asymmetries as a function of octant number after pass 4.

3.8 Other corrections

Other corrections include those for particle misidentification, residual transverse polarization, overall longitudinal polarization, and target window backgrounds.

3.8.1 Backgrounds due to particle misidentification

Particle misidentification in the pion data sample arises when an electron fails to generate a signal in the Cerenkov detector. A similar effect occurs when pions misfire the Cerenkov detector.

3.8.1.1 Special data taking mode for PID

Fastbus data (see Section 2.10.1) were acquired using a pulsed electron beam at the frequency of 31 MHz and average current of typically 1 μA. Data of this type were acquired for the following sets of data:

- LH_2 target, beam energy 362 MeV
- LD_2 target, beam energy 362 MeV

- LD_2 target, beam energy 687 MeV
- Carbon target, beam energy 362 MeV

The 31 MHz signal triggered data acquisition and provided a common start to the TDCs. Figure 3.12 displays the resultant ToF spectrum for one FPD. Electrons have a shorter ToF than pions because of their higher speed. Very conservative timing cuts defined relatively pure electron and pion samples for the purpose of quantifying the backgrounds due to particle misidentification, as demonstrated in Figure 3.12.

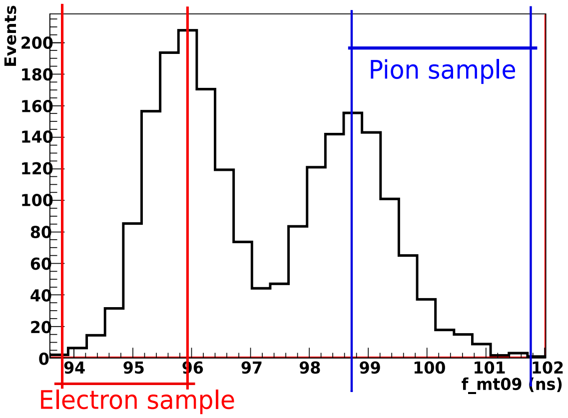

Figure 3.12: ToF spectrum of FPD09 at 362 MeV of beam energy and for the LD_2 target. The electrons correspond to the left peak and the pions to the right peak. The overlap between them is an issue since it decreases their purity.

The Cerenkov efficiency for electron detection $\boldsymbol{\epsilon}_e$ is determined from the fraction of pure electrons (defined by their ToF) which fire the Cerenkov trigger. The electron efficiencies for each FPD were averaged over the elastic and inelastic loci. The result is reported as a function of octant number in Table 3.4. An example of FPD dependence of the Cerenkov efficiencies is shown in Figure 3.13.

Octant	1	2	3	4	5	6	7	8
ϵ_e (%)	84.7	82.3	84.5	74.8	79.4	88.2	78.0	83.0
Statistical Error (%)	0.3	0.3	0.3	0.3	0.3	0.2	0.4	0.3

Table 3.4: Electron efficiencies averaged over the FPDs for the elastic and inelastic locus as a function of octant number. The averaging was performed using the statistical error on the electron yield as a weighting factor.

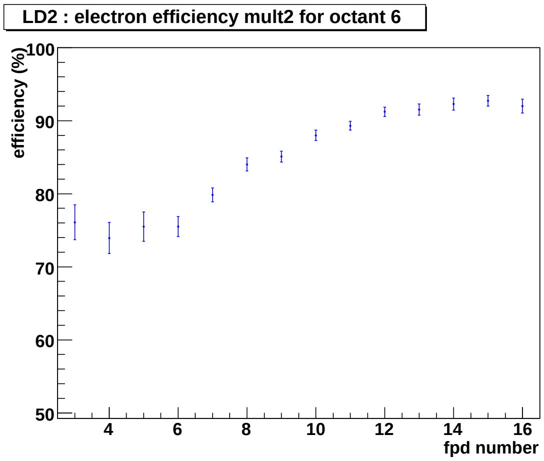

Figure 3.13: Cerenkov efficiency for LD_2 at 362 MeV as function of FPD summed over the elastic and inelastic loci.

A systematic check of the Cerenkov trigger recorded by the Fastbus electronics was made using the ARS data. Those results are presented in Appendix B.2 and give additional confidence to the Cerenkov efficiencies extracted from the ToF method [101] [102].

The Cerenkov efficiency for pion detection ϵ_π is similarly defined as the fraction of pure pions (defined by their ToF) which fire the Cerenkov trigger. As an example, let us consider the pion contamination of the electron sample $C_{\pi/e}$, expressed as:

$$C_{\pi/e} = \frac{\epsilon_\pi}{\epsilon_e} \cdot \frac{\phi_\pi}{\phi_e} \tag{3.36}$$

where ϕ_π and ϕ_e are the fluxes of electrons and pions respectively. The relative fluxes are determined from a two-Gaussian fit to the ToF spectrum for each FPD. The results for the contaminations, averaged over the FPDs for each octant, are summarized in Table 3.5. The ratio of the fluxes (ϕ_π/ϕ_e) is close to unity over the elastic+inelastic loci but is known absolutely at the 10 % level; a corresponding increase of the errors on the contaminations has to be accounted for.

At 687 MeV, the separation between the timing peaks for pion and electron signals is typically less than a nanosecond, making separation of the two peaks difficult. Figure 3.14 illustrates the ToF measurements under these conditions. An alternate method based on the ARS data and Monte Carlo simulations, discussed in Appendix B, was developed to resolve this problem. The results do not affect the 362 MeV pion data of interest.

Octant	1	2	3	4	5	6	7	8
$C_{\pi/e}$ (%)	0.41	0.48	0.37	0.32	0.57	0.41	0.53	0.46
Error (%)	0.13	0.12	0.13	0.10	0.17	0.12	0.16	0.14

Table 3.5: Pion contamination in the electron sample (elastic+inelastic) for the LD_2 target at 362 MeV beam energy. The errors correspond to statistical uncertainties increased by 10 % to account for the overall uncertainty in the flux ratio (ϕ_π/ϕ_e).

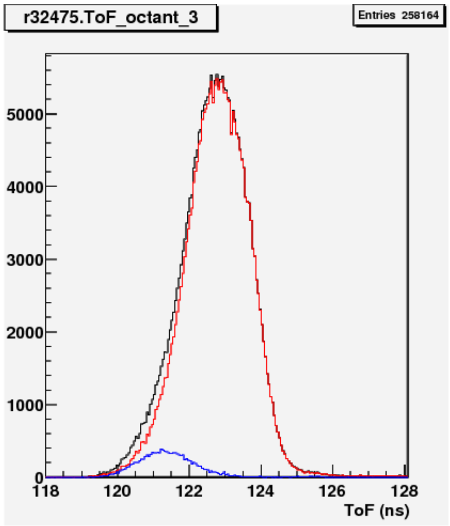

Figure 3.14: Time of flight spectrum for all elastic and inelastic cells of octant 3, LD_2 at 687 MeV. The smaller peak on the left represents events triggered by the Cerenkov detector. The large peak on the right represents events that do not trigger the Cerenkov detector. The spectrum encompassing both represents all the events producing a CED/FPD coincidence. Figure taken from [103].

3.8.1.2 Results for electron contamination of the pion sample at 362 MeV for the LD_2 target

Of importance for the interpretation of the A_π asymmetry measurements, the electron contamination of the pion sample is given by:

$$C_{e/\pi} = \frac{(1-\boldsymbol{\epsilon}_e)\phi_e}{(1-\boldsymbol{\epsilon}_\pi)\phi_\pi} \qquad (3.37)$$

The pion Cerenkov efficiency $\boldsymbol{\epsilon}_\pi$ (∼0.2%) is small compared to unity, and all other factors were determined using the ToF method [103]. Figure 3.15 shows an example of electron contaminations in the pion coincidence matrix. The averaged $C_{e/\pi}$ is $2.6 \pm 0.03_{stat}$%. The pion locus was defined by limiting the contamination to $< 10\%$ and requiring the pion rate to be more than 100 Hz/μA.

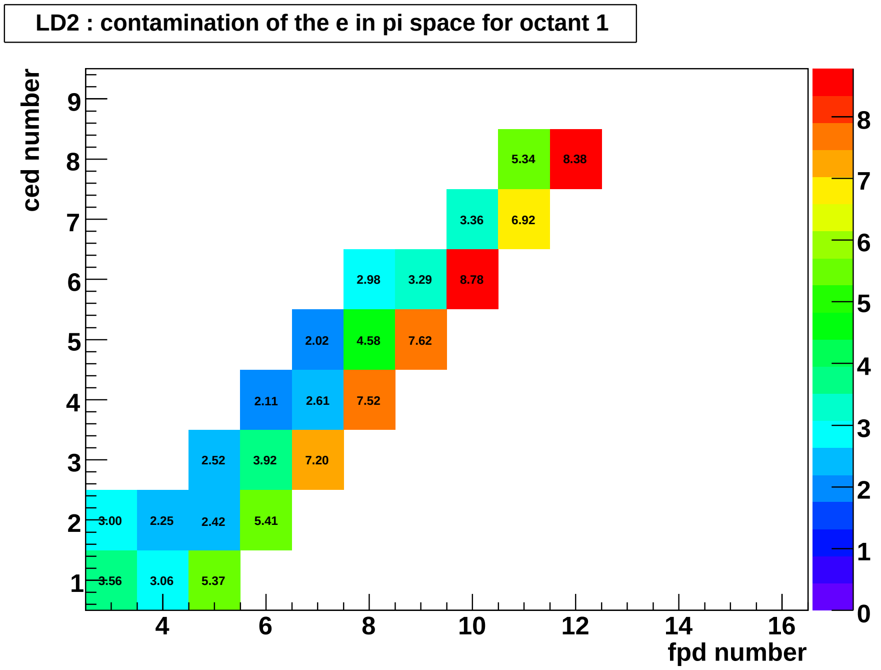

Figure 3.15: Octant 1 values of $C_{e/\pi}$ in percent for the relevant cells of the coincidence matrix.

The pion asymmetries were corrected cell by cell for each octant using:

$$A^{i,j}_{\pi,corr} = \frac{A^{i,j}_{\pi,p4} - A^{i,j}_{e,p4} C^{i,j}_{e/\pi}}{1 - C^{i,j}_{e/\pi}} \qquad (3.38)$$

where $A^{i,j}_{\pi,p4}$ and $A^{i,j}_{e,p4}$ are the pass 4 pion and electron cell asymmetries respectively and $A^{i,j}_{\pi,corr}$ is the pion asymmetry corrected for contamination. The statistical errors on $C^{i,j}_{e/\pi}$, $A^{i,j}_{\pi,p4}$ and $A^{i,j}_{e,p4}$ were included to determine the statistical error on $A^{i,j}_{\pi,corr}$. For reference, the pass 4 electron asymmetry averaged over the pion locus is $-5.75 \pm 0.9_{stat}$ ppm which gives the scale of the correction to be 0.15 ppm[8].

---

[8] Number calculated by simply multiplying the average of A_e over the pion locus by the corresponding average of $C_{e/\pi}$.

The corrected cell asymmetries $A^{i,j}_{\pi,corr}$, were then averaged with their statistical errors as weighting factors. This increased the average statistical error to 0.88 ppm, in contrast to the average value from pass 4, which is 0.82 ppm when the averaged pion asymmetry is calculated from the asymmetries in each cell of the pion locus. There is indeed a small discrepancy on the order of 0.04 ppm between the averaging of asymmetries over the locus and calculating the asymmetries directly from the total locus yields, the latter giving a statistical error of 0.78 ppm for pass 4 as seen in Figure 3.11.

For the systematic error estimate, the method presented above was compared with an approximate analysis from Ref. [104] where a single ToF cut t_{cut} in the middle of the electron and pion distributions was applied to the total number of events N that did not fire the Cerenkov trigger. In that case, the contaminations $C^{i,j}_{e/\pi}$ were determined by the ratio $N(t < t_{cut})/N$, where the numerator represents the fraction of events N detected before t_{cut}. The resulting average value $C_{e/\pi}$ was found to be 50 % higher than for the method presented above. The discrepancy is assumed to be due to the approximate nature of the analysis performed in Ref. [104]. Since the correction to the value of A_π is so small and we wish to present a conservative estimate of the uncertainty, the contaminations $C^{i,j}_{e/\pi}$ calculated from Equation (3.37) were increased by half of this discrepancy, and corrections were applied using the method described by Equation (3.38). Comparing the resulting average pion asymmetry with the one corrected with the nominal values of $C^{i,j}_{e/\pi}$, the difference between the two was taken as the systematic error of the correction, that is 0.10 ppm.

The average pion asymmetry after these additional background corrections is:

$$A_\pi^{back} = -0.22 \pm 0.88_{stat} \pm 0.10_{back} \text{ ppm} \tag{3.39}$$

3.8.2 False asymmetries from transverse polarization

As described in Section 2.4, the electron spin is not perfectly aligned with the incident beam direction, due to imperfect correction by the Wien filter in the 5 MeV section of the accelerator. One can decompose the spin direction into longitudinal $\vec{s}_L$ (along the beam) and transverse $\vec{s}_T$ (transverse to the beam) components as:

$$\vec{s} = \vec{s}_T + \vec{s}_L \tag{3.40}$$

and define:

$$\cos\xi \equiv \frac{\|\vec{s}_L\|}{\|\vec{s}\|} \tag{3.41}$$

so that $\xi = 0°$ for a perfectly longitudinal spin orientation. For imperfect spin alignment, the measured pion asymmetry, A_π^{meas} will be:

$$A_\pi^{meas} = A_\pi^L \cos\xi + A_{\pi,T} \sin\xi \tag{3.42}$$

where A_π^L is the asymmetry for longitudinally polarized electrons and $A_{\pi,T}$ corresponds to a pion asymmetry for fully transversely polarized electrons. For small misalignments, $\xi \leq 2°$, so that $\cos\xi$ is unity to a very good approximation. Therefore the measured pion asymmetry can be written as:

$$A_{\pi}^{meas} = A_{\pi}^{L} + A_{\pi,T}^{R} \tag{3.43}$$

where $A_{\pi,T}^{R}$ is a residual transverse asymmetry coming from spin misalignment and A_{π}^{L} is the longitudinal pion asymmetry of interest. The quantity $A_{\pi,T}$ was constrained with ancillary measurements with transversely polarized electrons. The result, corrected for electron contamination, is shown in Figure 3.16. The pion transverse asymmetry is on the order of 150 ppm, much larger than the pion and electron longitudinal asymmetries of interest to G^0.

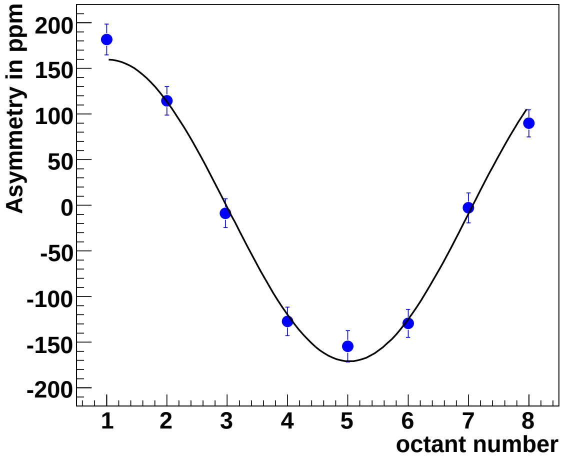

Figure 3.16: Transverse pion asymmetry ($A_{\pi,T}$) as a function of octant number. Note that a first order electron contamination correction was applied to these data.

In fully transverse mode, $\vec{s}_T$ is aligned with octant 1. Thus, taking $\Phi = 0$ for octant 1 and considering that the 8 octants cover 2π, the data were fitted using:

$$A_{\pi,T}(\Phi) = A_{\pi,T}^{max} \cos(\Phi + \Phi_0) + A_{\pi,T}^{0} \tag{3.44}$$

which led to the following parameters determinations:

$$A_{\pi,T}^{max} = 165.2 \pm 8.1 \text{ ppm} \tag{3.45}$$

$$A_{\pi,T}^{0} = -5.7 \pm 5.6 \text{ ppm} \tag{3.46}$$

$$\Phi_T^0 = -0.02 \pm 0.05 \text{ rad} \tag{3.47}$$

$$\chi^2 = \frac{4.86}{5} \tag{3.48}$$

where the error bars are statistical. The constant parameter $A_{\pi,T}^0$ was allowed to vary from zero but the result from the fit leads to a value consistent with zero within errors. If the statistical errors were smaller, non zero value for $A_{\pi,T}^0$ would be due to a small detector asymmetry. The large amplitude of the pion transverse asymmetry $A_{\pi,T}$ is known to be parity conserving. It would arise from a cross term related to the transverse and longitudinal virtual photon polarizations (LT') in the expression of the pion electro-production cross section [105].

The degree of transverse polarization was determined using the luminosity monitors (LUMI) asymmetries, which are of good statistical quality. The asymmetries detected by the LUMI correspond principally to scattered electrons at small angle (Moller e^-) and hence they arise from a different process, i.e. the transverse electron asymmetry analogous to Equation (3.42). The LUMI asymmetries, while of a different scale are directly proportional to $\vec{s}_T$ which is needed for the pion asymmetry correction. Figure 3.17 shows LUMI asymmetries as a function of octant number for both longitudinal and transverse beam polarizations. An analogous sinusoidal fit as Equation (3.44) leads to the parameters in Table 3.6. A small phase shift of 0.33 rad between the transverse and longitudinal data for the LUMI asymmetries should be noted. The quality of the longitudinal LUMI data indicates a very stable intrinsic phase of the residual transverse polarization.

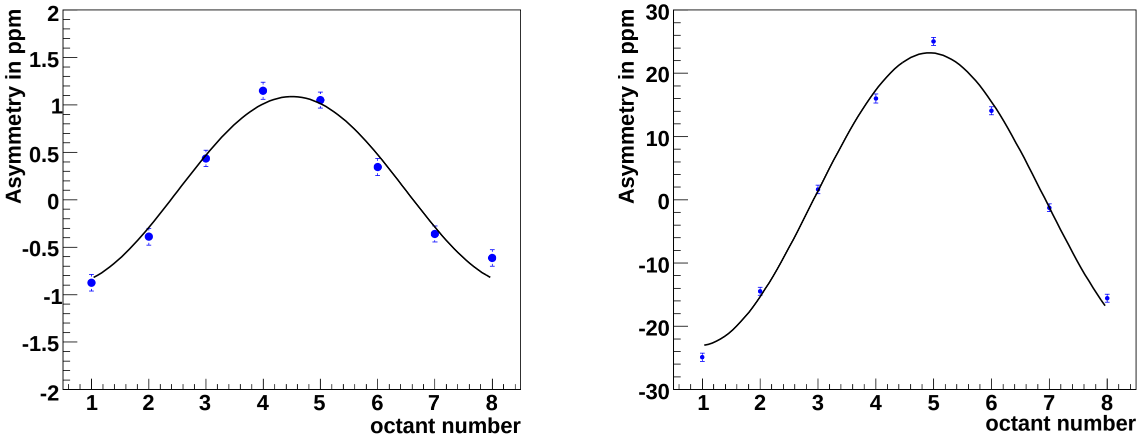

Figure 3.17: Luminosity monitor asymmetry as a function of octant number for longitudinally (left) and transversely (right) polarized electron beam.

	A^{max}_{Lumi} (ppm)	A^{0}_{Lumi} (ppm)	$\Phi^{0}_{L,Lumi}$ (rad)	χ^2_{Lumi}
Transverse	23.15 ± 0.32	0.08 ± 0.02	-3.08 ± 0.02	$31.93/5$
Longitudinal	0.99 ± 0.04	0.09 ± 0.03	-2.75 ± 0.04	$12.86/5$

Table 3.6: Fit parameters from the fits to the LUMI asymmetries as a function of octant number. Transverse and longitudinal refer to the beam polarization.

The quantity $\sin\xi$ from Equation (3.42) is extracted from the ratio of these asymmetries:

$$\sin\xi = \frac{A^{max}_{L,Lumi}}{A^{max}_{T,Lumi}} = \frac{0.99 \pm 0.04 \text{ ppm}}{23.15 \pm 0.32 \text{ ppm}} = 0.0427 \pm 0.0018 \tag{3.49}$$

This value compares reasonably well with a value determined by a Wien filter scan of $\sin 1^\circ \approx 0.017$, which is uncertain to $\sim 2^\circ$ [106]. Scaling the amplitude of the pion asymmetry in fully transverse mode $A^{max}_{\pi,T}$ by $\sin\xi$, and shifting the phase Φ^0_T by 0.33 rad provides the parameters needed for the transverse correction, which are the amplitude of $A^R_{\pi,T}$ and its phase respectively. These parameters are 7.05 ± 0.45 ppm for the amplitude and 0.26 ± 0.07 rad for the phase. Subtracting the residual transverse pion asymmetry from the longitudinal data removed the azimuthal dependence of the asymmetry, as shown in Figure 3.18. The average value decreased from -0.22 to -0.45 ppm with this correction, well within the error bar of 0.9 ppm (Equation (3.39)), and the reduced χ^2 improved from 3.75 to 1.23.

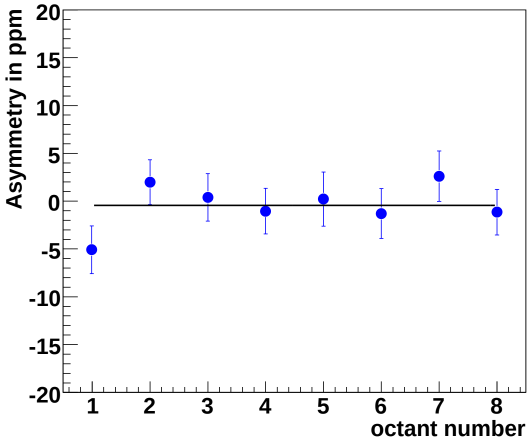

Figure 3.18: Pion asymmetry versus octant number for LD_2 at 362 MeV after transverse correction. The average value from the fit is -0.45 ± 0.89 ppm with a reduced χ^2 of 1.23.

The value of $\sin\xi$ is known to about 5 % as shown above, and the transverse pion asymmetry is well measured. Therefore, to estimate the systematic error due to this correction, the amplitude was varied by 0.5 ppm, giving the range: $A^{R,max}_{\pi,T} = 6.5$ to 7.5

ppm. The phase of the correction was varied by half of the phase difference between longitudinal and transverse LUMI asymmetries, that is by 0.16 rad, according to Table 3.6.

A numerical calculation leads to a systematic error of 0.06 ppm which corresponds also to about a third of the difference between the averaged asymmetry values from linear fits before and after transverse correction. The pion asymmetry after correction due to transverse spin effect is:

$$A_{\pi}^{L} = -0.45 \pm 0.89_{stat} \pm 0.06_{tr} \text{ ppm} \tag{3.50}$$

As an independent check, we can consider the azimuthal dependence of the PV pion asymmetry data, corrected for all other effects discussed so far. Figure 3.19 shows the pion asymmetry versus octant number before residual transverse asymmetry corrections. The sinusoidal fit gives:

$$A_{\pi,L}^{max} = 5.64 \pm 1.26 \text{ ppm} \tag{3.51}$$

$$A_{\pi,L}^{0} = -0.42 \pm 0.88 \text{ ppm} \tag{3.52}$$

$$\Phi_{L}^{0} = 0.26 \pm 0.22 \text{ rad} \tag{3.53}$$

$$\chi^2 = \frac{6.12}{5} \tag{3.54}$$

The fitted value $A_{\pi,L}^{max} = 5.64 \pm 1.26$ ppm agrees well with the independently deduced residual transverse correction 7 ± 0.5 ppm applied to the data, and the fitted constant $A^0_{\pi,L} = -0.42 \pm 0.88$ ppm agrees well with the corrected value $A^L_\pi = -0.45 \pm 0.89$ ppm quoted in Equation (3.50). These results indicate that the transverse polarization correction is appropriate and that the error has been assigned conservatively.

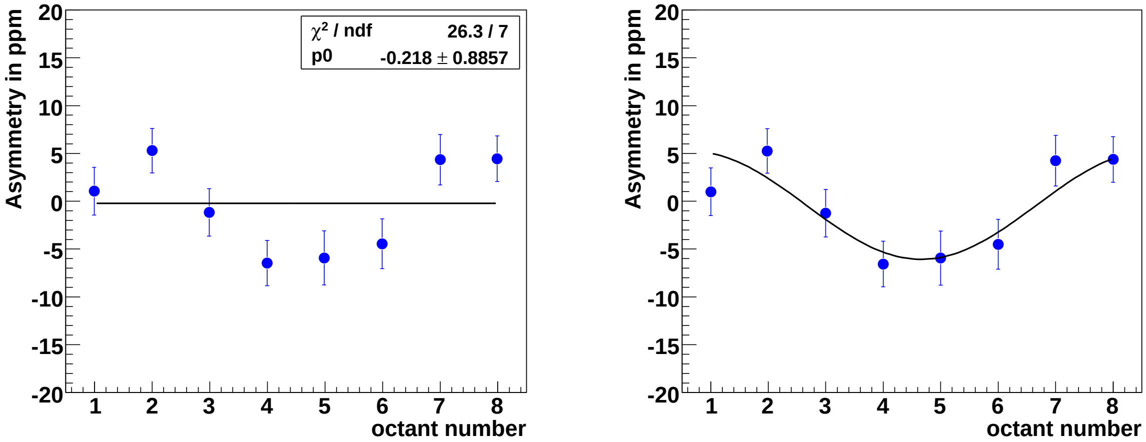

Figure 3.19: Pion asymmetry versus octant number for LD_2 at 362 MeV of beam energy. A linear fit was performed on the left graph with the average asymmetry corresponding to the parameter p0. A cosine fit was performed on the right graph with the parameters listed in the text. These data are corrected from all the effects described in the previous sections but not from transverse asymmetry.

3.8.3 Beam polarization

The beam polarization P_b, was discussed in Section 2.5 of Chapter 2 and was determined to be $P_b = 85.78 \pm 0.07_{stat} \pm 1.95_{sys}$ %. The resulting pion physics asymmetry is then:

$$A^{LR}_\pi = \frac{A^L_\pi}{P_b} = -0.55 \pm 1.03_{stat} \pm 0.01_{pol} \text{ ppm} \tag{3.55}$$

where the statistical error has been increased by 15 % due to the value of P_b and the last error represents the contribution from the uncertainty on the beam polarization itself.

3.8.4 Target windows

Backgrounds due to π^- production in the aluminium (Al) target walls were estimated to be 2%, as mentioned in Chapter 2, and are not corrected for. In a model where quasi-free π^- production from neutrons is assumed, the inelastic aluminium asymmetry would be the same size as that of the deuteron. We do not include the nuclear corrections to the PV asymmetry in our case, since they have never been evaluated theoretically and are likely not warranted yet given the present precision of our data. We do attempt to include them for unpolarized cross section estimations as will be described in 3.9. For reference, nuclear corrections of the quasi-elastic electron asymmetry from a deuteron target to an aluminium target were found to be of order 5 % in Ref. [15].

3.9 Physics corrections

3.9.1 Strategy

At this stage of the analysis, the pion asymmetry given in Equation (3.55) above represents a physics asymmetry that has been corrected for all experimental systematic effects. The next step is to extract the low energy constant d_Δ from this result and the associated kinematics. For that purpose, Monte Carlo simulations were performed. These reproduced the measured pion rates and allowed an extraction of other physical quantities associated with the pion physics asymmetry, which are the average 4-momentum transfer $\langle Q^2 \rangle$ and the photon depolarization $\langle D(y) \rangle$. The latter quantities enable us to deduce the photoproduction asymmetry A_π^γ by using the relation:

$$A_\pi^{LR} = (1 - f_{virt})\langle D(y)\rangle A_\pi^\gamma + f_{virt} A_{PV}^{inel}(\langle Q^2\rangle) \tag{3.56}$$

where f_{virt} is the fraction of virtual photon contribution to the pion rates in the G^0 experiment and A_{PV}^{inel} is the inelastic electron asymmetry. Details of the method used to extract A_π^γ and therefore d_Δ are discussed in Chapter 4.

The simulation strategy used in this analysis is indicated in Figure 3.20. The pion electro- and photo-production differential cross sections were taken from the Mainz unitary isobar model (MAID) [107] [108], which agrees well with experimental data. The differential cross sections were then implemented in a Monte Carlo generator to simulate the virtual and real photon contributions to π^- production. Results were then compared to cross section measurements from Ref. [109] and the Short Orbit Spectrometer (SOS) [110] data taken in Hall C. Once tested, the generator was implemented in the G^0 simulation framework and compared with the LD$_2$ pion data at 362 MeV. When good agreement was reached, the physics quantities needed to implement Equation (3.56) were calculated from the simulation.

3.9.2 Cross-sections and photon fluxes

In the case of a 362 MeV electron beam scattering from a 20 cm liquid deuteron target, negative pion production may be initiated by both virtual photons, and by real photons

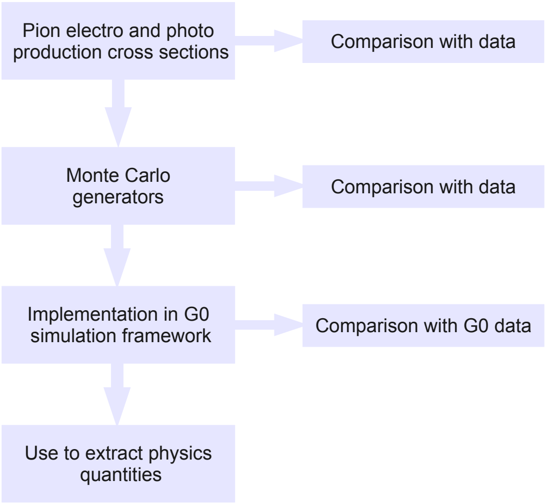

Figure 3.20: Strategy to extract reliable values of physics quantities from the Monte Carlo simulation.

originating from bremsstrahlung in the target. The two contributions are of similar size and cannot be disentangled experimentally, but both can be used because of their sensitivity to the pion photoproduction asymmetry. Contributions of both processes to unpolarized cross-sections are also needed for the analysis.

The π^- electroproduction process displays a relatively small average four-momentum transfer, since the corresponding electron scattering cross section is highly peaked near zero scattering angle. Hence, a very careful treatment of the corresponding cross section is required. The first part of this section will be focused on an accurate calculation of the virtual photon flux in this regime, without neglecting the electron mass.

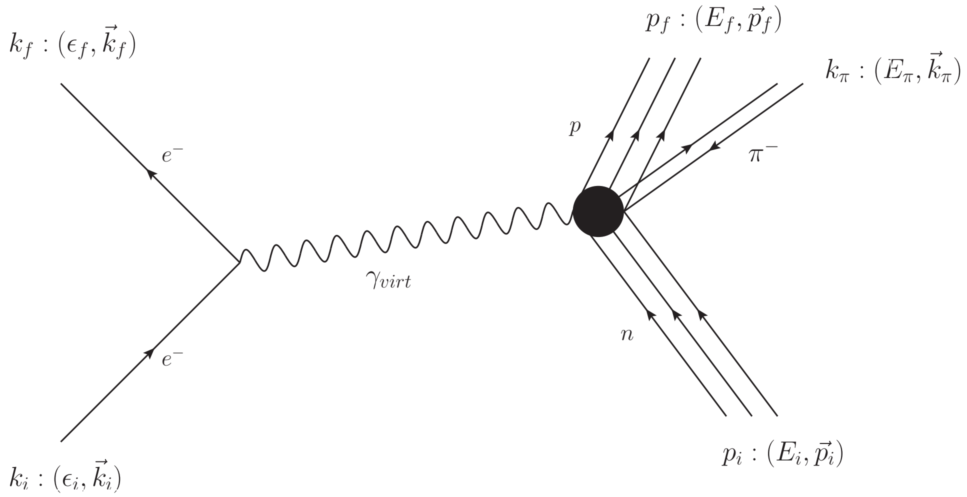

Figure 3.21: Feynman diagram of the inclusive pion electroproduction process.

3.9.2.1 Contributions from virtual photons

Using the notations of Figure 3.21, the 5-fold[9] differential cross section for electoproduction of π^- is given by [107]:

$$\frac{d\sigma}{d\Omega_f d\epsilon_f d\Omega_\pi^{CM}} = \Gamma_v \frac{d\sigma_\omega}{d\Omega_\pi^{CM}} \tag{3.57}$$

where σ is the exclusive pion production cross section, Ω_f is the solid angle of the outgoing electron in the laboratory frame, ϵ_f is the electron final energy, Ω_π^{CM} is the pion solid angle in the center of mass, and $d\sigma_\omega/d\Omega_\pi^{CM}$ is the differential pion photoproduction cross section. The virtual photon flux, Γ_v is defined as:

$$\Gamma_v = \frac{\alpha K_\gamma}{2\pi Q^2} \left(\frac{\epsilon_f^2}{\epsilon_i^2}\right)^{1/2} \frac{1}{1-\varepsilon} \tag{3.58}$$

---

[9] 5-fold accounts for: (θ_f, ϕ_f, ϵ_f, θ_π^{CM}, ϕ_π^{CM}).

where:

$$\varepsilon = \frac{1}{1 + \frac{2\vec{q}^{\,2}}{Q^2} \tan \frac{\theta_f}{2}} \tag{3.59}$$

in which $\vec{q}$ is the 3-momentum transfer, θ_f is the outgoing electron angle and Q^2 is the four-momentum transfer squared; ε is the degree of transverse polarization of the virtual photon. $K_\gamma = (W^2 - m_n^2)/(2m_n)$ is the photon equivalent energy, or the laboratory energy necessary for a real photon to excite a hadronic system with center of mass energy W. In these equations, the electron mass is assumed to be negligible, so that Γ_v diverges for $\theta_f \to 0$.

As Equation (3.57) needs to be integrated over electron kinematics, an accurate expression for Γ_v is therefore required. The correct expression including the electron mass was derived starting from the leptonic tensor (Equation (6.25) of Ref. [1]):

$$L_e^{\mu\nu} = 2(k_f^\mu k_i^\nu + k_f^\nu k_i^\mu - (k_f \cdot k_i - m_e^2) g^{\mu\nu}) \tag{3.60}$$

and the hadronic tensor (Equation (8.27) of Ref. [1]) removing the q^ν terms as they do not contribute to the contraction (Equation (8.25) of Ref. [1]):

$$W_{\mu\nu} = -W_1 g_{\mu\nu} + \frac{W_2}{m_n^2} p_{i,\mu} p_{i,\nu} \; . \tag{3.61}$$

Contraction gives:

$$\begin{aligned} L_e^{\mu\nu} W_{\mu\nu} &= 2(k_f^\mu k_i^\nu + k_f^\nu k_i^\mu - (k_f \cdot k_i - m_e^2) g^{\mu\nu})(\frac{W_2}{m_n^2} p_{i,\mu} p_{i,\nu} - W_1 g_{\mu\nu}) \qquad (3.62) \\ &= 4W_1(k_i \cdot k_f - 2m^2) + 2\frac{W_2}{m_n^2}[2(p_i \cdot k_i)(p_i \cdot k_f) - m_n^2(k_i \cdot k_f - m_e^2)] \; . \end{aligned}$$

Selecting the laboratory frame where $p_i : (m_n, \vec{0})$ gives:

$$L_e^{\mu\nu} W_{\mu\nu} = 2W_1(Q^2 - 2m_e^2) + W_2(4\epsilon_i \epsilon_f - Q^2) \tag{3.63}$$

and the differential cross section (Equation (8.33) of Ref. [1]) becomes:

$$\begin{aligned} d\sigma &= \frac{1}{4((k_i \cdot p_i)^2 - m_e^2 m_n^2)^{1/2}} \left[\frac{e^4}{Q^4} L_e^{\mu\nu} W_{\mu\nu} 4\pi m_n \right] \frac{d^3 k_f}{2\epsilon_f (2\pi)^3} \qquad (3.64) \\ &= \frac{(4\pi\alpha)^2 4\pi m_n}{4 m_n Q^4 (\epsilon_i^2 - m_e^2)^{1/2}} \left[2W_1(Q^2 - 2m_e^2) + W_2(4\epsilon_i \epsilon_f - Q^2) \right] \frac{k_f^2 dk_f d\Omega}{2\epsilon_f (2\pi)^3} \; . \end{aligned}$$

Performing a change of variables $dk_f = (\epsilon_f / k_f) d\epsilon_f$ leads to:

$$\frac{d\sigma}{d\epsilon_f d\Omega} = \frac{\alpha^2}{Q^4} \left(\frac{\epsilon_f^2 - m_e^2}{\epsilon_i^2 - m_e^2} \right)^{1/2} \left[2(Q^2 - 2m_e^2) W_1 + (4\epsilon_i \epsilon_f - Q^2) W_2 \right] \; . \tag{3.65}$$

Relating this to the photonuclear cross sections σ_T and σ_L defines the virtual photon flux via:

$$\frac{d\sigma}{d\epsilon_f d\Omega} = \Gamma_v' (\sigma_T + \varepsilon' \sigma_L) \tag{3.66}$$

where:

$$\sigma_T \equiv \frac{1}{2}(\sigma_+^{tot} + \sigma_-^{tot}) = \frac{4\pi^2\alpha}{K_\gamma} W_1(\omega, q^{\,2}) \tag{3.67}$$

$$\sigma_L \equiv \sigma_0^{tot} = \frac{4\pi^2\alpha}{K_\gamma}\left[\left(1 - \frac{\omega^2}{q^{\,2}}\right) W_2(\omega, q^{\,2}) - W_1(\omega, q^{\,2})\right] . \tag{3.68}$$

Comparing Equation (3.65) with Equations (3.66), (3.67) and (3.68), and defining ε' to be in agreement with Ref. [111] gives:

$$\varepsilon' = \frac{(4\epsilon_i\epsilon_f - Q^2) - 2m_e^2\dfrac{\vec{q}^{\,2}}{Q^2}}{(4\epsilon_i\epsilon_f - Q^2) + 2(Q^2 - 2m_e^2)\dfrac{\vec{q}^{\,2}}{Q^2}} \tag{3.69}$$

and:

$$\Gamma_v' = \frac{\alpha K_\gamma}{2\pi Q^2}\left(\frac{\epsilon_f^2 - m_e^2}{\epsilon_i^2 - m_e^2}\right)^{1/2} \frac{1}{1 - \varepsilon'} . \tag{3.70}$$

The use of ε' instead of ε is required as ε diverges for $\theta_f \to 0$. However, aside from ε, Γ_v is a good approximation of Γ_v' and does not affect the results. The 5-fold cross section is rewritten as:

$$\frac{d\sigma}{d\Omega_f d\epsilon_f d\Omega_\pi^{CM}} = \Gamma_v' \frac{d\sigma_\omega}{d\Omega_\pi^{CM}} . \tag{3.71}$$

For reference, the expression for Q^2 in the laboratory frame, keeping terms in m_e is:

$$\begin{aligned} Q^2 &= -q^2 = -(k_i - k_f)^2 \\ &= -2m_e^2 + 2(\epsilon_i\epsilon_f - \sqrt{\epsilon_i^2 - m_e^2}\sqrt{\epsilon_f^2 - m_e^2}\cos\theta_f) . \end{aligned} \tag{3.72}$$

3.9.2.2 Real photon flux

Real photons result from bremsstrahlung in the liquid deuterium target. The total number of bremsstrahlung photons per MeV per incident electron is given by [112]:

$$\Gamma_r \equiv \int_0^z \frac{d^2n}{d\omega dt} dt \tag{3.73}$$

where z is the position (here in g/cm^2) within the target at which the pion is photo-produced and:

$$\frac{d^2n}{d\omega dt} = \frac{3.495 \times 10^{-4}}{A\omega}[Z^2\Phi_n(Z, \epsilon_i, \omega) + Z\Phi_e(Z, \epsilon_i, \omega)] \tag{3.74}$$

where $d^2n/d\omega dt$ is the number of bremsstrahlung photons per MeV per incident electron per g/cm^2. Φ_n and Φ_e are the electron-nucleon and electron-electron terms in the bremsstrahlung cross-section respectively and are functions of the atomic number $Z = 1$, the initial electron energy ϵ_i, and the photon energy ω. $A = 2$ is the number of nucleons per atom. $d^2n/d\omega dt$ is the number of photons produced within an energy range $d\omega$ within a target thickness dt. Most of the bremsstrahlung flux is produced at forward angles with respect to the direction of the electron beam.

3.9.2.3 n(γ,π)p cross section and nuclear corrections

For the photonuclear cross-sections for a neutron target, the Mainz unitary isobar model (MAID) [107] [108] was used. A generator of the differential cross sections based on the calculations performed in [113] and [107] was available online [114] and also in the form of a subroutine written in FORTRAN (MAID2000) [113] [115].

The G^0 experiment used a liquid deuterium target. While the dominant process for π^- production is quasi-free production from neutrons, the following nuclear corrections had to be applied:

- Fermi motion: The neutron is not at rest within the deuteron. This leads to an initial target momentum $\vec{p}_F$, the Fermi momentum ($\|\vec{p}_F\| \leq 110$ MeV/c), that tends to smear the scattering cross section over a corresponding kinematic range.
- Pauli Blocking: The Pauli exclusion principle can have an effect on the cross section if the final state of the scattering process is not allowed.
- Final State Interactions (FSI): There is a possibility that the scattered particles interact with the proton spectator (p_s), hence affecting the cross section.

The method used to perform the nuclear corrections is to make use of the available cross section data for the reaction $d(\gamma,\pi^-)pp_s$ (where p_s is the proton spectator in the process). The ratio of the experimental values of π^- photoproduction cross sections from a deuterium target and the same cross sections predicted by MAID2000 assuming a neutron target was used as a scaling factor to perform the nuclear corrections.

The cross section for the process $d(\gamma,\pi^-)p_s$ was measured in Ref. [109] in a bubble chamber experiment at DESY with a bremsstrahlung beam of energies between 0.2

and 5.5 GeV. The data were corrected for nuclear effects in order to extract the cross section for $\gamma n \to \pi^- p$.

Figure 3.22 shows the deuteron cross section extracted from the bubble chamber experiment together with the neutron cross section recovered in Ref. [109]. There is a change in the amplitude of the resonance peak due to nuclear corrections, from 250 μb for d(γ,π)pp$_s$ to 300 μb for n(γ,π)p. As seen in Figure 3.22, the latter is in good agreement with MAID2000.

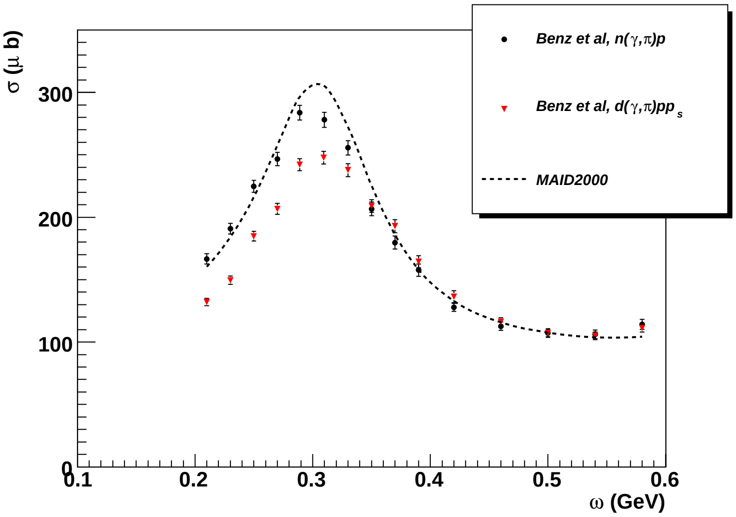

Figure 3.22: Comparison of neutron and deuteron cross sections as a function of photon energy. The dashed line represents the $\gamma n \to \pi^- p$ cross section generated by MAID2000. The triangles indicate the $\gamma d \to \pi^- pp_s$ cross section measured in Ref. [109]. The small bullets represents the $\gamma n \to \pi^- p$ cross section deduced from this experimental data.

3.9.3 Physics generators

The physics generator used the photoproduction cross section, $d\sigma_\omega/d\Omega_\pi^{CM}$, provided by the MAID2000 [114] routine based on Ref. [107]. A Monte Carlo integration was then performed as described in this section. The results were compared with a test code which performed an analytical integration using a forward peaking approximation method [116] [117]. In the latter case, it was assumed that most of the cross section is dominated by small scattering angles θ_f. The real photon part of the cross section was calculated using $d\sigma_\omega/d\Omega_\pi^{CM}$ and the photon flux given by Equation (3.74) [112].

A kinematic limit has to be applied to the pion electro- and photo-production generators. This limit arises from the center of mass energy threshold for creating a pion. This is given explicitly by:

$$W^2 \geq (m_p^2 + m_\pi^2)^2 \tag{3.75}$$

where W is the total energy in the center of mass and $m_{p,\pi}$ are the reaction product masses. Useful kinematic variables such as the pion energy and momentum as functions of the input variables are calculated in Appendix A.

While the magnitude of the cross section was corrected for Fermi motion, smearing effects of the pion momentum in the laboratory frame need be taken into account properly. The problem is due to an imprecise knowledge of the variation of nuclear corrections as a function of laboratory angle, and that the norm of the pion momentum needs to be calculated in the laboratory frame and not the neutron rest frame. A simple sketch of the initial conditions in those 3 frames is displayed in Figure 3.23. The best way to proceed is to calculate the pion kinematics and cross section in the center of mass, then perform a Lorentz boost to the reference frame in which the neutron is at rest, and at the end a Lorentz boost to the laboratory frame where the cross section is then corrected as described in Section 3.9.2.3. A detailed calculation of the kinematic variables in that case is discussed in Appendix A.

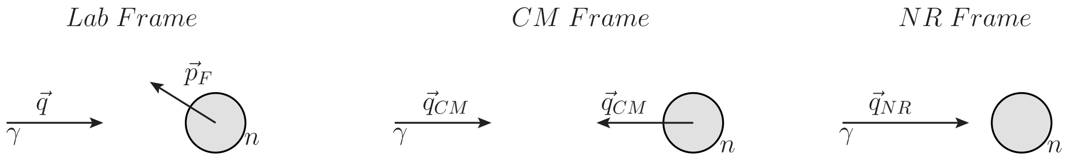

Figure 3.23: Initial photon momenta in the 3 different reference frames relevant to the calculation. From the left to the right, we can see the laboratory (Lab), center of mass (CM) and neutron at rest (NR) frames respectively.

For both virtual and real photon contributions, the Monte Carlo integration is done using $d\sigma_\omega/d\Omega_\pi^{CM}$ given by Ref. [107]. The difference between them resides in the integration procedure. The 5-fold differential cross section for virtual photons was given in Equation (3.57). The variables ϵ_f, Ω_f, Ω_π^{CM} are generated randomly; an integration is performed while calculating and recording all the relevant kinematic variables at each step. For the solid angles (Ω), flat spectra of $\cos\theta$ are generated, since the definition of the differential solid angle is $d\Omega = d\cos\theta d\phi$. The cross section being highly peaked at $\theta_f = 0$ makes the Monte Carlo integration very inefficient ($d\cos\theta_f \rightarrow 0$). The solution is to integrate over $\ln Q^2$ instead of θ_f by using:

$$\frac{d\sigma}{d\epsilon_f d\Omega_\pi^{CM} d\phi_f d\ln Q^2} = J \frac{d\sigma}{d\epsilon_f d\Omega_\pi^{CM} d\Omega_f} \tag{3.76}$$

where the the Jacobian factor J is given by:

$$J = \left| \frac{\partial \cos\theta_f}{\partial \ln Q^2} \right| = \left| \frac{\partial \cos\theta_f}{\partial Q^2} \frac{\partial Q^2}{\partial \ln Q^2} \right| = \frac{Q^2}{2\|\vec{k}_i\|\|\vec{k}_f\|} \tag{3.77}$$

where Equation (3.72) was used. Equation 3.76 then becomes:

$$\frac{d\sigma}{d\epsilon_f d\Omega_\pi^{CM} d\phi_f d\ln Q^2} = \frac{Q^2}{2\|\vec{k}_i\|\|\vec{k}_f\|} \frac{d\sigma}{d\epsilon_f d\Omega_\pi^{CM} d\Omega_f} \tag{3.78}$$

with the new integration limits for $\ln Q^2$:

$$\ln Q^2_{min} = \ln[2(\epsilon_i\epsilon_f - \|\vec{k}_i\|\|\vec{k}_f\| - m_e^2)] \tag{3.79}$$

$$\ln Q^2_{max} = \ln[2(\epsilon_i\epsilon_f + \|\vec{k}_i\|\|\vec{k}_f\| - m_e^2)] \tag{3.80}$$

The kinematic limits of the Monte Carlo generator were carefully checked before proceeding further. For virtual photons, we see in Figure 3.24 a 2 dimensional histogram of Q^2 as a function of the photon energy ω. The first limit is calculated from Equations (A.1) and (3.75), leading to:

$$Q^2 \leq m_n^2 + 2m_n\omega - (m_p + m_\pi)^2 \tag{3.81}$$

The second limit is derived from Equation (1.2) written explicitly as a function of ω:

$$Q^2 \leq 4\epsilon_i\epsilon_f = 4\epsilon_i(\epsilon_i - \omega) \tag{3.82}$$

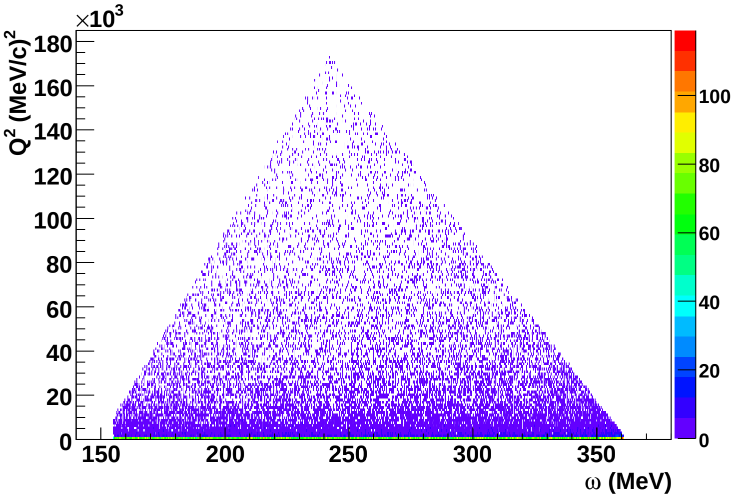

Figure 3.24: Graph of Q^2 vs ω in the virtual photon case. The limits are given in the text.

Another kinematic test was performed on the pion energy in the center of mass. Using Equation (A.4) with A.1 gives:

$$E_{\pi,CM} = \frac{m_n^2 + 2m_n\omega - Q^2 + m_\pi^2 - m_p^2}{2\sqrt{m_n^2 + 2m_n\omega - Q^2}} \tag{3.83}$$

The two Q^2 limits defined in Equation (3.82) and 3.81 were used to deduce those on $E_{\pi,CM}$ as a function of ω. This is what is shown in Figure 3.25.

Earlier simulations of pion photoproduction yields for the G^0 backward angle experiment were done at different beam energies [117]. However, since the original simulation code was still available, a direct comparison at 362 MeV was made possible.

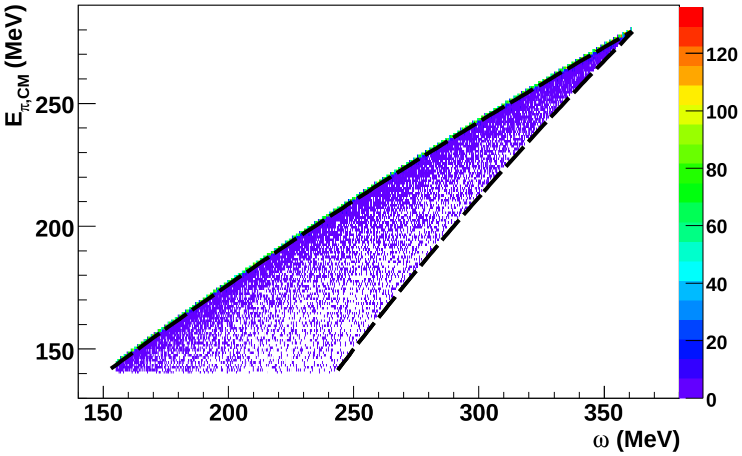

Figure 3.25: Graph of $E_{\pi,CM}$ vs ω in the virtual photon case. The overlaid black dashed lines are the limits given by taking the limits on Q^2 in Equation (3.83).

From the present Monte Carlo simulation, the quantity $d\sigma/dk_\pi d\Omega_\pi$ was generated for an out-going pion angle $\theta_\pi \approx 108°$. This was done by considering the pion momentum distribution in the laboratory frame with a cut on the pion angle and a weighting factor defined as:

$$w_v^{108} = \frac{1}{N_{Events}^v} \frac{\Delta\epsilon_f \Delta\phi_f \Delta \ln Q^2 \Delta\Omega_\pi^{CM}}{2\pi\delta\cos\theta_\pi \delta k_\pi} \tag{3.84}$$

in which $\delta\cos\theta_\pi$ is the cosine of the width of the cut in pion lab angle, δk_π is the number of MeV per bin in the histogram and the Δ's are the ranges of generation of the final electron energy (ϵ_f), azimuthal electron scattering angle (ϕ_f), $\ln Q^2$ and outgoing pion solid angle in the center of mass (Ω_π^{CM}). N_{Events}^v is the number of events generated by the MC. Figure 3.26 displays a fairly good agreement between the present MC simulation and the previous simulation based on the form of the cross section described by Tiator and Wright [116], which used a simpler analytical approach (forward peaking approximation).

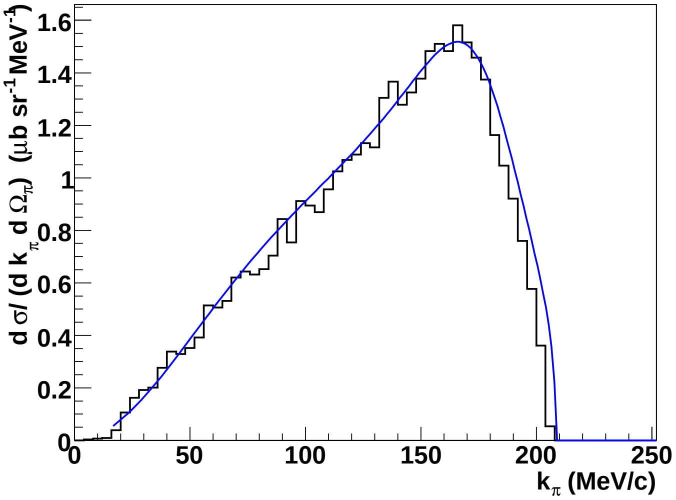

Figure 3.26: Virtual photon part of the differential cross section for $\theta_\pi \approx 108°$. The beam energy in the simulations is 362 MeV. The histrogram represents the present simulation, and the blue curve is the earlier simulation obtained from Ref. [116] [118].

For real photons, the integration must be done over the various photon energies and the pion solid angle. The integrand then becomes:

$$\frac{d\sigma}{d\omega d\Omega_\pi^{CM}} = \Gamma_r \frac{d\sigma_\omega}{d\Omega_\pi^{CM}} \tag{3.85}$$

The variables ω and Ω_π^{CM} were generated in the same fashion as discussed above, and a Monte Carlo integration was also performed. The event weight is given by:

$$w_r = \frac{d\sigma}{d\omega d\Omega_\pi^{CM}} \frac{\Delta\omega\Delta\Omega_\pi^{CM}}{N_{Events}^r} \tag{3.86}$$

The pion energy in the center of mass is completely determined by the real photon energy and the masses as described by Equation (3.83) when Q^2 is set to 0.

A comparison of the two simulations similar to the virtual photon case was performed. The results are expected to agree perfectly since the method is almost exactly the same in this case. $d\sigma/d\omega d\Omega_\pi$ was generated from the MC and compared with Ref. [117] as seen in Figure 3.27, in which good agreement with the previous study is displayed. In the course of these studies, a small mistake was found in the bremsstrahlung part of the code related to Ref. [117] as the deuteron density was set to twice the hydrogen density as a first approximation instead of its actual value. This was corrected in subsequent calculations.

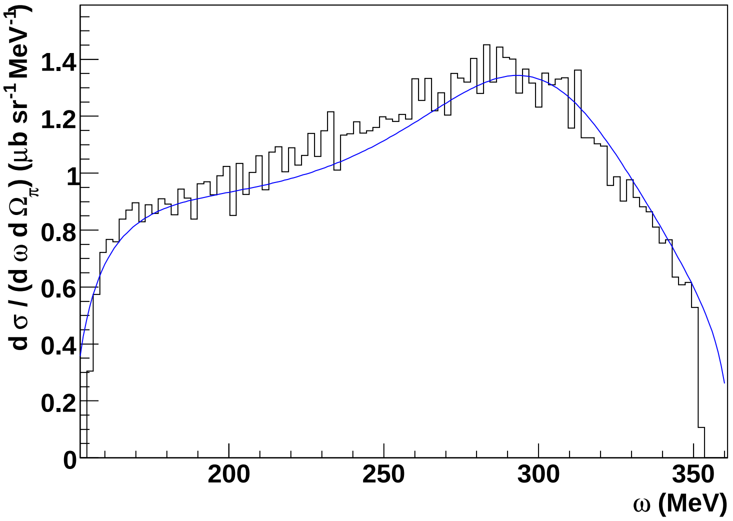

Figure 3.27: Real photon part of the cross section for $\theta_\pi \approx 108°$. The histogram is the current Monte Carlo simulation, The blue curve was obtained from the previous simulation based on Ref. [118][116][112].

A comparison of the real photon contribution to the MC cross sections with the data from Ref. [109] as a function of the pion lab angle is shown in Figure 3.28. A cut on the photon energy was applied ($280 < \omega < 300$ MeV) in this example. The error bars on the results from the MC generator (solid line) account for the spread due to the range of photon energies. The scaling factors applied to the MC representing nuclear corrections are given by the ratio between the data points corresponding to the dashed line and the solid line for sub-ranges of photon energies. The scaling factors are applied for ω sub-ranges that are typically 20 to 40 MeV wide.

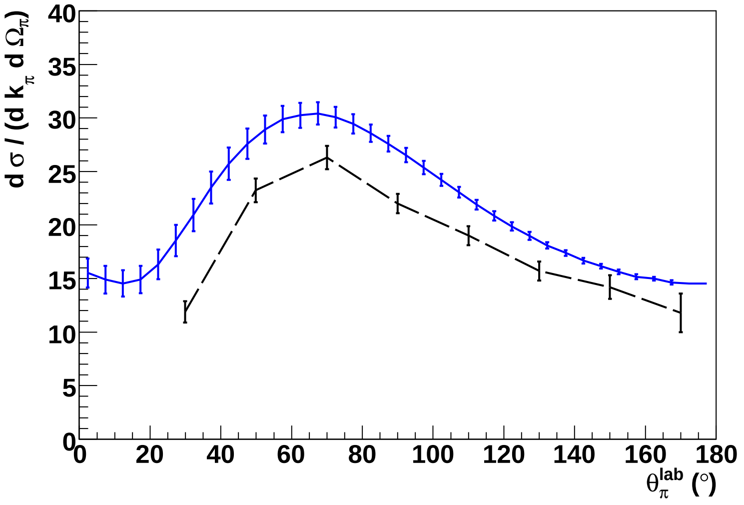

Figure 3.28: Real photon part of the cross section as a function of the pion lab angle. A cut was placed so that the photon energy is between 280 and 300 MeV. The smooth curve represents the Monte Carlo; the dashed line under it represents the measured cross section for the reaction $d(\gamma,\pi^-)pp_s$ from Ref. [109].

The present Monte Carlo was tested against the Short Orbit Spectrometer (SOS) [110] data taken in Hall C for background study purposes [119]. This comparison provides an additional check of the new generator. The SOS data taken in the context of Ref. [119] correspond to a pion scattering angle of about 136° and a beam energy of 824 MeV with different LD_2 target thicknesses. The purpose of the SOS data was to examine the size of possible π^- backgrounds for the main backward angle G^0 data at high energy

(687 MeV). From these measurements, the resulting cross sections corresponding to several deuterium target thicknesses are shown in Figure 3.29. The new generator is in good agreement with the SOS data for a 15 cm target; there appears to be an overall scale discrepancy for the 4 cm target data.

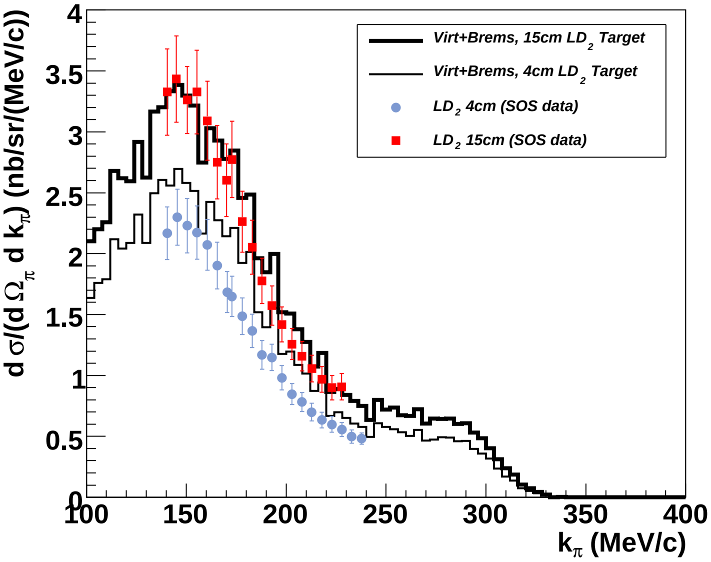

Figure 3.29: Monte Carlo simulation results compared with SOS data [119]. Cross section $d\sigma/d\omega d\Omega_\pi$ as a function of pion momentum in the lab frame. The simulation contains nuclear corrections and Fermi smearing of the pion momentum.

3.9.4 Implementation in G0Geant

The new π^- generator was implemented in the current G0-GEANT [120] simulation program which is a customized GEANT3 [121] code that describes the passage of elementary particles through the G^0 apparatus. The program was taken from the forward angle mode and adapted to perform G^0 backward angle simulations. G0-GEANT is set to track secondary particles such as negative muons (μ^-) arising from

π^- decay[10]. However, the G0-GEANT simulation is not necessarily complete; for example, the π^- or their decay products, μ^- have a small probability to be absorbed in materials hence not leading to a CED/FPD coincidence in some cases. While not explicitly implemented in G0-GEANT, those processes are found to not affect the rates by more than 1 % [122] [123].

3.9.5 Results for rate simulations and comparison to G^0 data

The simulated pion rates in Hz/μA for the virtual and real photon contributions to the 362 MeV LD_2 target data are shown in Figures 3.30 and 3.31 respectively. The secondary particles (μ^-) are automatically included as part of the standard G0-GEANT tracking. The virtual and real photon parts account for approximately half of the pion production rates respectively.

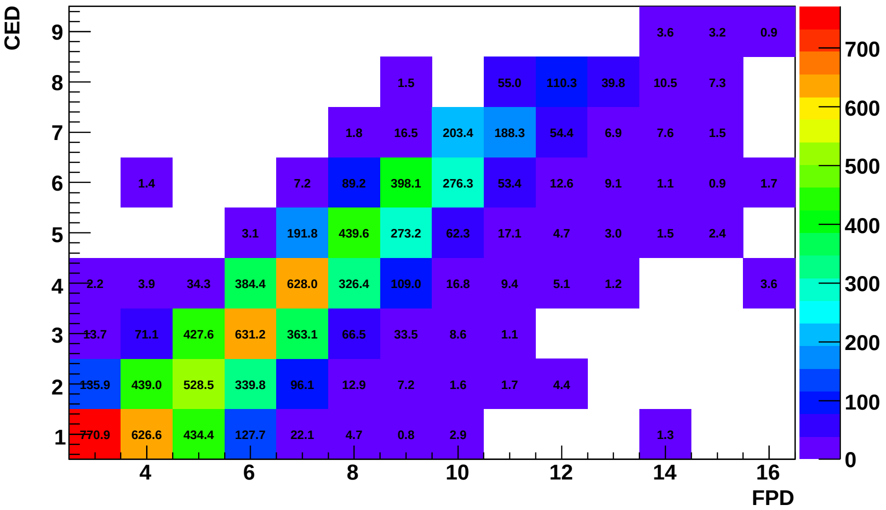

CED \ FPD	3	4	5	6	7	8	9	10	11	12	13	14	15	16
9												3.6	3.2	0.9
8							1.5		55.0	110.3	39.8	10.5	7.3	
7						1.8	16.5	203.4	188.3	54.4	6.9	7.6	1.5	
6		1.4			7.2	89.2	398.1	276.3	53.4	12.6	9.1	1.1	0.9	1.7
5				3.1	191.8	439.6	273.2	62.3	17.1	4.7	3.0	1.5	2.4	
4	2.2	3.9	34.3	384.4	628.0	326.4	109.0	16.8	9.4	5.1	1.2			3.6
3	13.7	71.1	427.6	631.2	363.1	66.5	33.5	8.6	1.1					
2	135.9	439.0	528.5	339.8	96.1	12.9	7.2	1.6	1.7	4.4				
1	770.9	626.6	434.4	127.7	22.1	4.7	0.8	2.9				1.3		

Figure 3.30: Virtual photon contribution to the simulated pion rates (Hz/μA) in the G^0 coincidence matrix for one octant (LD_2 target, 362 MeV).

---

[10] At the kinematics considered here, π^-'s have a half-life corresponding to a range of about 10 meters in the laboratory frame.

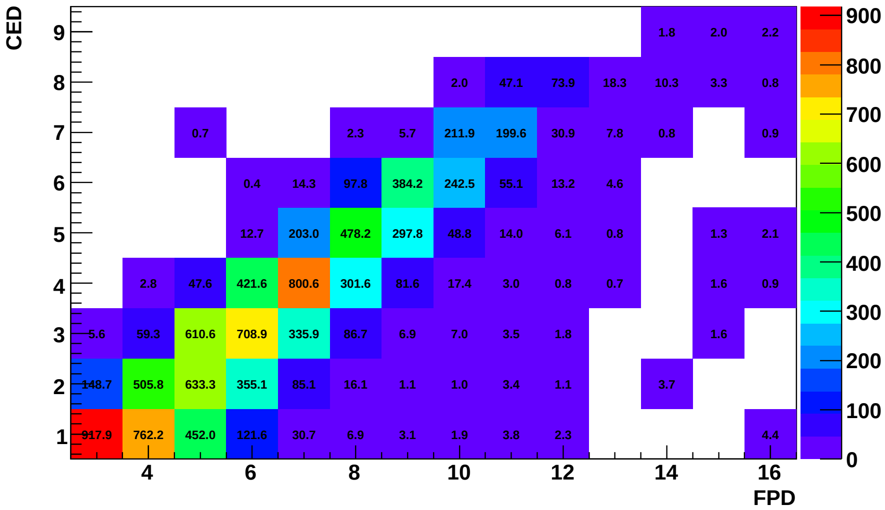

Figure 3.31: Real photon contribution to the simulated pion rates (Hz/μA) in the G^0 coincidence matrix for one octant (LD$_2$ target, 362 MeV).

The rates were summed over the pion locus defined earlier to compare the relative size of the 2 contributions. The total simulated rates corresponding to virtual(real) photons were found to be 7490(8978) Hz/μA respectively. One can extract the relative contribution from virtual photons defined as:

$$f_{virt} = \frac{V}{V+R} = \frac{7490}{7490+8978} = 0.45 \tag{3.87}$$

The measured pion coincidence matrix corrected from dead-time and randoms is shown for comparison in Figure 3.32.

The simulation and data are compared by looking at the normalized yields as function of FPD number, displayed CED by CED as shown in Figure 3.33. The simulation still overestimates the data by about $15-20\%$ in the high rate cells, which is nevertheless

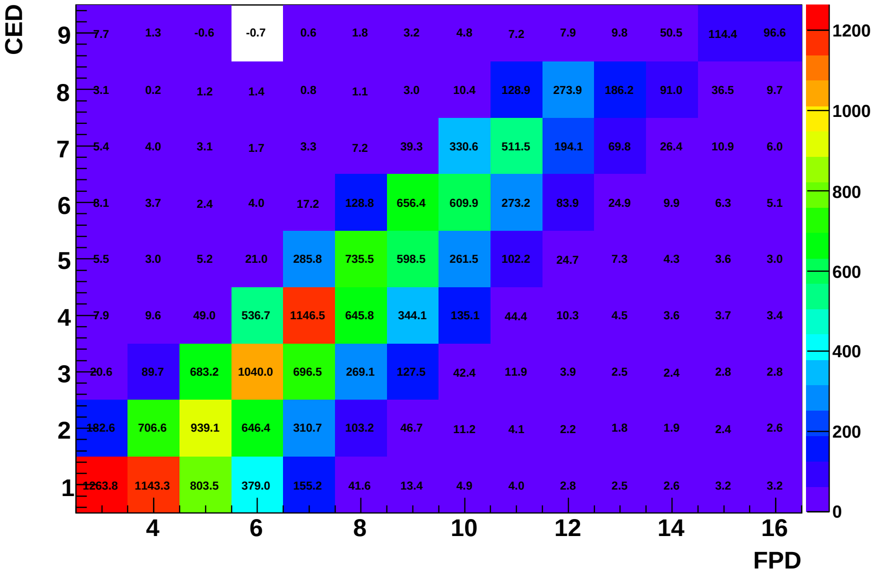

9	7.7	1.3	-0.6	-0.7	0.6	1.8	3.2	4.8	7.2	7.9	9.8	50.5	114.4	96.6
8	3.1	0.2	1.2	1.4	0.8	1.1	3.0	10.4	128.9	273.9	186.2	91.0	36.5	9.7
7	5.4	4.0	3.1	1.7	3.3	7.2	39.3	330.6	511.5	194.1	69.8	26.4	10.9	6.0
6	8.1	3.7	2.4	4.0	17.2	128.8	656.4	609.9	273.2	83.9	24.9	9.9	6.3	5.1
5	5.5	3.0	5.2	21.0	285.8	735.5	598.5	261.5	102.2	24.7	7.3	4.3	3.6	3.0
4	7.9	9.6	49.0	536.7	1146.5	645.8	344.1	135.1	44.4	10.3	4.5	3.6	3.7	3.4
3	20.6	89.7	683.2	1040.0	696.5	269.1	127.5	42.4	11.9	3.9	2.5	2.4	2.8	2.8
2	182.6	706.6	939.1	646.4	310.7	103.2	46.7	11.2	4.1	2.2	1.8	1.9	2.4	2.6
1	1263.8	1143.3	803.5	379.0	155.2	41.6	13.4	4.9	4.0	2.8	2.5	2.6	3.2	3.2

Figure 3.32: Measured pion rates (Hz/μA) in the context of the G^0 coincidence matrix for one octant.

a very significant improvement with respect to the previous implementation of pion generator in G0-GEANT where a factor 2 discrepency was found between the simulation and the pion rates in the coincidence matrix. The new simulation underestimates the data in two lowest rate elements, CED 8 and 9 by about 50 %. This could be due to Cerenkov inefficiency for the detection of elastic electrons in CED 9, but it is irrelevant in this context as the pion locus does not include CED 9. The missing rates in CED 8 seem to display the same FPD dependence as the simulated pion rates. This discrepancy could be due to an inaccurate implementation of Fermi smearing effects. It can also be due to geometry issues with the implementation of the G^0 apparatus in GEANT3. The discrepancy between the data and the simulation ($\sim$15 %) can be used as the uncertainty on f_{virt}.

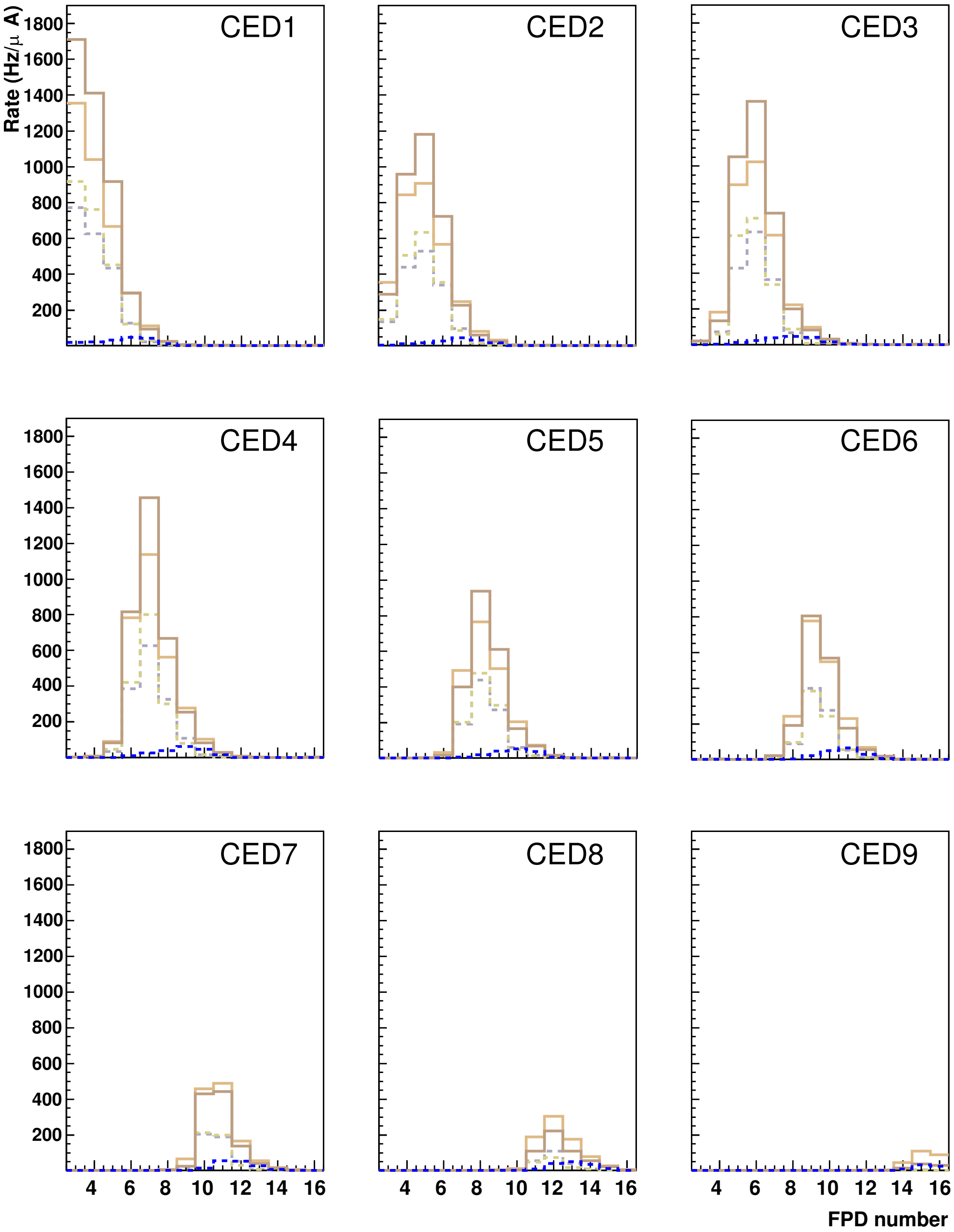

Figure 3.33: Pion rates (Hz/μA) as a function of FPD number. The dotted yellow and grey curves are the photon and virtual photon parts of the simulated pion rates. The blue curve is an estimate of the electron rates leaking into the pion data. The orange and brown curves are the data and total simulated rates plus the electron rates respectively. All the graphs are at the same scale.

A conservative error estimate for the simulated value of f_{virt} is obtained by comparing the effective radiation length of virtual photons $X_0^{virt} = 2$ % [124], and the radiation length of the material in the target contributing to bremsstrahlung, while assuming that $d\sigma_\omega/d\Omega_\pi^{CM}$ has the same value in either case. This gives a "back of the envelope" alternative calculation of f_{virt}. To a good approximation, the radiation length contributing to the bremsstrahlung flux within the LD$_2$ target is the sum of the radiation lengths of the material upstream of the target (X_0^{up}) added to 1/2 of X_0^{LD2} (see Table 2.5 for numbers). This is due to the fact that the bremsstrahlung flux increases linearly as the electron beam passes through the LD$_2$ target. Explicit calculation shows that:

$$f_{virt} = \frac{X_0^{virt}}{X_0^{virt} + (X_0^{LD2}/2 + X_0^{up})} \approx 0.54 \tag{3.88}$$

From Monte Carlo simulations, it was found that the acceptance of the G^0 apparatus along the z axis of the LD$_2$ target decreases linearly by a factor of 3 from the entrance to the exit of the target. Assuming a flat distribution of the virtual photon contribution along the target and an increasing bremsstrahlung flux as z increases, the real photon contribution from the LD$_2$ target (X_0^{LD2}) is reduced relative to the virtual photon contribution by a factor 5/6. This consideration increases the estimated relative contribution from virtual photons to $f_{virt} = 0.56$. The systematic error is then taken to be the discrepancy between the estimate discussed above and the Monte Carlo result, which is $0.56 - 0.45 = 0.11$, so that $f_{virt} = 0.45 \pm 0.11$.

3.9.6 Extraction of physics quantities

The real photon depolarization for a bremsstrahlung event, $D(y)$, with respect to the electron beam polarization, has a dilution effect on the pion asymmetry. This factor can be calculated formally [125] and has the form:

$$D(y) = \frac{y(1 + \frac{1}{3}(1-y))}{1 + (1-y)^2 - \frac{2}{3}(1-y)} \tag{3.89}$$

in which $y = \omega/\epsilon_i$ is the ratio of photon energy to the electron beam energy. A graph of $D(y)$ as a function of y is shown for G^0 kinematics in Figure 3.34.

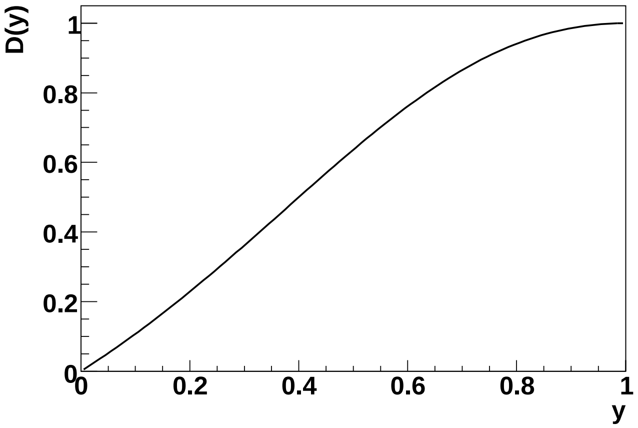

Figure 3.34: Photon depolarization as a function of $y = \omega/\epsilon_i$.

Figure 3.35 shows the spectrum of photon energy ω for events accepted by the G^0 apparatus. Given that ω tends to be close to the beam energy ϵ_i, the variable y is very close to unity, which translates into $D(y)$ being very close to 1, according to Figure 3.34.

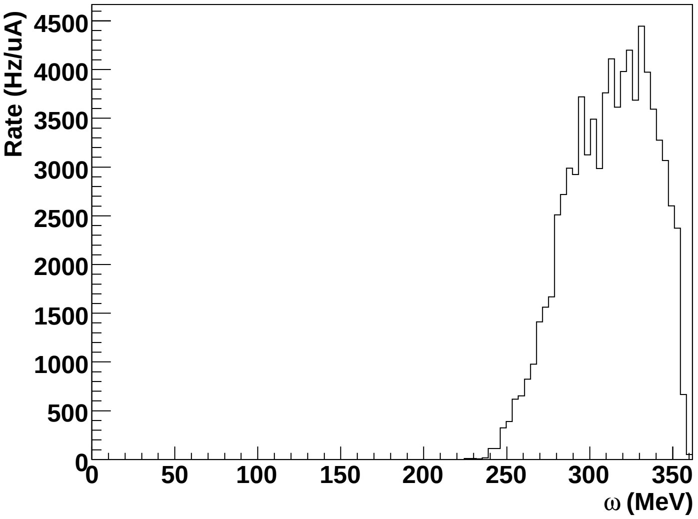

Figure 3.35: Rates in the coincidence matrix as a function of ω.

Equation (3.89) was implemented in G0-GEANT to extract the average $\langle D(y)\rangle$ for each cell of the coincidence matrix. Figure 3.36 shows a spectrum of $D(y)$ over the pion locus. Given the fact that the distribution of $D(y)$ is sharply peaked at 1 and that the average value is 0.95, it is reasonable to take 0.05 as a conservative systematic error on the average, which leads to an average photon depolarization of $\langle D(y)\rangle = 95 \pm 5\%$. This error would translate into an error on y of about 15 %. Effects due to Fermi smearing were not taken into account in the generation of the spectrum of ω, but those effects would certainly not affect the average y at the 15 % level. The assigned errors on y and $D(y)$ are thus demonstrated to be conservative.

For the virtual photon part of the cross section, the value of the average four-momentum transfer squared within the pion locus must be determined. Figure 3.37 shows the distribution of Q^2 within the pion locus, with an average of 0.00316 (GeV/c)^2.

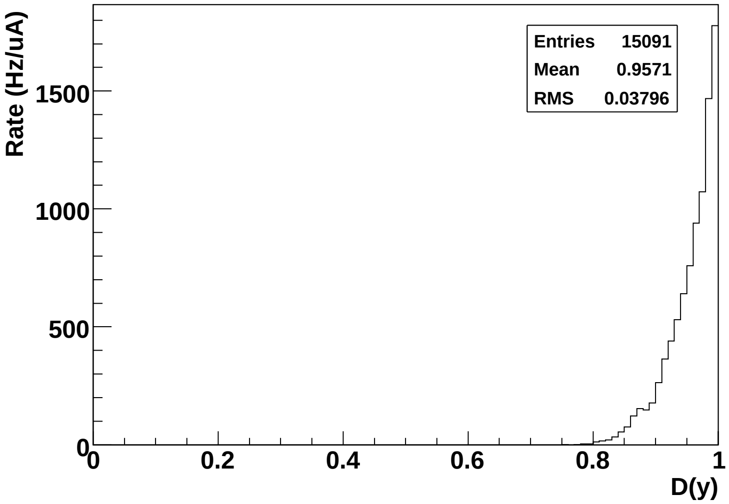

Figure 3.36: Photon depolarization factor (in %) spectrum calculated within the pion locus.

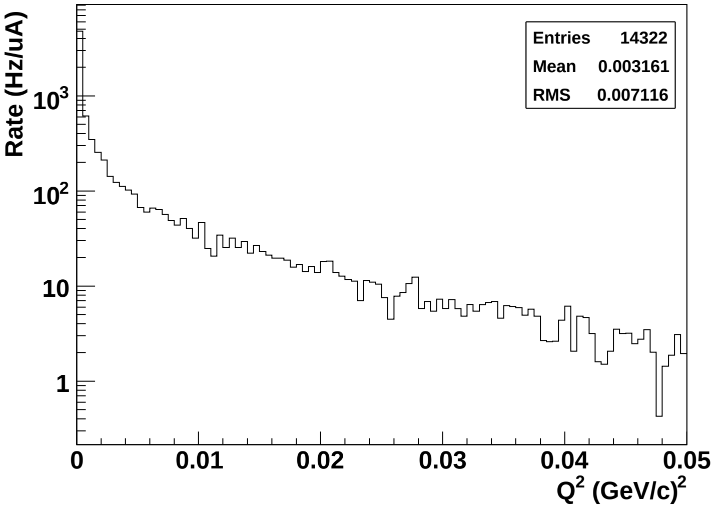

Figure 3.37: Histogram of Q^2 for events in the pion locus.

Systematic effects on the average Q^2 were estimated by changing various experimental parameters in the simulation. Table 3.7 shows the sensitivity of $\langle Q^2 \rangle$ with respect to relative changes of the SMS magnetic field, target position and beam energy. Given that the accuracy on experimental parameters is at least one order of magnitude [126] better than the variations shown in Table 3.7, the systematic error was conservatively assigned to be 10 % for $\langle Q^2 \rangle$.

Furthermore, an analytical estimate that approximates the cross section to be proportional to $1/Q^2$ as indicated by the flux factor defined in Equation (3.70) agrees with the simulation within 10 %, hence giving additional confidence in the assignment of the systematic error at this level.

Parameter	Shift from nominal value	$\langle Q^2 \rangle$ ((GeV/c)^2)
Magnetic field	+10 %	0.00292
Beam Energy	-5 MeV	0.00300
Target position	+4cm	0.00345

Table 3.7: Sensitivity of the average Q^2 to various parameters.

3.9.7 Impact of nuclear corrections to the pion asymmetry

Nuclear corrections to the unpolarized π^- production cross section were taken into account in the simulation. However, no nuclear correction were applied to the pion asymmetry. Those could include parity violating Final State Interactions (FSI) or higher order processes due to nucleon-nucleon interactions in the deuteron. Since the resonant π^- production process $\vec{\gamma} + d \rightarrow \pi^- + p + p_s$ is dominated by the subprocess $\vec{\gamma} + n \rightarrow \Delta^0 \rightarrow \pi^- + p$, nuclear effects on the asymmetry are expected to be relatively small [39] on theoretical grounds.

Nuclear effects related to π^- production in the Aluminium windows of the target cell can be potentially larger than those for deuterium. As discussed in Section 3.8.4, background rates from the aluminium windows were found to be only a ∼2%. Therefore, even if the nuclear corrections due to the π^- asymmetry for aluminium were of the order of 100 %, there would be no significant impact on the result for A_π given the experimental sensitivity of the pion asymmetry measurement in G^0.

3.10 Summary: Pion physics asymmetry, errors and kinematics

After all corrections, a pion physics asymmetry and its error were extracted from the data. Other parameters necessary to interpret the physics asymmetry and compare with theory are reported:

- The average momentum transfer of the virtual photon contribution to the pion data in the G^0 experiment.
- The relative contribution of the virtual and real photon contributions to the pion rates in the inelastic locus as well as their respective errors.
- The real photon depolarization factor, $D(y)$ and its error.

3.10.1 Pion asymmetry and errors

The final value of the pion asymmetry after all corrections is:

$$A_\pi^{LR} = -0.55 \pm 1.03_{stat} \pm 0.37_{sys} \text{ ppm} \tag{3.90}$$

A summary of the systematic corrections to the pion asymmetry after each step in the analysis is given in Table 3.8. A list of the dominant systematic errors is given in Table 3.9. The systematic errors were added in quadrature to arrive at the total systematic error in Equation (3.90).

Data analysis	Correction	Asymmetry (ppm)	Stat. Error (ppm)
Pass 2	RCS	-0.17	0.75
Pass 3	Rates	-0.54	0.78
Pass 4	Linear Reg.	-0.52	0.78
Additional corrections	Particle ID	-0.22	0.88
	Transverse	-0.45	0.89
	Beam pol.	-0.55	1.03

Table 3.8: Pion asymmetries at each step of the analysis.

Correction	Error (ppm)
Rates	0.26
Linear Reg.	0.21
Particle ID	0.12
Transverse	0.08
Beam pol.	0.01

Table 3.9: Systematic errors associated with each correction.

3.10.2 Kinematics and their errors

The physics pion asymmetry (3.90) was determined at the kinematic parameters listed in Table 3.10.

Parameter	Value	Error
$\langle Q^2 \rangle$	0.0032 $(\text{GeV/c})^2$	0.0003 $(\text{GeV/c})^2$
f_{virt}	0.45	0.11
$\langle D(y) \rangle$	95 %	5 %
E_b [126]	359.51 MeV	0.66 MeV

Table 3.10: Kinematic parameters used to interpret the pion asymmetry measurement. E_b is the mean electron beam energy at the center of the target.

The average four-momentum transfer, $\langle Q^2 \rangle$, is given for the virtual photon part of the pion data only. The quantity f_{virt} represents the fraction of events due to virtual photons. The average real photon depolarization factor $\langle D(y) \rangle$ is also given. In the next chapter, a preliminary extraction of d_Δ is presented using the work of Ref. [18] as a reference.

Chapter 4

Results and discussion

The low energy constant d_Δ can be calculated from the pion physics asymmetry A_π^{LR}. This is the principal goal of the present work. As discussed in Chapter 1, to first order, the relation[1] between d_Δ and A_π^γ is [39]:

$$A_\pi^\gamma \approx -\frac{2M_N d_\Delta}{C_3^V(0)\Lambda_\chi} \tag{4.1}$$

in which M_N is the neutron mass, $C_3^V(0) = 1.39$ is the dominant $N-\Delta$ vector transition form factor, and Λ_χ is the scale of chiral symmetry breaking. As discussed in Chapter 3, the pion physics asymmetry measured in the G^0 experiment (A_π^{LR}) is not the same as A_π^γ, since a fraction of the pion rates ($f_{virt} = 0.45$) arise from inelastic e-n scattering with a corresponding asymmetry A_{PV}^{inel}. This chapter will focus on the relation of A_π^{LR} to A_π^γ and the resulting world's first experimental limit on d_Δ.

---

[1] We refer in this section to d_Δ^- from Chapter 1.

4.1 Extraction of A_π^γ

As previously mentioned in Section 1.1.4 of Chapter 1, the inelastic asymmetry A_{PV}^{inel} in the process $e+n \rightarrow \Delta^0 \rightarrow p+\pi^-$ can be expressed as a sum of three contributions:

$$A_{PV}^{inel} = -\frac{G_F}{\sqrt{2}}\frac{Q^2}{4\pi\alpha}[\Delta_{(1)}^\pi + \Delta_{(2)}^\pi + \Delta_{(3)}^\pi] \qquad (4.2)$$

where G_F is the Fermi constant and α is the fine structure constant. The low energy constant d_Δ is included in $\Delta_{(3)}^\pi$, A_{PV}^{inel} coincides with Equation (4.1) in the $Q^2 \rightarrow 0$ limit. $\Delta_{(1)}^\pi$, $\Delta_{(2)}^\pi$ and $\Delta_{(3)}^\pi$ are shown again for reference as a function of Q^2 in Figure 4.1, calculated by the authors of Ref. [18], for beam energy 424 MeV. Since these contributions are dominantly a function of Q^2 and not beam energy, no additional theory uncertainty associated with the comparison to G^0 data at 362 MeV is assumed for the extraction of d_Δ.

The method used to calculate A_π^γ from A_π^{LR} is the following: the Q^2 dependence of A_{PV}^{inel} is essentially linear below 0.05 $(\mathrm{GeV/c})^2$, as seen in Figure 4.1. Moreover, as stated in Chapter 1, A_{PV}^{inel} coincides with A_π^γ in the limit of $Q^2 = 0$. Therefore, a linear extrapolation of A_{PV}^{inel} to the value of A_π^γ can be performed via:

$$A_\pi^\gamma = A_{PV}^{inel} + S\langle Q^2\rangle \qquad (4.3)$$

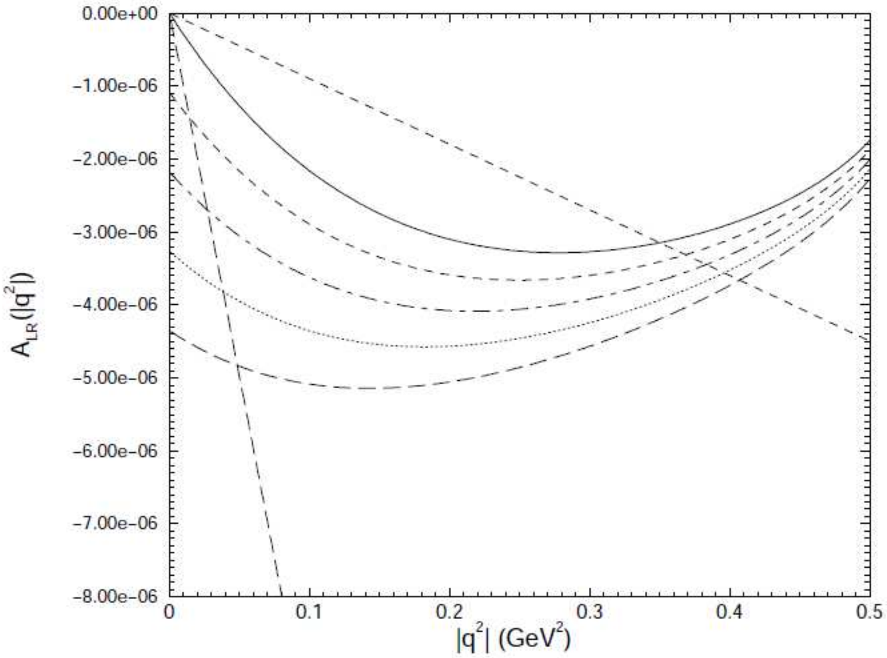

Figure 4.1: Different contributions to the inelastic asymmetries as a function of $|q^2|$. The long-dashed/dashed straight line corresponds to $A_{PV}^{inel}(\Delta_{(1)})$ / $A_{PV}^{inel}(\Delta_{(2)})$ respectively. The curves represent different possibilities for $A_{PV}^{inel}(\Delta_{(3)})$ depending on the value of d_Δ (Solid line corresponds to $d_\Delta = 0$ and the last dashed line corresponds to $d_\Delta = 100 g_\pi$). A beam energy of 424 MeV for inelastic scattering from the proton was used to make this figure, taken from [18].

where S represents the absolute value of the slope including the 3 above contributions to A_{PV}^{inel} below $Q^2 = 0.05$ (GeV/c)^2. To determine the slope, since A_π^γ is measured to be very small ($d_\Delta \approx 0$), and since $\Delta_{(1)}$ is very well known, we take the contributions $\Delta_{(1)}$, $\Delta_{(2)}$ and $\Delta_{(3)}(d_\Delta \approx 0)$ to determine S. For the uncertainty in S, we consider only the $\Delta_{(2)}$ and $\Delta_{(3)}$ terms. The uncertainty is very conservatively estimated as ±50% of these values. This uncertainty is larger than the slope variations with respect to d_Δ seen in Figure 4.1, and is larger than the slope variations due to the theoretical range of the low energy constant a_Δ (see Chapter 1) that is not shown in the figure. Taking the various contributions to the inelastic asymmetry from Figure 4.1 for $Q^2 = 0.05$

$(\mathrm{GeV/c})^2$ gives an estimated slope (S) of 133 ppm/$(\mathrm{GeV/c})^2$. The overall uncertainty on the slope S was found to be 18 ppm/$(\mathrm{GeV/c})^2$.

The pion physics asymmetry in the G^0 experiment can be expressed as a sum of virtual and real photon contributions:

$$A_\pi^{LR} = (1 - f_{virt})\langle D(y)\rangle A_\pi^\gamma + f_{virt} A_{PV}^{inel}(\langle Q^2\rangle) \tag{4.4}$$

where $\langle D(y)\rangle$ is the real photon depolarization, and $\langle Q^2\rangle$ is the average four-momentum transfer squared corresponding to the virtual photon contribution to pion production. Using Equation (4.3) and extracting A_π^γ gives:

$$A_\pi^\gamma = \frac{A_\pi^{LR} - f_{virt} S \langle Q^2\rangle}{(1 - f_{virt})\langle D(y)\rangle + f_{virt}} \tag{4.5}$$

Explicit calculation using the results presented in Chapter 3 and the numerical value of the slope S discussed above leads to:

$$A_\pi^\gamma = -0.36 \pm 1.06_{stat} \pm 0.37_{sys} \pm 0.03_{th} \text{ ppm} \tag{4.6}$$

where all the systematic uncertainty contributions are listed in Table 4.1. The last quoted error corresponds to a theory error associated with the slope S which does not depend on the G^0 experiment but on the theoretical input for A_{PV}^{inel}.

Contribution	Value (ppm)
RCS	0
Rates	0.26
Linear Regression	0.21
Particle ID	0.12
Transverse Polarization	0.08
Beam polarization	0.01
$\langle Q^2 \rangle$	0.02
$\langle D(y) \rangle$	0.01
f_{virt}	0.05
S	0.03

Table 4.1: List of all systematic error contributions to the final value of A_π^γ.

4.2 Results for d_Δ

The relation between d_Δ and A_π^γ was given in Equation (4.1) [18]. Neglecting the uncertainties in the input parameters of Equation (4.1) and propagating the statistical and systematic errors arising from A_π^γ, d_Δ is calculated to be:

$$d_\Delta = (8.3 \pm 23.9_{stat} \pm 8.3_{sys} \pm 0.7_{th})\ g_\pi \tag{4.7}$$

where $g_\pi = 3.8 \times 10^{-8}$ and the last quoted error represents a theory error due to the assigned uncertainty on S. This represents the first experimental determination of d_Δ; it excludes ~75 % of the theoretically possible range of values at 1 σ, as illustrated by Figure 4.2.

4.3 Comparison with theoretical predictions

A comparison of the extracted value of d_Δ from the G^0 pion asymmetry measurement at backward angle with respect to the range of theoretical predictions is given in Figure 4.2. As discussed in Chapter 1, the predicted range using the Resonance Saturation Model for the absolute value of d_Δ is $(9 \rightarrow 25)\ g_\pi$ [18]. Moreover, possible enhancements could arise from the ratio of the CKM matrix elements, V_{ud}/V_{us}. On the other hand, there is no reason for d_Δ to not be smaller than 9 g_π, and possibly lower than its natural scale, g_π. Therefore, the full range of possible values for d_Δ: $(-100 \rightarrow 100)\ g_\pi$, is shown on the left side of Figure 4.2. The best value, $|d_\Delta| = 25\ g_\pi$, which was calculated in Ref. [18], also appears in Figure 4.2.

With a 95 % confidence level (2 σ), the results of this work are that d_Δ was found to be in the range -42 to +59 g_π with the assumptions presented here. This result tends to favor smaller d_Δ, excluding the larger predictions in the theory range given by the authors of Ref. [18]. The result tends to rule out the possible enhancements by V_{ud}/V_{us} corrections suggested in Ref. [18]. However, given the precision of this measurement, the result is in agreement with both the enhancements due to the Resonance Saturation Model which lead to the "best value" suggested in Ref. [18], and with the natural scale. Higher statistical precision would be required to further distinguish between the resonance saturation model without V_{ud}/V_{us} enhancements and the natural scale.

The comparison made above is in the context of Ref. [18][39]. Further work on the theory would enable a more reliable determination of d_Δ. In preparing to publish this result, it is planned to contact the authors of Ref. [18] [39] to confirm the extrapolation of the experimental asymmetry to the photon point as described in Section 4.1. This interpretation must account for the specific combination of target, kinematics and selection of final state ($p\pi^-$) as studied in the G^0 experiment.

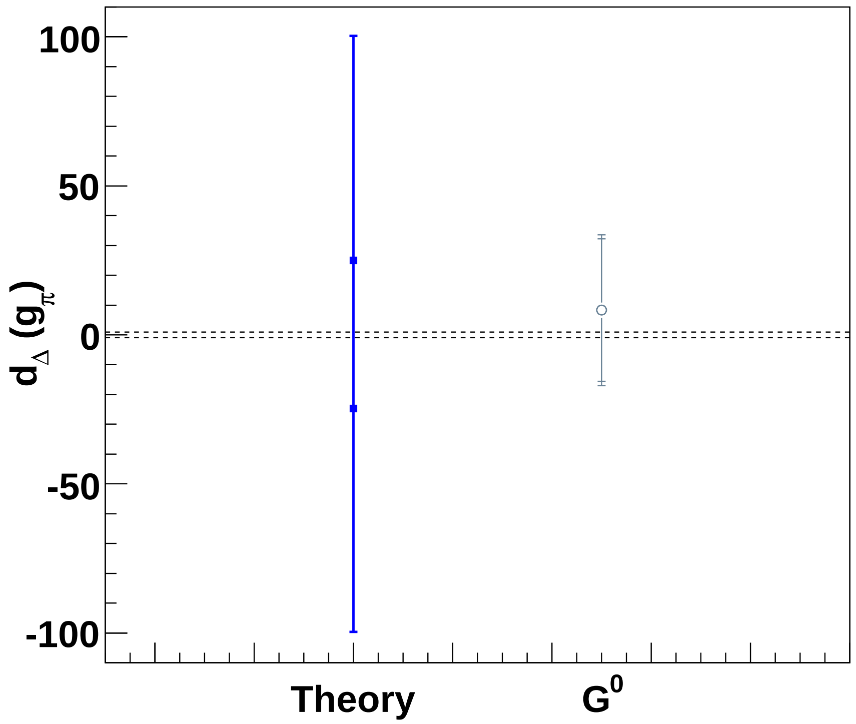

Figure 4.2: Comparison of d_Δ as calculated from the pion asymmetry measurement in the G^0 experiment with the theoretical predictions from Ref. [18]. The statistical error on the measurement is represented by the inner error. The total error (statistical, systematic and theory added in quadrature) is represented by the outer error. The dashed lines shows the natural scale of d_Δ, and the square markers represent the best values. The theory range on the left accounts for phase uncertainties and possible V_{ud}/V_{us} enhancements as discussed in the theory chapter.

4.4 Future prospects for d_Δ

A second experiment to constrain d_Δ using the Q_{Weak} experiment apparatus at Jefferson Lab has been proposed in Ref. [127]. The Q_{Weak} experiment is a measurement of the parity violating asymmetry in elastic electron proton scattering at very forward angles ($Q^2 = 0.03$ (GeV/c)^2), which could lead to a very precise determination of the weak charge of the proton, $Q_W^p = 1 - 4\sin^2\theta_W$ [128]. The apparatus of Q_{Weak} can be used to also measure the inelastic asymmetry A_{PV}^{inel} at $Q^2 \approx 0.022$ (GeV/c)^2, hence providing an independent evaluation of d_Δ. The goal for the statistical accuracy for the measurement of d_Δ in the Q_{Weak} experiment is approximately 7 g_π which is approximately 3 times smaller than the present result. For that purpose, it was proposed to dedicate 1 week of beam time in early 2011 to perform the inelastic asymmetry measurement with the Q_{Weak} apparatus.

Like G^0, the apparatus for the Q_{Weak} experiment also includes a toroidal magnet spectrometer. It is an 8-fold symmetric apparatus as for the G^0 experiment and uses quartz Cerenkov bars as the main detectors. Unlike G^0, it is a current mode experiment with beam intensity as high as 150 μA. For the inelastic asymmetry measurements, the magnetic field of the spectrometer will be lowered to focus inelastic electrons onto the detector bars.

Beyond the present work, further measurements of A_π are not currently foreseen. The G^0 experiment had several physics goals, with a high priority for the elastic asymmetry measurement. Fortunately, the versatility of the G^0 apparatus enabled extra data to be analyzed such as the pion asymmetry data presented in this work. The G^0 experiment also allowed measurements of inelastic electron asymmetries at $Q^2 = 0.35$ (GeV/c)^2 with the LH$_2$ target, for which the data analysis is currently under way [129]. However, lower statistical accuracy combined with significant backgrounds in the inelastic electron locus at those kinematics will make a clear interpretation of the inelastic electron asymmetry measurement more difficult.

Appendix A

Pion production kinematics

A.1 Kinematic variables

This appendix provides more information on the kinematics related to pion production from e-N scattering. All the kinematic variables derived in this section hold for the virtual photon part of the process. Setting $Q^2 = 0$ usually gives the result for real photons when applicable, that is when the equation does not involve the initial or final electron energy. The kinematic variables of the nucleon N and the pion π in the final state can be calculated starting from the center of mass[1] energy W defined as:

$$\begin{aligned} W^2 &= (p_i + q)^2 = p_i^2 + q^2 + 2p_i \cdot q \\ &= m_N^2 - Q^2 + 2(\omega E_i - \vec{p}_i \cdot \vec{q}) = m_N^2 - Q^2 + 2\omega m_N \end{aligned} \tag{A.1}$$

---

[1] Defined for the virtual photon - nucleon system in this context.

where m_N is the mass of the nucleon in the initial state, Q^2 is the four momentum transfer squared defined above and $p_i : (E_i, \vec{p_i})$ is the initial four-momentum of the nucleon in which $\vec{p_i} = 0$ as the nucleon is assumed to be at rest. W can also be expressed as a function of the final kinematic variables in the center of mass:

$$\begin{aligned}
W^2 &= (k_{\pi,CM} + p_{f,CM})^2 \\
&= m_\pi^2 + m_N'^2 + 2(E_{\pi,CM}E_{f,CM} - \vec{p}_{f,CM} \cdot \vec{k}_{\pi,CM}) \\
&= m_\pi^2 + m_N'^2 + 2(E_{\pi,CM}E_{f,CM} + \|\vec{p}_{f,CM}\|^2) \\
&= m_\pi^2 + m_N'^2 + 2(E_{\pi,CM}E_{f,CM} + E_{f,CM}^2 - m_N'^2)\ . \qquad \text{(A.2)}
\end{aligned}$$

where $m_N'^2$ is the mass of the nucleon in the final state and in the last step, momentum conservation was used in the center of mass of the final state decay products, that is $\vec{k}_{\pi,CM} = -\vec{p}_{f,CM}$. Using the energy conservation relation, $W = E_{f,CM} + E_{\pi,CM}$, $E_{f,CM}$ is expressed as:

$$E_{f,CM} = \frac{W^2 + m_N'^2 - m_\pi^2}{2W}\ . \qquad \text{(A.3)}$$

Applying the conservation of momentum relation $|\vec{k}_{\pi,CM}| = |\vec{p}_{f,CM}| = \sqrt{E_{f,CM}^2 - m_N'^2}$, the energy of the produced pion can be calculated to be:

$$E_{\pi,CM} = \frac{W^2 + m_\pi^2 - m_N'^2}{2W}\ . \qquad \text{(A.4)}$$

In order to obtain the above energies in the laboratory frame, one can just apply a Lorentz transformation to it with a Lorentz boost $\vec{\beta} = \vec{q}_{cm}/E_{i,CM}$, where $E_{i,CM}$ is the neutron energy in the photon-neutron center of mass. The standard Lorentz transformation applied to four-vectors is given in Ref. [74], but the expression for $\vec{\beta}$ is still needed. The Lorentz invariant formed by $q \cdot p_i$ is calculated in the laboratory and center of mass frame as:

$$\begin{aligned} q \cdot p_i &= q_{CM} \cdot p_{i,CM} \\ \omega\, m_n &= (\omega_{CM} E_{i,CM} + \vec{q}^{\,2}_{CM}) \ . \end{aligned} \tag{A.5}$$

Using the relations $\omega_{CM} = \sqrt{-Q^2 + \vec{q}^{\,2}_{CM}}$ and $E_{i,CM} = \sqrt{m_n^2 + \vec{q}^{\,2}_{CM}}$ gives:

$$\begin{aligned} (m_n\omega - \vec{q}^{\,2}_{CM})^2 &= (\vec{q}^{\,2}_{CM} - Q^2)(\vec{q}^{\,2}_{CM} + m_n^2) \\ m_n^2\omega^2 - 2\vec{q}^{\,2}_{CM} m_n\,\omega + \vec{q}^{\,4}_{CM} &= \vec{q}^{\,4}_{CM} - Q^2\vec{q}^{\,2}_{CM} - Q^2 m_n^2 + \vec{q}^{\,2}_{CM} m_n^2 \end{aligned} \tag{A.6}$$

which leads to:

$$\vec{q}^{\,2}_{CM} = \frac{m_n^2(\omega^2 + Q^2)}{m_n^2 - Q^2 + 2m_n\omega} = \frac{m_n^2(\omega^2 + Q^2)}{W^2} \tag{A.7}$$

Therefore, the Lorentz boost of the center of mass frame with respect to the laboratory frame is given by:

$$\vec{\beta}_{CM} = -\frac{\vec{q}_{CM}}{E_{i,CM}} \ . \tag{A.8}$$

A.2 Fermi Motion

A neutron inside a nucleus is not at rest; there is a momentum distribution of the neutron with respect to the deuteron rest frame, also referred to as Fermi motion. This can be represented by a momentum distribution $n(p_F)$. This distribution is shown in Figure A.1. When implementing Fermi motion corrections, a cut is placed to set a maximum possible value for the Fermi motion. This cut-off was varied from 80 to 200 MeV/c in the simulations and does not affect the results of the simulations described in Section 3.9.

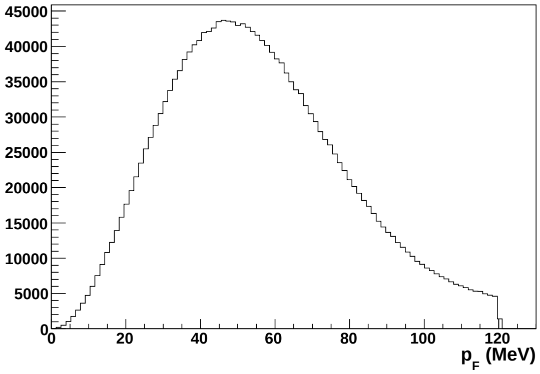

Figure A.1: Fermi momentum distribution with a cut off at 120 MeV. Histogram generated with part of the code of the G0GEANT simulation. Based on Ref. [130].

The Lorentz boost from the laboratory frame to the neutron rest frame associated with Fermi motion is:

$$\beta_{Fermi} = -\frac{\vec{p}_{Fermi}}{E_{Fermi}} \tag{A.9}$$

where $E_{Fermi} = \sqrt{\vec{p}^{\,2}_{Fermi} + m_n^2}$ is the neutron energy in the laboratory frame.

A.2.1 Effect of Fermi motion corrections on the cross section

The effect of Fermi motion corrections on the cross section was investigated. Figure A.2 shows the effect of Fermi motion on the real photon contribution to the pion production differential cross section.

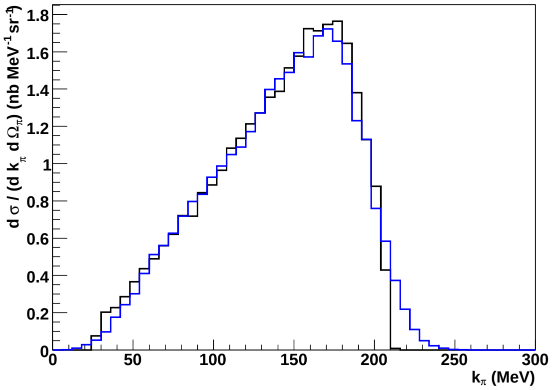

Figure A.2: Real photon differential cross section as a function of pion momentum for a beam energy of 362 MeV. The black curve does not include Fermi motion while the blue curve does. The impact of Fermi motion is not significant.

In the final analysis, the nuclear corrections to pion production cross sections were performed according to [109], and the pion momentum was smeared by a Lorentz boost in the appropriate laboratory frame.

Appendix B

Cerenkov Performance, ARS data

The time of flight method for separating pion and electron events has its limitations with a beam energy of 687 MeV, as a precise enough timing measurement can not be performed to resolve the separation between pion and electron signals. A different method mainly based on the signal amplitude and relying less on the time of flight can be used for the determination of the Cerenkov efficiencies for electrons and pions as well as the π/e and e/π contaminations, $C_{\pi/e}$ and $C_{e/\pi}$ respectively.

The G^0 DAQ contained a device called the Analog Ring Sampler (ARS). This device recorded samples of detector pulse height every ns over a span of 128 ns. For each Fastbus event, there was an array of 128 values that represented an oscilloscope trace of the Cerenkov photomultiplier tube (PMT) signals. These raw ARS data needed to be processed for each event to reconstruct some useful information such as the Integrated ARS (IARS) spectrum, which is equivalent to an Analog to Digital Converter (ADC) spectrum, and the Arrival Time (AT) of the pulse in the ARS module, equivalent to a TDC.

B.1 Integration and calibrations

The ARS signals could be integrated over a tight timing gate in order to obtain an accurate ADC equivalent spectrum. The Figure B.1 shows a typical Cerenkov signal seen by the ARS device.

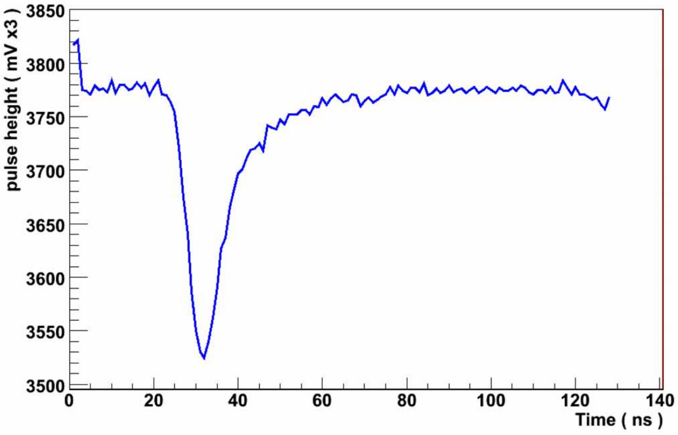

Figure B.1: Signal from one of the Cerenkov PMTs seen by the ARS module for one event. The timing of the ARS module with respect to the trigger system is such that most pulses come around 30-40 ns from the start of recording. There is a boundary effect for early times as seen on the left of the graph.

The signals are integrated over a tight timing gate of 28 ns, and the start of the integration period was given by an arbitrary low threshold setting (equivalent to one quarter of a photoelectron). If the trigger condition was not met, the integration was done within a gate set between 30 and 58 ns. The baseline and its slope were found by a simple linear regression.

This method has 2 main inconveniences; first, it reduces the time range to 95 ns $(= 128 - 28 - 5)$ where the 5 ns cut aims at removing boundary effects (see Figure B.1). Second, it may bias the integral for very small or very broad pulses. Despite those limitations, this method gives consistent results. Figure B.2 shows the reconstructed integrated (IARS) spectrum for octant 4 for each of the 4 PMTs.

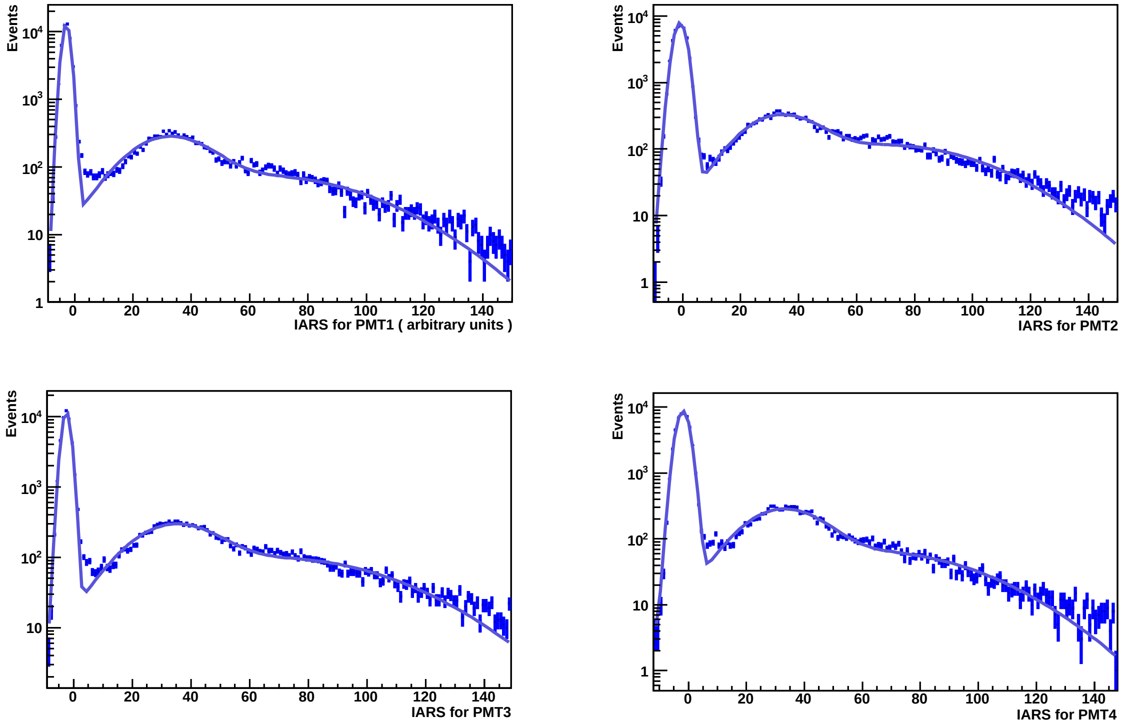

Figure B.2: Integrated ARS spectra (IARS) for each Cerenkov PMT of octant 4. A fit with 3 Gaussians was performed to obtain the distance between the pedestal and the first photoelectron signal (PE) to allow a calibration.

From the IARS distributions, a calibration in terms of number of photoelectrons for each PMT is performed. Figure B.3 shows the result of this calibration after summing the four IARS signals. The error on the location of the single photoelectron peak is not significant enough to affect the rest of the analysis.

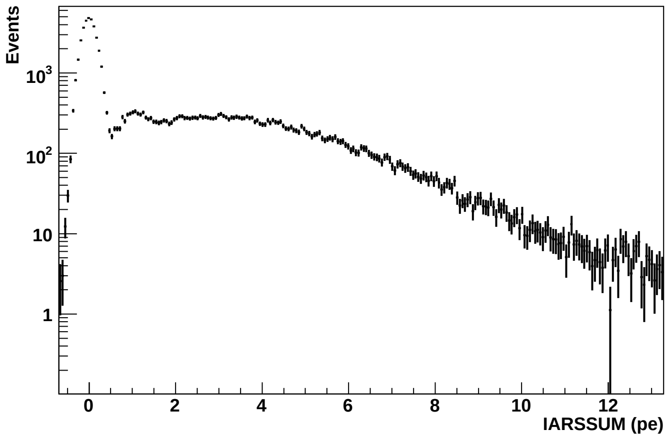

Figure B.3: Spectrum of the sum of the IARS signals over the 4 PMTs of one Cerenkov detector (or IARSSUM) in terms of number of photoelectrons (PE). A small peak corresponding 1 photoelectron can be seen.

B.2 Application: Trigger reconstruction

The behaviour of the G^0 hardware trigger was simulated using the ARS data. For that purpose (see Figure B.1), a new set of variables was generated in the data "ntuple":

- ATpmtX - The arrival time of the pulse[1] when it crossed a certain threshold (which is set to 27mV for FR octants and 20mV for NA octants) for a PMT X. This variable can be understood as the ARS trigger for each PMT.
- ATfirst - The AT of the first pulse in all 4 PMT's crossing that threshold.
- Nfirst - PMT that trigger first.

The first multiplicity 2 requirement was to have at least 2 ATpmtX[2] over 4 not equal to 0. The second condition was on the timing as the trigger requires the signals to be within 20 or 24 ns. This condition was generated by applying a cut on the spectrum

---

[1] When no pulse crossed the threshold, ATpmtX took the value 0.

[2] Basically 2 non-zero values of ATpmtX corresponding to 2 pulses crossing the threshold.

of (ATpmtX - ATfirst) when Nfirst $\neq$ X, Figure B.4 shows this distribution for the Cerenkov PMT 2 of octant 6.

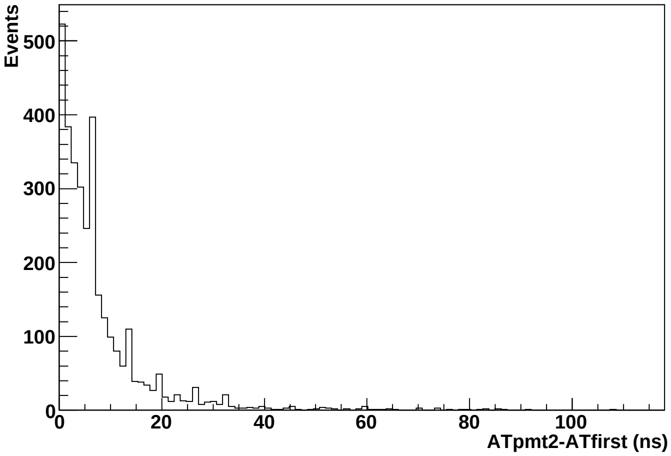

Figure B.4: Histogram of (ATpmt2 - ATfirst) when Nfirst $\neq$ 2 for octant 6. The cut was placed on 20ns for NA octants and 24 ns for FR octants.

The software threshold on the amplitude of the pulses was set to its nominal hardware value (27 mV) for the Fr octants, but was lowered to 20 mV when simulating the trigger for NA octants to improve the results.

The Cerenkov detector electron efficiencies calculated with either the hardware or software trigger are summarized in Table B.1. Results from Ref. [101] based on a similar ToF method are also shown for comparison.

The method presented here is based on the FPD ToFs, whereas the results presented in Table B.1 from Ref. [101] were obtained from averaging Cell by Cell (CbC) efficiencies or by calculating them globally for the relevant loci. Table B.1 shows that correlations

Octant	Hard. Trig.	Soft. Trig.	CbC [101]	Global [101]
1	84.7 ± 0.3%	82.4 ± 0.3 %	82.6 ± 0.3	86.8 ± 0.3
2	82.3 ± 0.3%	80.1 ± 0.3 %	81.3 ± 0.2	84.8 ± 0.3
3	84.5 ± 0.3%	82.5 ± 0.3 %	84.8 ± 0.3	86.3 ± 0.3
4	74.8 ± 0.3%	73.6 ± 0.3 %	73.1 ± 0.3	76.4 ± 0.3
5	79.4 ± 0.3%	75.4 ± 0.4 %	76.7 ± 0.3	82.7 ± 0.3
6	88.2 ± 0.2%	87.0 ± 0.2 %	86.2 ± 0.2	89.3 ± 0.2
7	78.0 ± 0.4%	72.2 ± 0.4 %	76.5 ± 0.3	81.4 ± 0.3
8	83.0 ± 0.3%	79.4 ± 0.3 %	80.2 ± 0.3	83.5 ± 0.2

Table B.1: Electron efficiencies for elastic+inelastic for the 2 different triggers (Software and Hardware). The two columns on the right are the results from Ref. [101]; the efficiencies were calculated either Cell by Cell (CbC) then averaged over the relevant loci, or calculated globally by superposing the ToF spectra for all cells.

between detectors can change the measured efficiencies if one calculates them cell by cell, FPD by FPD or octant by octant.

The large discrepancies between the software and hardware trigger methods for octant 5 and 7 could be explained for octant 5 by baseline noise likely originating from the postamplifiers of the PMTs, which biased the threshold value by a few mV. Figure B.5 shows that this baseline noise that appears very clearly on PMT 4 for octant 5.

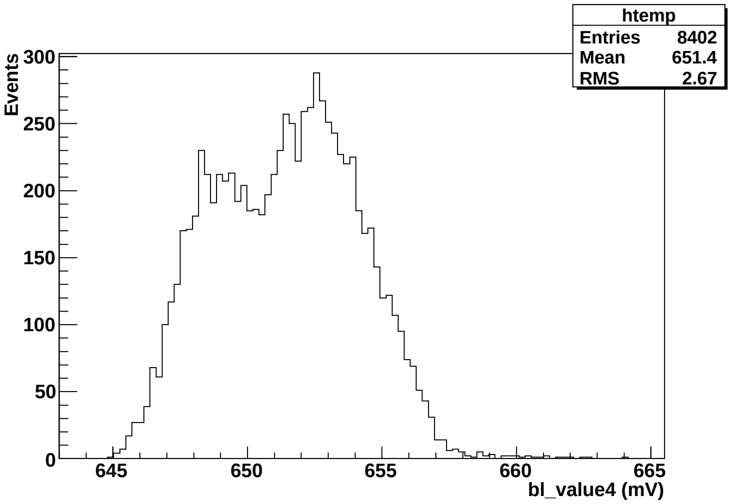

Figure B.5: Baseline spectrum for Cerenkov PMT 4, octant 5. A double peak appears with a separation of about 3-4 mV between the 2 peaks. This was assumed to be due to 60 Hz noise from the postamplifier.

B.3 Application: e/π separation for LD_2 at 687 MeV

As previously mentioned, extraction of the Cerenkov efficiencies[3] for a LD_2 target with a beam energy of 687 MeV was more difficult because of the poor timing resolution. An alternative method using the IARSSUM instead of the ToF spectrum was used in order to make that separation. The strategy was to understand the distribution of the signals detected by the PMT's for either pion or electron events at 362 MeV, where the time of flight separation was simple, and then to combine those two functions to extrapolate to what the contamination would be at 687 MeV. The method also had to rely heavily on simulations to take into account the additional pion contamination from delta rays at 687 MeV.

---

[3] The original setup of the Cerenkov trigger for the LD_2 data at 687 MeV was multiplicity 3, then it changed to multiplicity 2 after the phototubes were upgraded.

B.3.1 Cerenkov response functions at 362 MeV

By placing time of flight cuts on the LD_2 362 MeV data, which have both high pion and electron rates, the IARSSUM spectrum for either case was obtained, as seen in Figures B.6 and B.7.

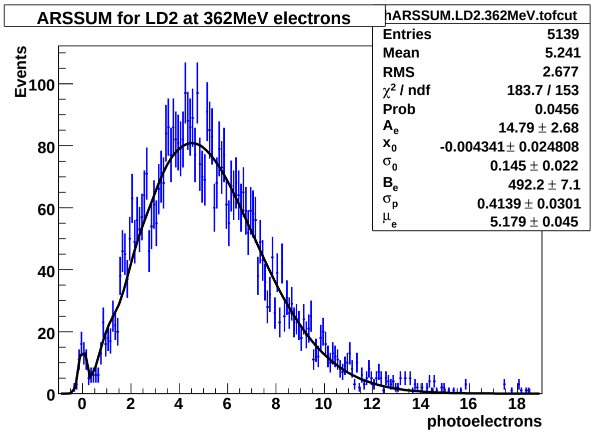

Figure B.6: IARSSUM with time of flight cut to select the electron signals for LD_2 at 362 MeV; the fit is a Poisson distribution convoluted with a Gaussian.

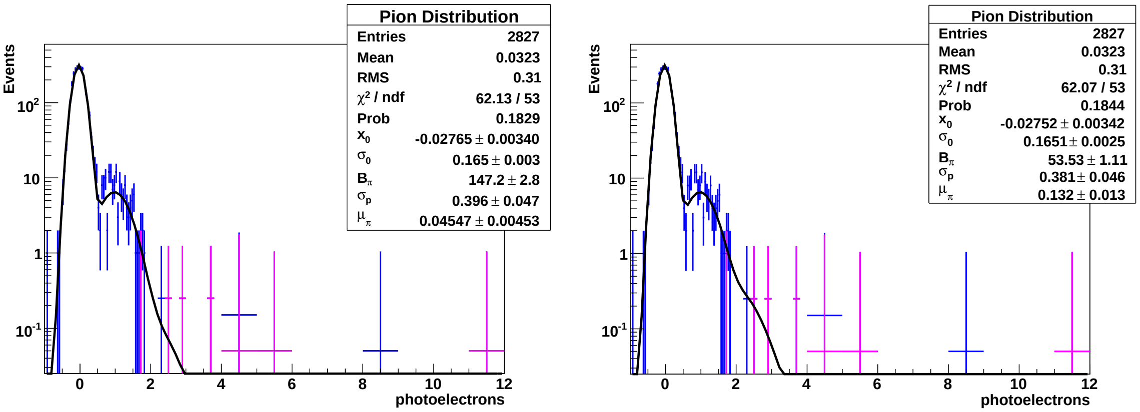

Figure B.7: IARSSUM for octant 6 with time of flight cut to select the pion signals for LD_2 at 362 MeV; the fit is a modified Poisson distribution convoluted with a Gaussian. In the left plot, $\alpha = 1$ and in the right plot, $\alpha = 3$. The purple data are the events selected by the Cerenkov multiplicity 2 trigger.

The IARSSUM spectrum in the electron case was fitted by the following modified

Poisson distribution [131]:

$$P_e(x) = A_e e^{-\frac{1}{2}\left(\frac{x-x_0}{\sigma_0}\right)^2} + \sum_{k=1}^{\infty} B_e \frac{\mu_e^k e^{-\mu_e}}{k!\sigma_p\sqrt{2k\pi}} e^{-\frac{1}{2k}\left(\frac{x-x_0-k}{\sigma_p}\right)^2} \tag{B.1}$$

containing the following parameters (noting the index "e" for electron):

- A_e: Amplitude of the pedestal.
- x_0: Residual shift from 0 after the calibration.
- σ_0: Width of the pedestal.
- B_e: Amplitude of the Poisson.
- σ_p: Width of the Gaussian that is convoluted with the Poisson (or width of single PE peak).
- μ_e: Average value of the Poisson distribution.

The ratio of the integral of the pedestal to the integral of the Poisson was used as a constraint in the electron fit and is be described by the relation:

$$r = \frac{B_e(1-e^{-\mu_e})}{\sigma_0\sqrt{2\pi}A_e} \tag{B.2}$$

Since the average number of photoelectrons is very low in the pion case, the first term ($k = 0$) in the Poisson sum can not be neglected. This term has to be written differently because for $k = 0$, the Gaussian would have zero width, so the width of the pedestal was taken instead. The function used to represent the pion distribution was:

$$P_\pi(x) = \alpha B_\pi \frac{\mu_\pi^0 e^{-\mu_\pi}}{0!\sigma_0\sqrt{2\pi}} e^{-\frac{1}{2}\left(\frac{x-x_0}{\sigma_0}\right)^2} + \sum_{k=1}^{\infty} B_\pi \frac{\mu_\pi^k e^{-\mu_\pi}}{k!\sigma_p\sqrt{2k\pi}} e^{-\frac{1}{2k}\left(\frac{x-x_0-k}{\sigma_p}\right)^2} \tag{B.3}$$

where an additional parameter (α) was added by hand and set to 1 by default. If α is set to a value higher than 1, this means that not all of the pion distribution obeys a Poisson, but instead a fraction of events are just producing a pedestal (as seen in the electron case). Leaving the parameter α free leads to nearly 100 % correlation between μ_π and B_π in the fitting process. α was increased from its default value by a factor of 3 as a test for systematic errors arising from the assumption that Cerenkov response to the pion events obeys a Poisson distribution at 362 MeV.

B.3.1.1 Pion contamination evaluated at 362 MeV using the ARS method

A global fit of the IARSSUM for the LD$_2$ (E_{beam} = 362 MeV) data with a linear combination of Equations (B.1) and (B.3) was performed. The fit function is written as:

$$P_{362}(x) = P_e(x) + P_\pi(x) \tag{B.4}$$

Using Equation (B.4) to fit the elastic LD$_2$ data at 362 MeV, one obtains Figure B.8. The global fit overestimates σ_p, but the reduced χ^2 is still less than 2.

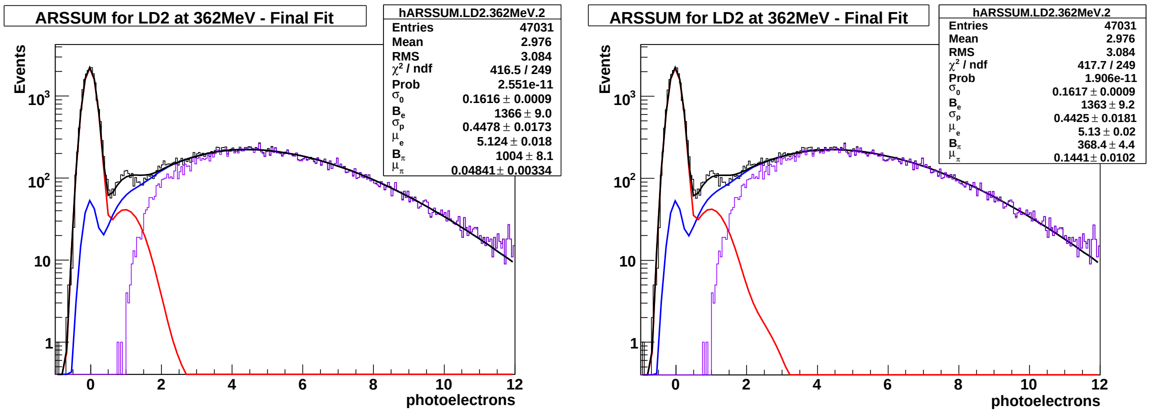

Figure B.8: IARSSUM for octant 6 for LD$_2$ at 362 MeV; the fit is a modified Poisson distribution convoluted with a Gaussian. In the left plot $\alpha = 1$ and in the right plot $\alpha = 3$. $P_e(x)$ appears in blue, $P_e(x)$ in red and the purple histogram represents the events triggered by the Cerenkov detector.

The pion contamination was then calculated using the following formula:

$$C_{\pi/e} = \frac{1}{\sum\limits_i N_i} \sum_i N_i f_i \tag{B.5}$$

where N_i is the bin content of the bin i of the histogram representing the events triggered by the Cerenkov detector and f_i is defined to be:

$$f_i \equiv \frac{P_\pi(i)}{P_e(i) + P_\pi(i)} \; . \tag{B.6}$$

An estimate of the statistical error can be performed. Differentiating with respect to N_j (where j may or may not be equal to i) leads to:

$$\frac{\partial C_{\pi/e}}{\partial N_j} = \frac{\partial}{\partial N_j}\left(\frac{1}{\sum\limits_i N_i} \sum_i N_i f_i \right) = \frac{f_j}{\sum\limits_i N_i} - \frac{\sum\limits_i N_i f_i}{\left(\sum\limits_i N_i \right)^2} \; . \tag{B.7}$$

Hence the statistical contribution to the error on the pion contamination is:

$$\sigma_{cont}^2 = \sum_j \left(\frac{\partial Cont}{\partial N_j}\right)^2 N_j = \sum_j \left(\frac{N_j}{\sum\limits_i N_i} \cdot (f_j - Cont)^2\right) \tag{B.8}$$

Applying this method to octant 6 for LD_2 at a beam energy of 362 MeV gives $Cont(\alpha = 1) = 0.38 \pm 0.02\%$ and $Cont(\alpha = 3) = 0.48 \pm 0.02\%$, which is consitent with the time of flight method besides a very small statistical error. The variation according to α provides a more reasonable information about the real error.

B.3.2 Pion contamination at 687 MeV using the ARS method

B.3.2.1 Inclusion of delta rays

The LD_2 data at 687 MeV are different than at 362 MeV in the sense that additional rates are expected in the Cerenkov detector from delta rays or “knock-on” electrons coming from pions moving through the material in front of the Cerenkov box. Those delta rays are produced either in one of the CEDs, in the Aluminium window or even in the aerogel itself. The kinetic energy spectrum of delta rays is given by [132]:

$$\frac{d^2N}{dTdh} = \frac{1}{2} K \frac{Z}{A} \frac{1}{\beta_\pi^2} \frac{1 - \beta_\pi^2 T/T_{max}}{T^2} \tag{B.9}$$

where T is the kinetic energy of the delta ray, β_π is the pion velocity relative to c, $\frac{d^2N}{dTdh}$ is the number of delta rays produced per incoming pion per unit of length per unit of energy and T_{max} is the maximum kinetic energy of a delta ray given by:

$$T_{max} = 2m_ec^2\beta_\pi^2\gamma^2 = 2m_ec^2\left(\frac{p_\pi}{m_\pi}\right)^2 \tag{B.10}$$

in which p_π is the incoming pion momentum. The average number of photoelectrons detected by the Cerenkov system depends on the kinetic energy of the incoming delta ray via the semi-empirical formula:

$$\bar{x}(T) = \frac{200}{\cos\theta_e}(n\beta_e - 1) \tag{B.11}$$

where the scattering angle of the knock-on electron (θ_e), and its velocity (β_e) are expressed as:

$$\cos\theta_e = \sqrt{\frac{1}{\beta_\pi^2\left(2m_e/T + 1\right)}}, \quad \beta_e = \sqrt{1 - \left(\frac{m_e}{T + m_e}\right)^2} \tag{B.12}$$

Equation (B.11) was defined to obtain $\bar{x} = 6$ for $\beta_e = 1$, that is for a "good" electron, neglecting the angular dependence $\cos\theta_e$.

The relations above were used to generate a Monte Carlo simulations of the Cerenkov detector response to pions via delta rays. Starting with a simplified case where the pion momentum p_π had a fixed value of $400 MeV/c$ in order to compare with the available test data taken at TRIUMF, the kinetic energy was generated flat between $T_{min} = 2$ MeV, which is slightly above Cerenkov threshold ($1.6 MeV$) and $T_{max}(p_\pi) = 8.4 MeV$.

A random number for $x = [-1, 12]$ (the number of photoelectrons detected in the Cerenkov) and $y = [0, y_{max}]$ (the amplitude of the response function) were also generated.

The values of $d^2N/(dTdh)$, $\bar{x}(T)$, $\cos\theta$ and $P(x, \bar{x}(T))$ (Poisson distribution described in Equation (B.3) but with no α and $\bar{x}$ replacing μ_π) were then calculated. For each generated event, the following condition was applied; if $y < d^2N/(dTdh)P(x, \bar{x})$ the event was kept, if not a new event was generated. The results from this procedure are shown in Figure B.9. The distribution of the delta ray signals is similar to a Poisson with a longer tail which can be successfully fitted by:

$$\begin{aligned} P_\delta(x) &= (ax^3 + bx^2 + cx + d) \\ &\times \left(B_\delta \frac{e^{-\mu_\delta}}{\sigma_0\sqrt{2\pi}} e^{-\frac{1}{2}\left(\frac{x-x_0}{\sigma_0}\right)^2} + \sum_{k=1}^{\infty} B_\delta \frac{\mu_\delta^k e^{-\mu_\delta}}{k!} \frac{1}{\sigma_p\sqrt{2k\pi}} e^{-\frac{1}{2k}\left(\frac{x-x_0-k}{\sigma_p}\right)^2} \right) \end{aligned} \tag{B.13}$$

where a, b, c and d are additional fit parameters.

In order to normalize this to the overall pion rates, a numerical integration of $d^2N/(dTdh)$ was performed and proved to be consistent with the analytical integral:

$$\Delta N = \Delta h \int_{T_{min}}^{T_{max}} \frac{d^2N}{dTdh} dT = \Delta h \frac{1}{2} K \frac{Z}{A} \frac{1}{\beta_\pi^2} \frac{1}{T_{min}T_{max}} \left(T_{max} - T_{min} - T_{min}\beta_\pi^2 ln \frac{T_{max}}{T_{min}} \right) \tag{B.14}$$

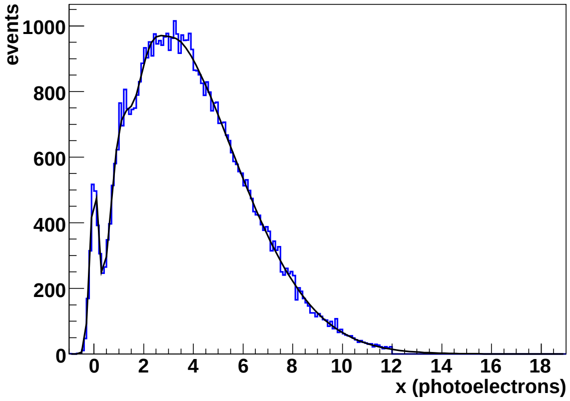

Figure B.9: Simulated response function of the Cerenkov detector to delta rays. This corresponds to a superposition of Poissons with different values of $\bar{x}$ and weighted by $d^2N/(dTdh)$.

where T was assumed to not depend on the thickness of the material which was taken to be $\Delta h = 1g/cm^2$. That value is justified by the fact that low energy knock-on electrons do not produce much light in the Cerenkov detector and by considering the radiation lengths of the various layers of material in front of and within the Cerenkov detector. Those values are summarized in Table B.2.

Material	thickness	Density	$\Delta h(g/cm^2)$	X_0 at 1.6 MeV
CED	1 cm	1.0	1	0.8 cm
Al Window	0.08 cm	2.7	0.21	0.3 cm
Aerogel	5 cm	0.14	0.7	6.5 cm

Table B.2: Radiation length of electrons at threshold passing through the different layers of material in front and in the Cerenkov detector. Taking an average value of $\Delta h = 1$ g/cm^2 is a reasonable choice.

For a 400 MeV/c incoming pion, the probability to create a delta ray is $\Delta N = 0.0238$. This value was used to normalize the simulation with the pion pedestal, as shown in Figure B.10.

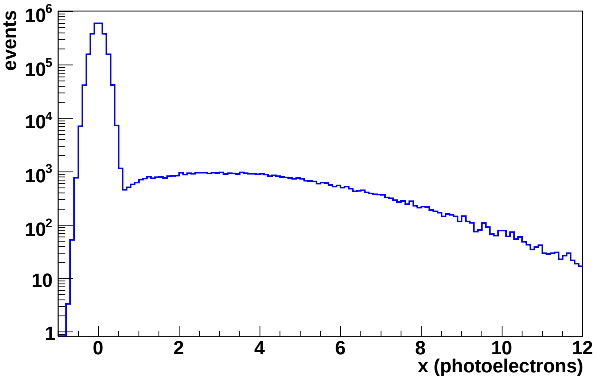

Figure B.10: Simulated response function of the Cerenkov detector to delta rays including the pions that contributed only to the pedestal.

These results can be combined with the results of Figure B.7 adding the delta ray distribution to the fitted LD_2 pion data, that is:

$$P_\pi^{Total}(x) = P_\pi(x) + \lambda P_\delta(x) \tag{B.15}$$

where λ is a normalization factor proportional to $\Delta N = 0.0238$. This function was used to compare the various pion efficiencies with respect to different pion momenta and analog sum Cerenkov thresholds. There is fairly good agreement between the delta-ray simulation and the beam test data taken at TRIUMF, as seen in Figures B.11 and B.12.

B.3.2.2 Results for LD_2 at 687 MeV

Before using the delta-ray simulation and the analysis at 362 MeV in Section B.3.1.1 to extract the pion contamination, an estimation of the amount of random signals detected by the Cerenkov detectors had to be performed. The main analysis of the production runs includes rate corrections, and the purpose here is to extract a contamination due to

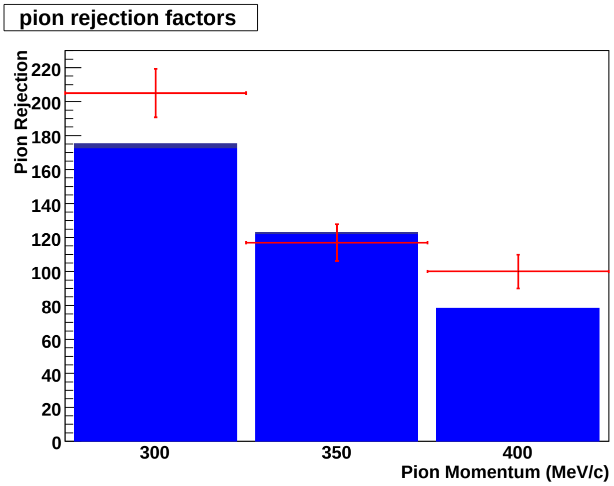

Figure B.11: Comparison of pion rejection factors for a 3 photoelectron sum threshold taken with different incoming pion momenta. The red dots are the results from the beam tests taken at TRIUMF with an incident pion beam angle of 15 degrees. The blue bars represent the results using $P_{\pi}^{Total}(x)$ which does not account for any incident pion beam angle. The lighter blue is for the $\alpha = 1$ case, and the darker blue is for $\alpha = 3$. Note that the data at 300 MeV/c were taken with a thicker CED (1.3 cm).

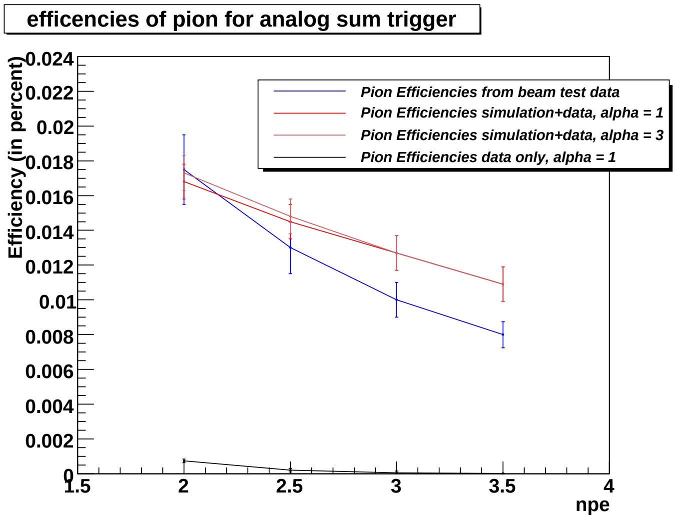

Figure B.12: Comparison of pion efficiencies as a function of the analog sum threshold taken at pion momentum of 400 MeV/c. The blue line is taken from the the beam tests taken at TRIUMF. The red lines are using P_{π}^{Total}. The black line is $P_{\pi}(x)$ only. The incident pion beam angle is 0° (that is entering the Cerenkov detector at normal incidence).

Cerenkov detector imperfections. The contribution from randoms is even larger at 687 MeV due to neutrons coming from the target being absorbed by the individual Cerenkov PMTs, as previously discussed. The best known way to estimate this contribution using the ARS is to use the 'ATfirst' spectrum shown in Figure B.13 for LD_2 at 362 MeV.

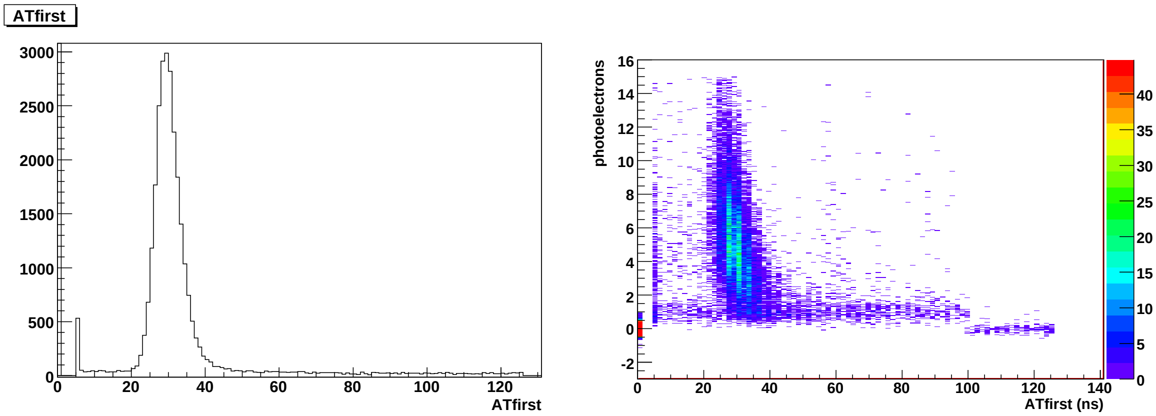

Figure B.13: The left plot represents the timing distribution of the Cerenkov signal or ATfirst; there is a high number of entries (off scale) at 0 which means no signal was detected, then a peak when the signals arrive at the right time window, and a flat layer of random events. The small peak at 5ns is an artifact of the calibration that is suppressed with timing cuts. The right graph shows the same on the horizontal axis but on the vertical axis is IARSSUM; most of the random events produce around 1 photoelectron in total.

A Cerenkov timing cut was placed to reduce the contribution of randoms to the IARSSUM spectrum. The cut consisted of keeping the pedestal at $ATfirst = 0$ and the events which were in time within a gate of 30 ns, and removing everything else. This approach clearly biases the shape of the pion distribution because random events were intended to contribute to the pedestal in the first place. This issue was resolved by integrating the random events arriving between $ATfirst = 60$ and $ATfirst = 90$, as seen in Figure B.13, and extrapolating to the range where they contribute to bias the pion distribution. In the case of Figure B.13, that would be over a range of 108 ns.

This integral was then related to the number of events in the pedestal. That led to a correction of 5 to 15% that was directly applied to the α parameter of the fit. The correction to α is written as:

$$\alpha' = \alpha \frac{N_{ped} + N_{rand}}{N_{ped}} \tag{B.16}$$

where N_{ped} and N_{rand} are the number of events in the pedestal and the number of random events respectively. This correction varies octant by octant and with the beam energy setting, so it was applied to ensure that the α parameter had the same meaning for all sets of data.

There is a residual amount of random events beneath the distribution of time events which arrive in the correct time window. For the LD_2 data at 362 MeV, one can simply apply a time of flight cut to select pion signals and use their $ATfirst$ spectrum to estimate the fraction of randoms under the pion distribution:

$$f_{rand} = \frac{N^{\pi}_{rand}}{N^{\pi}_{gate}} \tag{B.17}$$

where N_{gate} are the pion events occurring in time within a gate of 30 ns. The correct function to use in order to fit the LD_2 data at 687 MeV is:

$$P_{687}(x) = P_{\pi}^{Total}(x) + P_e(x) + \frac{A_{rand}}{\sqrt{2\pi}\sigma_p} e^{-\frac{1}{2}\left(\frac{x - x_0 - 1}{\sigma_p}\right)^2} \tag{B.18}$$

where $P_\pi^{Total}(x)$ and $P_e(x)$ were defined in the earlier sections, and the last term accounts for residual Cerenkov randoms mainly seen at 1 photoelectron. Several comments have to be made on $P_\pi^{Total}(x)$ and on how A_{rand} will be handled. The pion part of the fit is almost fully constrained, the only free parameter being its amplitude and the widths of the Gaussian terms. For the delta ray contribution, a customized simulation was done taking into account μ_e extracted from a first iteration of the final fit and used in the following way:

$$\bar{x}(T) = \frac{\mu_e}{6}\frac{200}{\cos\theta_e}(n\beta_e - 1) \tag{B.19}$$

which accounts for the fact that μ_e is different from 6 as assumed earlier, and depends on the octant. The fitting process was done using different hypothesis:

- The average number of photoelectrons in $P_\pi(x)$ is constrained by the fit at 362 MeV shown on Figure 13 but then multiplied by $1 - f_{rand}$ to correct for the Cerenkov randoms. In that case, A_{rand} is left as a free parameter.

- The average number of photoelectrons is a fit parameter and the value of A_{rand} is fixed to a value estimated in a similar way as what was done for f_{rand}.

- In either case, 2 different values for α (1 and 3) are tested.

All the fits are shown in Figure B.14 to B.21. The difference between the various assumptions was taken as a systematic error.

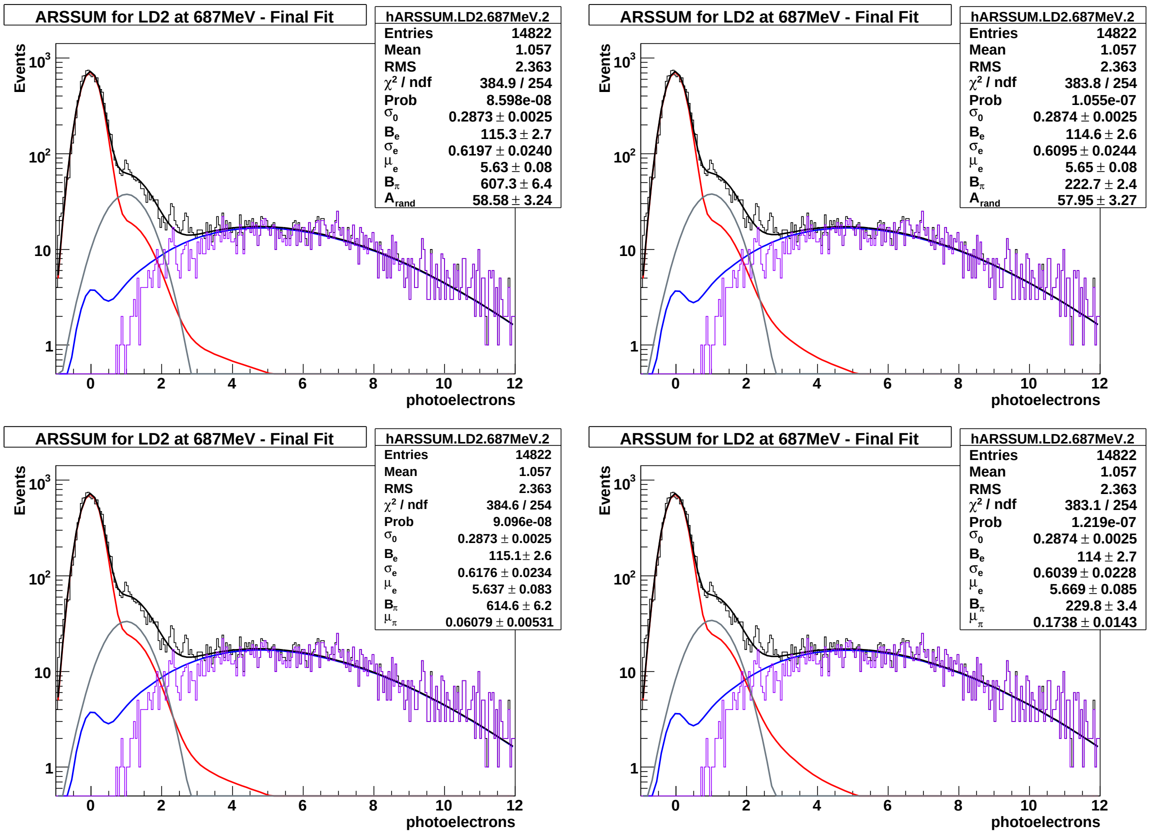

Figure B.14: Fit of the elastic LD_2 data at 687 MeV for octant 1. The grey curve represents the residual random contribution. The top graphs have the average number of photoelectrons constrained using the LD_2 data at 362 MeV. The graphs at the bottom have the fit parameter A_{rand} constrained by its estimate using the ATfirst spectrum. The left plots have α set to 1 and the right plots have α set to 3.

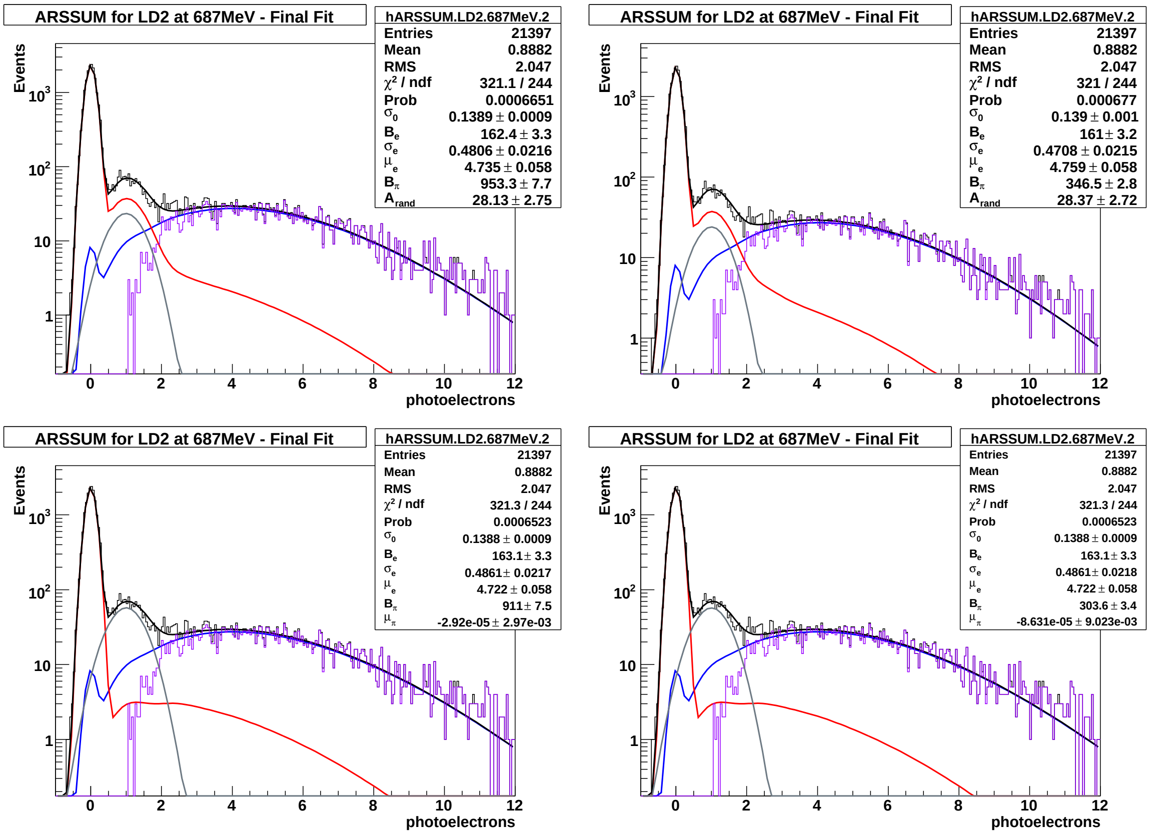

Figure B.15: Fit of the elastic LD_2 data at 687 MeV for octant 2. The grey curve represents the residual random contribution. The top graphs have the average number of photoelectrons constrained using the LD_2 data at 362 MeV. The graphs at the bottom have the fit parameter A_{rand} constrained by its estimate using the ATfirst spectrum. The left plots have α set to 1 and the right plots have α set to 3.

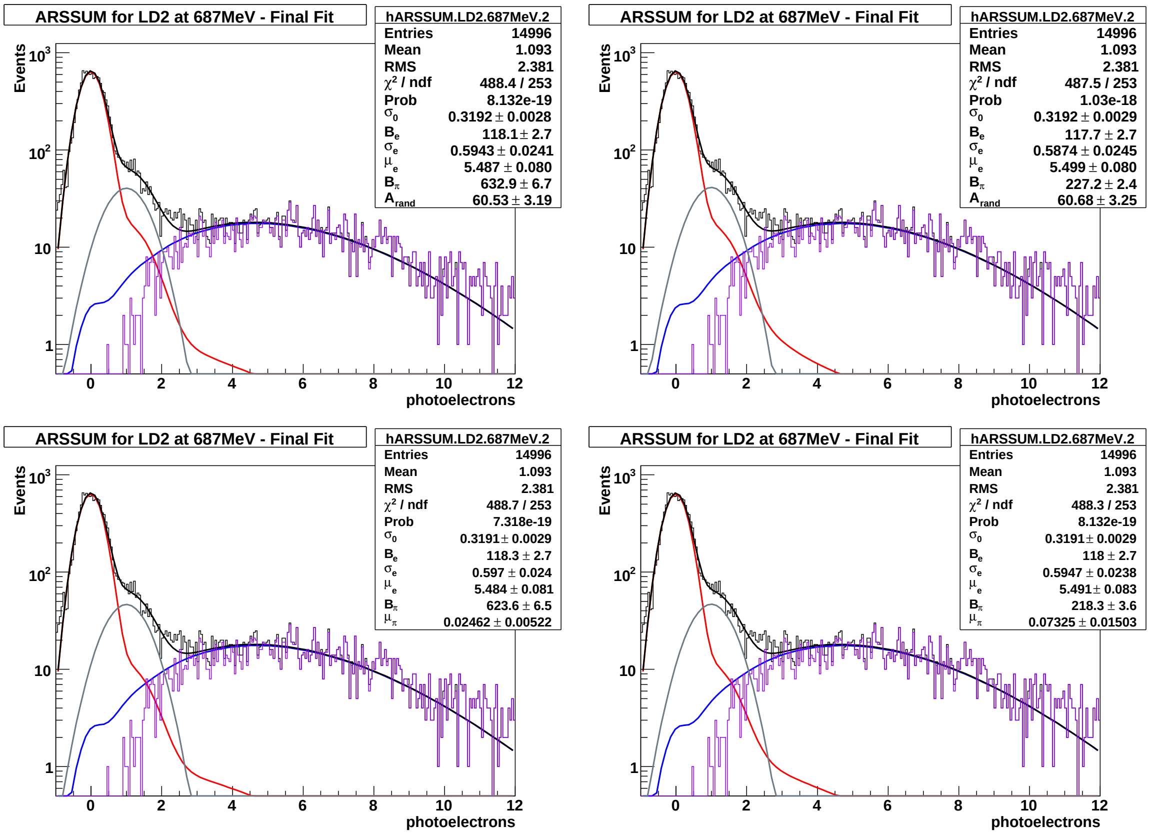

Figure B.16: Fit of the elastic LD$_2$ data at 687 MeV for octant 3. The grey curve represents the residual random contribution. The top graphs have the average number of photoelectrons constrained using the LD$_2$ data at 362 MeV. The graphs at the bottom have the fit parameter A_{rand} constrained by its estimate using the ATfirst spectrum. The left plots have α set to 1 and the right plots have α set to 3.

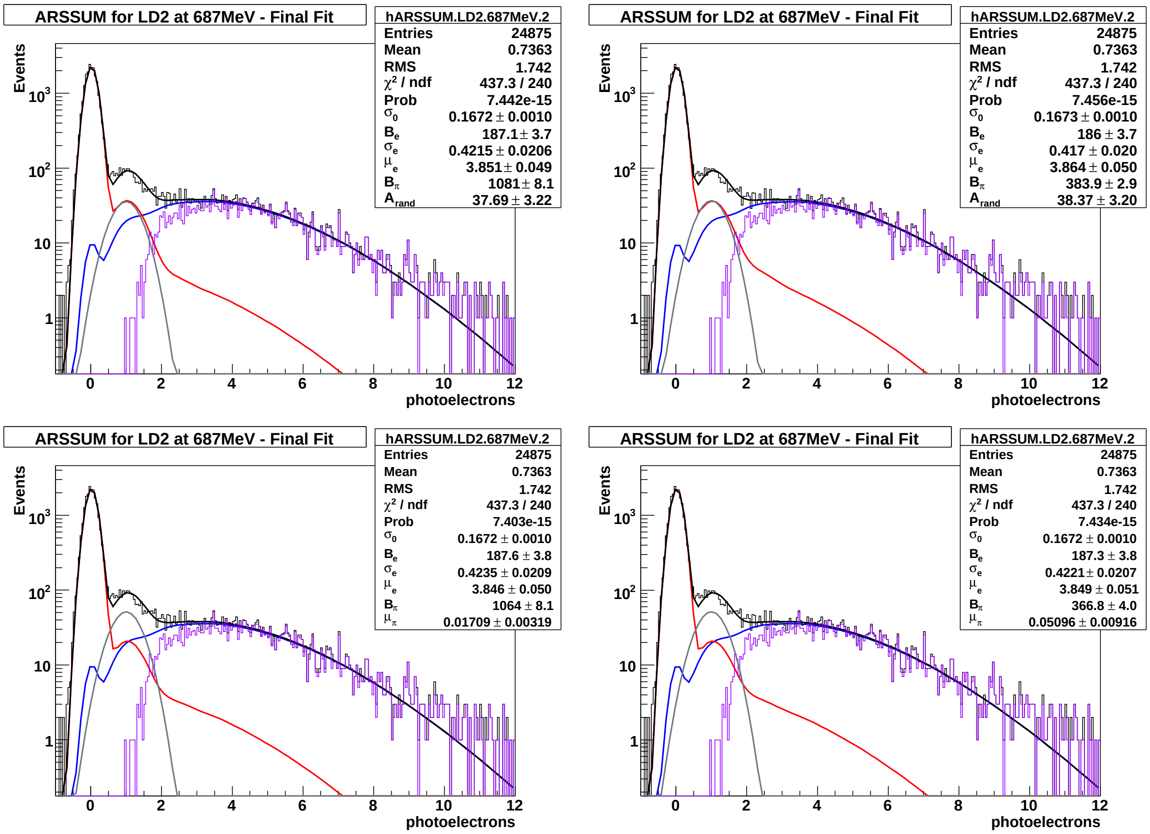

Figure B.17: Fit of the elastic LD_2 data at 687 MeV for octant 4. The grey curve represents the residual random contribution. The top graphs have the average number of photoelectrons constrained using the LD_2 data at 362 MeV. The graphs at the bottom have the fit parameter A_{rand} constrained by its estimate using the ATfirst spectrum. The left plots have α set to 1 and the right plots have α set to 3.

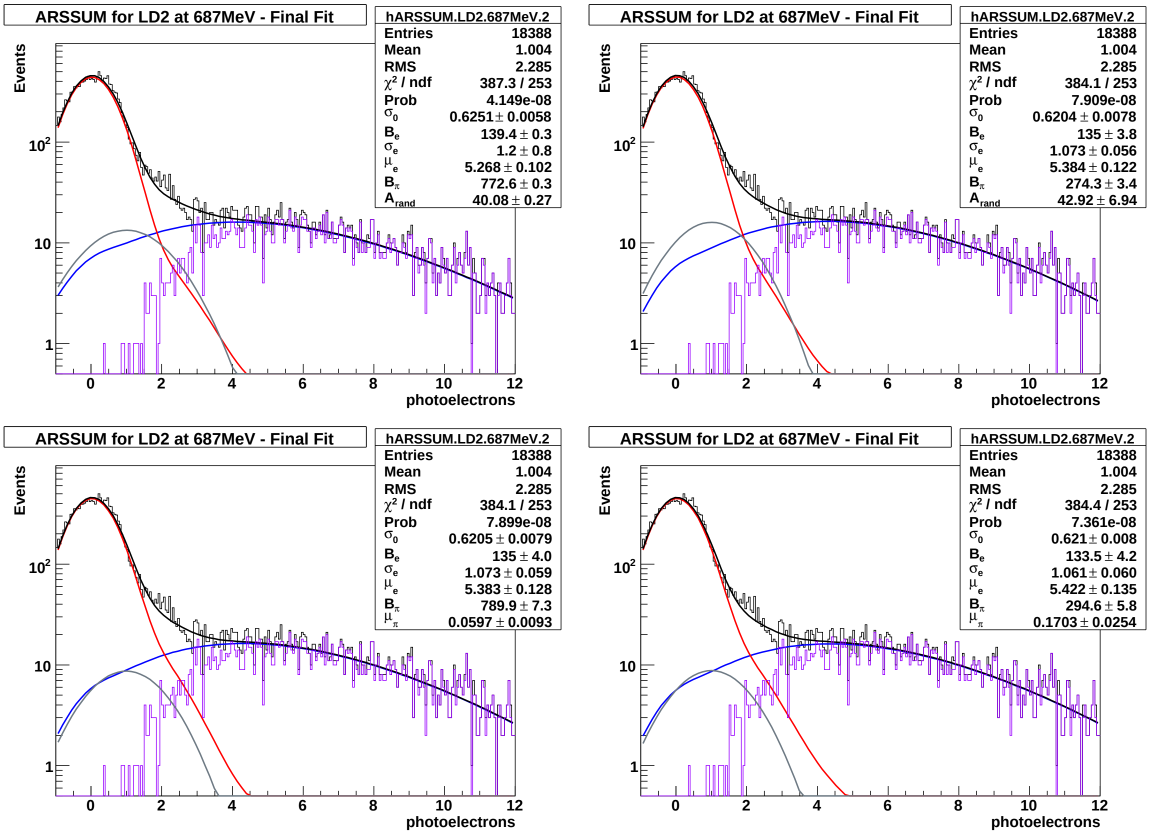

Figure B.18: Fit of the elastic LD$_2$ data at 687 MeV for octant 5. The grey curve represents the residual random contribution. The top graphs have the average number of photoelectrons constrained using the LD$_2$ data at 362 MeV. The graphs at the bottom have the fit parameter A_{rand} constrained by its estimate using the ATfirst spectrum. The left plots have α set to 1 and the right plots have α set to 3.

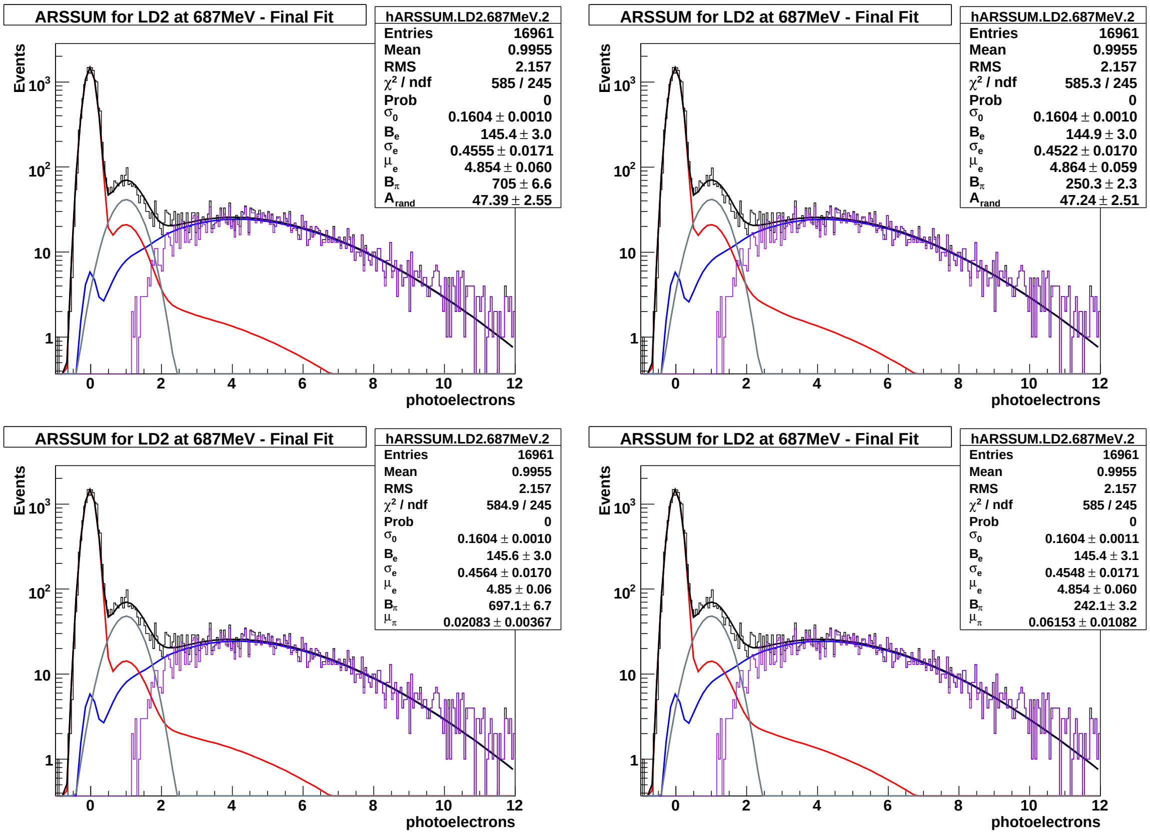

Figure B.19: Fit of the elastic LD_2 data at 687 MeV for octant 6. The grey curve represents the residual random contribution. The top graphs have the average number of photoelectrons constrained using the LD_2 data at 362 MeV. The graphs at the bottom have the fit parameter A_{rand} constrained by its estimate using the ATfirst spectrum. The left plots have α set to 1 and the right plots have α set to 3.

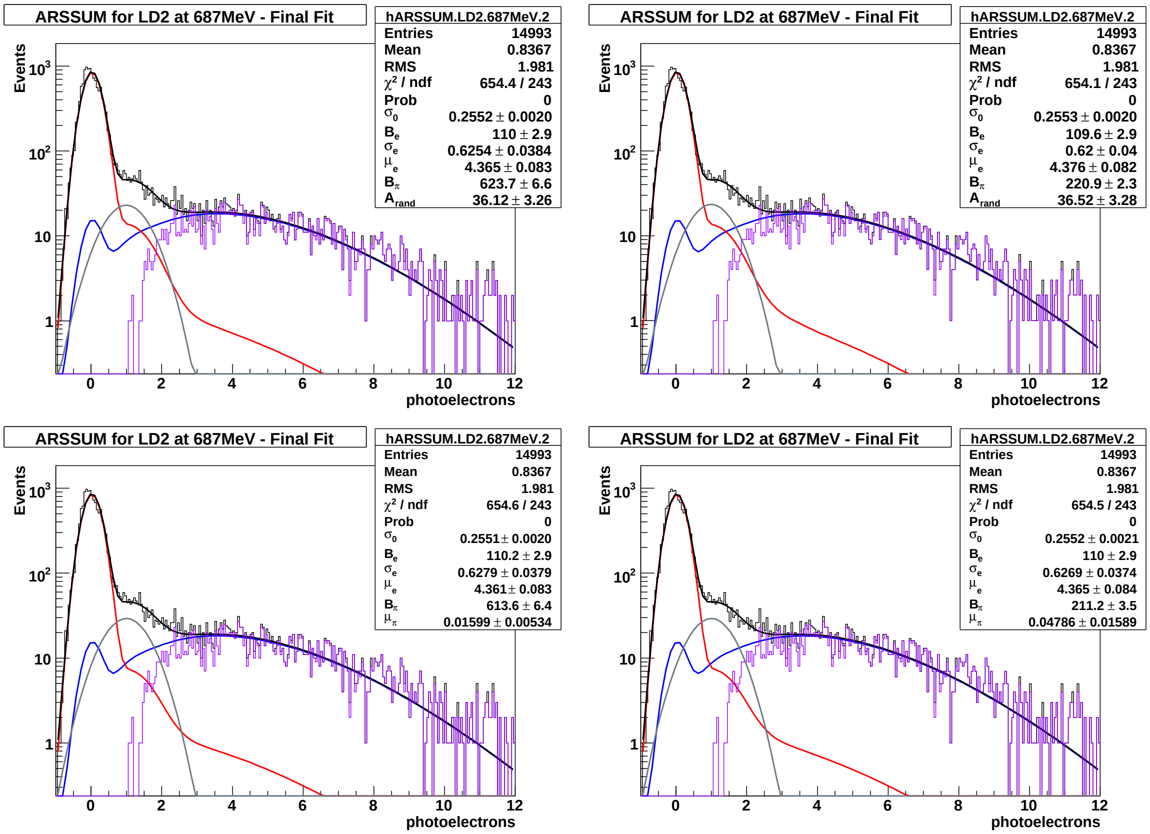

Figure B.20: Fit of the elastic LD$_2$ data at 687 MeV for octant 7. The grey curve represents the residual random contribution. The top graphs have the average number of photoelectrons constrained using the LD$_2$ data at 362 MeV. The graphs at the bottom have the fit parameter A_{rand} constrained by its estimate using the ATfirst spectrum. The left plots have α set to 1 and the right plots have α set to 3.

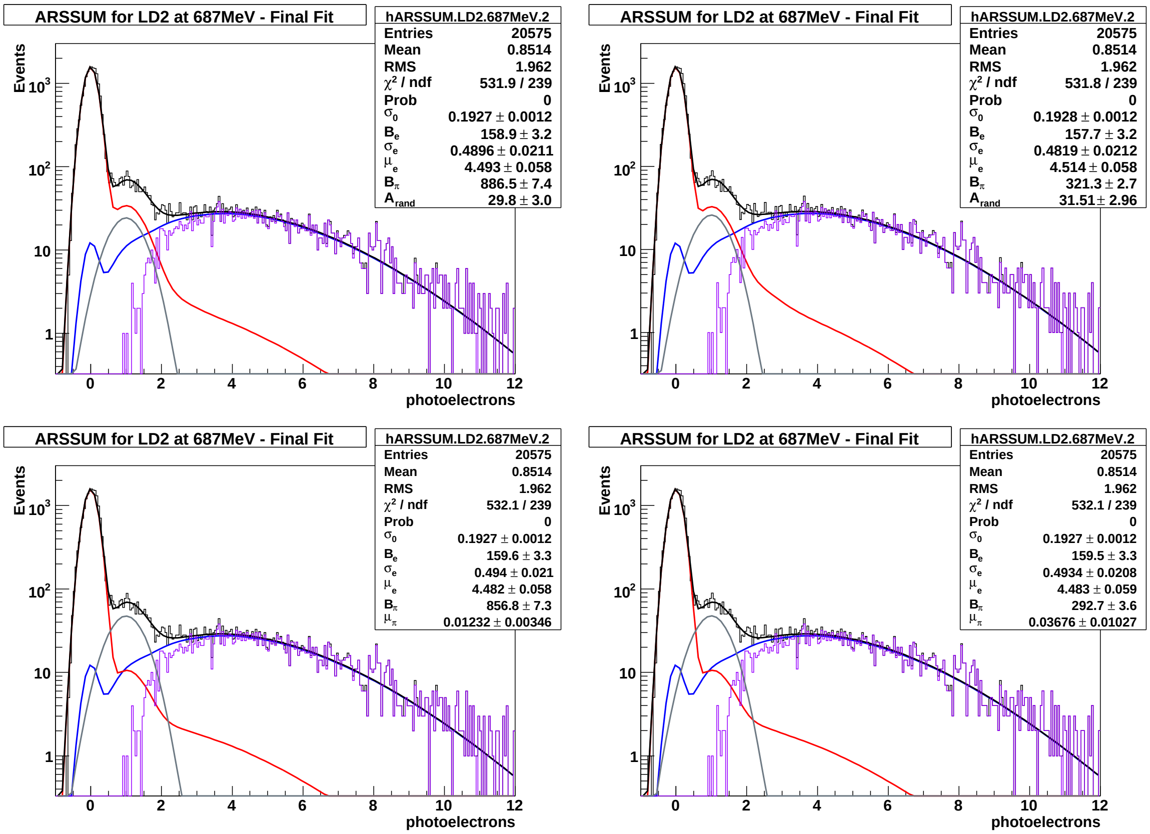

Figure B.21: Fit of the elastic LD_2 data at 687 MeV for octant 8. The grey curve represents the residual random contribution. The top graphs have the average number of photoelectrons constrained using the LD_2 data at 362 MeV. The graphs at the bottom have the fit parameter A_{rand} constrained by its estimate using the ATfirst spectrum. The left plots have α set to 1 and the right plots have α set to 3.

The pion contaminations with respect to different trigger setups and assumptions are summarized in Table B.3 and B.4. Octant 2 has a much worse contamination but is also much less consistent than the others, as seen by comparing the fit parameters shown in Table B.5.

Pion contamination and electron efficiencies in percent					
Octant	Pion Cont.($\alpha = 1$)		Pion Cont.($\alpha = 3$)		$\boldsymbol{\epsilon}_e$
	μ_π	A_{rand}	μ_π	A_{rand}	
1	6.08	6.50	6.48	7.04	88
2	7.64	6.11	8.08	6.11	86
3	4.74	4.17	4.98	4.30	93
4	5.52	5.07	5.79	5.15	74
5	4.93	5.77	4.75	6.26	70
6	5.36	5.10	5.57	5.18	87
7	5.33	4.49	5.50	4.56	78
8	5.80	4.71	6.19	4.75	81

Table B.3: Multiplicity 2 electron efficiencies and pion contaminations for the elastic LD_2 data at 687 MeV.

The overall variation of the contamination results with respect to the various assumptions is 4.17 to 8.08% for the multiplicity 2 trigger, and 1.73 to 4.72% for the multiplicity 3 trigger. Octant variations of the pion contamination do not scale as they should with their corresponding values of electron efficiencies. This should be taken as an additional systematic error. However, the origin of this discrepancy can be explained by comparing the ratio of Cerenkov triggered events over the non triggered ones with the electron to pion ratio from the pass 3 production data. This comparison is summarized in Table B.6.

Pion contamination and electron efficiencies in percent					
Octant	Pion Cont.($\alpha = 1$)		Pion Cont.($\alpha = 3$)		ϵ_e
	μ_π	A_{rand}	μ_π	A_{rand}	
1	2.40	2.45	2.50	2.60	51
2	4.61	4.47	4.72	4.47	49
3	1.78	1.73	1.85	1.76	53
4	3.32	3.27	3.39	3.29	35
5	1.96	1.98	1.80	2.19	33
6	3.52	3.48	3.58	3.50	51
7	2.93	2.82	3.00	2.84	38
8	3.27	3.12	3.39	3.14	47

Table B.4: Multiplicity 3 electron efficiencies and pion contaminations for the elastic LD_2 data at 687 MeV.

Pion contamination and electron efficiencies in percent						
Octant	A_{rand}^{fit}	A_{rand}^{est}	$\mu_\pi^{fit}(\alpha = 1)$	$\mu_\pi^{fit}(\alpha = 3)$	$\mu_\pi^{362}(\alpha = 1)$	$\mu_\pi^{362}(\alpha = 3)$
1	58	51	0.061	0.173	0.049	0.143
2	28	70	< 0.002	< 0.01	0.045	0.131
3	60	60	0.024	0.073	0.039	0.112
4	37	54	0.017	0.051	0.033	0.096
5	41	23	0.059	0.170	0.034	0.101
6	47	55	0.020	0.061	0.032	0.095
7	36	46	0.016	0.047	0.032	0.092
8	30	59	0.012	0.036	0.046	0.129

Table B.5: The fit parameters A_{rand} and μ_π compared with their estimated values. The estimations of randoms are consistent with the fit results. Constraining both parameters to their estimates at the same time would make the fit fail for some octants (2 in particular).

There is a 5 to 25 % difference between the ARS data and the pass 3 data. Taking the results to be correct for the production runs, it becomes clear that cuts performed on the ARS analysis biased the number of electron events with respect to the number of pion events. The direct consequence is assumed to be an overestimation of the pion

$Cer/\bar{C}er$ ratio for pass 3 and ARS data

Octant	pass3 ratio	ARS data ratio	Difference (%)	Y_e	Y_π
1	0.197	0.170	13.7	0.77	3.9
2	0.200	0.165	17.5	0.72	3.6
3	0.187	0.178	4.8	0.77	4.1
4	0.170	0.134	21.1	0.68	4.0
5	0.161	0.118	26.7	0.76	4.7
6	0.198	0.187	5.8	0.79	4.0
7	0.171	0.145	15.2	0.73	4.3
8	0.204	0.157	23.0	0.69	3.4

Table B.6: Ratio of events triggering the Cerenkov detector over events not triggering it for pass3 and ARS data. Y_e and Y_π are the pass3 elastic electron and pion yields in kHz/μA respectively.

contamination by 5 to 25%. The difference can be explained by several effects:

- The histograms are cut at 12 photoelectrons[4], hence biasing by a small amount the electron yield toward lower values.
- Cuts were made on the ARS data because a number of events were not synchronized with the rest of the Fastbus data, potentially biasing the e/π ratio.
- The trigger used in the Fastbus data might not fully represent the coincidence trigger used for the scalers.
- A change in the Cerenkov efficiency might have occurred between the 31 MHz runs and the multiplicity 2 production runs.

A correction to the pion contamination based on these values was performed. This

---

[4] The main reason is that the calibration procedure for each Cerenkov PMT require a integration range of 28 ns, which is not enough to integrate accurately much more than 3 PE (per PMT). The fitting method used would therefore be biased if IARSSUM events at more than 12 PE were included.

corrects would fix the octant dependence of the pion contamination and also lowers its average value by about 15 %. This was done for the multiplicity 2 and 3 triggers and the results are shown in Table B.7 and B.8 respectively.

Pion contamination and electron efficiencies in percent					
Octant	Pion Cont.($\alpha = 1$)		Pion Cont.($\alpha = 3$)		$\boldsymbol{\epsilon}_e$
	μ_π	A_{rand}	μ_π	A_{rand}	
1	5.22	5.20	5.57	6.05	88
2	6.26	5.01	5.01	6.62	86
3	4.50	3.96	4.54	4.08	93
4	4.36	4.00	4.57	4.06	74
5	3.59	4.06	3.46	4.56	70
6	5.03	4.79	4.79	4.86	87
7	4.53	3.81	4.67	3.87	77
8	4.46	3.62	4.76	3.65	81

Table B.7: Multiplicity 2 electron efficiencies and pion contaminations for the elastic LD_2 data at 687 MeV. These data are corrected toward lower values by a percentage according to Table B.6.

The latter results are relatively more sensible than the previous ones, so the median value for each octant was taken and a systematic error according to the magnitude of contamination variations was assigned. This leads to the results shown in Table B.9 and B.10 for multiplicity 2 and 3 triggers respectively. Those values are used for an octant to octant correction to the pion contamination. A global error of 30% on the average contamination from the simulation was also assigned. That conservative error is justified by the worse agreement between the TRIUMF data and the fact that the latter were not taken exactly under the same conditions as the G^0 experiment.

Pion contamination and electron efficiencies in percent					
Octant	Pion Cont.($\alpha = 1$)		Pion Cont.($\alpha = 3$)		ϵ_e
	μ_π	A_{rand}	μ_π	A_{rand}	
1	2.07	2.11	2.15	2.24	51
2	3.80	3.69	3.89	3.69	49
3	1.69	1.64	1.76	1.67	53
4	2.62	2.58	2.67	2.59	35
5	1.43	1.45	1.31	1.60	33
6	3.32	3.27	3.37	3.30	51
7	2.48	2.39	2.54	2.41	38
8	2.51	2.40	2.61	2.41	47

Table B.8: Multiplicity 3 electron efficiencies and pion contaminations for the elastic LD_2 data at 687 MeV. These data are corrected toward lower values by a percentage according to Table B.6.

Pion contamination and electron efficiencies		
Octant	Pion Cont. (%)	ϵ_e (%)
1	$5.6 \pm 0.4_{sys} \pm 0.3_{stat}$	88
2	$5.8 \pm 0.8_{sys} \pm 0.2_{stat}$	86
3	$4.2 \pm 0.3_{sys} \pm 0.2_{stat}$	93
4	$4.3 \pm 0.3_{sys} \pm 0.1_{stat}$	74
5	$4.1 \pm 0.6_{sys} \pm 0.2_{stat}$	70
6	$4.9 \pm 0.1_{sys} \pm 0.1_{stat}$	87
7	$4.2 \pm 0.5_{sys} \pm 0.2_{stat}$	77
8	$4.2 \pm 0.6_{sys} \pm 0.2_{stat}$	81

Table B.9: Multiplicity 2 electron efficiencies and pion contaminations summary for the elastic LD_2 data at 687 MeV.

Pion contamination and electron efficiencies		
Octant	Pion Cont. (%)	$\boldsymbol{\epsilon}_e$ (%)
1	$2.2 \pm 0.1_{sys} \pm 0.1_{stat}$	51
2	$3.8 \pm 0.2_{sys} \pm 0.1_{stat}$	49
3	$1.7 \pm 0.1_{sys} \pm 0.1_{stat}$	53
4	$2.6 \pm 0.1_{sys} \pm 0.1_{stat}$	35
5	$1.5 \pm 0.1_{sys} \pm 0.1_{stat}$	33
6	$3.3 \pm 0.1_{sys} \pm 0.1_{stat}$	51
7	$2.5 \pm 0.1_{sys} \pm 0.1_{stat}$	38
8	$2.5 \pm 0.1_{sys} \pm 0.1_{stat}$	47

Table B.10: Multiplicity 3 electron efficiencies and pion contaminations summary for the elastic LD_2 data at 687 MeV.

Bibliography

[1] F. Halzen and A. D. Martin, *Quarks & Leptons*, Wiley, 1984. 4, 5, 6, 7, 8, 10, 139, 140

[2] J. Liu, *A measurement of the strange quark contributions to the electromagnetic form factors of the nucleon.*, PhD thesis, University of Maryland., 2006. 5, 8, 13, 16, 43, 44, 73, 75, 115, 117

[3] D. R. Yennie, The Rosenbluth formula, in *Nucleon Structure*, edited by R. Hofstadter and L. I. Schiff, page 11, 1964. 7

[4] R. McKeown, Phys. Lett. B, **219**, 2-3, p. 140–142, 1989. 8

[5] D. Beck, Phys. Rev. D (Particles and Fields), **39**, 11, p. 3248–3256, 1989. 8

[6] M. J. Musolf et al., Phys. Rept., **239**, p. 1–178, 1994. 10, 16, 19

[7] C. Amsler et al., (Particle Data Group), Physics Letters B, **667**, 1, 2008. 10, 17, 26, 27, 28, 70

[8] M. Versteegen, *Mesure par violation de parité de la contribution étrange à la structure électromagnétique du nucléon dans l'expérience* G^0, PhD thesis, Université Joseph Fourier - Grenoble 1, 2009. 11, 45, 64, 67, 88, 101, 102, 105, 107, 109, 110, 111, 112, 113, 117

[9] E. Reya and K. Schilcher, Phys. Rev. D, **10**, p. 952, 1974. 11

[10] S.-L. Zhu, S. Puglia, B. R. Holstein, and M. J. Ramsey-Musolf, Phys. Rev. D, **62**, 033008, 2000. 12, 22, 36

[11] D. B. Kaplan and A. Manohar, Nuclear Physics B, **310**, 1988. 13

[12] G. A. Miller, Phys. Rev. C, **57**, p. 1492, 1998. 13

[13] W. M. Alberico, S. M. Bilenky, C. Giunti, and K. M. Graczyk, Phys. Rev. C, **79**, 6, p. 065204, 2009. 14

[14] D. S. Armstrong et al., Phys. Rev. Lett., **95**, 092001, 2005. 17

[15] D. S. Armstrong et al., Phys. Rev. Lett., **104**, 012001, 2010. 17, 33, 35, 37, 41, 110, 135

[16] F. Close, S. Donnachie, and G. Shaw, *Electromagnetic interactions and hadronic structure*, Cambridge University Press, 2007. 17

[17] N. C. Mukhopadhyay, M. J. R. Musolf, S. J. Pollock, J. Liu, and H.-W. Hammer, Nuclear Physics A, **633**, p. 481–518, 1998. 18, 19, 38

[18] S.-L. Zhu, C. M. Maekawa, G. Sacco, B. R. Holstein, and M. J. Ramsey-Musolf, Phys. Rev. D, **65**, 3, p. 033001, 2001. 19, 20, 21, 22, 23, 26, 27, 28, 29, 165, 168, 169, 171, 172, 173

[19] L. M. Nath, K. Schilcher, and M. Kretzschmar, Phys. Rev. D, **25**, 2300, 1982. 21

[20] T. Kitagaki et al., Phys. Rev. D, **42**, 5, p. 1331–1338, 1990. 21, 38

[21] S. P. Wells, N. Simicevic, K. Johnston, and T. A. Forest, Measurement of the Parity Violating Asymmetry in the $N - \Delta$ transition, Jefferson Laboratory PAC proposal: E97-104., 2001. 21

[22] M. J. Musolf and B. R. Holstein, Phys. Lett. B, **242**, 461, 1990. 22

[23] M. J. Musolf and B. R. Holstein, Phys. Lett. D, **43**, 2956, 1991. 22

[24] J. L. Friar and S. Fallieros, Phys. Rev. C, **29**, 5, 1984. 23

[25] A. J. F. Siegert, Phys. Rev., **52**, 787, 1937. 23

[26] J. J. Sakurai, *Currents and mesons*, the University of Chicago Press, 1969. 24

[27] M. E. Peskin and D. V. Schroeder, *An Introduction to Quantum Field Theory*, Addison-Wesley Advanced Book Program (now Perseus Books), 1995. 25

[28] B. Desplanques, J. F. Donoghue, and B. R. Holstein, Annals of Physics, **124**, p. 449–495, 1980. 25

[29] B. Borasoy and B. R. Holstein, Phys. Rev. D, **59**, 054019, 1999. 25, 27, 28

[30] A. LeYaounac, O. Pene, and J.-C. Raynal, Nucl. Phys. B, **149**, p. 321–342, 1979. 25

[31] M. Gavela, A. LeYaounac, O. Pene, and J.-C. Raynal, Phys. Lett. B, **101**, 6, p. 417–421, 1981. 25

[32] J. Lach and P. Zenczykowski, Int. J. Mod. Phys. A, **10**, 3817, 1995. 25

[33] B. Borasoy and B. R. Holstein, Eur. Phys. J. C, **6**, p. 85–107, 1999. 25

[34] Y. Hara, Phys. Rev. Lett., **12**, 378, 1964. 25

[35] R. H. Graham and S. Pakvasa, Phys. Rev. B, **140**, 1144, 1965. 26

[36] E. Golowich and B. R. Holstein, Phys. Rev. D, **26**, 182, 1982. 26

[37] H. Neufeld, Nuclear Physics B, **195**, 281, 1993. 26

[38] J. J. Sakurai, Phys. Rev., **156**, 5, p. 1508–1510, 1967. 29

[39] S.-L. Zhu, C. M. Maekawa, B. R. Holstein, and M. J. Ramsey-Musolf, Phys. Rev. Lett., **87**, 201802, 2001. 30, 162, 167, 173

[40] C. Y. Prescott et al., Phys. Lett. B, **77**, 347, 1978. 33

[41] C. Y. Prescott et al., Phys. Lett. B, **84**, 524, 1979. 33

[42] D. Spayde et al., Phys. Rev. Lett, **84**, 1106, 2000. 33

[43] D. T. Spayde, *Measurement of the strange magnetic form factor of the proton using elastic electron scattering*, PhD thesis, University of Maryland, 2001. 33

[44] E. Beise, M. Pitt, and D. Spayde, Progress in Particle and Nuclear Physics, **54**, p. 289–350, 2005. 33, 36

[45] S. Baunack et al., Phys. Rev. Lett., **102**, 151803, 2009. 33, 36

[46] F. E. Maas et al., Phys. Rev. Lett., **94**, 152001, 2005. 33

[47] D. S. Armstrong et al., Phys. Rev. Lett., **95**, 092001, 2005. 33, 34, 35, 41

[48] K. A. Aniol et al., Phys. Rev. C, **69**, 065501, 2004. 33

[49] K. A. Aniol et al., Phys. Rev. B, **635**, 275, 2006. 33

[50] K. A. Aniol et al., Phys. Rev. Lett., **96**, 022003, 2006. 33

[51] A. Acha et al., Phys. Rev. Lett., **98**, 032301, 2007. 33

[52] D. Beck et al, Measurement of the flavor singlet charge form factor for the proton, G_E^o, Jefferson Laboratory PAC proposal: PR-91-017, 1993. 34, 41

[53] D. Beck et al., The G^0 Experiment: Forward Angle Measurements, Jefferson Laboratory PAC proposal (PR-00-006), 2000. 34

[54] D. Beck, G0 Backward Angle Experiment, G0 Collaboration Document 833-v1. 36

[55] J. Liu, R. D. McKeown, and M. J. Ramsey-Musolf, Phys. Rev. C, **76**, 025202, 2007. 36

[56] D. B. Leinweber et al., Phys. Rev. Lett., **94**, 212001, 2005. 36

[57] D. B. Leinweber et al., Phys. Rev. Lett., **97**, 022001, 2006. 36

[58] P. Wang, D. B. Leinweber, A. W. Thomas, and R. D. Young, Phys. Rev. C, **79**, 065202, 2009. 36

[59] T. Doi et al., Phys. Rev. D, **80**, 094503, 2009. 36

[60] A. Bodek, S. Avvakumov1, R. Bradford, and H. Budd, Eur. Phys. J. C, **53**, 349, 2008. 37

[61] D. B. Leinweber, T. Draper, and R. M. Woloshyn, Phys. Rev. D, **46**, 7, p. 3067–3085, 1992. 38

[62] T. R. Hemmert, B. R. Holstein, and N. C. Mukhopadhyay, Phys. Rev. D, **51**, 1, p. 158–167, 1995. 38

[63] S. L. Adler, Phys. Rev. D, **12**, 9, p. 2644–2665, 1975. 38

[64] R. Carlini, S. Page, and M. Pitt, Beam parameter specifications for the G^0 experiment (back angle running). Technical Report, G0 Collaboration Document 640-v1, 2005. 50

[65] J. Hansknecht and M. Poelker, Phys. Rev. ST Accel. Beams, **9**, 6, p. 063501, 2006. 51

[66] E. Stangland, R. Flood, and H. Dong, G0 helicity digital controls, g0 collaboration document 572-v1, 2001. 53

[67] J. M. Grames, *Measurement of a Weak Polarization Sensitivity to the Beam Orbit of the CEBAF Accelerator*, PhD thesis, University of Illinois, 2000. 54, 56, 59, 60, 61

[68] M. Hauger et al., NIM A, **462**, 382, 2001. 54, 55

[69] S. Phillips et al, Moller polarimetry in the G0 Experiment, g0 collaboration document 614-v1, 2005. 54

[70] M. Steigerwald, MeV Mott Polarimetry at Jefferson Lab, Jefferson Lab Document. 54, 59, 60

[71] D. Gaskell and T. Horn, Beam polarization for G0 backward angle, G0 Collaboration Document 804-v1, 2007. 57, 58, 61, 62

[72] N. Sherman, Phys. Rev., **103**, 6, p. 1601, 1956. 60

[73] K. B. Unser, Cern report cern-sl-91-42-bi, 1991. 64

[74] J. D. Jackson, *Classical Electrodynamics, Third Edition*, Wiley, 1999. 65, 79, 179

[75] V. Tvaskis, *Longitudinal-Transverse Separation of Deep-Inelastic Scattering at low Q^2 on Nucleons and Nuclei*, PhD thesis, Vrije Universiteit Amsterdam, 2004. 66

[76] K. A. Aniol et al., Phys. Rev. C, **69**, 065501, 2004. 67

[77] S. D. Covrig et al., Nuclear Instruments and Methods, **551**, p. 218–235, 2005. 68

[78] S. D. Covrig, *A measurement of parity-violating asymmetries in the G^0 experiment in forward mode*, PhD thesis, California institute of technology, 2004. 70

[79] C. Ellis, Luminosity monitors for the gzero backward angle measurement, G0 Collaboration Document 845-v1, 2009. 72

[80] Apparatus for the G0 Experiment, G0 Collaboration Document 716-v1, 2007. 73

[81] M. Muether, Dilutions from field scan analysis, G0 Collaboration Document 850-v1, 2009. 74, 88

[82] J.-S. Real, Pictures from G0Geant, G0 Collaboration Document 843-v3, 2009. 76

[83] J. W. Martin, Aerogel Cerenkov Counter Design, G0 Collaboration Document 180-v1. 79

[84] L. Hannelius, Aerogel Cherenkov Test Counter Studies, G0 Collaboration Document 217-v1. 79

[85] Photonis, Brive, France, www.photonis.com. 80, 81

[86] H. Breuer, C. L. Ellis, and T. R. Gentile, Neutron detection studies in bare phototubes using cold neutrons at NIST, UMD Technical Report Number: PP# 06-052, 2006. 80, 81

[87] G. F. Knoll, *Radiation detection and measurement*, John Wiley & sons, 1979. 81

[88] W. A. Watson, et al., CODA: a scalable, distributed data acquisition system, in Proc. of the Real Time 1993 Conf., p. 296; G. Heyes et al., The CEBAF on-line data acquisition system, in Proc. CHEP Conf., 1994, p. 122; D.J. Abbott, et al., CODA Performance in the real world, 11th IEEE NPSS Real Time 1999 Conf., JLab-TN-99-12; coda.jlab.org. 85

[89] C. Ellis, Electromagnetic radiative corrections for the gzero experiment at backward angles, G0 Collaboration Document 840-v4, 2009. 87

[90] J.-S. Real, Scaler simulation update, G0 Collaboration Document 776-v1, 2009. 101, 102

[91] J.-S. Real, Scaler: description of the RCS pb, G0 Collaboration Document 693-v1, 2007. 101, 102

[92] C. Furget, Systematic uncertainty for rcs, G0 Collaboration Document 821-v1. 101

[93] P. Pillot, Deadtime correction, G0 Collaboration Document 679-v1. 102, 105, 106

[94] M. Versteegen, Global dead time correction analysis, G0 Collaboration Document 726-v1. 108

[95] M. Versteegen, Private Communication. 108

[96] M. Versteegen, Final error budget on rate correction for electronics effects, G0 Collaboration Document 818-v5. 112

[97] C. Furget, Private Communication. 113

[98] P. R. Bevington and D. K. Robinson, *Data reduction and analysis for physical science, second edition*, McGraw-Hill, Boston, 1992. 115

[99] P. King and J. W. Martin, Private Communication. 117

[100] H. J. Beise, http://g0web.jlab.org/backanglelog/Simulation/46. 117

[101] M. Versteegen, Cerenkov efficiency estimation (LD_2 362 MeV), G0 Collaboration Document 764-v1, 2008. 123, 187, 188

[102] J. Mammei, Cerenkov efficiencies summary, G0 Collaboration Document 839-v1, 2009. 123

[103] M. Versteegen, Cerenkov efficiency estimation (LD_2 687 MeV), G0 Collaboration Document 765-v1, 2008. 125

[104] J. W. Martin, g0log: Entry number 133150. 127

[105] T. Donnelly and A. Raskin, Annals of Physics, **169**, 2, p. 247–351, 1986. 130

[106] J. Mammei, Private Communication. 132

[107] D. Dreschsel and L. Tiator, Journal of Physics G (Nuclear and Particle Physics), **18**, 3, p. 449–97, 1992. 136, 138, 142, 143, 145, 146

[108] O. Hanstein, D. Drechsel, and L. Tiator, Nuclear Physics A, **632**, 4, p. 561–606, 1998. 136, 142

[109] P. Benz et al., Nuclear Physics B, **65**, 1, p. 158–209, 1973. 136, 143, 144, 151, 152, 181

[110] M. I. Niculescu, *Inclusive resonance electroproduction data from hydrogen and deuterium and studies of quark-hadron duality*, PhD thesis, Hampton University, 1999. 136, 152

[111] H. Fraas, Z. Phys. A, At. Nuclei (West Germany), **234**, 5, p. 472–478, 1970. 141

[112] J. Matthews and R. Owens, Nuclear Instruments and Methods, **111**, 1, p. 157–168, 1973. 142, 145, 151

[113] S. S. Kamalov, S. Nan Yang, D. Drechsel, O. Hanstein, and L. Tiator, Phys. Rev. C, **64**, 3, p. 032201, 2001. 143

[114] http://wwwkph.kph.uni-mainz.de/MAID//maidnew/maidnew.html. 143, 145

[115] L. Tiator, Private Communication. 143

[116] L. Tiator and L. Wright, Nuclear Physics A, **379**, 3, p. 407–414, 1982. 145, 149, 150, 151

[117] J. W. Martin, Possibility to Measure Parity Violation in Δ photoproduction, 2001. 145, 148, 151

[118] J. W. Martin, Private Communication. 150, 151

[119] R. Tieudent et al., Experimental background contributions to the g0 backward angle measurements, G0 Collaboration Document 195-v1, 2001. 152, 153

[120] E. Rollinde, G0-Geant Manual, G0 Collaboration Document 101-v1, 1999. 153

[121] CERN Program Library Long writeup W5013, GEANT, Detector Description and Simulation Tool Version 3.2.1, 1994. 153

[122] Frischknecht, A. and Döbeli, M. and Stehling, W. and Strassner, G. and Truöl, P. and Alder, J. C. and Joseph, C. and Loude, J. F. and Perroud, J. P. and Ruegger, D. and Tran, M. T. and Panke, H., Phys. Rev. C, **38**, 5, 1988. 154

[123] H. Baer, K. Crowe, and P. Truol, Advances in Nuclear Physics, **9**, 3, 1977. 154

[124] Y.-S. Tsai, Review of Modern Physics, **46**, 4, 1974. 158

[125] H. Olsen and L. C. Maximon, Phys. Rev., **114**, 3, p. 887–904, 1959. 159

[126] J. Mammei, Final Q2 report, G0 Collaboration Document 829-v3. 161, 165

[127] S. P. Wells, T. A. Forest, and K. E. Myers (For the Qweak Collaboration), A Proposal to use Existing TBA time on the JLab Experiment Schedule: A Hadronic PV Measurement to Probe QCD Symmetry Breaking Effects via the

Parity Violating N-Δ Asymmetry at Low Q^2, Jefferson Laboratory PAC Letter Of Intent: LOI-105, 2009. 174

[128] D. S. Armstrong et al, The QWeak Experiment: A Search for New Physics at the TeV Scale via a Measurement of the Protons Weak Charge, Jefferson Laboratory PAC proposal: E02-020, 2004. 174

[129] C. Capuano, Private Communication. 175

[130] P. Bosted, R. G. Arnold, S. Rock, and Z. Szalata, Phys. Rev. Lett., **49**, 19, p. 1380–1383, 1982. 180

[131] M. Iodice et al., Nuclear Instruments and Methods in Physics Research Section A: Accelerators, Spectrometers, Detectors and Associated Equipment, **411**, 2-3, p. 223–237, 1998. 191

[132] J. W. Martin, Pion Rejection of Aerogel Cerenkov Counter, G0 Collaboration Document 229-v1, 2001. 194